High Index Contrast Platform for Silicon Photonics

Shoji Akiyama

B. Eng. Applied Chemistry (1995)
Kyoto University, Kyoto, Japan

M. S. Chemistry (1997)
Kyoto University, Kyoto, Japan

Submitted to the Department of Materials Science and Engineering in Partial Fulfillment of the Requirements for the Degree of

Doctor of Philosophy in Electronic, Photonic and Magnetic Materials

at the

MASSACHUSETTS INSTITUTE OF TECHNOLOGY
September 2004

© Massachusetts Institute of Technology, 2004. All rights reserved

Author: ______________________________
Department of Materials Science and Engineering
August 5, 2004

Certified by: ______________________________
Lionel C. Kimerling
Thomas Lord Professor of Materials Science and Engineering
Thesis advisor

Accepted by: ______________________________
Carl V. Thompson II
Stavros Salapatas Professor of Materials Science and Engineering
Chair, Departmental Committee on Graduate Students

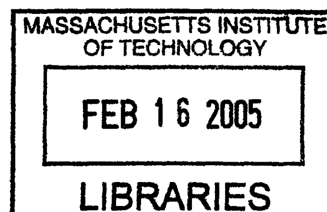

ARCHIVES

High Index Contrast Platform for Silicon Photonics

by

Shoji Akiyama

Submitted to the Department of Materials Science and Engineering on August 5, 2004, in partial fulfillment of the requirements for the Degree of Doctor of Philosophy in Electronic, Photonic and Magnetic Materials

Abstract

This thesis focuses on silicon-based high index contrast (HIC) photonics. In addition to mature fiber optics or low index contrast (LIC) platform, which is often referred to as Planar Lightwave Cirrcuit (PLC) or Silica Optical Bench (SiOB), the use of HIC platform has been attracting considerable attention recently for the purpose of dense integration of optical components on chip. There are two ultimate solutions to mold of the flow of light. One is high index contrast HIC optics, where the index difference (Δn) of core and cladding is more than 0.5 and light is strongly confined in the core, which enables us to integrate optical circuits in μm order. Another technique is the introduction of photonic crystal, with which the flow of light is controlled by its photonc bandgap (PBG) and the defect. The concept of photonic crystal can be applied to optical wavgeuides by placing the defect, which is surrounded with photonic crystal structures. In addition to wavgeuide applications, there are lots of unexplored attractive applications for photonic crystal, especially for high index contrast photonic crystal (HIC-PC or HIC-PBG), such as Si/SiO_2 or Si/Si_3N_4 materials systems, due to the wide stop-band. In this thesis, the various applications based on HIC-PBG platform are proposed and investigated. All of the works in this thesis are based on Silicon CMOS-compatible techniques for practical applications. In first three chapters (chapter 2,3 and 4), waveguide applications are mainly focused based on HIC or HIC-PBG platform. In the latter chapters (chapter 5, 6 and 7), the applications of HIC-PBG are explored such as visible-light reflector, semiconductor saturable absorber (SESAM) and thermophotovoltaic (TPV) applications.

Thesis Supervisor: Lionel Cooper Kimerling
Title: Thomas Lord Professor of Materials Science and Enginnering.

Acknowledgement

In this acknowledgement, I afresh found so many people supported my research and helped me out. In the concept of Buddhism, everyone is related to each other more or less and I strongly feel it is true especially here at M.I.T. First of all, I am deeply grateful to my fearless advisor, Professor Kimerling. He has been a great teacher, a scientist, an engineer and a colleague. It is thanks to his great guidance that I could survive a graduate life at this severe and challenging environment here at M.I.T. for four years. His leadership and deep understanding of materials science have always encouraged me to go ahead. Since I arrived here, he always welcomed discussions and I was really inspired by his vision for the future. He never forced or pressured me to do something but guided me to think about what is necessary to achieve the purpose and to realize our dream. Working with him was always fun. He was much more than a thesis advisor.

I would also like to thank the late professor Haus for having discussion many times to talk about air trench waveguide and other topics. Discussion with him was always inspiring and encouraging. I sincerely pray for the repose of his soul. I learned a lot about other applications of PBG devices and many things from Prof. Kaertner. He has always been friendly and welcomed my questions and discussions. Working and discussing with him was stimulating. I am really appreciative of that. Prof. Ross encouraged me during the most difficult period. When I had a first child here and took an oral exam, she taught me how to overcome this tough situation with maximum patience. I have no words to express my gratitude to her.

I would like to devote my gratitude to Kazumi (Wada-sensei). I often visited his office when I encountered a problem or try to find something new and interesting. I was always amazed his infinite idea and vast background knowledge. He always kept his friendly attitude no matter how busy he was. And he introduced many of his friends to me, which opened new world to me. Jurgen's vast background always helped me understand not only photonics but also other fields. It is my precious memory to attend MRS at San Francisco in 2003 with him.

Other EMAT members also enriched my research life. I guess that my thanks will exceed my Ph.D. thesis I pages if I write how much I appreciate their help and support. I have so many memories with Aimee, Anu, Anat, Atsushi, Ching-yin, Dan, Dave,

Donghwan, Douglas, JaeHyung, Jessica, Jifeng, Mike, Mitra, Mindy, Nok, Nori, Pascal, Sajan, Trisha, Yasha, Yasu, Victor and Xiaoman. I have good memories with each member. And I would also like to mention about EMAT graduates. Andy, Dezmond, Kevin (Lee) and Kevin (Chen) helped me out since my first day in Boston. I still remember that they brought me to "Muddy Charles Pub" on my first day and to "No Name Seafood" on my second day in Boston.

Outside EMAT, I also got many friends. Miloš Popović was always something like a teacher for me as well as a good friend. His insight into photonics taught me lots of things and "educated" me. The trip to Colorado with him to attend LEOS was nothing but fun. And Felix Grawert was also a good friend and a research partner. Thanks to his eager attitude toward optics field, I could find many new applications, which are in this Ph.D. thesis. Our "Coffee meeting" at Dome Café was my imagination epicenter.

MTL staff members also helped me a lot without any exaggeration. Especially, Vicky Diadiuk, Bernard Alamariu, Bob Bicchieri and Paul Tierney gave me valuable assistance at the most difficult times. They provided me with the most important information and great help for successful fabrication which was not on any textbook or papers. I really appreciate their help.

Dr. Takao Abe at Shin-Etsu Handotai Co.,Ltd. (SEH) has been helping me out in various ways. He provided a lot of samples, which cannot be realized at academic environment and ideas. He didn't hesitate to share the results with me despite the fact that it was him who came up with a new idea and realized it. I deeply appreciate it.

Ms. Kathleen R. Farrell at DMSE head quarter also supported my graduate life patiently. Without her infinite help and support, I could have not survived. I really appreciate her warm and professional help.

Last but not least, I would have not survived the graduate life at M.I.T. without help from my wife, Naoko. She always supported me when I was in the most difficult situations. She always set up the environment so that I could concentrate on my study and helped me out. I still remember she prepared night meals and coffee overnight when I was preparing for exams without sleeping. I deeply appreciate her constant support and encouragement. This thesis is totally devoted to her.

Cambridge, Massachusetts, July 2004.

Table of Contents

Chapter 1: Introduction 19

1.1 Motivation 19
1.2 Outline of thesis 20

Waveguide chapters

Chapter 2: HIC waveguide 23
2.1 Introduction of optical waveguides 23
2.2 Prior arts 26
2.3 Outline of HIC waveguide 29
2.4 Silicon-rich nitride as a waveguide material 30
2.5 Waveguide loss measurement 35
2.6 Results 37
2.7 Discussion and summary 41

Chapter 3: Air trench waveguide 45
3.1 Background 45
3.2 Air trench bend theory and simulations 47
3.3 FDTD simulation examples 55
3.4 Realization of ATB and AT T-splitter 57
3.5 Measurement results 64
3.6 Discussion and summary 69

Chapter 4: PBG waveguide 73
4.1 Background 73
4.2 Prior arts 72
4.3 PBG waveguide designing approach 76
4.4 PBG designing and fabrication 77
4.5 One dimensional slab PBG asymmetric waveguide 83
4.6 Two dimensional PBG channel waveguide 86
4.7 Waveguide loss measurement 91
4.8 Bend loss 95
4.9 Summary 97

PBG chapters

Chapter 5: HIC PBG for visible light 99

5.1 Introduction..99
5.2 Background.. 100
5.3 VisPBG designing.. 102
5.4 Fabrication..105
5.5 Data analysis.. 115
5.6 The effect of film strain on reflectance improvement.....116
5.7 Summary... 121

Chapter 6: IR-PBG for semiconductor saturable absorber mirror (SESAM) 123
6.1 Background.. 123
6.2 Fabrication of IR-PBG.......................................125
6.3 Bonded and Etched-back PBG (BE-PBG)................ 127
6.4 CMOS-compatible semiconductor saturable absorber (SESAM) 132
6.5 Fabrication of SESAM.......................................134
6.6 Germanium epitaxial growth...............................136
6.7 Evaluation of Si/Ge SESAM................................141
6.8 Summary... 146

Chapter 7: PBG filter for TPV application..............................147
7.1 Introduction.. 147
7.2 Prior arts...148
7.3 TPV system modeling.. 153
7.4 PBG filter designing and fabrication........................156
7.5 Anti-reflection coating (ARC) for pass-band..............159
7.6 ARC fabrication and evaluation.............................161
7.7 System efficiency improvement by PBG filter............ 163
7.8 Discussion and summary.................................... 166

Chapter 8: Summary and future work..................................169

Appendix A: Basic waveguide theory.................................... 171

Appendix B: Basic physics of photonic crystal..........................193

Bibliography.. 199

List of Figures

Chapter 2:

2.1: Propagation and gate delay in microprocessor unit with time [2].

2.2: Optical clock circuits. Top interconnects are photonic circuits (waveguide).

2.3: Minimum bending radius and scattering loss dependence on index difference [2] (σ and L denote the amplitude of roughness and the period of roughness respectively)

2.4: Optical loss in the telecommunication window [10] of PECVD SiON (n=1.48).

2.5: Nitride waveguide dimension (not to scale). The top and bottom claddings are approximately 3μm thick.

2.6: Mode profile of Silicon-rich nitride. n_{core} and n_{cladd} are assumed to be 2.25 and 1.45. respectively and The width and height to be 1.0 and 0.325μm, respectively.

2.7: Schemmatic of waveguide loss measurement system (not to scale)

2.8: Figure 2.8: Test structure for bend loss evaluation. (Top) Mask layout for bend loss evaluation and (Bottom) optical microscope images of bending and straight waveguides.

2.9: Bend losses for nitride waveguides with various sidewall angles. The larger loss is observed with larger sidewall angle.

2.10: Waveguide cross sections patterned with various etchant gases. Sidewall angles and propagations losses are also shown.

2.11: Propagation loss vs. deposition temperature plot for nitride waveguides at 1550nm. It is shown that both deposition temperature and post-annealing can reduce the loss.

2.12: Propagation loss vs. deposition temperature plot for nitride waveguides at 1510nm. It is shown that both deposition temperature and post-annealing can reduce the loss. The effect of N-H absorption can be clearly seen from this plot and it shows that substrate temperature is more effective to suppress the loss.

2.13: The temperature dependence of hydrogen dissociation rate (left axis) and hydrogen content at 0.3μm depth by out-diffusion (right diffusion). The hydrogen dissociation increases exponentially as deposition temperature rises whereas hydrogen out-diffusion decreases almost linearly as post-anneal temperature goes down.

Chapter 3:

3.1: Air trench bend (ATB)– (A) Cross sectional view of low index (straight) waveguide, (B) Air trench region (bend). Contour plots representative of the dominant modal electric field component are superimposed on the cross sections (not to scale).

3.2: Bend (radius and "total box") size for regular waveguide bends and ATBs, showing improvement in size for the case of 0.1-dB loss. It is also shown that, on this scale of size variation, the relative change in radius is small for 0.01- and 0.001-dB loss.

3.3: Mode shape conversion along the air trench bend. The shape of the mode changes depending on the location inside the ATB.

3.4: Schematic of (a) actual trench cross section with finite trench depth and (b) the idealized trench with infinite trench depth [36].

3.5: Calculating substrate loss: (a) Setup of 2-D equivalent current sheet method (ECSM). (b) Mode solver LM solution example: Real part of the E_y field component for the waveguide of Example B with the bulk cladding 0.6 core heights from the axis [36].

3.6: Bulk cladding loss versus trench etching depth for waveguides of examples A-C computed by approximate ECSM (lines) and numerical vector-field mode solver for leaky wavguide (symbols). The discrepancy is due to reflection at the interface with bulk cladding, not accounted in the ECSM calculation [36].

3.7: FDTD simulations for ATB. (Left) Light is squeezed by adiabatic tapers (mode matching process to bend/splitter), (Middle) then traverses air trench bends, (Right) and emerges into the output mode via the trailing taper [36].

3.8: FDTD simulation of (Left) air trench bend without tapers. Raius=9µm. n_{core}=1.56, n_{clad}=1.46. (Right) air trench bend with tapers. Radius=7µm, n_{core}=1.56, n_{clad}=1.46.[36]

3.9: FDTD simulations for AT T-splitter (left) Light is squeezed by adiabatic tapers (mode matching process to bend/splitter), (Middle) then traverses air trench bends, (Right) and emerges into the output mode via the trailing taper [36].

3.10: Bend radius design plot [43]. Claddings are assumed to be silicon dioxide(SiO_2). Radiation loss in regular and AT bend is evaluated numerically according to the approaches in [22] and [23] after the customery conformal transformation for bent waveguides [21]. The result is a theoretical reduction in bending radius by a factor of 10-1000 and in total bend structure edge length by a factor of 4-60.

3.11: Air trench design schematic (photomask layout).
(a) Cross sectional view of (A) low index straight waveguide and (B) bend.
(b) Air trench bend (ATB). Radius = 2, 3, 4.5, 7 and 9μm and Θ = 55,65,76 and 80°.
(c) Ait trench T-splitter schematic. R = 9μm and Θ = 80°.

3.12: Brief schematic of air trench bend/T-splitter process flow (not to scale). All steps are done using conventional CMOS processes [43].

3.13: Refractive index and thickness changes of PECVD SiON after anneal (1554nm TE mode). The refractive index increases by 0.033 and thickness decreases by 15.7% as a result of consolidation annealing [43].

3.14: Images of fabricated structures. Optical microscope images: (a) AT bend; (b) T-splitter. SEM images: (c) AT bend (6,000x); (d) AT T-splitter (3,500x) [43].

3.15: SEM images of etched structures using conventional techniques.

3.16: An example of raw data of Fabry-Perot resonance measurement from air trench bend. Loss was obtained by averaging the results from 10 peaks and valleys in the Fabry-Perot spectrum near 1550nm.

3.17: An experimental setup for waveguide loss measurement (the same as Figure 1.7).

3.18: (Left column) Bending loss for ATB using TM mode (a) and TE mode (b). Radii are varied from 2 to 9mm. Taper angle is fixed at 80°. Experimental results are in good agreement with theoretical curves for transmission, as shown.

(Right column) Bending loss for ATB using TM mode (a)' and TE mode (b)'. Taper angle is varied from 55 to 80°. Experimental results are in good agreement with theoretical curves for transmission, as shown.

3.19: Relationship between lateral misalignment and power splitting ratio. ±0.05μm alignment accuracy is required to achieve 49:51 power splitting ratio.

3.20: Mode profiles for air trench waveguides. (a): W=1.0μm, TE (quasi-TM) mode. (b): W=10μm, TM (quasi-TE) mode. (c): W=0.45μm, TE (quasi-TM) mode. (d): W=0.45μm TM (quasi-TE) mode. It is shown that air trench waveguide works as a polarizer by narrowing the width. Simulations were done Apollo®.

3.21: Schematic of air trench waveguide amplifier. It becomes possible to integrate long waveguide on a small chip even on LIC platform by employing air trench bends. By its low loss property and compact bend size, a compact EDWA can be expected even on a small chip.

Chapter 4:

4.1: Simulation of the propagation of an optical mode traveling around a sharp bend in a 2-D photonic crystal composed of a cubic array of dielectric cylinders. [48]

4.2: Examples of PBG wavgeuide [49]. PBG structures are fabricated laterally and dielectric confinement is used vertical confinement.

4.3: SEM image of a periodic array of silicon pillars fabricated using deep anisotropic etching. The silicon pillars are 205nm in diameter and 5μm tall [50]

4.4: Cross section of the proposed PBG waveguide. The core is surrounded by PBG cladding layers. Uniform layers are achieved by LPCVD technique.

4.5: Wafer surface region in CVD process showing concentrations and fluxes of reactant species [52].

4.6: Growth velocity vs. 1/T for APCVD (760 torr) and LPCVD (1 torr) systems. The total pressure (with P_G and C_G remaining fixed) shifts the h_G curve upward, extending the surface reaction regime to higher temperature [52].

4.7: Fabrication scheme of PBG stack. (a) Deposit nitride, (b) Deposit poly-Si, (c) Repeat steps (a) and (b).

4.8: Poly-Si and nitride layers deposited on V-groove made by KOH anisotropic etch. It is shown that uniform layers are formed independent of surface morphology.

4.9: Cross sectional TEM images pf 6pair PBG. (Left: 6,000x) and (Right: 30,000x). Courtesy of Dr. Xiaoman Duan.

4.10: Theoretical and experimental reflectance for 6pair poly-Si/nitride PBG. (Top) Reflectance from 1.0mm to 2.4um. (Bottom) Reflectance over the stop-band. Discrepancy from the theory is approximately 0.6%.

4.11: Schematic of prism coupler (left), and intensity of reflected light vs. angle of incidence (Θ) [53].

4.12: Schematic of one dimensional asymmetric slab waveguide. The thickness of oxide core is 4 and 5um. This is used for prism coupling measurement.

4.13: Cross sectional TEM image for 1D asymmetric PBG slab waveguide. The thickness of core layer is 5μm here. Courtesy of Dr. Xiaoman Duan.

4.14: An example of raw data of the mode coupling between the prism and the PC cladding waveguide for 4mm oxide core. Five dips represent the five propagation modes; effective index is measured as 1.4383, 1.4173, 1.3812, 1.3287 and 1.2577. Courtesy: Y Yi.

4.15: Dispersion relations of metallic channel waveguide (lines) and PBG cladding channel waveguide (dots). They have very similar dispersion relations. Courtesy of Y.Yi [54].

4.16: The mode structures for PBG cladding channel waveguide for some higher modes. The strong confinement of the field in the low index core is seen. Courtesy of Y.Yi [54]

4.17: Cross section of 2-D PBG waveguide. The width and height varies as shown (not to scale).

4.18: Waveguide fabrication scheme. All steps are done by conventional CMOS process. (a) Deposit oxide (LTO) and densify it. (b) Patterning. (c) Deposit top cladding layers using LPCVD process.(not to scale).

4.19: SEM and TEM images of PBG waveguide. (Left) SEM images of PBG waveguide with 12um width and 4um thickness(a: 1,600x) (b: 4,500x) (Right) TEM images (c: 5,000x) (d: 8,000x). TEM images: Courtesy of Dr. Xiaoman Duan.

4.20: (a, b and d) SEM images for PBG waveguides after polishing off the top cladding. (b) Visualized FDTD simulation corresponding to (a). FDTD simulation: Courtesy Y.Yi.

4.21: An example of raw data for output intensities of PBG waveguides. The propagation loss is obtained using Cut-back approach. Eqns. (12-14).

4.22: Output intensities from two identical PBG waveguides (W=16μm and H=5μm) on different chips. It is shown that the transmittance strongly depends on wavelength.

4.23: SEM images of fabrication defects which are considered to be loss source. (a): Rough sidewall and slanted wadewall observed from the outside of PBG cladding. (b): Cracks crossing the waveguide. The cracks were generated mainly during dicing process.

4.24: Comparisons of theoretical and experimental data. (Left) Width is fixed at 20mm. It is shown that loss is lower for higher waveguide. (Right) Width is fixed at 16mm. It is also shown that loss is lower for higher waveguide.

4.25: Transmission spectrum around a 90° dend for PBG waveguide. Radius = 2.4μm. Courtesy of Y. Yi [54].

4.26: Experimental bend losses for PBG waveguides. (Left) Bend losses/90° for waveguides with W=20μm. (Right) Bend losses/90° for waveguides with W=16μm. Losses don't simply depend on radii.

Chapter 5:

5.1: Geometries of flux and deposition of small areas on a flat wafer holder for a point source [66].

5.2: Reflection plots for Δn=0.5, 1.0 and 2.0. Stop band becomes wider and reflection also gets higher with Δn.

5.3: Optical absorption of crystalline silicon [67]

5.4: Reflectance of 4 pair-PBG based on crystalline silicon's absorption. The maximum reflectance is 98.5%.

5.5: Spatial distributions of electrons described by the functions Ψ+ and Ψ− [68]

5.6: (Left) E-field distribution and power distribution inside PBG stack. (a) and (c) corresponds to dielectric band in the band structure. (b) and (d) corresponds to air band [69].

5.7: Fabrication scheme of prototype1. LPCVD poly-Si deposition and thermal oxidation are employed. (a) Grow thermal oxide, (b) Deposit poly-Si, (c) Partially oxidize poly-Si layer. (d) Repeat step (b) and (c)

5.8: Theoretical and experimental reflectance of 3pair-PBG. Degradations of reflectance at the stop-band edges are observed.

5.9: Cross sectional TEM image of PBG made by p-Si deposition and thermal oxidation. Courtesy of Dr. T. Abe at Shin-Etsu Handotai Co.,Ltd.

5.10: Fabrication scheme of prototype2. LPCVD poly-Si deposition and LTO are employed. (a) Grow thermal oxide, (b) Deposit poly-Si, (c) Deposit LTO and densify it (d) Repeat step (b) and (c).

5.11: Theoretical and experimental reflectance of prototype2 (poly-Si and LTO 5pair-PBG). The performance as compared o theory was improved.

5.12: xTEM picture of prototype2 (LPCVD poly-Si and LTO PBG). Interface roughness is suppressed as compared to prototype1, however, slight roughening can be observed due to partial oxidation by LTO's excess oxygen. Courtesy of Dr. T. Abe at Shin-Etsu Handotai Co.,Ltd.

5.13: Fabrication scheme of prototype3. (a) Grow thermal oxide, (b) implant H+ ion, (c) Wafer bonding with a base wafer, (d) Delamination, annealing and CMP, (e) Repeat steps (b)-(d)

5.14: xTEM picture of prototype3 (SmartCut® PBG)   It is observed that Interface roughness is totally suppressed and Si layers are crystalline. Courtesy of Dr. T. Abe at Shin-Etsh Handotai Co., Ltd.

5.15: Theoretical and experimental reflectance of prototype3 (SmartCut™ PBG). The experimental data shows higher reflectance over the stop-band. Refectance data was provided by Dr. T. Abe at Shin-Etsu Handotai Co., Ltd.

5.16: Actual and modified reflectance with 0.4 x $k_{theoretical.}$ Both curves fit well with each other. It is shown that *k* was changed by external factor.

5.17: Fabrication scheme of prototype4. (a) Grow thermal oxide, (b) Thin nitride and poly-Si are deposited, (c) Thin nitride and poly-LTO are deposited. LTO is densified at 950ºC (d) Repeat steps (b)-(c).

5.18: Theoretical and experimental reflectance of prototype4 (poly-Si + nitride + LTO 4pair-PBG). The performance as compared o theory was slightly improved.

5.19: Relationship between surface roughness and PBG performances. It is shown that the roughness is quite important for higher reflectance.

5.20: (Left) Band structure of Si plotted along the [100] and [111] directions [65]. (Right) Calculated bandgaps depending on the film strain.

5.21: Reflectance change before and after RTP. The reflectance at shorter wavelength is improved without changing the stop-band width. It is considered to be attributable to the absorption reduction in silicon layer.

Chapter 6:

6.1: A comparison of Si/SiO_2 6pair-PBG, TiO_2/SiO_2 11pair-PBG. and GaAs/AlAs 22pair-PBG. It isshown that Si/SiO_2 PBG has a stop-band twice as wide as TiO_2/SiO_2 PBG. Reflectance was obtained by theoretical simulation based on propagation matrices approach.

6.2: Schematic of IR-PBG. LPCVD poly-Si and thermal oxidation are employed for batch process. (a) Grow thermal oxide, (b) Deposit poly-Si, (c) Partially oxidize poly-Si layer. (d) Repeat step (b) and (c)

6.3: The effect of oxidation temperature on reflectance. It is shown that higher oxidation temperature degrades reflectance especially around short wavelength (1150-1550nm) within the stop-band.

6.4: AFM pictures of PBGs made with various wet oxidation temperatures. It is shown that the surface is roughened as temperature goes up.

6.5: Schematic of the fabrication of Bonded and Etched-back (BE) PBG

6.6: Field intensity of 6pair-PBG at center wavelength 1.4μm. The most of the filed is located in the first pair.

6.7: IR images of bonded wafers. (left): two wafers are nicely bonded. (middle): Central part is not bonded and edge part is bonded but bonding quality is not so good as left example. (right): Bonding is unsuccessful. This is due to rough surface. Wafers are delaminated and re-polished and bonded again.

6.8: Reflectance of as-deposited and BE-PBGs. Reflectance is improved by backside etch process especially for the shorter wavelength in the stop-band.

6.9: AFM images of as-deposited and BE-PBGs. The surface roughness is minimized by a factor of 14.

6.10: Refractive index profile and standing wave pattern of the SESAM. The fields decays rapidly in the 6-pair Si/SiO2 mirror due to the large index contrast. All interfaces of exposed to high field intensities are created by thermal oxidation, reducing scattering loss. The Bragg mirror is terminated with an SOI layer that allows for subsequent growth of crystalline Germanium.

6.11: Schematic of fabrication of BE-SOI-PBG.

6.12: AFM image of BE-SOI-PBG. The surface roughness is as low as RMS 0.136nm(/1μm^2)

6.13: Standing wave pattern of saturable absorber. Design is optimized so that the peak field intensity resides in Ge absorption layer.

6.14: Schematic of fabrication of saturable absorber based on Si/SiO_2 PBG.

6.15: X-ray diffraction peak from (100) germanium epitaxially grown at 350°C directly on silicon. It is shown germanium is crystalline even at low growth temperature. The film is compressively strained as much as –0.236%.

6.16: Absorption in poly-Si/LTO/Ge layers. Absorption is observed below 1600nm which corresponds to Ge's bandgap

6.17: AFM image of 20nm Ge on DSP wafer. It is shown that no islanding occurred due to lattice mismatch. It is expected that Ge is amorphous as deposited. No islanding is observed

6.18: Cross sectional TEM image of SESAM. It is shown that roughness is suppressed at the interface between top poly-Si and SiO_2 layers.

6.19: The experimental setup for Erbium-Yitterbium glass laser.

6.20: Pump-probe traces of the Si/Ge-SBR taken at various fluence values along with the crosscorrelation of the pump probe laser source.

6.21: Optical spectrum of the Er-Yb:glass laser modelocked with the Si/Ge-SBR on linear and logarithmic scale. Width of the C-band of optical communications (shaded). **b**, RF-spectrum of the laser and autocorrelation (inset).

Chapter 7:

7.1: Basic scheme of TPV system. This research focuses on the filter performance to improve the total efficiency.

7.2: (Left): Three dimensional plot of blackbody radiation. As temperature goes up, the peak intensity rises and the peak wavelength shifts to shorter wavelength. (Right): Blackbody radiations from 1250, 1500 and 1750K heat sources. The most of the radiated light is not converted especially at lower temperature.

7.3: Theoretical calculations for plasma filter. Reflectance (left) and absorbance (right) of light depending on wavelength [93]. it is shown that high μ and high doping level are required. 10^{21} cm^{-3} for electron concentration and $1000cm^2/Vs$ for mobility are required for sharp edge and low loss, respectively.

7.4: Reflectance from InP/MgF_2/Ti/Au backside reflector [97]. This type of reflector shows high reflectance for all of infrared.

7.5: Transmittance spectrum for ZnS/MgF_2 dielectric spectrum [97]. The stop-band ranges from 2.6 to 3.2μm.

7.6: Process scheme for TPV PBG filter (not to scale). All steps are done using conventional CMOS processes. Films are deposited on both sides of the wafer actually.

7.7: Cross sectional TEM picture for 5pair-PBG.(Courtesy of Dr. T.Abe at Shin-Etsu Handotao Co.,Ltd.)

7.8: Reflectance of 5pair-PBG (Top-left), 4pair-PBG (Top-right), 3pair-PBG (Bottom-left) and Comparison of 3 PBGs over the stop-band.

7.9: A Comparison between theoretical and experimental reflectance. (Left): Pass-band and stop-band and (right): Pass-band. It is shown that both theoretical and experimental reflectance fairly matches each other.

7.10: Theoretical reflectivity of 5pair-Si/SiO_2 PBG (Left): Pass-band and stop-band and (right): pass-band where seven photonic states exist.

7.11: Filed intensity distribution inside PBG layers with state 4(left: λ=1.004mm) and state 3(right: λ=1.1mm). It is shown that standing waves are formed with $\lambda c/2$ period in both cases.

7.12: Theoretical simulation results for PBG with and without ARCs. It is shown that transmission over the pass-band is improved by adding ARC on top.

7.13: Reflectance spectrum for PBGs with and without ARC. It is shown that photonic states are suppressed by adding ARC layers.

7.14: Cross sectional TEM images of PBGs with ARC. (Top) 4pair-PBG with SiO_2 ARC and (Bottom) 5pair-PBG with SiON ARC. Courtesy of Dr. T. Abe at Shin-Etsu Handotai Co.,Ltd.

7.15: TPV system schematic. The factors which determine the system efficiency are mainly emitter temperature *T(K)*, *L*, *Tr*, and *R*.

7.16: Experimental responsivity of Ge epitaxially grown directly on Si substrate reported by Cannon et al. [86].

7.17: System efficiency depending on emitter temperature and photon recycling loss. It is shown that higher efficiency can be expected by adding PBG filter and realizing low-loss photon recycling.

7.18: System efficiency with and without Anti reflection coatings(SRCs). It is shown that efficiency is improved by adding ARCs.

7.19: A conventional TPV generator [97]. It usually has a cylindrical shape.

7.20: A proposed configuration of TPV cell. Unit cells are cascaded to share cooling system and both emitter and PV cell have large area and are placed parallel to each other for effective photon interchange.

List of Tables

Chapter 2:

2.1: Characteristics for three platforms (HIC, LIC and MIC).

2.2: Refractive indices (R.I.) and thickness of deposited nitride films.

2.3: Propagation loss for nitride waveguides.

Chapter 3:

3.1: Regular and ATB radii and total sizes for 98% transmission. AEdge length of a box enclosing the entire bend structure and accommodating > 99.9% of the input and output power. The minimum bend size possible is a square with an edge equal to this 99.9% mode width.

3.2: (Left) Refractive indices of films employed for air trench waveguides. Indices are changed after consolidation annealing and close to design values. (Right) Waveguide dimensions after fabrication. Dimensions are obtained by SEM observation and close to design values. The sidewall angle of AT waveguide is 86°.

3.3: Power distribution ratios between right and left arms for TM and TE modes. The wavelength ranges from 1540-1560nm. Power splitting ratios for both TM and TE modes are around 55 : 45. The expected misalignment between waveguide and AT layers is 0.1μm.

Chapter 4:

4.1. Effective indices (n_{eff}) of 1-D asymmetric slab waveguide. Effective indices are lower than indices of silicon (n=3.5) or nitride (2.0).

4.2: Propagation losses for 1-D PBG asymmetric slab wavegudies. These low-losses indicate that the light propagates in low index material (oxide).

4.3: Propagation loss for 2-D PBG waveguides. Loss was obtained by Cut-back method.

Chapter 5:

5.1: Summary of experimental results for VisPBGs. Roughness were obtained from AFM analysis and scanning range is 1μm^2. Theoretical maximum reflectance is about 98.6% for all the samples.

Chapter 6:

6.1: Roughness and mean reflectance over the stop-band for PBGs discussed so far.

Chapter 7:

none

Chapter 1: Introduction

1.1 Motivation

This thesis focuses on silicon-based high index contrast (HIC) photonics. In addition to mature fiber optics, where the index difference (Δn) ranges from 0.01-0.05, or low index contrast (LIC) platform, which is often referred to as Planar Lightwave Circuit (PLC) or Silica Optical Bench (SiOB), the use of high index contrast (HIC) platform has been attracting considerable attention recently for the purpose of dense integration of optical components on chip.

There are two ultimate solutions to mold of the flow of light. One is high index contrast (HIC) optics, where the index difference (Δn) of core and cladding is more than 0.5 and light is strongly confined in the core, which enables us to integrate optical circuits in μm order. Another technique is the introduction of photonic crystal, with which the flow of light is controlled by its photonc bandgap (PBG) and the defect. The concept of photonic crystal can be applied to optical wavgeuides by placing the defect, which is surrounded with photonic crystal structures. By introducing the defect, new photonic states are formed within photonic bandgap (PBG). Above or below these defect-induced modes, the photonic density of states (DOS) becomes zero. As a result, the light traveling in the photonic crystal using the defect modes cannot leak from these states to neighboring modes and the loss is ideally zero. In addition to wavgeuide applications, there are lots of unexplored attractive applications for photonic crystal, especially for high index contrast photonic crystal (HIC-PC or HIC-PBG), such as Si/SiO_2 or Si/Si_3N_4 materials systems, due to the wide stop-band. In this thesis, the various applications based on HIC-PBG platform are proposed and investigated. All of the works in this thesis are based on Silicon CMOS-compatible

techniques for practical applications.

1.2 Outline of Thesis

In first three chapters (chapter 2, 3 and 4), waveguide applications are mainly focused based on HIC or HIC-PBG platform. In the latter chapters (chapter 5, 6 and 7), the applications of HIC-PBG are explored such as visible-light reflector, semiconductor saturable absorber (SESAM) and thermophotovoltaic (TPV) applications.

Waveguide chapters

In chapter 2, compact high index contrast (HIC) waveguide is constructed and evaluated by employing optimum Δn material such as silicon-rich nitride. Siricon-rich nitride ($n = 2.1$-2.35) is a relatively unexplored material as compared to silicon waveguide and expected to be a good candidate for compact optical circuit for Optical add/drop multiplexing (OADM) application. The discussion focus on the material property of silicon-rich nitride and the optimization of deposition process. Thermal budget is also considered as an important factor taking into account the compatibility with other electronic devices such as germanium detector or modulator. The low-loss nitride deposition process is developed even with low process temperature.

In chapter 3, a new and novel optical waveguide, which is referred to as air trench (AT) waveguide, is proposed. Waveguides are fabricated based on low index contrast (LIC) platform but HIC is locally introduced only at bends and T-splitters by introducing air trenches to overcome LIC's size. The fabricated waveguide shows low propagation loss due to low index contrast and low bending loss due to local high index contrast. We first demonstrated that it is possible to achieve the dense integration of optical waveguides on a

small chip even on low index contrast platform by employing air trench waveguide structure.

In chapter 4, photonic bangap (PBG) structure is employed to mold the flow of the light. Different from dielectric waveguide, in which the light propagates depending on total internal reflection (TIR), the light is confined in the core by PBG claddings. Various applications, such as high power transmission waveguide, waveguide amplifier or biosensor devices, can be expected other than optical interconnects using this structure. PBG waveguides are fabricated based on Si/Si_3N_4 platform using conventional CMOS-compatible techniques. On-chip integration of PBG waveguide is first demonstrated using our approach and the performance is discussed.

PBG chapters

In chapter 5, Si/SiO_2 PBG for short wavelength, such as visible light (Vis) or 0.85μm, is investigated. The PBG performance is discussed in terms of material property and interface/surface roughness. It is expected that PBGs for Vis or 0.85μm range have various applications such as light reflector or FTTH-application with the combination of GaAs laser and plastic optics fiber (POF).

In chapter 6, Si/SiO_2 PBG for near infrared (NIR) is investigated. In addition to passive mirror applications, the application for short laser pulse formation is also discussed by combining germanium epitaxial growth and the employment of silicon-on insulator (SOI) wafer (Si/Ge saturable absorber mirror). In addition to the excellent performance of NIR-PBG, we demonstrated the shortest pulse generated in a bulk erbium-ytterbium glass laser using this PBG platform by employing conventional CMOS-compatible techniques.

In chapter 7, Si/SiO_2 PBG for mid infrared (MIR) is investigated. We focused on the application for thermo photovoltaic (TPV) device. The PBG wavelength filter is used to recycle photons, which have longer wavelength than cut-off wavelength (λ_g) and do not contribute for the generation of electricity. By placing PBG directly on PV cell, it is expected to improve the total system efficiency. In this chapter, not only the stop-band but also the pass-band characteristics is discussed to improve the photon incorporation into the cell. We demonstrated that Si/SiO_2 PBG with silicon oxynitride (SiON) PBG anti-reflection coating shows high reflectance over the stop-band and high transmittance over the pass-band.

Finally, chapter 8 summarizes this thesis work and concludes with suggestions for future development of Silicon-based HIC platform technology.

Chapter 2: HIC waveguide

2.1 Introduction of optical waveguides

The 20th century is often referred to as "the silicon age". For more than thirty years, computer systems have developed according to Moore's law. Today computer systems are composed of tens of millions of transistors and gigabytes of memory, which support multimedia society. However, it is also the fact that there have been big arguments on fundamental limits in silicon LSIs related to their speed, integration density, and heat dissipation [1]. Figure 1 depicts one of the fundamental limits of microelectronic circuits; propagation delay as a function of time (minimum design rule)[2].

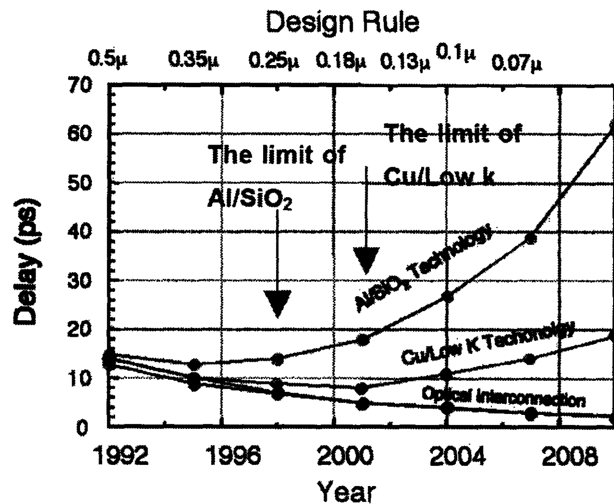

Figure 2.1: Propagation and gate delay in microprocessor unit with time [2].

The gate metal and insulator have been Al and SiO_2 respectively for more than 30 years, but these traditional interconnect materials can not maintain their positions to further reduce the delay beyond the 0.25 μm design rule as shown in figure 2.1. Cu and low-k dielectrics have been introduced recently by IBM to overcome the speed limit problem [3]. The

improvement is indeed appreciable but will soon reach the minimum delay, as shown in figure 2.1. Silver and air are the current candidates for the metal-based interconnects, but have serious problems such as corrosion and poor electromigration resistance whereas bring less substantial technological breakthroughs. Thus, the metal interconnection intervenes the future progress of Si-LSIs.

On the other hand, there are several reasons to believe that these limits will not limit the coming of the new Si age with the aid of disruptive technology, that is, Microphotonics. Photons are 1000 times faster than electrons in semiconductors. There is no resistance or capacitance associated with photons, so photonic waveguides are essentially free from the RC delay. In the following sections, we will report the current status of on-chip optical interconnection based on silica-based platforms.

Figure 2.2 shows a schematic diagram of optical clock distribution circuits, which is called as "H-tree". In terms of the H-tree configuration, each block (16 blocks in this case) is able to receive each clock signal at the same time.

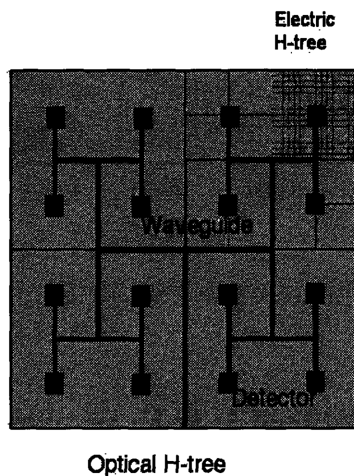

Figure 2.2: Optical clock circuits. Top interconnects are photonic circuits (waveguide).

The detectors at the end of waveguides convert optical clock signals for electronic circuits underneath as shown in the figure. The path length of electric H-trees is shorter than without optical H-tree (1/16th of that of optical H-tree in this case), thus the clocking electrons only need to travel for the short distance which minimizes skews and jitters of clocks at each end of electric H-tree. Thus, simple estimation yields that introduction of the optical H-trees should increase the clock speed by the number of the blocks.

The optical H-tree shown in figure 2.2 basically consists of three components, i.e., waveguides, T-splitters, and detectors. One challenge in on-chip optical clock distribution is to minimize the footprints of these components. The sharp bends of waveguides are extremely important for clock distribution on a small chip. However, the sharp bends result in substantial power loss (micro bending loss), since they enhance coupling of evanescence tail to radiation modes [4].

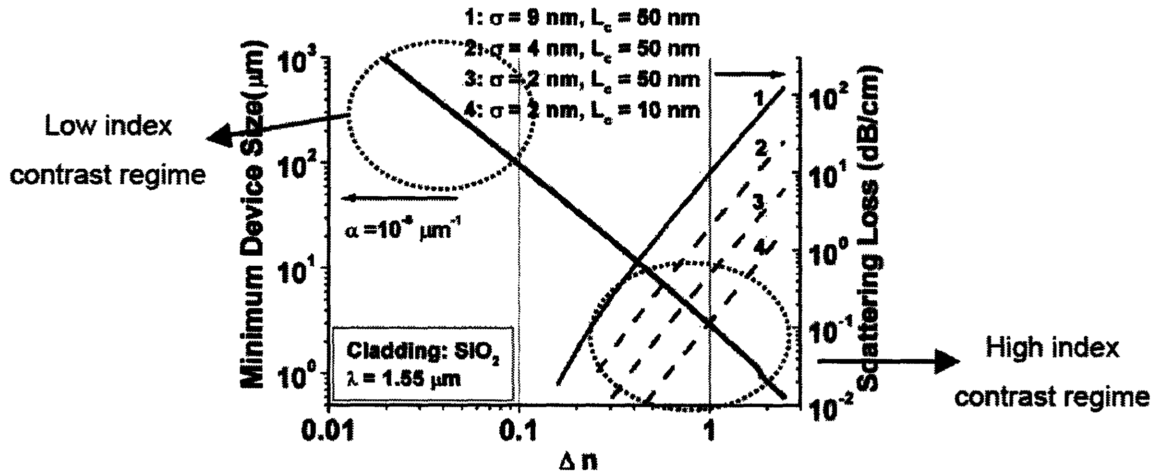

Figure 2.3: Minimum bending radius and scattering loss dependence on index difference [2] (σ and L denote the amplitude of roughness and the period of roughness respectively)

Minimum bending radius can be calculated using Marcatili's approach [4]. Scattering loss is calculated based on the analyses of roughness of waveguides [2]. Here, the roughness is approximated to sinusoidal function with the amplitude σ and the period L.

Figure 2.3 shows the minimum bending radius (0.1dB/turn) as a function of refractive index difference (Δn), based on Marcatili's approach [4], where the cladding is assumed to be SiO_2 with refractive index n = 1.45 and the wavelength is 1.55 μm.

Provided that the radius should be smaller than 100 μm, Δn should be higher than 0.1 as shown in figure 2.3. Therefore, high index contrast material systems are seemingly our natural choice for the optical platform, where light is strongly confined in the core. However, high index contrast platforms have large propagation loss as compared to low index contrast systems [2]. Figure 2.3 shows the sidewall roughness is dominant cause of propagation loss, which is almost proportional to the 3rd power of index difference between core and cladding.

The core materials can be silicon (n = 3.5), silicon nitride SiN_x (n = 2.0 - 2.3), and silicon oxinitride SiO_xN_y (n = 1.46 - 2.0). It should be emphasized that these materials as well as silica cladding are compatible with current silicon technology and can be used to fabricate the optical platform on a Si-LSIs' chip.

2.2 Prior arts

The focus of this chapter is to understand the optical properties of waveguide systems with low transmission and bending loss and to fabricate them. Many efforts have been devoted for the realization of optical waveguide so far and there have been two main streams. One is low index contrast system (denoted as "LIC") whose index difference between core and cladding is approximately 0.25-1.5% such as Ge-doped silica and silica system [5-7]. This low index contrast silica technology, which is often referred to as PLC

(Planar Lightwave Circuit) or SiOB (Silica Optical Bench), has gained wide spread use in practice by virtue of its use of well-tested IC manufacturing processes and technology.

Another candidate is high index contrast system, which is often denoted as "HIC" whose index difference between core and cladding is much higher than low index contrast system [2][8-9]. For example, silicon and silica system has been investigated intensively recently [2] since Silicon-On-Insulator (SOI) can be used as a platform to construct high index contrast waveguides where the crystalline silicon layer can be used as a waveguide material. Using this high index contrast platform, it is expected to achieve dense integration of optical components according to Marcatili's method, where even 2 μm radius is possible [2] without significant loss.

However, both HIC and LIC platforms have some potential problems. A major drawback of low index contrast platform, such as PLC or SiOB, is its relatively large component size where minimum bending size is in the order of millimeter or centimeter. This problem leads to high production cost and low yield problems and prohibits dense integration. On the other hand, high index contrast platform, such as Silicon/Silica material platform, offers dense integration but has several problems such as huge fiber-to-chip insertion loss due to the mode size mismatch and misalignment, high propagation loss, sensitivity to fabrication defects, relatively large polarization dependence and so on.

Recently, the use of Silicon Oxynitride (SiO_xN_y) has been proposed to solve the above problems [10-13]. By using SiON, the refractive index can be easily adjusted by changing the gas composition during deposition, therefore we can get medium index contrast (Δn=0.02-0.6). But even with SiON, fundamental problems such as integration problem, insertion loss and propagation loss still exist. Table 2.1 summarizes the general characteristics of common waveguide material systems.

	HIC (e.g. Si/SiO_2: Δn=2.0)	LIC (e.g.PLC or SiOB: Δn=0.01)	Between LIC & HIC (e.g. $SiON/SiO_2$: Δn=0.2)
Dense Integration of Optical components	Excellent	Very poor	Between HIC and LIC
Insertion loss bet. Fiber/Waveguide	Very poor	Very good	Between HIC and LIC
Propagation loss	Very poor	Very good	Between HIC and LIC
Fabrication (production yield)	Very difficult (in terms of resolution)	Poor (in terms of its huge size)	Between HIC and LIC
Polarization sensitivity	Very poor (very sensitive)	Very good (not sensitive)	Between HIC and LIC

Table 2.1 Characteristics for three platforms (HIC, LIC and MIC).

As shown in table 2.1, the major problem with LIC is its large size. If this size problem can be solved, LIC waveguides can be considered as a good interconnect candidate for integration of optical and electronic components on a small chip.

In first three chapters (2-4), I employ three approaches to overcome these optical interconnection problems. In chapter 2, compact high index contrast (HIC) waveguide is constructed and evaluated by employing optimum Δn material such as silicon-rich nitride. In chapter 3, a new and novel waveguide, which is referred to as air trench (AT) waveguide, is proposed. Waveguides are fabricated based on low index contrast (LIC) platform but HIC is locally introduced only at bends and T-splitters to overcome LIC's size problem. In chapter 4, photonic bangap (PBG) structure is employed to mold the flow of the light. Different from dielectric waveguide, in which the light propagates depending on total internal reflection, the light is confined in the core by PBG claddings. Various applications, such as high-power transmission waveguide, waveguide amplifier such as EDWA, or biosensor devices, can be expected other than optical interconnects using this structure.

PBG waveguides are fabricated using conventional CMOS-compatible techniques.

2.3 Outline of HIC wavgeuide

High index contrast (HIC) waveguides have been attracting considerable attention for dense integration of optical waveguides [2][14]. It is well known that compact size bends can be realized by increasing the index difference between core and cladding. One of the major candidates is the Si/SiO_2 waveguide, where index difference is as much as 2. This is partly because Si/SiO_2 waveguide can be made from Silicon-On-Insulator (SOI) wafer, which has crystalline silicon layer on thermal oxide. However, it has been reported that scattering loss is proportional to the 3rd power of index difference [2], and mode shape mismatch is a potential problem for waveguide-to/from-fiber coupling since the width for this waveguide is around 0.5μm, whereas the core diameter of a single mode fiber is around 9μm. In this chapter, the deployment of silicon-rich nitride/SiO_2 waveguide, where index difference (Δn) ranges from 0.6-0.8 depending on the nitride's stoichiometry, is proposed for an optimum index contrast. For the Si/SiO_2 waveguide, even a 1μm radius is achievable due to its large index contrast, but scattering loss and fiber-to-waveguide coupling are critical problems. For silicon nitride/SiO_2 waveguides, scattering loss is lowered to 4% as compared to the Si/SiO_2 material system with the same scale of roughness. Coupling efficiency is also higher due to the larger mode size. Using the nitride/SiO_2 material system, a small bend size is still possible. For 98% transmission (~0.1dB/turn), only a 7μm radius is required, and this is small enough to satisfy the demands for future microphotonics. In this chapter, the properties of various kinds of nitride films are evaluated in terms of material loss using Fabry-Perot resonance approach.

2.4 Silicon-rich nitride as a waveguide material

Silicon nitride (Si_xN_y) is investigated hereafter as an attractive core material for future integrated optical circuits, where the index difference (Δn) ranges from 0.5-0.8, depending on its stoichiometry. There are several techniques to deposit silicon nitride, such as sputtering, plasma enhanced chemical vapor deposition (PECVD) and low pressure chemical vapor deposition (LPCVD). However, it has been reported that nitrogen-hydrogen (N-H) covalent chemical bonds, which are formed during the deposition process [10-13], absorb light in the 1.55μm communication range as shown in figure 2.4 [10]. The source of N-H bonds has been reported to be NH_3 precursor, which works as a nitrogen source for nitride. For lower transmission loss, hydrogen must be removed from the film by high temperature out-diffusion. This high temperature process may not be compatible with the integration of detector, modulator and other electric devices. High temperature anneal also causes film cracking problem due to high tensile film stresses [10-11]. Therefore optimizing material loss and process temperature are keys for constructing a HIC platform. Silicon-rich nitride (n=2.1-2.3) was chosen as waveguide core material. Several process conditions were chosen. Below is a list of waveguide core materials used in this chapter.

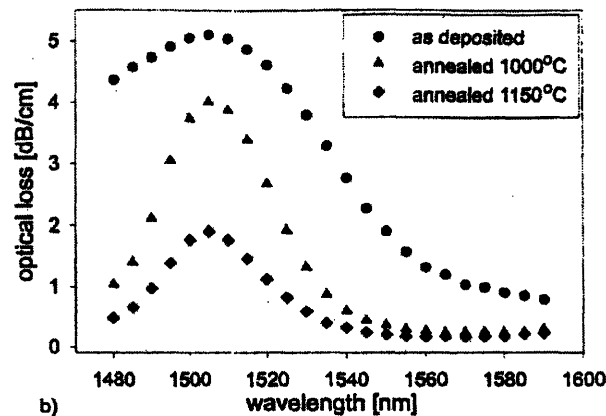

Figure 2.4: Optical loss in the telecommunication window [10] of PECVD SiON (n=1.48).

Sample 1: PECVD silicon-rich nitride without post-annealing

Sample 2: PECVD silicon-rich nitride with post-annealing

Sample 3: LPCVD silicon-rich nitride

Sample 4: HD (High Density)-PECVD low-hydrogen silicon-rich nitride without post annealing.

Sample 5: HD-PECVD low-hydrogen silicon-rich nitride with 1050°C post annealing

Sample 6: HD-PECVD low-hydrogen silicon-rich nitride deposited at higher substrate temperature (500°C) without post annealing

Sample 7: Sputtered silicon-rich nitride without post-annealing

Sample 8: Sputtered silicon-rich nitride with 1050°C post-annealing

PECVD process is known as a fast and convenient technique to deposit nitride or oxynitride film. However, due to N-H bonds formed during deposition, the film usually has strong absorption peak at the 1.55μm communication window [11]. The film is formed by a chemical reaction and physical deposition on the substrate [15]. By applying post high temperature annealing such as at 1050°C in N_2 ambient, hydrogen atoms can be diffused out of the film. However, the compatibility with low-temperature process may be lost. LPCVD process can provide high-quality films since deposition is done at a relatively high temperature such as 775°C with a relatively low deposition rate, which enhances the diffusion of hydrogen out of the film during the deposition. The deposition is dominated mainly by chemical reactions at the surface [15]. Therefore, it is expected that the film has low hydrogen incorporation and denser even without post high temperature anneal.

Hydrogen incorporation can be totally suppressed by using sputtering process, since there is

no hydrogen source such as NH_3 and SiH_4 gases during deposition. The film is formed purely by physical deposition. Due to lower substrate temperature, the film is expected to be more porous than PECVD and LPCVD films.

Below are descriptions of the nitride films employed in this chapter.

Sample 1: The deposition was done using a Novellus Concept1 PECVD system. Gas precursor SiH_4 is flown at 600 sccm and NH_3 at 4000 sccm and N_2 as dilutant at 1600 sccm. The substrate temperature is 400°C. The deposition rate is approximately 1264Å/min. This tool is not able to completely dissociate the precursors, most hydrogen remains in the film as N-H and Si-H bonds.

Sample 2: Post-annealing was applied to sample 1 to remove hydrogen out of the nitride film. Annealing was done at 1050°C for 2 hours in N_2 ambient. After annealing, thickness and refractive index significantly changed as listed in table 2.2 as a result of hydrogen and nitrogen out-diffusion.

Sample 3: Nitride was deposited using a SVG/Thermco-7000 LPCVD system. Gases used here were SiH_2Cl_2 250 sccm and NH_3 25 sccm. Deposition was done at 775°C at 250mTorr. The deposition rate is approximately 29Å /min.

Sample 4: The deposition was done by an Applied materials Centura HD-PECVD (High density plasma enhanced chemical vapor deposition) system. A new deposition process, which uses N_2 gas instead of NH_3 as nitrogen source, was developed to suppress hydrogen incorporation. The hollow cascade design of the faceplate enables localized high density

plasma to create nitrogen radicals from N_2 gas. N_2 is flown at 4.9 sccm, SiH_4 at 0.14 sccm. The deposition rate was 2900Å /min at substrate temperature of 400°C.

Sample 5: Post-annealing was applied to sample 4 to remove hydrogen out of the nitride film. Annealing was done at 1050°C for 2 hours in N_2 ambient. After annealing, thickness and refractive index changed as is listed in table 2.1 as a result of hydrogen and nitrogen out-diffusion.

Sample 6: The deposition was done by an Applied materials Centura HD-PECVD system. N_2 gas was used instead of NH_3 as nitrogen source as in sample6 to suppress hydrogen incorporation. N_2 is flown at 4.9 sccm, SiH_4 at 0.16 sccm. The deposition rate was 3118 Å /min at substrate temperature of 500°C.

Sample 7: Sputtering was done using a Kurt J. Lesker RF magnetron sputtering system using argon plasma. A Si_3N_4 target was used and the target power was 500W. The substrate temperature was room temperature. The Ar flow rate into the chamber was 7sccm and the pressure during deposition was 3.7×10^{-4} Torr.

Sample 8: Post-anneal was applied to sample7 to densify the sputtered film. Annealing was done at 1050°C for 2 hours in a N_2 ambient.

These films were deposited on 3μm thick thermal oxide under-cladding. Lithography was done on a Nikon i-line (365nm) stepper NSR-2205i9. Shipley SPR700 at 1μm thick was used for photoresist. After the lithography exposure, the photoresist was irradiated by UV

light using Fusion M150PC Photostabilizer to avoid deformation during the successive post bake. The post bake was done at 130°C for 3minutes, then at 200°C for another 3 minutes on a hot plate. Then the waveguide was defined by a dry etching process by Applied Materials AME5300. The etching conditions were as follows. Etching gases are flown at C_2F_6 30 sccm, source RF and wafer bias are 1650W and 450W, respectively. Oxide top-cladding at 3μm thick was deposited using a Concept1 PECVD system. The waveguide dimensions are shown in figure 2.5. This waveguide was designed to have TE-polarization as a fundamental mode.

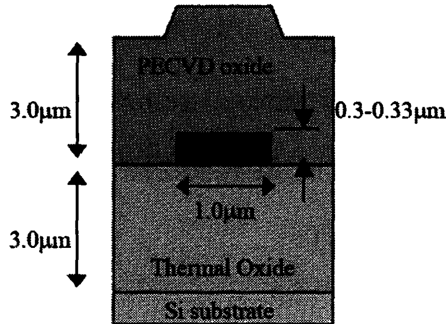

Figure.2.5: Nitride waveguide dimension (not to scale). The top and bottom claddings are approximately 3μm thick.

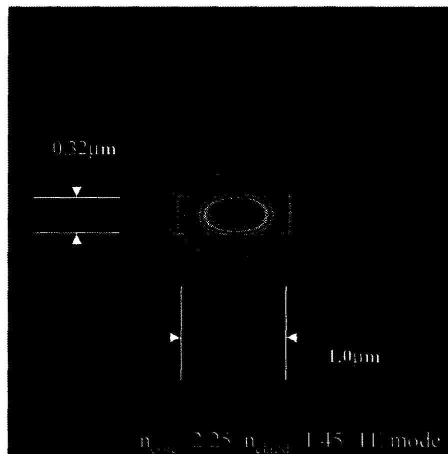

Figure 2.6: Mode profile of Silicon-rich nitride. n_{core} and n_{cladd} are assumed to be 2.25 and 1.45. respectively and The width and height to be 1.0 and 0.32μm, respectively.

Table 2.2 summarizes refractive indices and thickness obtained for each film. All films are within an acceptable range in terms of single mode condition. The thickness was obtained by ellipsometer (Gaertner L125B) and KLA tencor UV1280.

In addition to simple straight waveguides, bends were also fabricated. The radii range from 5-40μm. The wafer was then diced and the facets were polished using Buehler ECOMET3 to achieve good coupling between fiber and waveguide.

Sample No.		R.I (n) at 633nm	Thickness (μm)
1	(conventional PECVD)	2.116	0.327
2	(conventional PECVD+anneal)	2.281	0.302
3	(LPCVD)	2.250	0.306
4	(HD-PECVD)	2.144	0.309
5	(HD-PECVD+anneal)	2.144	0.302
6	(HD-PECVD w/ higher dep.temp.)	2.252	0.332
7	(Sputter)	2.221	0.307
8	(Sputter+anneal)	2.281	0.308
	Reference: (thermal oxide)	1.458	

Table 2.2: Refractive indices (R.I.) and thickness of deposited nitride films.

2.5 Waveguide loss measurement

The waveguide loss measurement set-up is briefly outlined in figure 2.7. Waveguide loss was evaluated using the Fabry-Perot resonance method. Different from conventional cut-back technique, this Fabry-Perot resonance method can provide more reliable loss values since the loss obtained here does not depend on coupling conditions between fiber and waveguide, which is very sensitive to alignment accuracy [14]. The loss can be obtained using the following equation:

$$\alpha = -\frac{1}{L}\ln\left(\frac{1}{R}\frac{\sqrt{I_{\max}/I_{\min}}-1}{\sqrt{I_{\max}/I_{\min}}+1}\right)$$

where α (/cm) is the propagation loss coefficient ($4.3\alpha(/\text{cm}) = \alpha_T(\text{dB/cm})$). L is the length of the waveguide, R is the facet modal reflectivity. I_{max} and I_{min} are the peak and bottom intensities of each resonance, respectively. The reflectivity R is obtained by 3D-FDTD simulation and found to be around 10.5%. Loss was obtained by averaging the results from 5-10 peaks and valleys in the Fabry-Perot spectrum near 1550nm. In addition to 1550nm, the propagation losses were also obtained at 1510nm, where the absorption by N-H bonds has a peak as shown in figure 2.4.

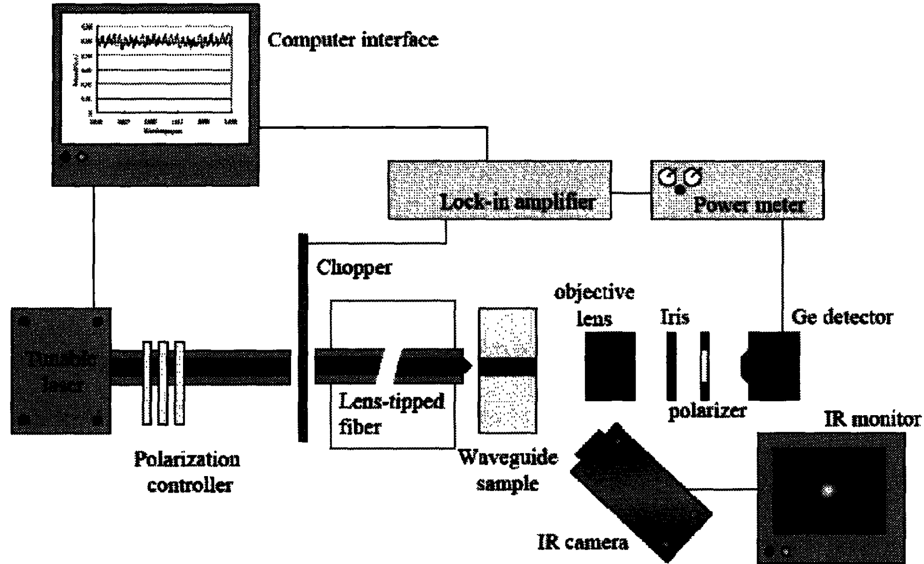

Figure 2.7: Schemmatic of waveguide loss measurement system (not to scale).

2.6 Results

A. Propagation loss

Table 2.3 summarizes the results of waveguide loss (α_T) measurement.

Sample No.		Propagation loss(dB/cm) at 1550nm	Propagation loss(dB/cm) at 1510nm
1	(conventional PECVD)	2.54±0.3	5.57±1.0
2	(conventional PECVD+anneal)	1.79±0.7	3.28±1.0
3	(LPCVD)	1.44±0.9	1.80±0.7
4	(HD-PECVD)	1.77±0.6	2.43±1.2
5	(HD-PECVD+anneal)	1.46±0.6	1.93±0.7
6	(HD-PECVD w/ higher dep.temp.)	1.56±0.7	1.79±0.5
7	(Sputter)	>40	NA
8	(Sputter+anneal)	22.6±12	NA

Table 2.3: Propagation losses for nitride waveguides.

A-1: Conventional PECVD (samples No.1 and 2)

PECVD samples from conventional PECVD (No.1 and 2) showed an improvement after high temperature annealing. The effect is due to both denser film and the lowering of N-H bond density. It is shown in table 2.2 that the film shrinks by 8% and the index increases by 8%, which indicates hydrogen atoms are removed out of the film by out-diffusion. These samples show relatively high loss, especially at 1510nm. The loss at 1510nm indicates that there still exists a considerable amount of N-H bonds in the nitride film and a long-time high-temperature anneal is required to achieve the low loss nitride, which is, however, not compatible with other electronic devices.

A-2: **LPCVD (sample No.3)**

This sample showed the lowest loss at 1550nm and the second lowest at 1510nm even without post annealing. This indicates that the deposition temperature is an important factor to achieve low-loss nitride. And it is also expected that low deposition rate is effective to remove hydrogen out of the film and dense film.

A-3: **HD-PECVD (samples No.4, 5, and 6)**

HD-PECVD samples (No.4 and 5) showed relatively low loss as compared to conventional PECVD samples (No.1 and 2). This indicates that by substituting NH_3, a conventional nitrogen source in PECVD nitride process, with N_2, N-H bond formation is effectively suppressed. It is also seen that the loss is lowered by high temperature anneal. As shown in table 2.2, HD-PECVD samples do not show significant change in terms of thickness and refractive index even after high temperature anneal. This indicates that hydrogen incorporation is minimized even without anneal. However, the lower loss is also achieved by slightly increasing the deposition temperature from conventional 400°C to 500°C, which indicates that the deposition temperature is more effective than applying high temperature anneal such as 1050°C N_2 anneal.

A-4: **Sputter (samples No.7 and 8)**

Sputtered samples (No. 7 and 8) showed high propagation loss although slight improvement is seen after high temperature annealing. This result indicates that the sputtered nitride is not dense enough even after high temperature annealing. Since the deposition was done at low temperature, it is considered that the film incorporated Ar and was porous and cannot be densified only by high temperature annealing.

B. Bend loss

Bends with 5 to 40μm radii were fabricated using sample No.3 and evaluated. Figure 2.8 shows schematically the test structure for bend loss evaluation. Figure 2.9 shows bend losses per 90° turn measured by the Fabry-Perot resonance method. These bend losses were obtained by subtracting straight waveguide's propagation loss from the total loss of the test structure.

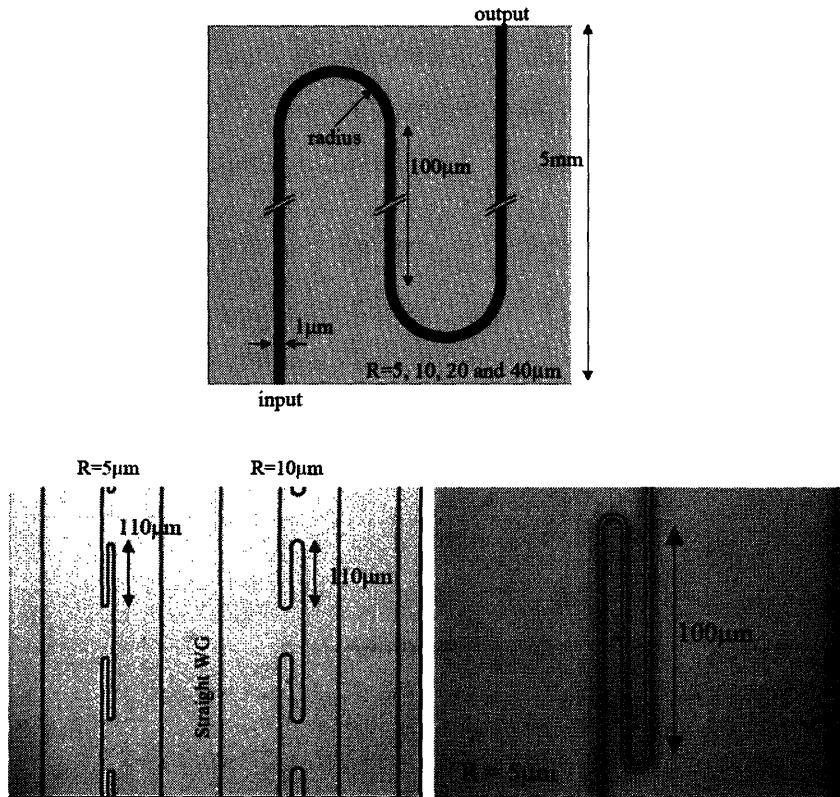

Figure 2.8: Test structure for bend loss evaluation. (Top) Mask layout for bend loss evaluation and (Bottom) optical microscope images of bending and straight waveguides.

To evaluate the dependence of sidewall angle on bend loss, three kinds of dry etching were employed to fabricate different sidewall angle. Figure 2.10 shows waveguide cross sections with different etching process. Thicker films were used to obtain the sidewall angle caused by dry etching.

A 5μm bend shows larger deviation from theoretical value obtained from FDTD simulations. However, larger radii keep bend loss within acceptable bounds. The larger deviation from the theory at 5μm radius can be attributed to sidewall roughness and slanted sidewall, which introduces polarization dependent loss (PDL) [16]. The mode conversion from TE to TM mode can lead to leaky mode radiation loss at bend. And the waveguide is considered to be more sensitive to sidewall roughness at bends since the mode is pushed outward and the larger portion of the propagating light is affected by rough sidewall. The more detailed study is needed to explain it quantitatively.

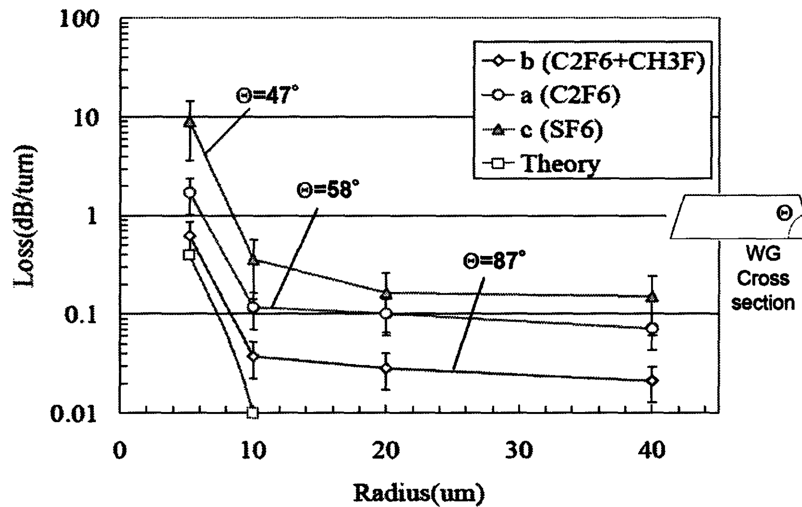

Figure 2.9: Bend losses for nitride waveguides with various sidewall angles. The larger loss is observed with larger sidewall angle.

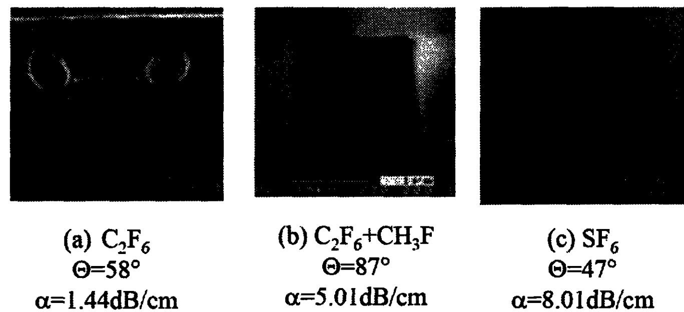

(a) C_2F_6	(b) C_2F_6+CH_3F	(c) SF_6
Θ=58°	Θ=87°	Θ=47°
α=1.44dB/cm	α=5.01dB/cm	α=8.01dB/cm

Figure 2.10: Waveguide cross sections patterned with various etchant gases. Sidewall angles and propagations losses are also shown.

Therefore, it is considered to be important to develop a proper dry etching process. However, it is expected to be challenging to suppress both sidewall roughness and slanted sidewall as shown in figures 2.9 and 10.

2.7 Discussion and summary

Figure 2.11 and 12 show the loss dependence on substrate temperature at 1550nm and 1510nm, respectively.

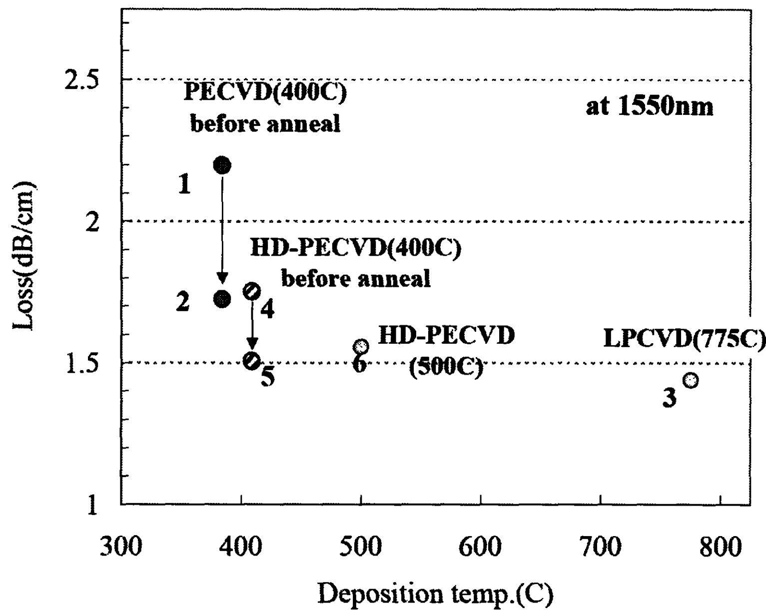

Figure 2.11: Propagation loss vs. deposition temperature plot for nitride waveguides at 1550nm. It is shown that both deposition temperature and post-annealing can reduce the loss.

The loss plot for 1510nm (figure 2.12) clearly shows how the absorption by N-H bonds is affected by deposition and post-anneal temperatures. Although the high temperature anneal is effective to reduce the loss, it is challenging to remove all the hydrogen out of the film even at 1050°C. On the other hand, raising the deposition temperature is more effective to reduce the loss and compatible with other electronic devices. It is also considered to be effective to lower the deposition rate by diluting the precursors to give enough time to

hydrogen atoms to diffuse out of the film. In this case, N_2 is not appropriate as a dilutant since it is also a precursor for nitride deposition. Therefore other inert species, such as Ar, may be a good candidate for a dilutant.

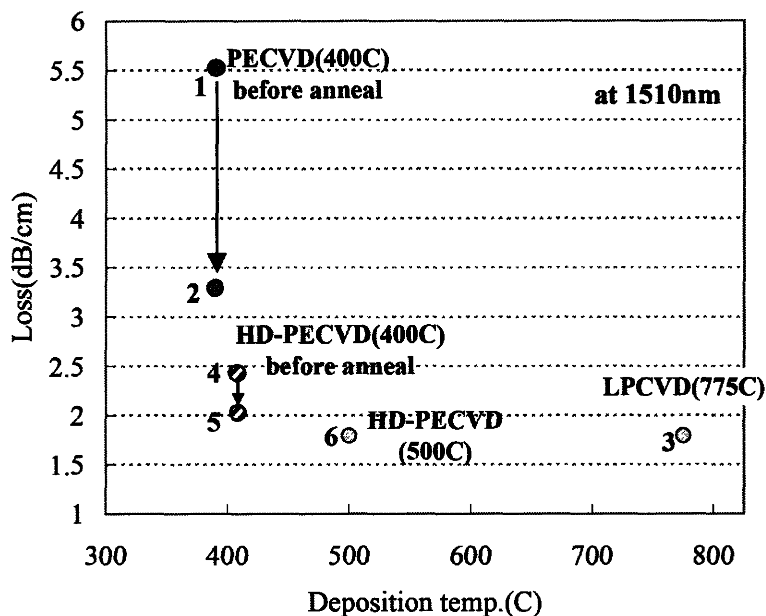

Figure 2.12: Propagation loss vs. deposition temperature plot for nitride waveguides at 1510nm. It is shown that both deposition temperature and post-annealing can reduce the loss. The effect of N-H absorption can be clearly seen from this plot and it shows that substrate temperature is more effective to suppress the loss.

Figure 2.13 depicts the temperature dependence of hydrogen dissociation rate at the surface (left axis) and the hydrogen bulk concentration at 0.3μm depth normalized by initial concentration as a function of anneal temperature (right axis). The dissociation rate is expressed by;

$$\nu = \nu_0 \, exp\left(\frac{-E_{dissoc}}{kT}\right)$$

Where ν and $E_{dissoc.}$ denote vibrational frequency and dissociation energy, respectively. 0.45eV and 10^{14} (Hz) is used for E_{dissoc} and ν_0, respectively [17]. The value is normalized at 400°C. The hydrogen bulk concentration is obtained from an error function.

$$\frac{C(x,t)}{C_0} = erf\left(\frac{x}{\sqrt{4Dt}}\right)$$

where D, x and t denote diffusion coefficient, depth and time, respectively. D is obtained experimentally and expressed as :

$$D = D_0 \exp\left(\frac{-E_a}{kT}\right)$$

where 5E10^{-4} cm^2/sec. and 1.55eV are used for D_0 and E_a (activation energy), respectively [18]. E_a is obtained experimentally so that experimental results fit the diffusion behavior [18]. Therefore, the experimentally obtained E_a takes both N-H dissociation and H out-diffusion into account. Due to the large difference of E_{dissoc} and E_a, dissociation rate increases exponentially as a function of deposition temperature whereas the hydrogen bulk concentration decreased almost linearly as a function of post-anneal temperature.

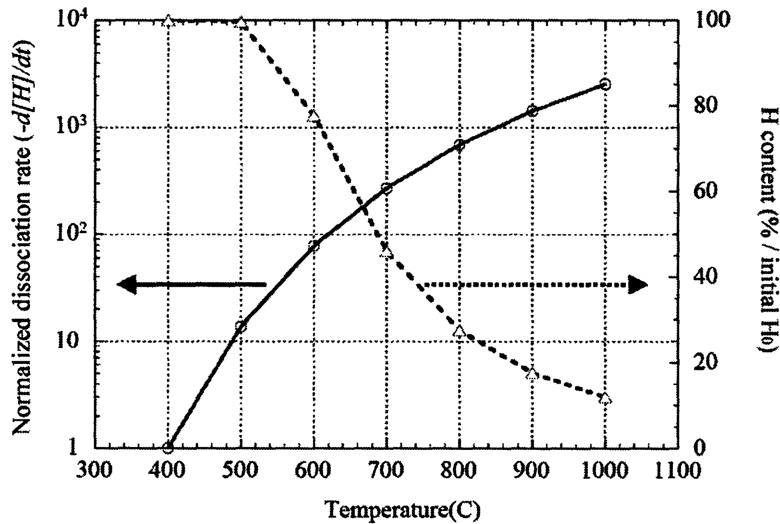

Figure 2.13: The temperature dependence of hydrogen dissociation rate (left axis) and hydrogen content at 0.3μm depth by out-diffusion (right diffusion). The hydrogen dissociation increases exponentially as deposition temperature rises whereas hydrogen out-diffusion decreases almost linearly as post-anneal temperature goes down.

As a conclusion, it is considered to be the most effective to deposit nitride with N_2 precursor as nitrogen source under high-density plasma condition with a relatively high deposition temperature such as 500°C. If other electronic devices can tolerate with 750-775°C, which is conventional LPCVD deposition temperature, LPCVD process is also a good choice to obtain low-loss nitride.

Chapter 3: Air trench waveguide

3.1 Background

Low index contrast silica bench technology, which is often referred to as PLC (planar lightwave circuit) or SiOB (silica optical bench) has been widely used in the fabrication of passive integrated optical components such as arrayed waveguide gratings (AWGs) [19]. It is well known that PLC (or SiOB) structures provide low fiber-to-chip coupling and low propagation losses due to their low index contrast between core and cladding. A major drawback of PLC (or SiOB) technology is a relatively large footprint, where a critical factor is the minimum waveguide bend radius. Due to weak light confinement, low index contrast waveguide circuits require large bend radii, ranging from millimeters to a centimeter ($\Delta = 0.25\text{-}1.5\%$) [19], to reduce radiative loss. On the other hand, high index contrast materials systems, such as Si/SiO_2 where the index difference is as much as 2, offer dense integration but pose challenges in fiber-to-chip coupling and scattering loss from sidewall roughness. A technology that allows a drastic reduction in the bending radius would overcome one of silica's major obstacles to attaining truly large scale optical integration. I propose a scheme using air trenches (AT) to provide locally enhanced lateral mode confinement. I use adiabatic tapering to avoid abrupt junction-induced mode mismatch and Fresnel reflection in order to miniatualize optical waveguide bends while preserving low-loss performance. Air trench (AT) waveguide is expected to provide a drastic reduction in the bend radius, while permitting simple fabrication. By eliminating this scaling limitation, AT design allows large-scale optical integration to be achieved on low- and medium index contrast platforms

Bend loss is a fundamental performance property of dielectric waveguide circuits,

increasing bend radii [20-24] and index contrast decrease. A small bend radius with small radiation loss can be achieved by increasing the index difference between core and cladding. High index contrast seems the natural choice to achieve dense integration of optical components, but fabricated high index contrast waveguides suffer high propagation loss, caused by sidewall roughness of the waveguide [25-26], and poor coupling between the fiber and waveguide due to mode shape mismatch and alignment sensitivity. It was reported that propagation loss is proportional to the 3rd power of the sidewall roughness [25-26]. On the other hand, low index contrast waveguides provide small propagation loss and good coupling between fiber and waveguide but require relatively large bend radii to achieve low bend loss. This size problem is critical for the dense integration of optical components. As another candidate for dense optical integration, photonic crystal waveguides are attracting considerable attention [27-29], but due to poor vertical mode confinement and fabrication complexity, they have shown high propagation loss. Recently the use of medium index contrast waveguides has been proposed where index difference ranges from Δn=0.05-0.3 to avoid the problems of high index contrast and low index contrast waveguides [30-35]. But the bend radius is still a problem for dense integration. For example, when index difference is Δn=0.1(Δ=6.8%), 100-200μm radius is required to achieve 98% transmission (0.09dB loss) in one 90° turn. Thus, the density of integration in low-to-medium index contrast using conventional waveguides is limited by bend loss.

We have recently proposed a new scheme using air trenches to provide locally-enhanced lateral confinement, enabling small bends and T-splitters [36]. We use adiabatic tapering to avoid abrupt junction-induced mode mismatch and Fresnel reflection. Optical waveguide bends are thus miniaturized while preserving low-loss performance. The basic configuration of an AT bend is depicted in figure 3.1.

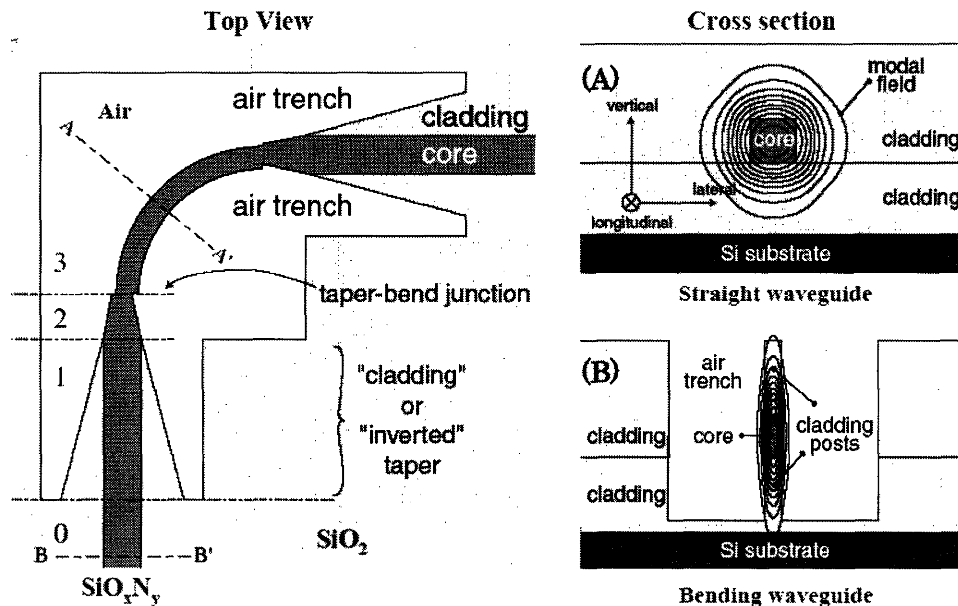

Figure 3.1: Air trench bend (ATB)– (A) Cross sectional view of low index (straight) waveguide, (B) Air trench region (bend). Contour plots representative of the dominant modal electric field component are superimposed on the cross sections (not to scale)

3.2 Air trench bend theory and simulations

The employment of air trenches for sharp bending radii has been proposed previously in the context of optical fiber, slab [37], and ridge waveguide bend loss [38]. In the former case, the trench is placed away from the core and to extend the reach of the evanescent part of leaky-mode (LM) field. The radiation-caustic is pushed radially outward without significantly altering the shape of the LM [37]. In the latter case, trenches were deep etched next immediately next to the core of InP/InGaAsP-ridge waveguides, providing higher lateral mode confinement at the expense of junction loss [38].

In typical silica index contrasts such as PLC or SiOB where index difference (Δn) ranges from 0.0036-0.022 [19], the abrupt junction loss at the interface between the standard waveguide and the trench region becomes unacceptable for any bend radii small

enough to make the air trench useful in reducing size. This is the reason why an adiabatic taper is placed at the junction as in figure 3.1. The bend in the trench region is analyzed using some standard semianalytic tools [20-24]. The trench tapers are designed and optimized through simulations using FDTD in the later discussions.

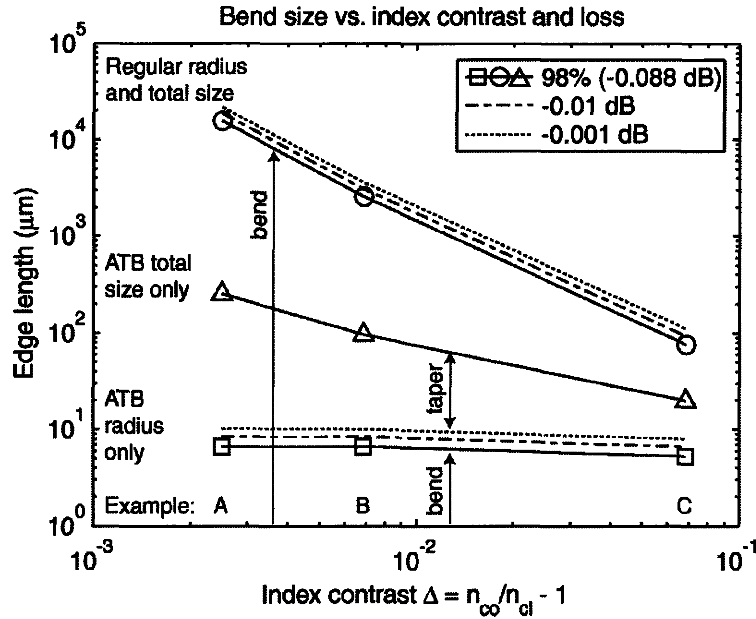

Figure 3.2: Bend (radius and "total box") size for regular waveguide bends and ATBs, showing improvement in size for the case of 0.1-dB loss. It is also shown that, on this scale of size variation, the relative change in radius is small for 0.01- and 0.001-dB loss [36].

Property		Example A	Example B	Example C	units
Index	Contrast (Δ)	0.25	0.68	6.85	%
Regular Bend	Radius	15700	2565	76	μm
	Total Size[a]	15708	2570	78	μm
Air Trench Bend	Radius	15.35	9.25	7.25	μm
	Total Size[a]	252.60	95.85	19.75	μm
Size Reduction	by Length	62	27	4	
	by Area	3867	719	16	

Table 3.1: Regular and ATB radii and total sizes for 98% transmission. AEdge length of a box enclosing the entire bend structure and accommodating > 99.9% of the input and output power. The minimum bend size possible is a square with an edge equal to this 99.9% mode width [36].

A. Regular and ATB loss

Bending loss in regular waveguide bends without an air trench, or in case of of the ATB, the curvature loss in the bend-containing trench region was considered. Radiation loss in regular bends and ATBs was evaluated numerically according to the approaches [21] after customary transformation for bend waveguides [21]. Bends were designed for overall 98% transmission (~ 0.1-dB) loss per right-angle bend, and the bend parameters are shown in figure 3.2 and table 3.1 for three chosen index contrasts. The regular bend was constrained to have single-mode input and output waveguides, while ATB bend region is only constrained to have them smaller than the low-index waveguide (straight waveguide), which effectively presents no constraint. The bending loss was evaluated in the usual way by solving for the complex propagation constant of the lowest order LM using either the linearized, conformally transformed dielectric constant profile, where the modal field is expressed in terms of Airy functions [22-23] or the Wentzel-Kramers-Brillouin (WKB) method for very low loss bends [39]. The second contributor to loss in a finite-angle bend is junction loss at start and end points. For a straight-to-bend junction, and neglecting scattering into reflected (backward) radiation modes, a simple expression was obtained, which includes the overlap integral of the leaky bend mode field computed previously with the mode of the straight waveguide [36]. The appropriate expression for power coupling efficiency at a straight to a bent slab junction is given by,

$$\eta = \frac{\beta_2}{\beta_1}\left(\frac{2\beta_1}{\beta_2 + \beta_1 \dfrac{\langle E_2|E_2\rangle}{\langle E_2|\frac{R}{r}|E_2\rangle}}\right)^2 \frac{\langle E_2|E_1\rangle^2}{\langle E_2|\frac{R}{r}|E_2\rangle\langle E_1|E_1\rangle} \tag{1}$$

resulting in a junction loss of $L_J = 10 \log \eta$ (dB). Here $\beta_{1,2}$ are propagation constants,

$E_{1,2}$ are the modal electric field amplitudes of the two waveguides at the junction, R is the bend radius and r is the radial coordinate which is identical to the transverse x-coordinate of the straight waveguide along the junction. The one-dimensional overlap integral in this slab waveguide case is, for example,

$$\left\langle E_2 \left| \frac{R}{r} \right| E_1 \right\rangle = \int_0^\infty E_2^*(r) \cdot \frac{R}{r} \cdot E_1(x) dx \Big|_{r=x} \qquad (2)$$

and simplifies to the case for straight waveguides for $R \to \infty$, where $R/r \to 1$ over the range of r-values where the integrand (modal field) significantly contributes to the integral. For the straight slab junction case, FDTD simulations were done to check on the validity of ignoring reflected radiation modes, and confirmed a high accuracy for low junction losses of <1dB. In low index contrast, such as that considered here, loss in regular waveguide bends is dominated by bending loss, and junction loss can be ignored. For trench-clad bends (the bend region of ATBs), junction loss must be incorporated into the loss figure.

B. Cladding tapers

In the case of ATB, the purpose of the cladding taper is to adiabatically shape the fundamental mode of the low-index contrast input waveguide to the shape of the fundamental mode in the high index contrast (air trench clad) output. In low-index contrast, this output mode can be much smaller than the minimum possible width of the input waveguide mode. The tapers were finally characterized by full 2-D FDTD simulations, which should provide an accurate estimate of performance. Results are listed in table 3.1 with equal throughput efficiency. Figure 3.3 shows that how the mode shape changes as the input light propagates along the taper.

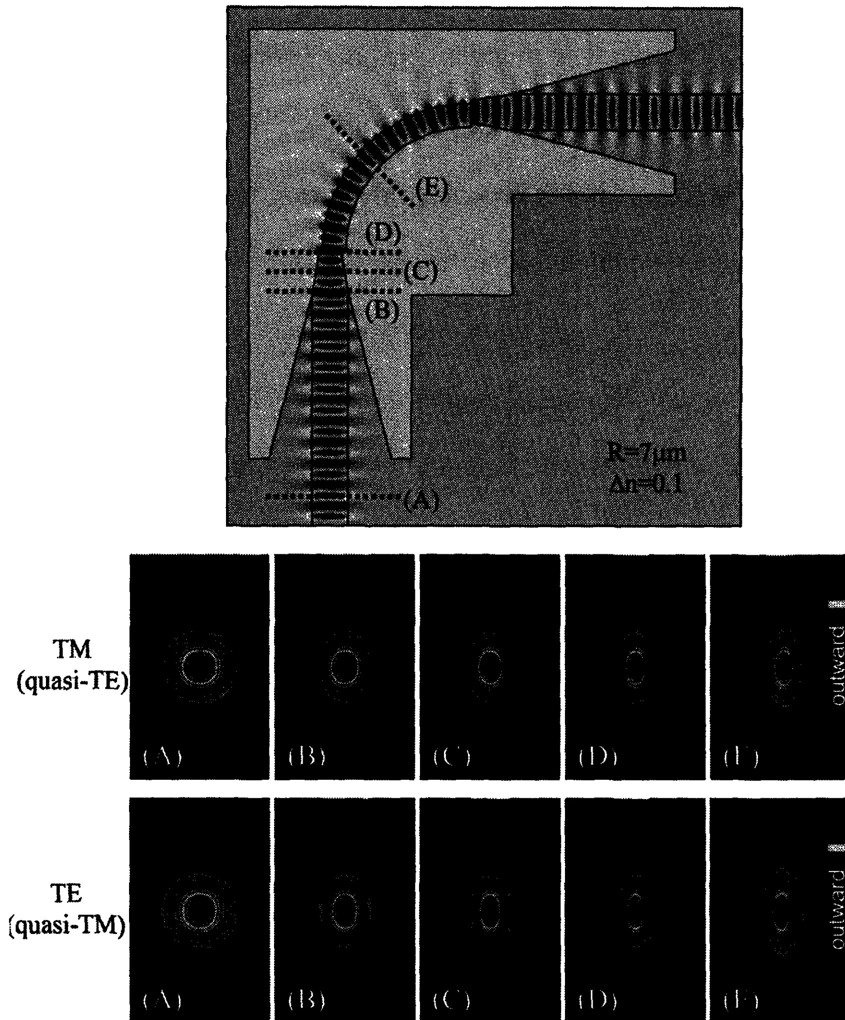

Figure 3.3: Mode shape conversion along the air trench bend. The shape of the mode changes depending on the location inside the ATB.

C. Substrate loss and minimum trench depth

In order to curb the substrate loss in the actual ATB, the air trench has to be etched sufficiently deep beneath the core for the evanescent tail of the field to be small where it reaches the bulk cladding. With $n_{mode} < n_{cladding}$, the modal field will be oscillatory in the bulk substrate below the trench, and the mode will exhibit leakage through a tunneling

process from the core, through the cladding ridge beneath it, into the bulk cladding (the field is evanescent in the vertical direction in the ridge). A deep trench, as demanded here, requires high aspect ratio etching. The mode is weakly confined in the vertical direction, so the air trenched have to be several core heights deep for acceptable substrate loss. Since the aspect ratio increases with lower index contrast, fabrication issues will place a lower limit on the index contrast range for which this technique is practical. It is of interest to evaluate the required depth of the air trench given an acceptable substrate loss, which is much less than ATB loss. Two approach were employed to evaluate substrate loss [36]. A semianalytic perturbation method using the mode solution of the ideal (guiding trench) and a numerical, full-vector mode solver for LMs, both taking into consideration the 2-D cross section of the waveguide.

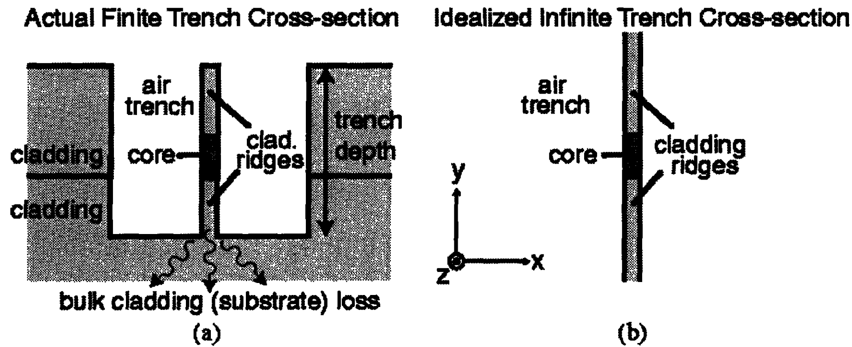

Figure 3.4: Schematic of (a) actual trench cross section with finite trench depth and (b) the idealized trench with infinite trench depth [36].

(A) 2-D equivalent current sheet method.

An equivalent current sheet was defined and a cylindrical-vector Green's function approach was used to evaluate the far-field radiation and loss per unit length [40]. It was assumed that silica cladding continues below the trench and the mode shape remains unperturbed

above the air trench-bulk cladding interface and this field was used to define an equivalent current sheet just above the bottom of the air trench-bulk cladding interface and use this field to define an equivalent current sheet just above the bottom of the air trench to represent the fields below as in figure 3.4(a), region of interest.

Assuming that the field does not change much in crossing the interface, the current sheet can be moved just below the trench, where we now have a region of uniform index (bulk cladding or substrate). For a more accurate treatment, I can account for Fresnel reflection due to the interface when translating across it fields that generate the current sheet. A far-field solution of the radiation pattern into the bulk cladding can then easily be calculated integrating a cylindrical-vector Green's function over this source (factoring out first the propagation direction z). A field attenuation coefficient results in:

$$\alpha = \frac{1}{2}\frac{\left(\frac{dP_{radial}(z, z_0)}{dz}\right)}{P_{guided}}$$

Where the numerator represents the radial component of far field radiated power per unit waveguide length, the denominator represents power guided in the mode, and substrate loss is $Ls = -20\log e^{-\alpha}$.(dB/m). For air trench waveguide substrate loss calculations, the original equivalent current sheet was used and reflection from the interface was ignored, as proper compensation for the reflection on a 2-D interface would complicate the calculation. Normalized 2-D substrate loss results obtained for ATB examples A-C are shown in figure 3.6, where guided-mode solutions of the ideal air trench waveguide from a vector field mode solver were used to define the current sheet. From these plots, a trench depth for which the substrate loss is much smaller than ATB loss of 0.1dB was chosen.

(B) Numerical mode solver for 2-D vector modes.

A second set of substrate loss results comes with less physical intuition but with exct solutions and was obtained directly from a vectorial mode solver designed for leaky waveguides. A staggered vector-field was used like that in FDTD [41], and [42] and implemented PML absorbing boundary conditions in the frequency domain to allow for LMs. The resulting complex problem was solved using a parse matrix iterative eigenvalue solver. The substrate loss results directly from the imaginary part of the mode propagation constant. The computed substrate loss values are plotted in figure 3.6 along with the current sheet results. The discrepancy is attributable to ignored refelction in the current sheet results. An example modal solution is shown in figure 3.5. It is shown in figure 3.6 that twice the core height is deep enough for the trench depth to suppress the substrate loss.

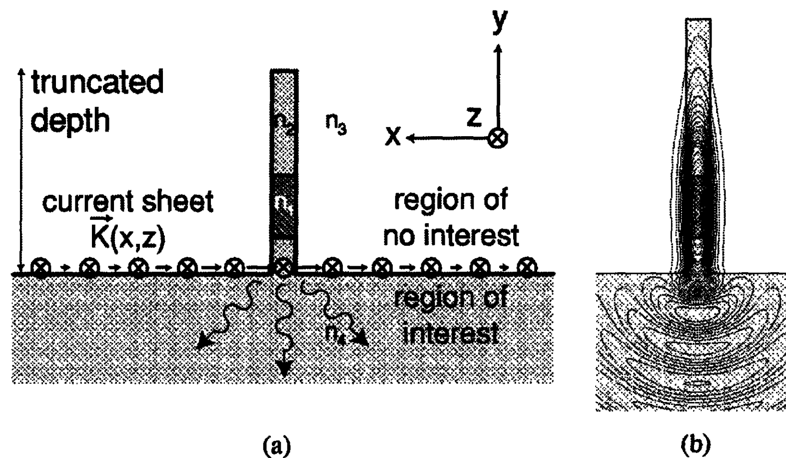

Figure 3.5: Calculating substrate loss: (a) Setup of 2-D equivalent current sheet method (ECSM). (b) Mode solver LM solution example: Real part of the E_y field component for the waveguide of Example B with the bulk cladding 0.6 core heights from the axis [36].

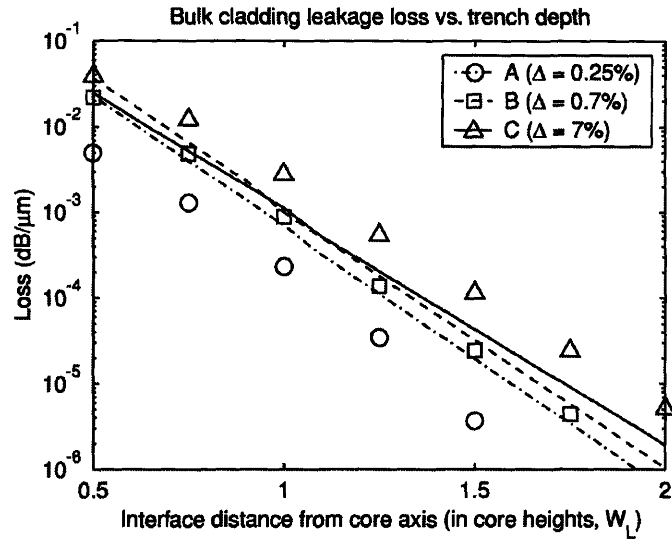

Figure 3.6: Bulk cladding loss versus trench etching depth for waveguides of examples A-C computed by approximate ECSM (lines) and numerical vector-field mode solver for leaky wavguide (symbols). The discrepancy is due to reflection at the interface with bulk cladding, not accounted in the ECSM calculation [36].

3.3 FDTD simulation examples

In this section, some FDTD simulations are carried out and visualized to explain how the air trench waveguide works. All the simulations were done based on $\Delta n = 0.1$. Figure 3.7 is a set of visualized FDTD simulation results for ATB.

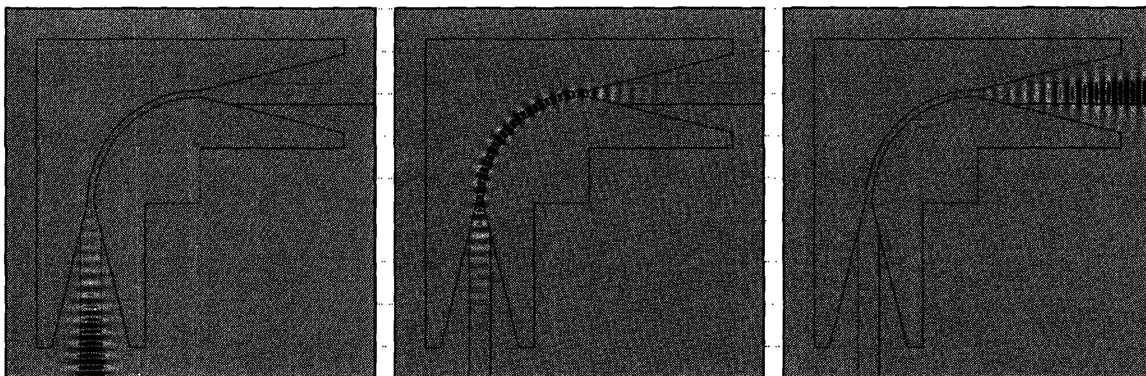

Figure 3.7: FDTD simulations for ATB. (Left) Light is squeezed by adiabatic tapers (mode matching process to bend/splitter), (Middle) then traverses air trench bends, (Right) and emerges into the output mode via the trailing taper [36].

It is shown in figure 3.7 that the light is transmitted through the air trench bend maintaining single-mode without significant scattering. Figure 3.8 is a comparison with and without cladding tapers. It is shown that junction loss is suppressed by placing cladding tapers. The junction loss is reduced from –1.5dB (31% loss) to –35dB (2.0% loss).

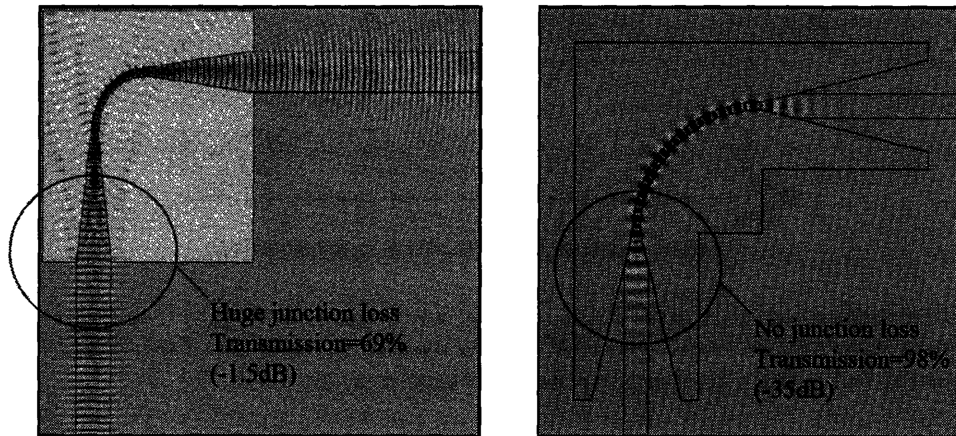

Figure 3.8: FDTD simulation of (Left) air trench bend without tapers. Raius=9μm. n_{core}=1.56, n_{clad}=1.46. (Right) air trench bend with tapers. Radius=7μm, n_{core}=1.56, n_{clad}=1.46 [36].

By employing the same designing approach as ATB, the air trench (AT) T-splitter was evaluated. Figure 3.9 shows the FDTD simulations for AT T-splitter.

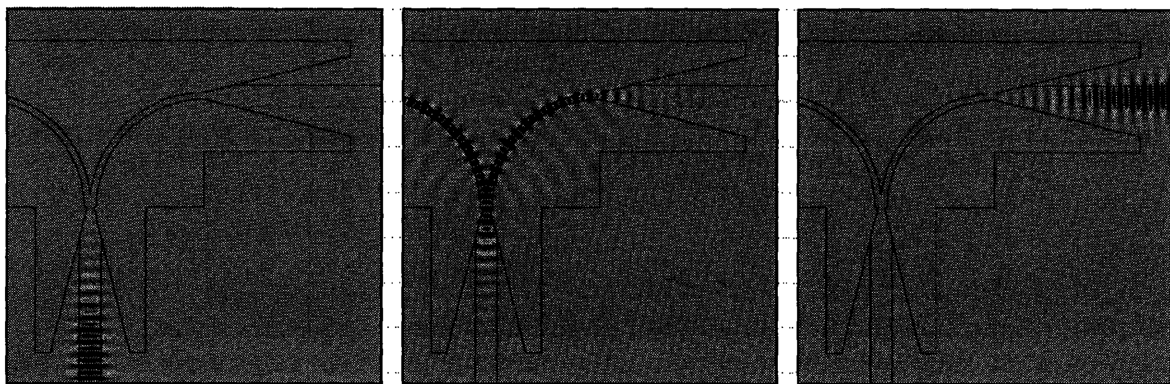

Figure 3.9: FDTD simulations for AT T-splitter (left) Light is squeezed by adiabatic tapers (mode matching process to bend/splitter), (Middle) then traverses air trench bends, (Right) and emerges into the output mode via the trailing taper [36].

3.4 Realization of ATB and AT T-splitter

From this section, the realization of ATB and AT T-splitter is discussed. Theoretical details of AT bend design are discussed in the previous section. Figure 3.10 summarizes bend design for conventional waveguides and AT sections for the case of 0.09dB loss, which corresponds to 98% transmission. Three examples (A, B, and C) depict the case where $\Delta(n_{core}/n_{cladding}-1) = 0.25\%$, 0.68% and 6.8% , respectively. Radiation loss in regular and AT bends is evaluated numerically according to the approaches in [22] and [23] after the customary conformal transformation for bent waveguides [21]. The result is a theoretical reduction in bend radius by a factor of 10-1000 and in total bend structure edge length by a factor of 4-60.

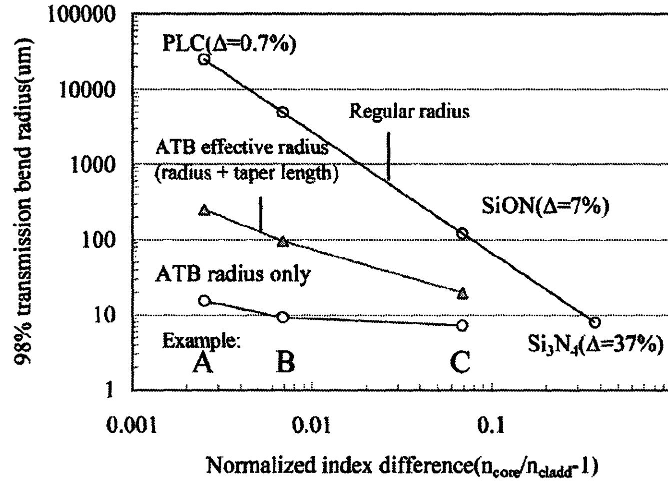

Figure 3.10: Bend radius design plot [43]. Claddings are assumed to be silicon dioxide(SiO_2). Radiation loss in regular and AT bend is evaluated numerically according to the approaches in [22] and [23] after the customery conformal transformation for bent waveguides [21]. The result is a theoretical reduction in bending radius by a factor of 10-1000 and in total bend structure edge length by a factor of 4-60.

Figure 3.11 summarizes the structural components of the AT design. In straight propagation, the structure is a simple low index contrast channel waveguide (cross section A in Figure 3.11). At bends, air trenches are placed to enhance lateral mode confinement by introducing local high index contrast (cross section B in Figure 3.11). To avoid junction

loss between the straight and bending sections, an adiabatic taper is placed at the input and output junction. These adiabatic tapers provide fast mode transition between straight and bending waveguides. This type of AT bend can result in a drastic reduction in bend radius depending on the index contrast between core and cladding.

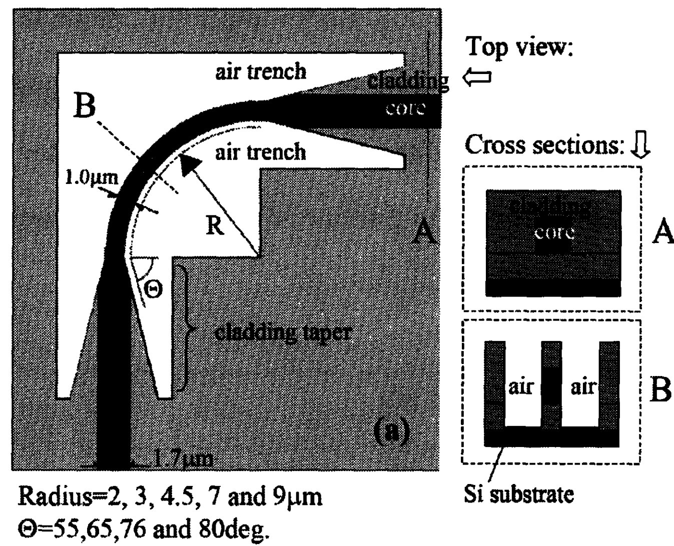

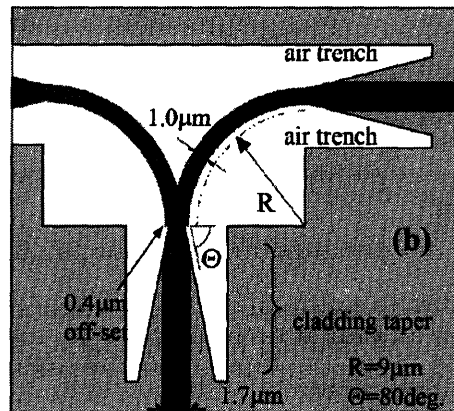

Figure 3.11: Air trench design schematic (photomask layout).
(a) Cross sectional view of (A) low index straight waveguide and (B) bend.
(b) Air trench bend (ATB). Radius = 2, 3, 4.5, 7 and 9μm and Θ = 55,65,76 and 80°.
(c) Ait trench T-splitter schematic. R = 9μm and Θ = 80°.

For the fabrication of ATBs and T-splitters, the index difference is targeted at $\Delta n=0.1$ ($\Delta=6.8\%$: Example C in figure 3.11). Silicon oxynitride (SiON) is chosen as core material since its refractive index can be easily adjusted during deposition just by changing gas composition [35]. Radii and linear taper angles are varied from 2 to 9μm and 55° to 80°, respectively, as in figure 3.11 since they are the most important factors for miniaturization of bend. A radius is defined by the inner radius of channel waveguide. The width of channel waveguide and AT waveguide are 1.7μm and 1μm respectively to keep single mode in low index contrast (straight) region and high index contrast (bend) region. Trench depth is chosen to be 4μm to minimize substrate loss. The trench depth should be more than twice as deep as core thickness to achieve 0.01dB substrate loss [36]. This low loss is achieved by laterally confining the evanescent tail of guided in-between deep air trenches. For the T-splitter, the radius and taper are fixed at 9μm and 80°, respectively (Figure 3.11b).

The fabrication process is schematically outlined in Figure 3.12. All of the processes are CMOS compatible. The starting substrate was 1mm thick Czochralski (Cz) grown p-type (0.1-100Ωcm) silicon wafer and under cladding was grown by high pressure thermal oxidation process (HIPOX) at 1050°C (figure 3.12a). The thickness of under cladding was 16μm. After growing the under cladding, a silicon oxynitride (SiON) core layer was deposited by Plasma Enhanced Chemical Vapor Deposition (PECVD) process (figure 3.12b). The target index is 1.5456 at 1.55μm so that index difference between core and cladding is 0.1. SiON deposition was done using a Novellus Concept1. The thickness and refractive index (at 633nm) of SiON film were 2.0498μm and 1.5294, respectively as deposited. This evaluation was done by Metricon model 2010 prism coupler. The wavelengths used here were 633nm and 1550nm, in TE mode.

After core layer deposition, a high temperature anneal (N_2 ambient, 1050°C 1-6 hours) was applied to consolidate the SiON film and to remove nitrogen-hydrogen covalent bonds which introduce absorption loss in the 1.55μm wavelength range [30]. During the annealing process, the SiON layer refractive index and thickness change as shown in figure 3.13. Both the thickness and refractive index converge to stable values after 4 hours. We used SiON which had been annealed for 4 hours for all the structures in this work. Photolithography was done using a Nikon i-line (365nm) stepper NSR-2205i9. The photoresist used here was Shipley SPR700(1.2). After the lithography process, the photoresist was irradiated by UV light using Fusion M150PC Photostabilizer to avoid photoresist deformation during the succeeding post bake. Post bake was done at 130°C for 3min and at 200°C for 3min on a hot plate. The waveguide pattern was transferred by a dry etching process (figure 3.12c). The etching was done with an Applied Materials AME5300 using C_2F_6 17.9 sccm and CH_3F 12.1 sccm and source RF and wafer biases of 1800W and 470W, respectively. Under these conditions, a high etch rate (-60Å/sec.) was achieved and high selectivity over photoresist (>3) and high aspect ratio were also achieved since CH_3F works as a sidewall protection layer due to its high carbon ratio. The obtained sidewall angle of air trench is 86°. Then wafers were cleaned by oxygen plasma ashing and piranha cleaning. Top cladding SiO_2 was deposited also by PECVD (figure 3.12d). Chemo-mechanical polishing (CMP) was applied to obtain a smooth surface for the second lithography step by Strasbaugh Harmony 6EC (figure 3.12e). A second photolithography and dry etching step were performed to fabricate the air trench using the same procedure as for waveguide fabrication (figure 3.12g-h).

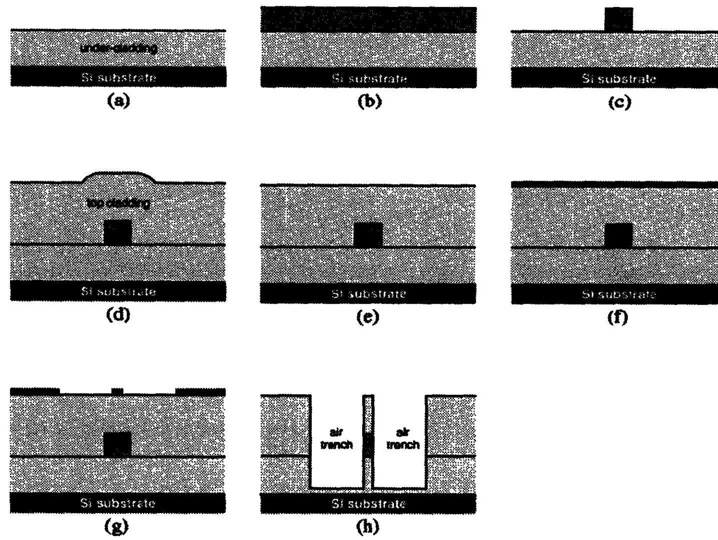

Figure 3.12: Brief schematic of air trench bend/T-splitter process flow (not to scale). All steps are done using conventional CMOS processes [43].

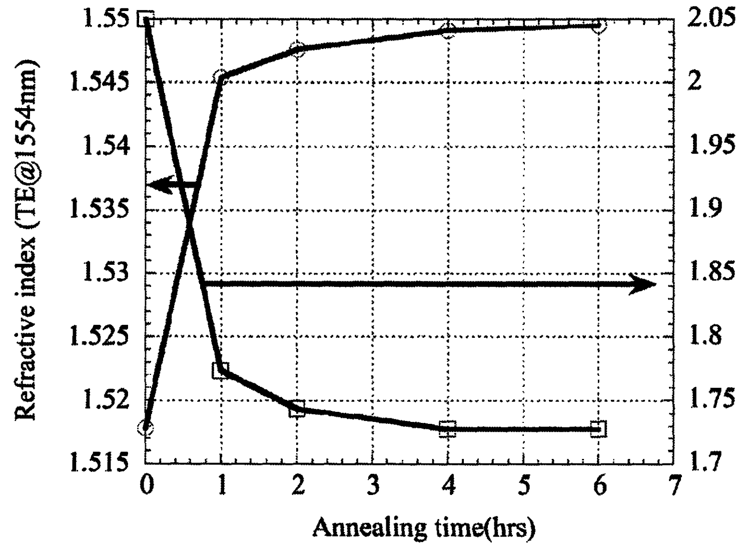

Figure 3.13: Refractive index and thickness changes of PECVD SiON after anneal (1554nm TE mode). The refractive index increases by 0.033 and thickness decreases by 15.7% as a result of consolidation annealing [43].

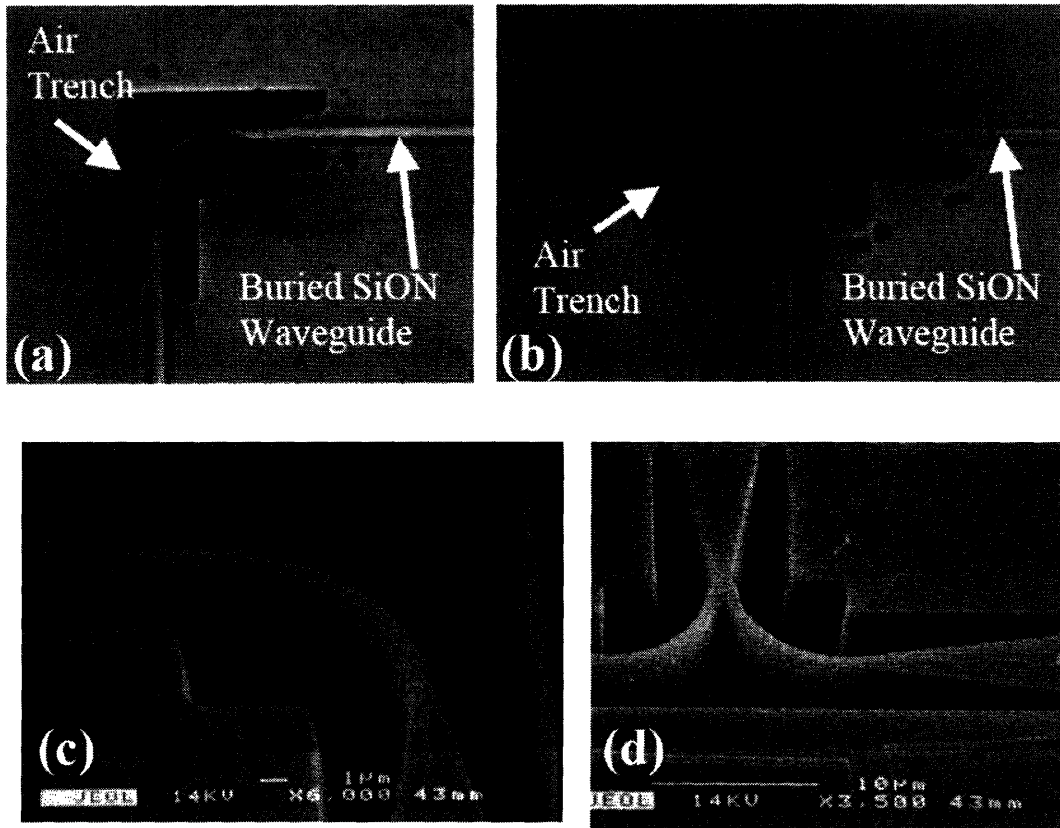

Figure 3.14: Images of fabricated structures. Optical microscope images: (a) AT bend; (b) T-splitter. SEM images: (c) AT bend (6,000x); (d) AT T-splitter (3,500x) [43].

Figure 3.14 shows a set of optical microscope top view images of an AT bend and a T-splitter where the radius is 9μm and the taper angle is 80°. It can be seen that the two layers (waveguide and air trench layers) are well aligned with each other. Figure 3.14 (c) and(d) show a set of scanning electron microscope (SEM) pictures of the AT bend and T-splitter. Table 3.2 summarizes the fabrication results in terms of dimensions realized in this process. The fabricated waveguides are close to design value as shown in table 3.2. All dimensions were obtained by SEM analysis.

	633nm TE mode	1550nm TE mode
Core (PECVD SiON) before anneal	1.5294	1.5430
Core (PECVD SiON) after anneal	1.5621	1.5485 (targeted at 1.5456)
Under- cladding(HIPOX thermal oxide)	1.4583	1.4456
Top- cladding(PECVD oxide) before anneal	1.4639	1.4531
Top- cladding(PECVD oxide) after anneal	1.4644	1.4531 (targeted at 1.4456)

	Designed	Actual
Waveguide top width(W_T)	1.7μm	1.59μm
Waveguide bottom width(W_B)	1.7μm	1.82μm
Trench top width(T_T)	1.0μm	0.65μm
Trench bottom width(T_B)	1.0μm	1.35μm
Trench depth	4.0μm	5.0μm

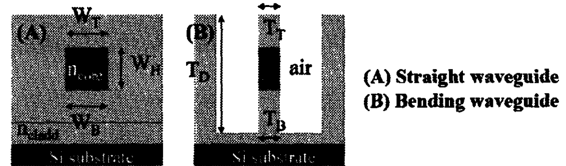

Table 3.2: (Left) Refractive indices of films employed for air trench waveguides. Indices are changed after consolidation annealing and close to design values. (Right) Waveguide dimensions after fabrication. Dimensions are obtained by SEM observation and close to design values. The sidewall angle of AT waveguide is 86°.

Figure 3.15 shows unsuccessful etching results done by conventional dry etching technique. (top-left: a) Cross section of etched SiON waveguide. AME5000 was used with CHF_3 etchant. Poor aspect ration was obtained due to photoresist corrosion as a result of long-time etch (25min.). (top-right: b) Bird's eye view of etched T-splitter waveguide. AME5300 (Centura) was used with C_2F_6 gas. Poor aspect ratio and rough sidewall roughness were observed due to unexpected photoresist sidewall etching. (bottom-left: c) Etched air trench made by the same etching recipe as in (b). (bottom-right: d) Etched air trench with higher wafer bias (600W). Better aspect ration was obtained but small structures such as air trench waveguide were vanished.

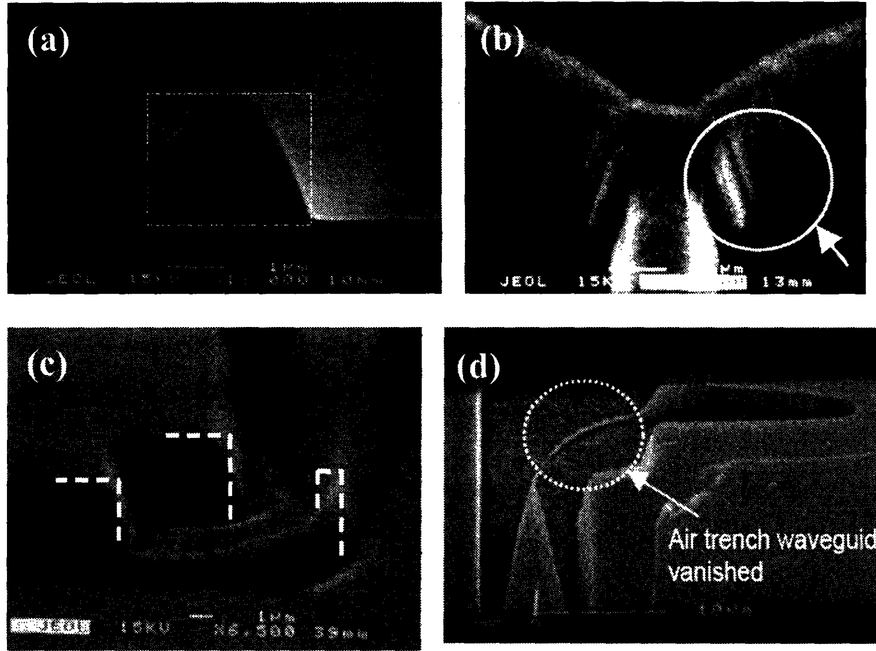

Figure 3.15: SEM images of etched structures using conventional techniques.

3.5 Measurement results

Waveguide loss measurements were done using the Fabry-Perot resonance method. Compared with the conventional cut-back method, this technique provides more precise measurement since optical contrast (I_{max}/I_{min}) does not depend on the coupling condition between optical fiber and waveguide, which is very sensitive to alignment conditions [25], [45]. The loss is simply calculated from the ratio of maximum to minimum intensity according to

$$\alpha = -\frac{1}{L}\ln\left(\frac{1}{R}\frac{\sqrt{I_{\max}/I_{\min}}-1}{\sqrt{I_{\max}/I_{\min}}+1}\right)$$

where α(/cm) is the propagation loss coefficient, L is the length of the waveguide, and R is facet modal reflectivity. I_{max} and I_{min} are the peak and bottom intensities of the

Fabry-Perot spectrum, respectively. The reflectivity R was calculated by a three-dimensional finite-difference time-domain (FDTD) simulation. The input and output facets were polished using a Buehler ECOMET3 system to suppress scattering at facets during measurement. $\alpha_T(\text{dB/cm}) = 4.3\alpha(\text{/cm})$. The experimental setup is shown in figure 3.17.

For both TE and TM modes, this waveguide shows propagation loss as low as 0.27±0.1dB/cm. Loss was obtained by averaging the results from 10 peaks and valleys in the Fabry-Perot spectrum near 1550nm.

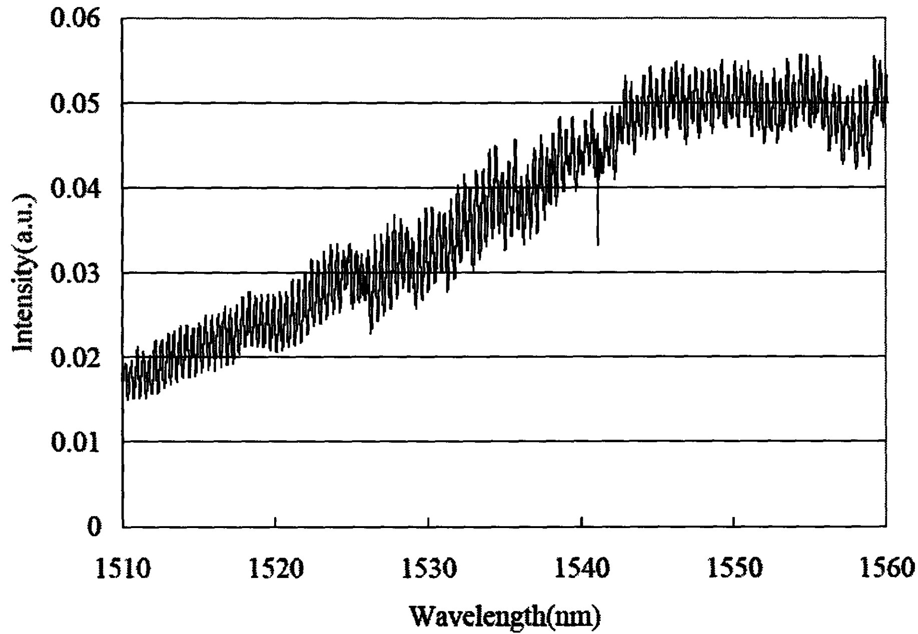

Figure 3.16: An example of raw data of Fabry-Perot resonance measurement from air trench bend. Loss was obtained by averaging the results from 10 peaks and valleys in the Fabry-Perot spectrum near 1550nm.

A. Air trench bend results

Figure 3.18 (a) and (b) show bend losses for a 90° AT bend for TM ('quasi-TE' in [36], out-of-plane) and TE ('quasi-TM' in [36], in-plane) modes, respectively. The cladding taper angle is fixed at 80° and radii of the bend section are varied from 2 to 9μm. Bend loss

is as small as 0.1dB/turn and matches to a reasonable degree the 2D FDTD simulation results for both polarizations. The geometry of air trenches is very well suited to approximation by 2D FDTD using the effective index method [36]. However, the experimental results have as much as ~0.15dB standard deviation. The values shown in Figures. 6a and 6b are the averages of 10 Fabry-Perot resonance points near 1550nm.

Another important factor for the miniaturization of bends while maintaining low loss is the cladding taper angle. Larger taper angles result in lower reflection and radiation losses, but increase device size. Finding an adequate taper angle is key to achieving compact, low-loss bends. Figure 3.18 (a)' and (b)' show bending loss per 90° AT bend for TM (quasi-TE) and TE (quasi-TM) modes, respectively, for several taper angles with the radius fixed at 9μm. Experimental results match the simulation with some deviation. From these results, it is confirmed that the taper design has a significant impact on the bend loss as predicted from theoretical simulation and that cladding tapers permitting low-loss bends can be fabricated.

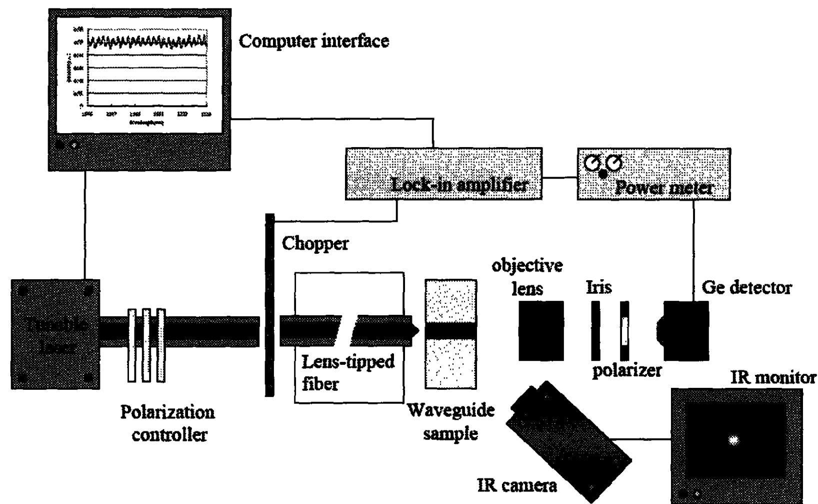

Figure 3.17: An experimental setup for waveguide loss measurement (the same as Figure 1.7).

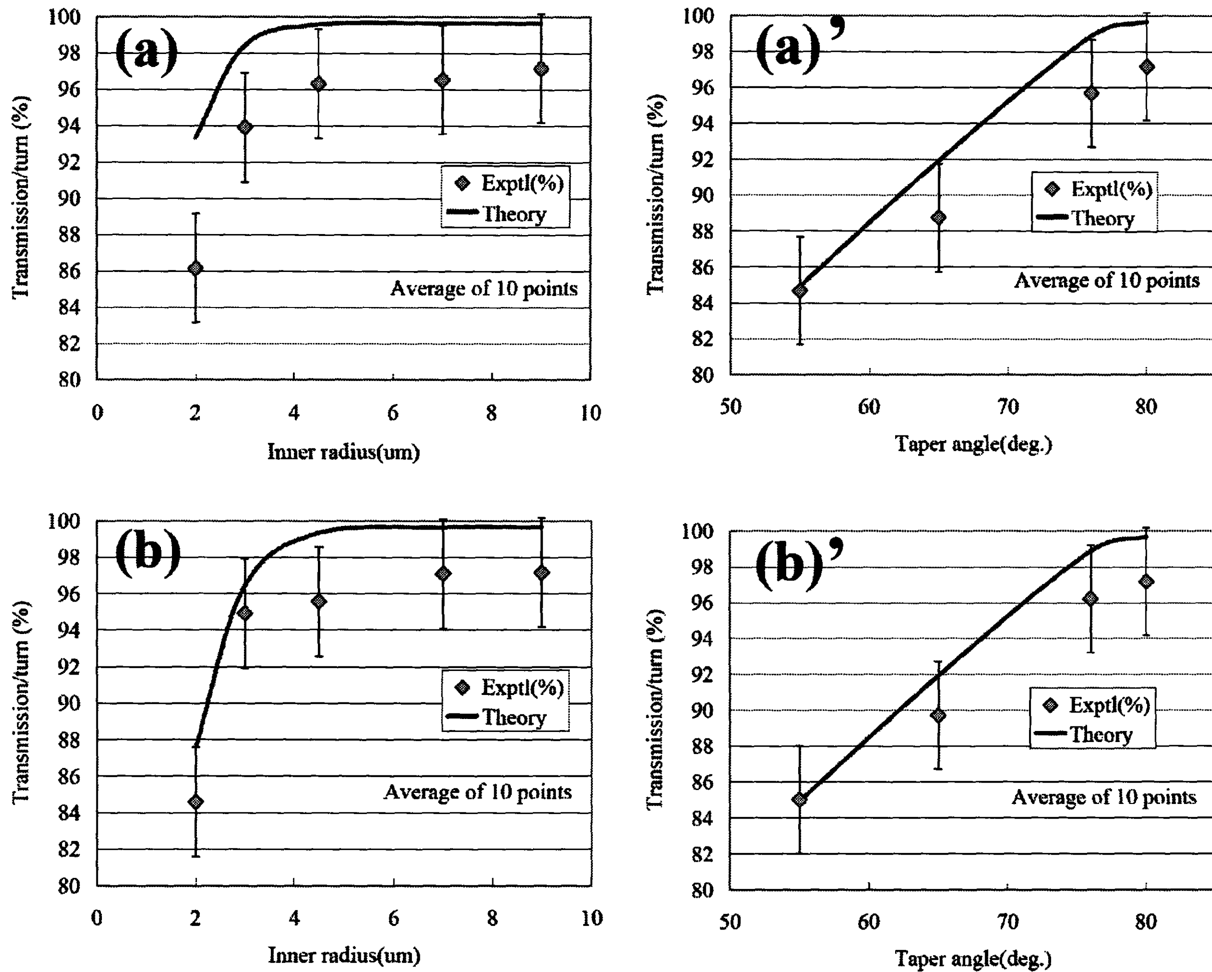

Figure 3.18: (Left column) Bending loss for ATB using TM mode (a) and TE mode (b). Radii are varied from 2 to 9mm. Taper angle is fixed at 80°. Experimental results are in good agreement with theoretical curves for transmission, as shown.

(Right column) Bending loss for ATB using TM mode (a)' and TE mode (b)'. Taper angle is varied from 55 to 80°. Experimental results are in good agreement with theoretical curves for transmission, as shown.

B. Air trench T-splitter results

In the T-splitter illustrated in figure 3.11(b) and shown in Figure 3.14(b) and (d), the radius and taper angle are fixed at 9µm and 80°, respectively. A straight throughput loss measurement was employed to find approximately less than 0.6dB loss per junction. A key factor in T-splitters is even (or by design controllable) power distribution. Even power splitting is particularly important for optical clock distribution. Table 3.3 gives the measured power distribution for TM (quasi-TE) and TE (quasi-TM) modes. The splitting

ratio for the device shown is approximately 45:55 for both TM and TE modes in the 1540-1565nm wavelength range. It was found that accurate alignment between the two structures (waveguide core and air trench structures) is an important factor for even power distribution. The splitting ratio was degraded to 30:70 when there is 0.3μm lateral misalignment between the waveguide layer and air trench layer as shown in figure 3.19. By paying attention to precise alignment, compact, low-loss and even-power-splitting T-splitters can be realized using AT bends.

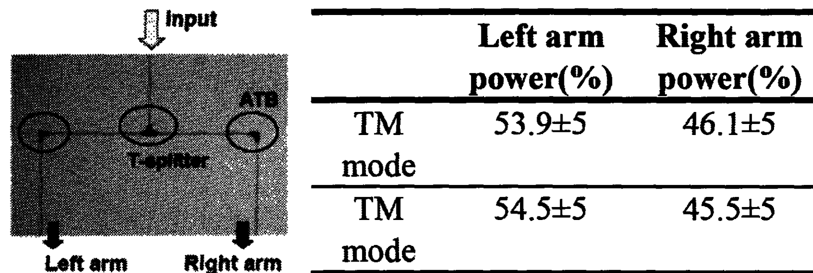

	Left arm power(%)	Right arm power(%)
TM mode	53.9±5	46.1±5
TM mode	54.5±5	45.5±5

Table 3.3: Power distribution ratios between right and left arms for TM and TE modes. The wavelength ranges from 1540-1560nm. Power splitting ratios for both TM and TE modes are around 55 : 45. The expected misalignment between waveguide and AT layers is 0.1mm.

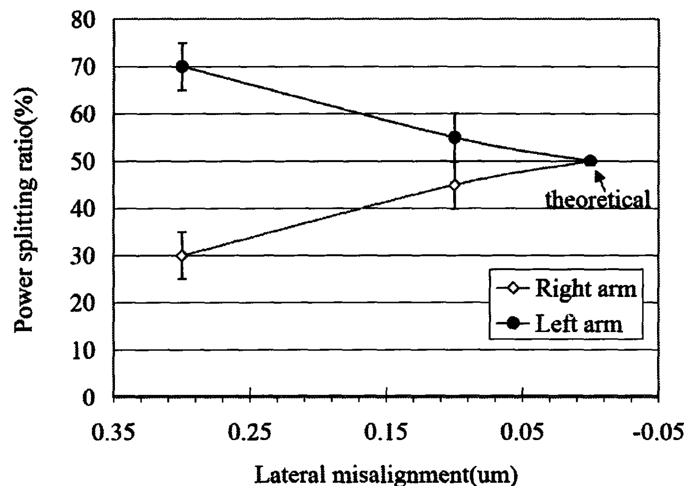

Figure 3.19: Relationship between lateral misalignment and power splitting ratio. ±0.05μm alignment accuracy is required to achieve 49:51 power splitting ratio.

3.6 Discussion and summary

We presented the realization of novel waveguide structures by which sharp bend radii and dense integration can be achieved even in low-index contrast (LIC) waveguides while keeping propagation loss and radiation (bend) loss within acceptable bounds. By introducing local high index contrast (the air trench) at the bend gradually, away from the core first, in a configuration which allows for adiabatic mode transition from low to high index contrast regions, a dramatic reduction in the bend radius of otherwise low index contrast waveguides is possible without causing large junction losses through mode mismatch and Fresnel reflection. This air trench technique can be applied to various kinds of index contrast system ranging from Δ=0.7% (current PLC technology) to Δ=20% (high refractive index SiON) depending on future demands just by placing an air trench at the bend. We have demonstrated that this is a promising technique to achieve compact waveguide system using current well-established CMOS technology. The results match theoretical simulations. The larger deviation from the theory in figure 3.18 at smaller radii and larger taper angles can be explained by scattering loss at bends and cladding tapers. At bends and tapers, the waveguide experiences local high index contrast and scattering loss becomes a more dominant loss source due to larger index difference.

The total bend length (radius and taper) was reduced by a factor of 5 to 50 in our silica examples depending index contrast. Because bend radius is one of the primary factors limiting the integration density in silica based PLCs, the use of AT bends such as the ones presented here will allow dense integration leading to reduced cost and better yield, while preserving the good fiber coupling and propagation loss properties of silica PLCs.

We furthermore demonstrated a low-loss, compact AT T-splitters with the potential of reliable, even splitting ratios. To achieve even splitting ratios, precise alignment is required between the first (waveguide) and the second (air trench) layers, although this can

be achieved using state-of-the-art lithography tools.

In addition to the low-loss property, the air trench waveguide has various applications. As a first example, this air trench waveguide works as a polarizer by optimizing the width of air trench waveguide. Figure 3.20 shows mode profiles for TE and TM polarizations when the widths of the air trench waveguide are 0.45μm and 1.0μm. For 1.0μm width (a and b), a significant difference is not observed between TE and TM polarizations. However, when the width is 0.45μm, the strong selectivity between TE and TM polarizations is observed due to the asymmetric structure (The detail is discussed in Appendix A).

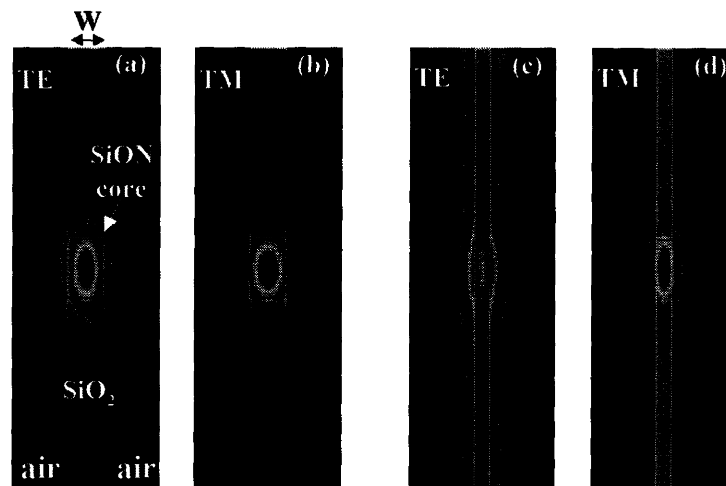

Figure 3.20: Mode profiles for air trench waveguides. (a): W=1.0μm, TE (quasi-TM) mode. (b): W=10μm, TM (quasi-TE) mode. (c): W=0.45μm, TE (quasi-TM) mode. (d): W=0.45μm TM (quasi-TE) mode. It is shown that air trench waveguide works as a polarizer by narrowing the width. Simulations were done Apollo®.

As a second application, the air trench waveguide can be used as an erbium doped waveguide amplifier (EDWA). By utilizing the low-loss property and compact bend size, it is possible to integrate 10m long waveguide on a 1cm^2 chip even when Δn=0.1. The brief outline is shown in figure 3.21. Different from HIC waveguide, where propagation loss is usually more than 1dB/cm [2], air trench waveguide can achieve low propagation loss due to its low index contrast for straight wavegude.

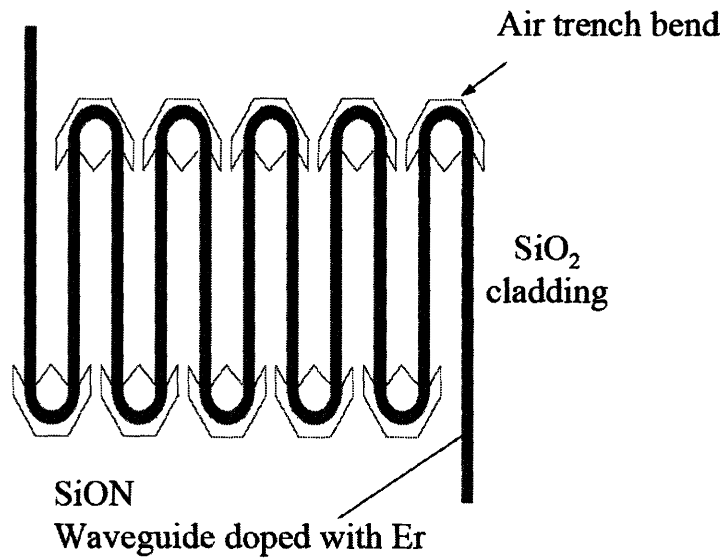

Figure 3.21: Schematic of air trench waveguide amplifier. It becomes possible to integrate long waveguide on a small chip even on LIC platform by employing air trench bends. By its low loss property and compact bend size, a compact EDWA can be expected even on a small chip.

Chapter 4: PBG waveguide

4.1 Background

Photonic crystal has been attracting considerable attention since its introduction in 1987 by John [46] and Yablonovitch [47]. Photonic crystal has an ultimate potential to mold the flow of the light since photonic bandgap forbids photons with certain frequencies to propagate and brings about a huge reduction of the group velocity. The concept of photonic crystal has been applied to optical wavgeuides by placing the defect, which is surrounded with photonic crystal structures as shown in figure 4.1 [48]. By introducing the defect, new photonic states are formed within photonic bandgap (PBG). Above or below these defect-induced modes, the photonic density of states (DOS) becomes zero. As a result, the light traveling in the photonic crystal using the defect modes cannot leak from these states to neighboring modes and the loss is ideally zero. Many attempts have been made to realize photonic crystal wavgeuide (hereafter, PBG waveguide) for the purpose of dense integration of optical waveguides, however, in actual situations the loss is usually high as much as 4-20dB/mm due to the fabrication difficulty and poor vertical confinement [63-65]. For 1.55μm communication range, the feature size becomes around $1.55/(4n) = 0.1 - 0.4\mu m$ depending on the indices of materials, where n denotes the index of the material. It is challenging to control the feature size precisely with nm order with current exposure system such as a stepper. In most cases, e-beam exposure system is used to realize PBG wavgeuide to attain the maximum resolution. However, this approach has some fundamental problems. The first problem is the difficulty of feature size control. To achieve the acceptable dimension control and to suppress unexpected scattering, the holes or poles have to be fabricated as precisely as possible using e-beam exposure system and metal etching mask, which are not suitable for mass production and not CMOS-compatible any

more. The second problem is that it is usually significantly challenging to fabricate three dimensional photonic crystal structure, therefore, dielectric guiding is often employed for vertical light confinement. Figures 4.2 and 4.3 show examples of conventional approach to realize PBG waveguide.

4.2 Prior arts

As shown in figures 4.1-3, all of these PBG waveguides are proposed by fabricating tiny poles or holes two dimensionally by employing the techniques mentioned in the previous section. However, these approaches usually suffer from the discrepancy between theoretical and experimental results for the reason of dimension control.

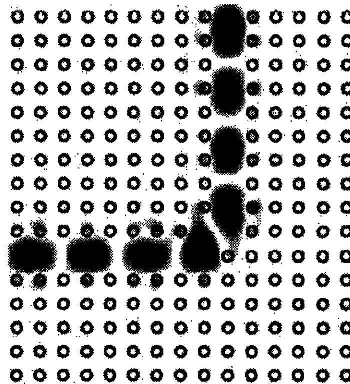

Figure 4.1: Simulation of the propagation of an optical mode traveling around a sharp bend in a 2-D photonic crystal composed of a cubic array of dielectric cylinders. [48]

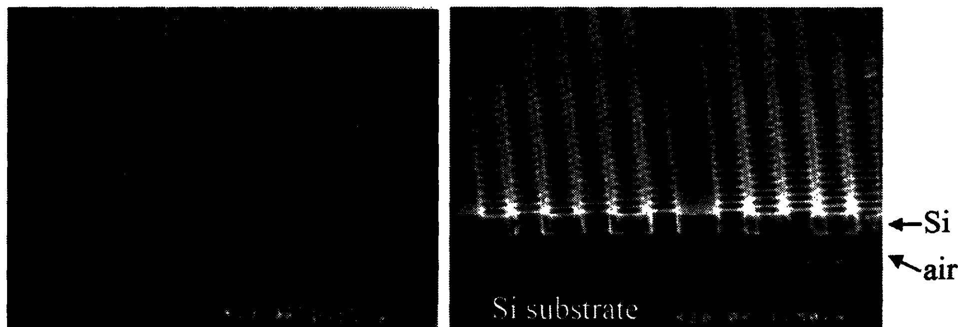

Figure 4.2: Examples of PBG wavgeuide [49]. PBG structures are fabricated laterally and dielectric confinement is used vertical confinement.

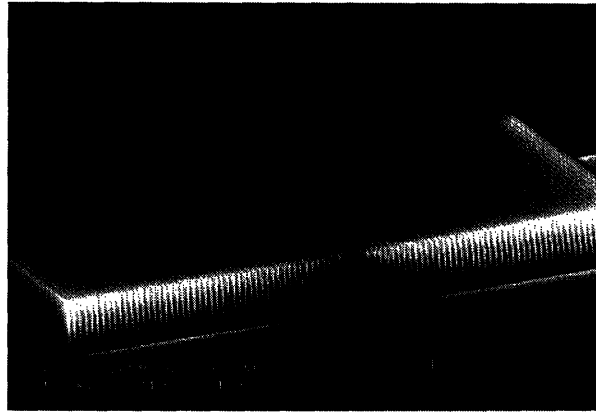

Figure 4.3: SEM image of a periodic array of silicon pillars fabricated using deep anisotropic etching. The silicon pillars are 205nm in diameter and 5μm tall [50].

On the other hand, a completely different approach has been proposed recently to realize 3-D structures by using two-photon polymerization of photoresist and advanced scanning tools [51]. However, this kind of 3-D photonic crystal usually shows poor performance due to the difficulty of dimension control or fabrication defects, therefore, their application is limited to academic researches. The reported losses are usually within 4-20dB/mm [63-65]. It is reported that the origin of such high propagation loss is scattering caused by various imperfections in fabricated waveguides [63]. More importantly, it poses a significant challenge to the integration with other CMOS materials such as SiO_2, Si, Si_3N_4 and so forth which are made above 400°C depending on the process. As a conclusion, PBG waveguides have to satisfy the requirements mentioned below for the real applications.

(a) CMOS compatible for easy fabrication.

(b) Easy dimension control for higher performance, lower cost and higher yield.

(c) Can be integrated on chip.

4.3 PBG waveguide designing approach

Our approach is totally different from conventional ones. The problem of the previous approaches is that they depend on e-beam lithography and successive dry etching to control the feature dimensions. These techniques are well matured and established, however, it is still challenging to control the required feature sizes. Our proposed structure is briefly depicted in figure 4.4. The core is surrounded with PBG layers. The core and under cladding PBG layers are both etched by dry etching technique. Different from lithographic approach, where photonic structures are fabricated by etching, a simple deposition process is employed to fabricate PBG structure. It is well known that it is easy to control the thickness of each layer since the deposition rate is as slow as 2-10nm/min. and well-controllable with conventional techniques [52]. High quality PBG layers are required to realize acceptable propagation loss. To achieve good step coverage, low pressure chemical vapor deposition (LPCVD) technique is proposed in this chapter. The principle is discussed in the next section.

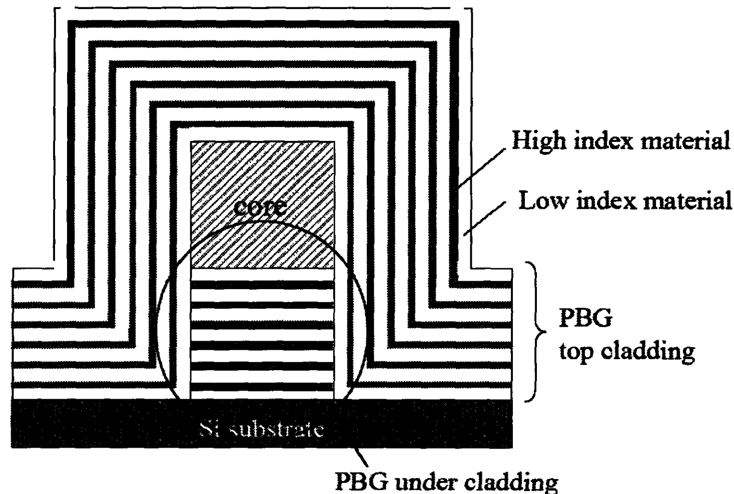

Figure 4.4: Cross section of the proposed PBG waveguide. The core is surrounded by PBG cladding layers. Uniform layers are achieved by LPCVD technique.

4.4 PBG designing and fabrication

Silicon nitride (Si_3N_4: n = 2.0) and poly-Si (n = 3.45) were chosen as high index contrast materials. Both materials are deposited using Low Pressure Chemical Vapor Deposition (LPCVD) process at 775°C and 625°C, respectively. Due to low deposition pressure as low as 200mTorr and relatively high deposition temperature, depositions are done at surface reaction limited regime not at mass-transport reaction limited regime. This indicates that deposition rate depends only on substrate temperature not on gas flow inside the reaction furnace with this temperature and pressure. By employing LPCVD process, diffusion length of reaction species can be much longer as compared to atmospheric deposition, which leads to uniform deposition rate across the wafer or among wafers. It is expected that deposition rate is uniform independent of surface morphology due to these properties. Physical explanation is given below.

Figure 4.5 is a schematic wafer surface region in CVD process showing concentrations and fluxes of reactant species. The flux of reactant species from the vapor phase to the substrate surface through the boundary layer, F_1 (in mol/cm^{2}sec) is described by:

$$F_1 = h_G(C_G - C_S) \quad \text{-(1)}$$

where h_G, C_G and C_S are the mass transfer coefficient (cm/sec), concentrations of gas species in the main gas flow and at the substrate surface, respectively. The flux of reactant consumed by the surface reaction is defined as F_2 and can be expressed as below, assuming first-order reaction kinetics.

$$F_2 = k_S C_S \quad \text{-(2)}$$

where k_S is the reaction coefficient (cm/sec) at the surface. At steady state, following equation is obtained since these two processes act in series and must be equal to each other. The overall reaction proceeds at the rate of slower process.

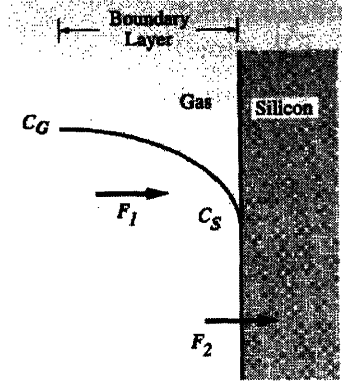

Figure 4.5: Wafer surface region in CVD process showing concentrations and fluxes of reactant species [52].

$$F = F_1 = F_2 \quad \text{-(3)}$$

Then, the following equation is obtained.

$$C_S = C_G \left(1 + \frac{k_S}{h_G}\right)^{-1} \quad \text{-(4)}$$

The growth rate is given by:

$$v = \frac{F}{N} = \frac{k_S\, h_G}{k_S + h_G} \frac{C_G}{N} \quad \text{-(5)}$$

The fraction of the incorporating species is defined as:

$$Y \equiv \frac{C_G}{C_T} \quad \text{-(6)}$$

where C_T is the concentration of all molecules in the vapor phase. Y is also equal to the partial pressure of the incorporating species, P_G, divided by the total pressure in the system.

$$Y = \frac{P_G}{P_{Total}} = \frac{P_G}{P_G + P_{G'} + \ldots} \quad \text{-(7)}$$

Now the equation for the deposition rate can be written as:

$$v = \frac{k_S h_G}{k_S + h_G} \frac{C_T}{N} Y \quad -(8)$$

At low pressure, e.g. below 1Torr, h_G is written as:

$$h_G = \frac{D_G}{\delta_S} \quad -(9)$$

and D_G is inversely proportional to P_{total}.

$$D_G \propto \frac{1}{P_{total}} \quad -(10)$$

Therefore, at low pressure, $h_G >> k_S$, then equation (8) is rewritten as:

$$v \approx k_S \frac{C_T}{N} Y \quad -(11)$$

which mostly depends on substrate temperature.

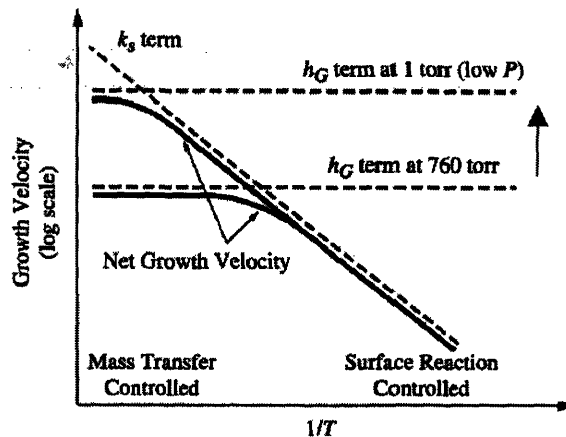

Figure 4.6: Growth velocity vs. 1/T for APCVD (760 torr) and LPCVD (1 torr) systems. The total pressure (with P_G and C_G remaining fixed) shifts the h_G curve upward, extending the surface reaction regime to higher temperature [52].

Figure 4.6 explains how LPCVD process works. As total pressure goes down, h_G curve shifts upwards and extend the surface reaction limited regime to higher temperature, which ensures uniform deposition and better film quality. 6pair-PBG whose center wavelength

was 1.55μm was fabricated using LPCVD poly-Si (n = 3.48) and LPCVD nitride (n = 2.0). The thickness were 110nm and 194nm, respectively. The deposition was done using a SVG/Thermco 7000 series. Poly-Si deposition was done at 625°C under 200 mTorr using SiH_4 150sccm as a reactant. Nitride was deposited at 775°C under 200 mTorr using SiH_2Cl_2 50 sccm and NH_3 150 sccm as reactants. The deposition rates are 98Å/min. and 27Å/min. for poly-Si and nitride, respectively. For this application, high reflectance is required to achieve low transmission loss since light travels inside core for a long distance such as mm or cm order, experiencing lots of bounces.

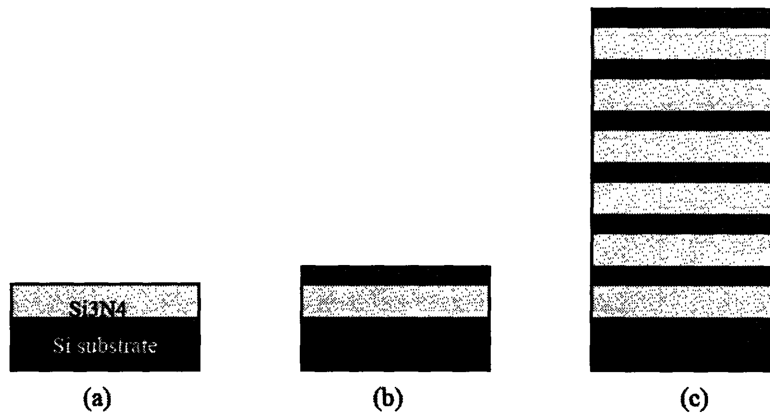

Figure 4.7: Fabrication scheme of PBG stack. (a) Deposit nitride, (b) Deposit poly-Si, (c) Repeat steps (a) and (b)

Figure 4.8 is a cross sectional SEM picture of poly-Si/nitride layers formed on V-groove made by KOH anisotropic etch. It is shown that uniform layers are made independent of surface morphology. It was concluded at this point that the LPCVD approach is suitable for our PBG waveguide.

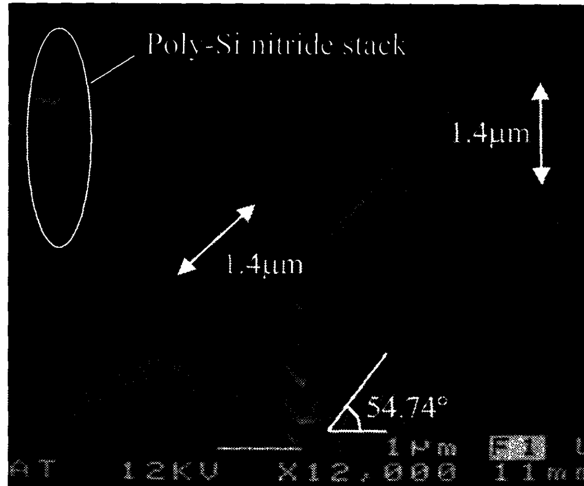

Figure 4.8: Poly-Si and nitride layers deposited on V-groove made by KOH anisotropic etch. It is shown that uniform layers are formed independent of surface morphology.

6 pair-PBG stack was also made on planar 6inch Si wafer. The target thickness for poly-Si and nitride was 110nm and 194nm, respectively. Figure 4.9 is a cross sectional TEM pictures for the PBG taken by Courtesy of Dr. Xiaoman Duan at National Semiconductor.

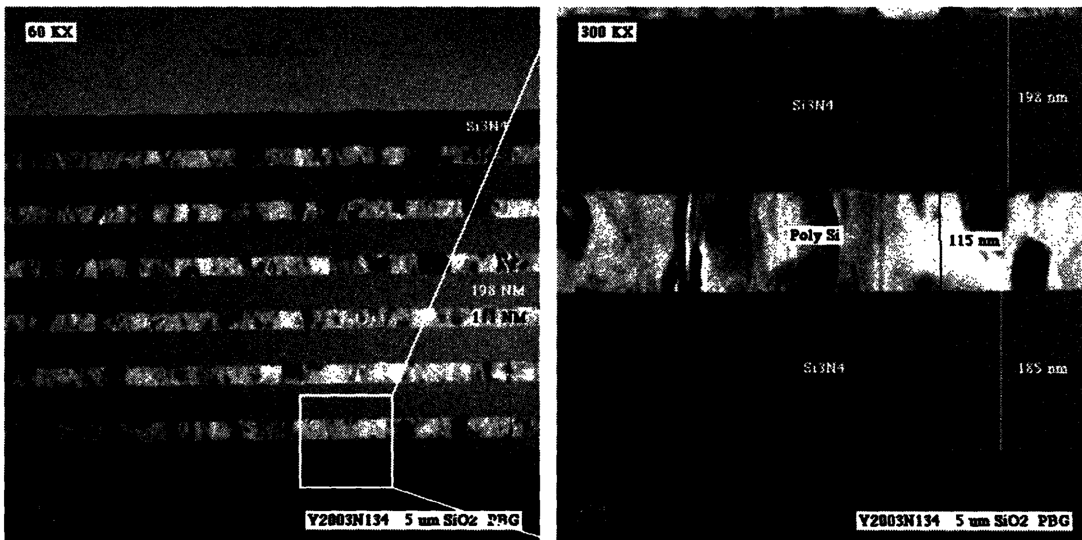

Figure 4.9: Cross sectional TEM images pf 6pair PBG. (Left: 6,000x) and (Right: 30,000x). Courtesy of Dr. Xiaoman Duan

Experimental reflectance was obtained using a Varian Cary 5E spectrometer. Figure 4.10 is theoretical and experimental reflectance. Experimental data fairly matches theoretical one. The maximum reflectance was 99.4% whereas the theoretical maximum is 99.9%.

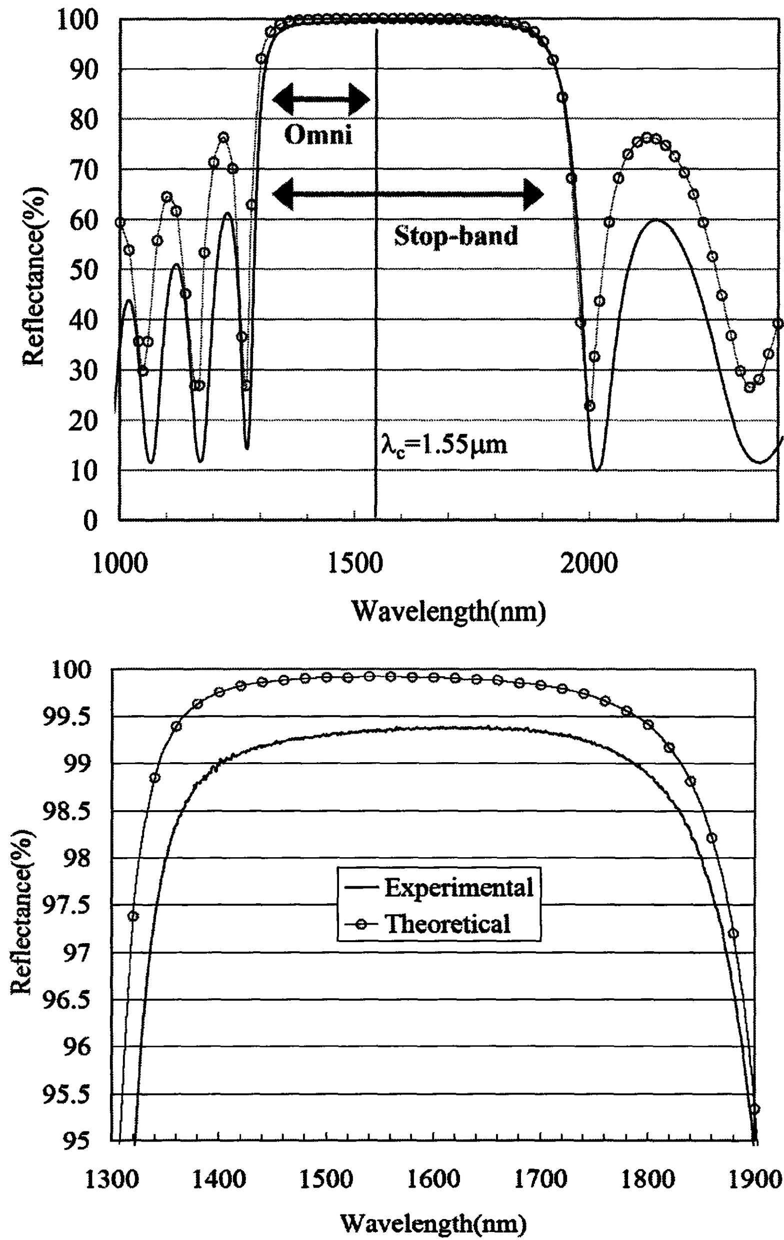

Figure 4.10: Theoretical and experimental reflectance for 6pair poly-Si/nitride PBG. (Top) Reflectance from 1.0mm to 2.4um. (Bottom) Reflectance over the stop-band. Discrepancy from the theory is approximately 0.6%.

4.5 One dimensional slab PBG asymmetric waveguide

To evaluate the quality of poly-Si/nitride PBG stack as a waveguide cladding, transmission loss was evaluated using a prism coupling technique. For PBG waveguide application, high reflectance is required since the propagating light experiences lots of bounces at PBG surface. The principle of prism coupling is as follows. The sample to be measured is brought into contact with the base of a prism by means of a pneumatically-operated coupling head, creating a small air gap between the film and the prism. A laser beam strikes the base of the prism and is normally totally reflected at the prism base onto a photodetector. At certain discrete values of the incident angle Θ, called mode angles, photons can tunnel across the air gap into the film and enter into a guided optical propagation mode, causing a sharp drop in the intensity of light reaching the detector [53].

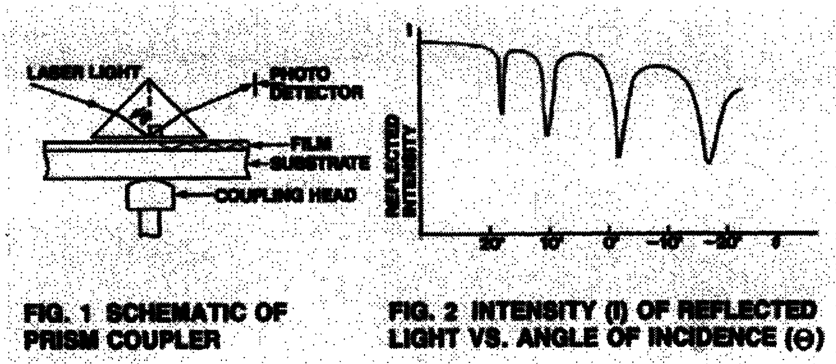

Figure 4.11: Schematic of prism coupler (left), and intensity of reflected light vs. angle of incidence (Θ) [53]

For the evaluation, the sample shown in figure 4.12 was prepared. The oxide was deposited on 6pair-PBG by LPCVD process (LTO) at 400°C under 200mTorr pressure with SiH_4 and O_2 as reaction gases. The film was densified at 950°C in N_2 ambient for 4 hours to remove excess oxygen out of the film.

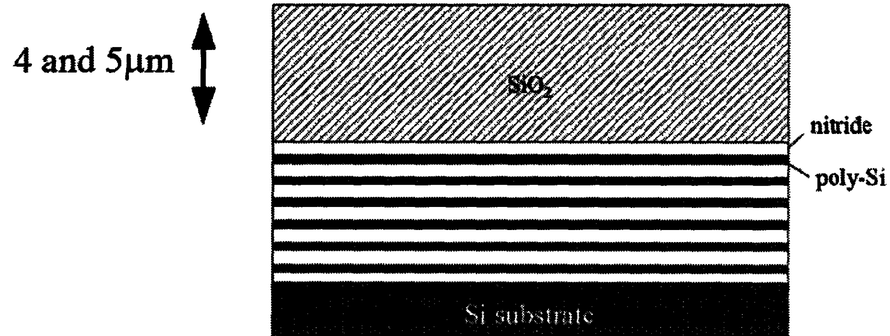

Figure 4.12: Schematic of one dimensional asymmetric slab waveguide. The thickness of oxide core is 4 and 5um. This is used for prism coupling measurement.

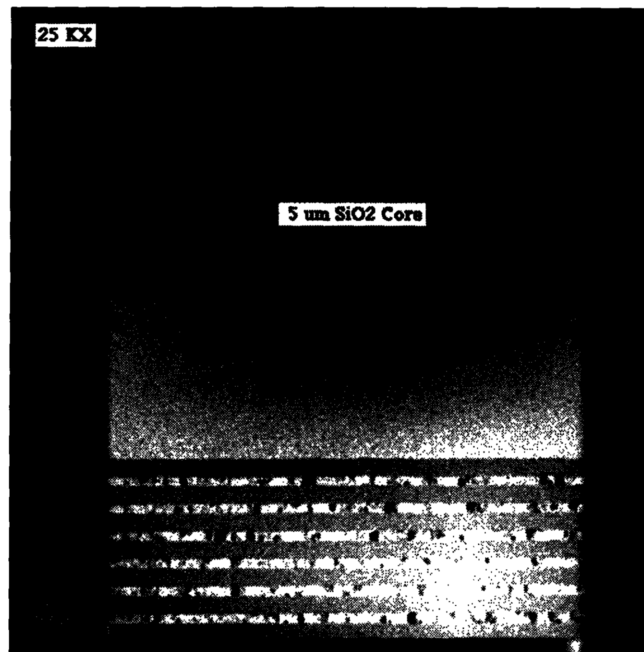

Figure 4.13: Cross sectional TEM image for 1D asymmetric PBG slab waveguide. The thickness of core layer is 5μm here. Courtesy of Dr. Xiaoman Duan.

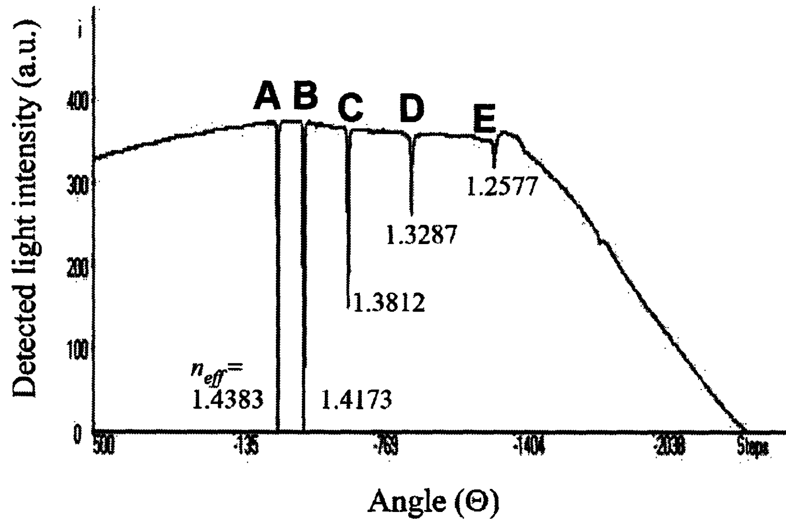

Figure 4.14: An example of raw data of the mode coupling between the prism and the PC cladding waveguide for 4mm oxide core. Five dips represent the five propagation modes; effective mode indices are measured as 1.4383, 1.4173, 1.3812, 1.3287 and 1.2577. Courtesy of Y. Yi.

Wavelength(nm)	1550nm		1307nm	
Thickness of oxide core (μm)	4	5	4	5
n_{eff}: TE polarization	1.4435	1.4078	1.4325	1.4383
n_{eff}: TM polarization	1.4408	1.4346	1.4425	1.4425

Table 4.1: Effective mode indices (n_{eff}) of 1-D asymmetric slab waveguide. Effective mode indices are lower than indices of silicon (n=3.5) or nitride (2.0).

As shown in table 4.1, mode propagation constant or effective indices (n_{eff}) of fundamental modes are lower than the indices of silicon or nitride, where refractive indices are 3.5 and 2.0, respectively. Despite the fact that index of core layer is lower than both PBG materials (nitride and Si in this case), the light is well coupled into the oxide layer and guided. This is a strong demonstration of PBG principle and indicates that the core can be chosen from various materials regardless of refractive index.

As a next step, the propagation loss of these 1-D PBG asymmetric waveguide was evaluated. The light incident angle was fixed at the guided-condition angle (angle A in Figure 4.14) and scattered light was scanned along the slab waveguide. From the slope of the corrected scattered light, the propagation constants for fundamental modes were obtained.

Wavelength(nm)	1550nm	1307nm
TE polarization	0.42dB/cm	0.24dB/cm
TM polarization	0.47dB/cm	0.69dB/cm

Table 4.2: Propagation losses of fundamental modes for 1-D PBG asymmetric slab waveguides. These low-losses indicate that the light propagates in low index material (oxide).

This results indicates that omni directional PBG bandgap leads to low propagation loss for both TE and TM modes and this is the experimental evidence of light propagation in low index material.

4.6 Two dimensional PBG channel waveguide

In this section, two dimensional PBG waveguide is discussed. From appendix B, the time-independent Maxwell's equation (master equation) is expressed as:

$$\nabla\times\left(\frac{1}{\varepsilon(\mathrm{r})}\nabla\times H(\mathrm{r})\right)=\left(\frac{\omega}{\mathrm{c}}\right)^{2}H(\mathrm{r}) \quad \text{-(12)}$$

which can be rewritten as [54]:

$$-\nabla_{\mathrm{T}}\,\mathbf{E}=\left[\left(\frac{n\omega}{c}\right)^{2}-k_z^2\right]\mathbf{E} \quad \text{-(13)}$$

where n and z are the refractive index of the core and the direction of uniform translational symmetry, respectively. If the core of the waveguide is surrounded by perfectly conducting material, such as metal with infinite k (absorption), it is possible to divide the problem into TE ($E_z = 0$) and TM ($H_z = 0$) polarizations. For a rectangular cavity of dimensions lx by ly

and refractive index n, solutions will take the form as:

$$\omega = \frac{1}{n}\sqrt{k_z^2 + \omega_{pq}^2} \quad \text{-(13)}$$

where $$\omega_{pq}^2 = \left(\frac{p}{2l_x/a}\right)^2 + \left(\frac{q}{2l_y/a}\right)^2 \quad \text{-(14)}$$

TEM modes ($p = q = 0$) are not allowed due to the fact that the metal cavity has an equipotential surface unable to support a non-trivial TEM mode. TE modes will have at least one non-zero quantum number, whereas TM modes are required to have both be non-zero. These findings are summarized in figure 4.15.

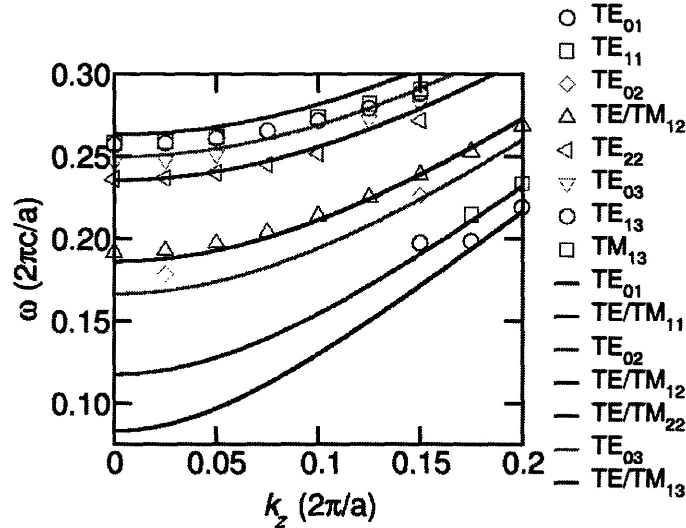

Figure 4.15: Dispersion relations of metallic channel waveguide (lines) and PBG cladding channel waveguide (dots). They have very similar dispersion relations. Courtesy of Y.Yi [54].

The difference between PBG cladding and perfectly conducting metal is that there exist a small amount of loss for PBG cladding, which comes from a finite number of layers, and also a phase-shift that changes frequency within the gap. The first problem can be ignored by placing sufficient number of layers. The phase shift is less than p for the lower half of the gap, and more than p in the upper half of the gap. Qualitatively, it is possible to predict that modes predicted by the theory for the metallic waveguide will be pushed toward the

center of the gap. The results obtained numerically (figure 4.15) show modes that behave in a quite similar manner to those predicted for the metallic waveguide, as well as dispersion relations, which are close to the metallic predictions but still differ from them in the qualitative way mentioned above. The mode structure and electric field confinement are visually shown in figure 4.16, which shows the most of the electric field are confined in the low index core materials.

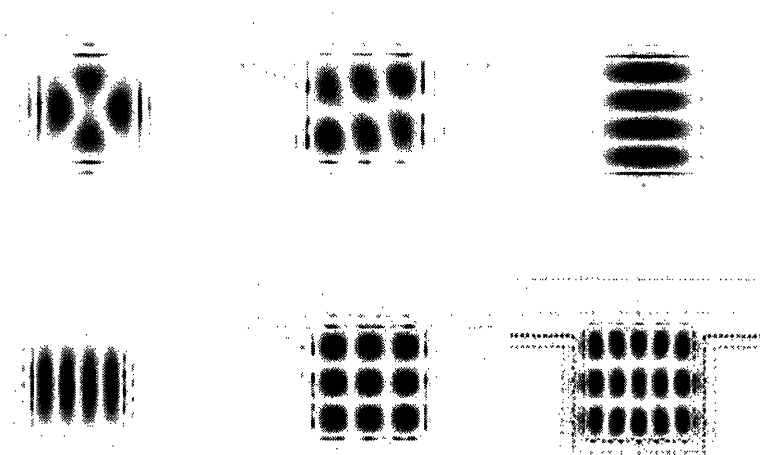

Figure 4.16: The mode structures for PBG cladding channel waveguide for some higher modes. The strong confinement of the field in the low index core is seen. Courtesy of Y.Yi [54]

As a next step, two dimensional waveguide was actually fabricated. Design parameters are shown in figure 4.17. The waveguide (core) widths are 16 and 20μm and the heights are 4, 5 and 6μm.

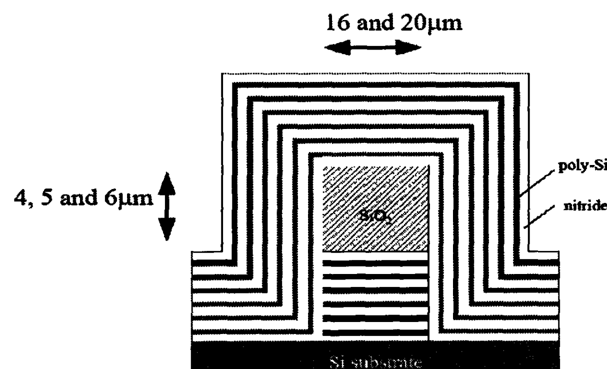

Figure 4.17: Cross section of 2-D PBG waveguide. The width and height varies as shown (not to scale).

Fabrication scheme is shown in figure 4.18. After depositing 4-6μm LTO and densification anneal at 950°C in N_2 ambient (figure 4.18a), Shipley SPR 700 photoresist was coated repeatedly until 3.5μm thick photoresist was obtained. After patterning the photoresist using a Nikon i-line (365nm) stepper NSR-2205i9, the photoresist was developed. After the lithography process, UV light was irradiated to the photoresist using Fusion M150PC Photostabilizer to avoid photoresist deformation during the successive post bake. Post bake was done at 130°C for 3min and at 200°C for 3min on a hot plate. The waveguide pattern was transferred by a dry etching process (figure 4.18b). The etching was done with an Applied Materials AME5300 using C_2F_6 17.9 sccm and CH_3F 12.1 sccm and source RF and wafer biases of 1800W and 470W, respectively. 6pair PBG top cladding layers were deposited by the same procedure as in section 4.4 (figure 4.18c). Due to LPCVD process employed here, good step coverage can be expected.

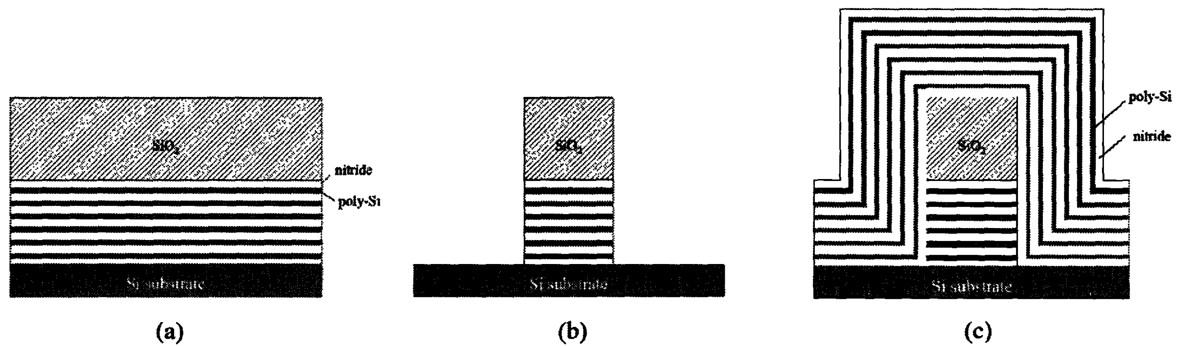

Figure 4.18: Waveguide fabrication scheme. All steps are done by conventional CMOS process. (a) Deposit oxide (LTO) and densify it. (b) Patterning. (c) Deposit top cladding layers using LPCVD process.(not to scale).

Figure 4.19 shows SEM and TEM images of PBG waveguide. As shown, the waveguide has uniform PBG layers due to good step coverage of LPCVD process. TEM pictures show that the thickness control was done successfully.

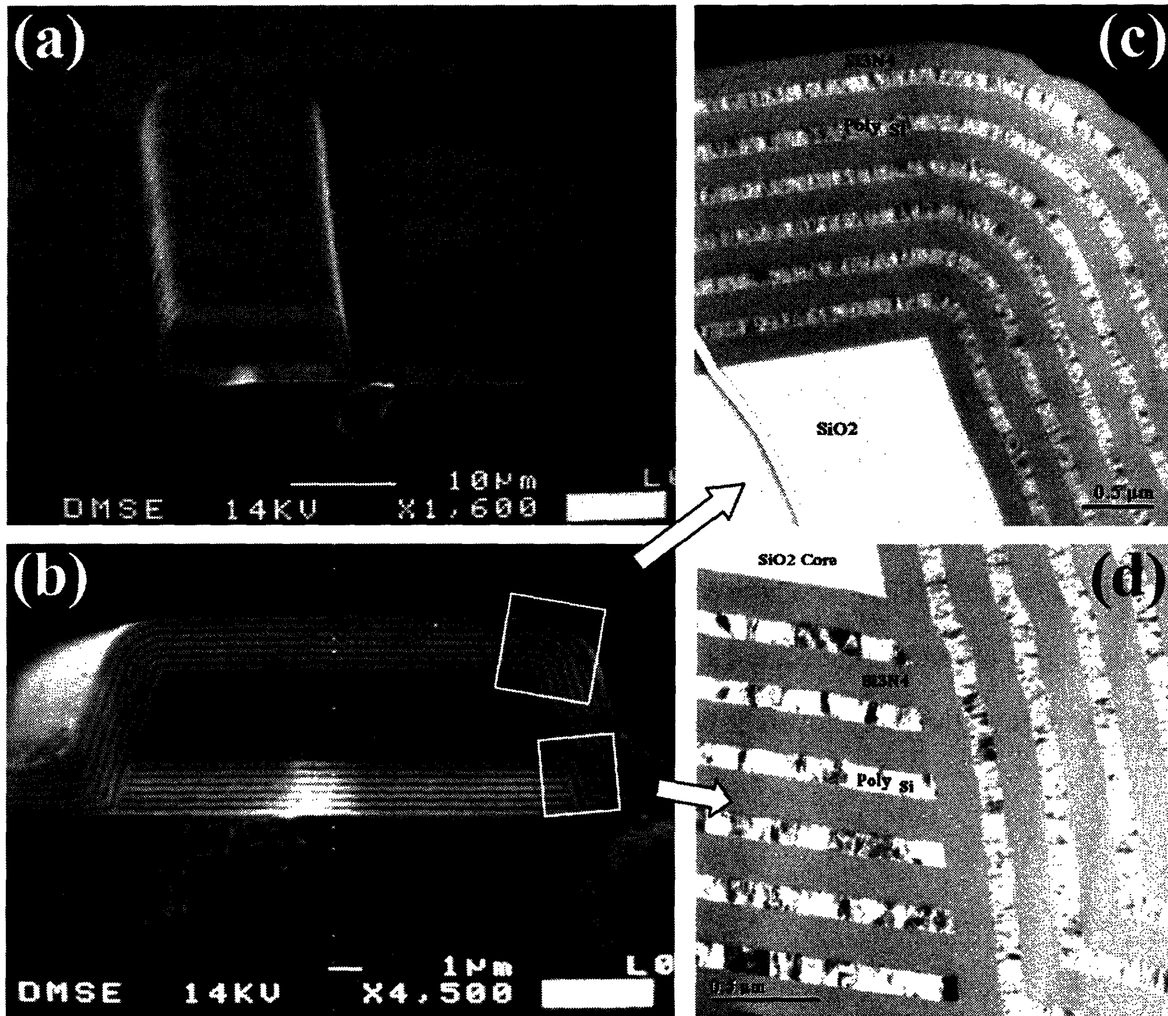

Figure 4.19: SEM and TEM images of PBG waveguide. (Left) SEM images of PBG waveguide with 12um width and 4um thickness(a: 1,600x) (b: 4,500x) (Right) TEM images (c: 5,000x) (d: 8,000x). TEM images: Courtesy of Dr. Xiaoman Duan.

For figures 4.19 and 4.20, SEM samples were dipped into buffered HF (7:1) solution for 1min. and then 10% KOH 30°C solution for 90sec. to emphasize the surface morphology. Figure 4.20 is top views of PBG waveguides. Top cladding was polished off to expose oxide core, where the width of the core is 4μm. It is visually shown that the core is uniformly surrounded by PBG cladding.

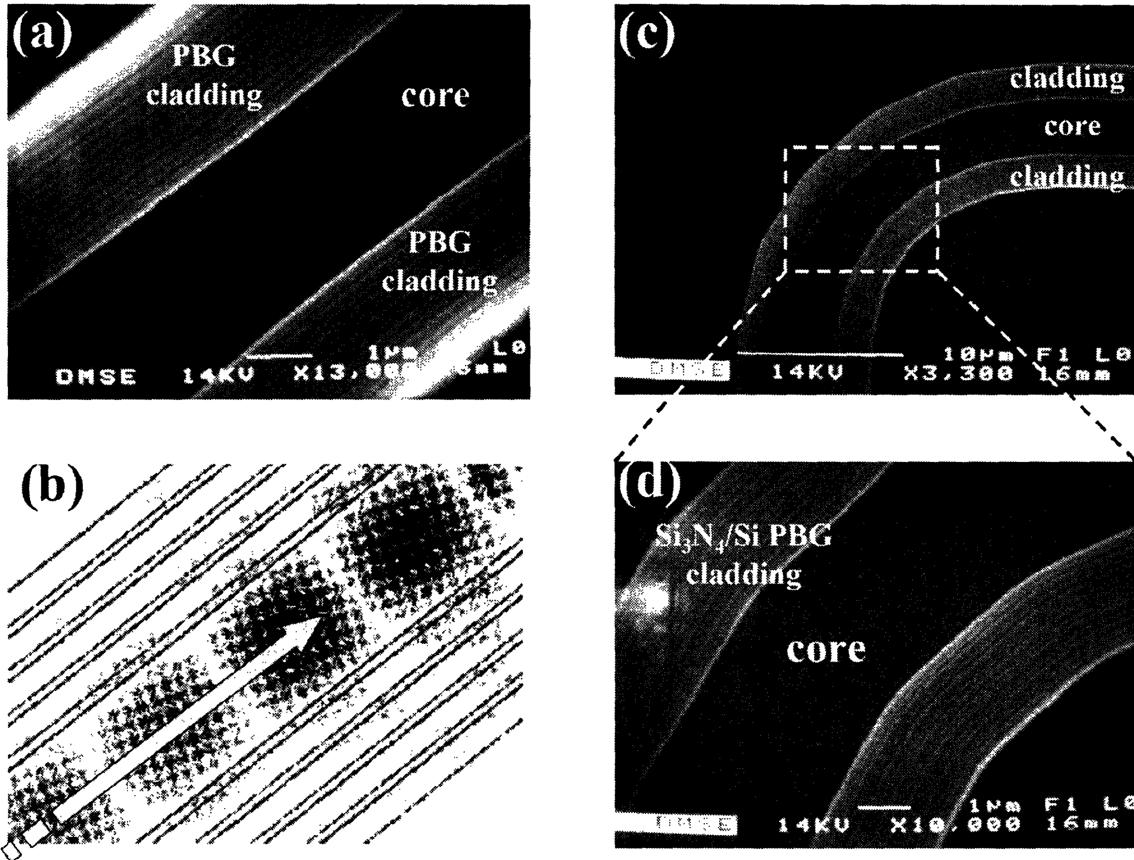

Figure 4.20: (a, b and d) SEM images for PBG waveguides after polishing off the top cladding. (b) Visualized FDTD simulation corresponding to (a). FDTD simulation: Courtesy of Y.Yi.

4.7 Waveguide loss measurement

For waveguide loss measurement, conventional cutback method was employed since these PBG waveguides are multi-moded and Fabry-Perot resonance method is not available in this case. Due to waveguides' larger core size, it can be expected that the alignment between waveguide and fiber is relatively easy. Propagation loss of waveguide is defined as:

$$\alpha_T = \frac{10}{d} \log_{10}\left(\frac{P_{in}}{P_{out}}\right) \quad \text{-(12)}$$

where is the ratio of the input and output powers as the light travels over a distance (d), or the ratio of the short and long waveguides' output powers. Its unit is dB. Or it is directly proportional to the waveguide attenuation coefficient:

$$\alpha = \frac{1}{d} ln\left(\frac{P_{in}}{P_{out}}\right) \quad -(13)$$

α and α_T are related to each other by the following simple equation.

$$\alpha_T = 4.3\alpha \quad -(14)$$

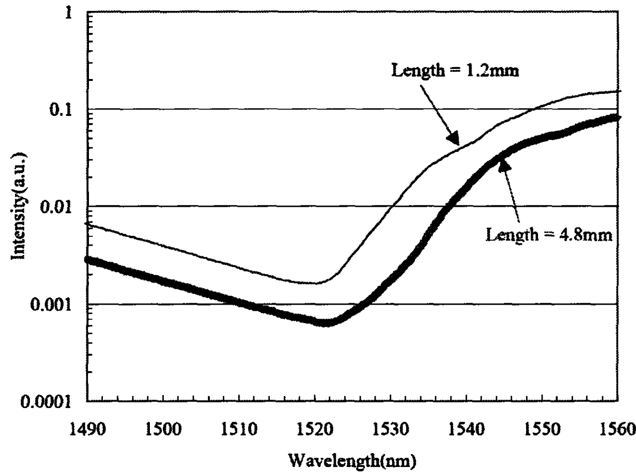

Figure 4.21: An example of raw data for output intensities of PBG waveguides. The propagation loss is obtained using Cut-back approach. Eqns. (12-14).

We have found experimentally that the coupling of laser light into the PBG waveguide is much easier as compared to other high index contrast waveguide due to its large core size. Table 4.3 is the result of loss measurement. TE polarizations were used for analysis.

Waveguide height (μm)	4	5	6
16μm wide	9.89±2.5dB/cm	8.26±3.3dB/cm	3.78±0.6dB/cm
20μm wide	9.51±2.0dB/cm	7.88±3.5dB/cm	3.68±1.5dB/cm

Table 4.3: Propagation loss for 2-D PBG waveguides. Loss was obtained by cut-back method.

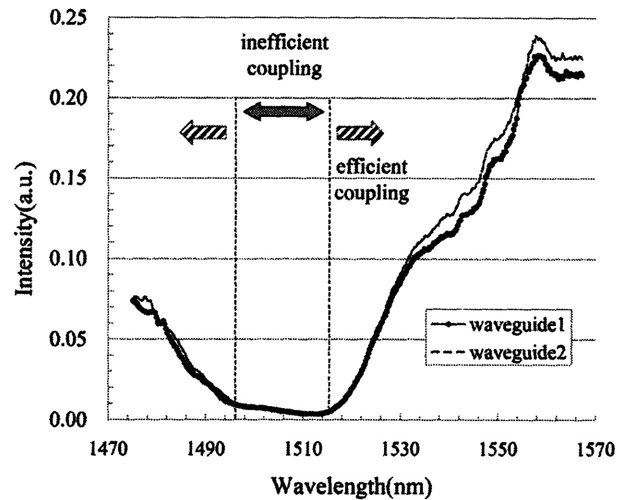

Figure 4.22: Output intensities from two identical PBG waveguides (W=16μm and H=5μm) on different chips. It is shown that the transmittance strongly depends on wavelength.

Figure 4.22 shows raw data of output intensities from two identical PBG waveguides, with width = 16μm and height = 5μm on different chips, where laser intensity is kept constant at 5mW. Two outputs show the close value to each other. This is attributable to easy and reproducible alignment due to large core size. It is shown that output intensity strongly depends on wavelength. The light from the fiber needs to couple into defect modes of photonic bandgap to propagate otherwise it is simply reflected back from the waveguide. Since the incident angle is fixed in this measurement, wavelength plays an important role in coupling of light. This is peculiar phenomena to PBG waveguide and strong evidence of PBG guiding. In the case of dielectric waveguide, output intensity is relatively constant if single mode condition is kept.

It was also found that the experimental losses are higher than those obtained from theory. This can be attributed to fabrication defects such as sidewall roughness, slanted sidewall and unexpected cracks in waveguides. Figure 4.21 is an example of fabrication defects. It was found that there exists rough and slanted sidewall, which are expected to be caused by photoresist corrosion and unexpected side-etching during dry etching process.

We etched 4-6μm thick oxide and 2μm thick under-clad PBG layers. Therefore, the process development, such as the usage of hard etching mask, is necessary to improve the performance of two dimensional PBG waveguide. In this chapter, nitride is used as a low index material for PBG layers, however, SiO_2 is also a good candidate if the fabrication situation allows. For example, LTO is deposited between surface reaction limited regime and mass transfer controlled regime. Therefore, good step coverage cannot be expected. LPCVD Tetraethyl orthosilicate (TEOS) is expected to have good step coverage due to its high deposition temperature (500-800°C) and low sticking coefficient [55].

.

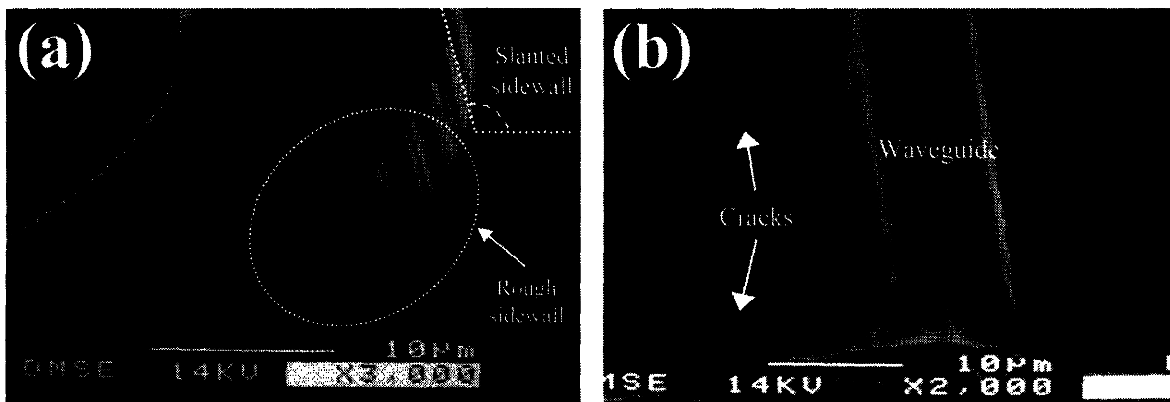

Figure 4.23: SEM images of fabrication defects which are considered to be loss source. (a): Rough sidewall and slanted wadewall observed from the outside of PBG cladding. (b): Cracks crossing the waveguide. The cracks were generated mainly during dicing process.

Figures 4.23 shows the comparisons of theoretical losses and experimental ones. Approximate theoretical losses are obtained based on the combination of 2D-FDTD, asymptotic matrix theory [56] and experimental reflectance results. It is shown in these figures that the experimental loss is higher than theoretical on by factor of 3-6. It is expected attributable to fabrication defects mentioned above.

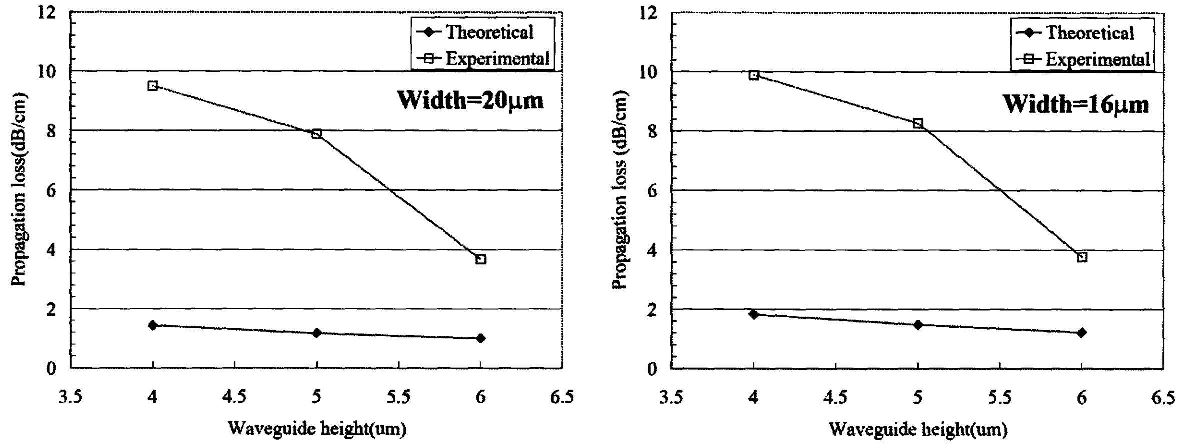

Figure 4.24: Comparisons of theoretical and experimental data. (Left) Width is fixed at 20mm. It is shown that loss is lower for higher waveguide. (Right) Width is fixed at 16mm. It is also shown that loss is lower for higher waveguide.

4.8 Bend loss

Bend losses were obtained by subtracting bending waveguide output power from straight waveguide output power. Figure 4.25 shows the experimental bend losses for PBG wavgeuides. As well as experimental propagation losses, it was found that bend losses are also higher than theory. Theoretical bend loss was calculated and plotted in figure 4.24 by comparing the total integrating Poynting flux density going into the bend, which is compared to the total output, for a Gaissian pulse centered around $\omega = 0.203(2\pi c/a)$ and $k_z = 0.191(2\pi/a)$, with a core of $10a$, by $10a$, which is meant to correspond to the parameters for TM11 mode [54], where a denotes the period of PBG (0.3μm in this case). The calculation was done for inner radii of $8a$, $15a$ and $22a$. The results were a transmission of 91.6% for the smallest inner radius, corresponding to a value of 2.4μm for $a = 0.3$μm, and 92.9% for the largest inner radius, corresponding to a value of 6.6μm. It is found that the transmission as a function of frequency is relatively flat around the central pulse frequency. It should be mentioned that this analysis ignores factors, which are important for a bend in

a dielectric waveguide, such as mode mixing and losses due to a finite number of layers [54]. Figure 4.24 shows the bend loss for PBG waveguide with 2.4 x 2.4μm cross section.

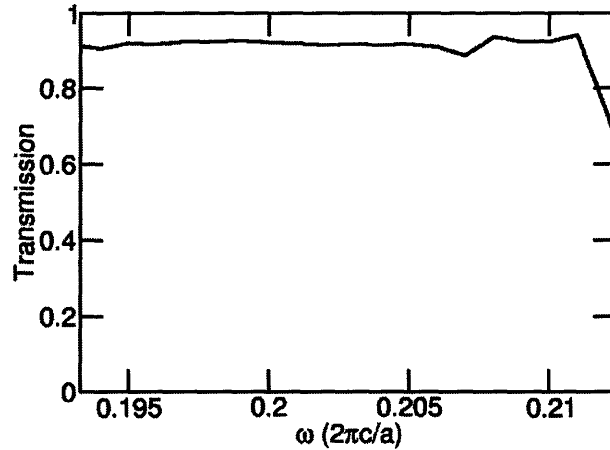

Figure 4.25: Transmission spectrum around a 90° dend for PBG waveguide. Radius = 2.4μm. Courtesy of Y. Yi [54].

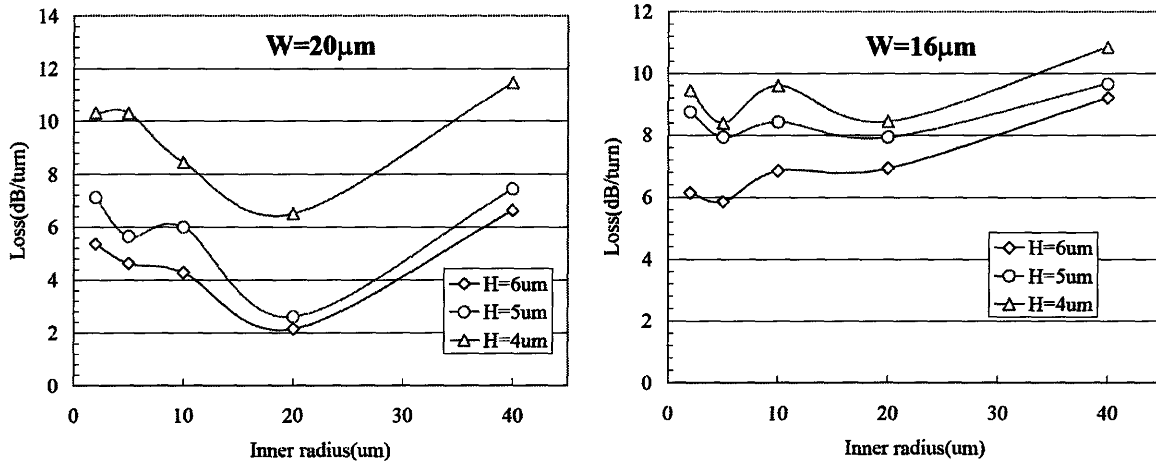

Figure 4.26: Experimental bend losses for PBG waveguides. (Left) Bend losses/90° for waveguides with W=20μm. (Right) Bend losses/90° for waveguides with W=16μm. Losses don't simply depend on radii.

On the other hand, experimental bend losses are much higher than theory by a factor of 10 or more. This is also attributable to fabrication defects. However, figure 4.25 shows that the loss is not a simple function of bending radius and relatively flat and there exist optimized radii in terms of bending loss (R=20μm for W=20μm, and R=5μm for W=16μm). It is

considered that this minimum-bend-loss radius corresponds to the minimum of the sum of theoretical bend loss and large propagation loss caused by fabrication defects. For precise analysis, more sophisticated device would be necessary.

4.9 Summary

We have demonstrated the first PBG waveguide, which can be integrated on chip using conventional CMOS compatible techniques. The loss results are not close to theoretical ones, however, we believe that the loss can be reduced by improving fabrication processes. In addition to integrate optics, this PBG waveguide has various unique applications such as high power transmission, bio sensor/bioMEMS applications [57]. And we can also expect an easy coupling between optical fiber, such as plastic optical fiber (POF), and waveguide due to its large core size. This is considerably important for FTTH applications. In this chapter, we employed oxide core. However, by replacing oxide core with hollow core by employing wafer bonding technique, this PBG waveguide can have various applications such as bio/medical applications [58-62]. As an example, by confining specimen fluid or gas in defect layer with PBG claddings, it becomes possible to enhance both absorption and fluorescence of bio-molecules otherwise the fluorescence from the specimen is too week by traditional or conventional measurement systems.

Chapter 5: HIC PBG for Visible Light

5.1 Introduction

Photonic bandgap (PBG) crystal for visible light which ranges roughly from 400nm to 700nm is an attractive photonic crystal due to its various applications such as back-reflector of liquid crystal display (LCD), lamp mirror of LC projector and so forth. Since this visible light wavelength is significantly important since it is related to computer-to-human interface. All the information are transmitted from a computer to human via visible light, in other words, eyes, therefore, PBG for visible light has a huge impact on various mirror applications. So far two major technologies are common in fabrication of visible light mirror. One is a metal mirror, which utilizes mainly aluminum or silver. However, aluminum has poor reflectance as much as 90% and the surface is easily oxidized which degrades the reflectance even worse though its oxide (Al_2O_3) functions as a protection layer. Silver has better reflectance as much as 95% but the surface is also easily oxidized and its oxide (Ag_2O) significantly degrades the reflectance and the lifetime of the mirror. Another candidate for visible light mirror is Distributed Bragg Reflector (DBR). MgF_2 (n=1.38) and SiO_2 (n=1.46) are often used as alternating materials where index difference is approximately Δn=0.08. Due to its small index difference, it is necessary to cascade DBR structures as many as 30-40 layers to cover all the visible light. This mirror has been quite successful so far due to its high reflectivity, its long lifetime and thermal stability. These mirrors are usually fabricated using sputtering method or other physical vapor deposition (PVD) techniques, therefore, the cost per sample is relatively high as compared to mature CMOS compatible processes. It is said that the future lamp mirror for LCD will be elliptical rather than spherical, therefore it will be more challenging to deposit

uniform film over the curved surface since the deposition of PVD system is proportional to the square of the inverse of the distance between target and substrate [66]. In this chapter, I pursue to establish the low-cost and high-performance visible light HIC PBG mirror using well matured CMOS-compatible techniques.

5.2 Background

Photonic crystal has been attracting considerable attention due to its ultimate controllability of molding the light. In this chapter, I focus on the PBG for visible light ranging from 400-700nm. As mentioned in the introduction, PBG in this wavelength regime can work as an interface between a computer and a human. For example, back-reflector of LCD or lamp mirror for LC projector is a good example as an application of PBG mirror. To utilize well-matured CMOS-compatible process to construct PBG for visible light (hereafter, VisPBG), CMOS-compatible dielectric materials are good candidates to construct PBG layers. In this chapter, I employ silicon, poly-Si, SiO_2 and Si_3N_4 as CMOS compatible dielectric materials.

So far metals such as Aluminum or Silver are widely used as a mirror for visible light. However, their application is limited due to poor reflectance (90% in Al, 95% for Ag), unstable surface and short lifetime. DBR cascade mirrors can provide better reflectance and longer lifetime due to its thermal stability. For DBR cascade mirrors, MgF_2 (n=1.38) and SiO_2 (n=1.46) are often used due to its low absorption in visible light and are widely used for LC projector mirror and other applications such as dental mirrors and other medical use. The problem of this DBR cascade mirror is that the production cost is high since it is made by PVD method which is usually done at ultra high vacuum (UHV) condition and the number of loaded sample has to be limited since its deposition rate is proportional to the

square of the inverse of the distance between target and substrate [66]. The deposition rate is expressed as follows. Even worse, the deposition rate strongly depends on the distance between the target and source and incident angle.

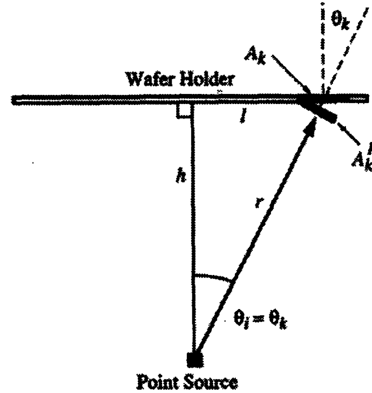

Figure 5.1: Geometries of flux and deposition of small areas on a flat wafer holder for a point source [66].

$$\nu = \frac{R_{evap}}{\Omega \, \mathrm{N} r^2} \cos\theta_k$$

where R_{evap}= the evaporation rate from the point source

r = the distance from the source to the spot on the surface

N = the density of the material being deposited

θ_k = the angle between the surface normal and the direction of the source to a spot on the surface.

Therefore, it can be concluded that it is difficult to maintain the uniform film across the substrate or among substrates. This is especially the case when the sample size is relatively large. And it is said that the shape of the LC projector's lamp mirror will become elliptical rather than current spherical shape. As a conclusion, it is necessary to develop a new technique to satisfy the future demand for visible light mirror. In this chapter, dielectric materials such as Si, SiO_2 and Si_3N_4 are proposed for VisPBG since these materials are

matured CMOS-compatible ones and various deposition techniques such as CVD, LPCVD, PECVD and PVD, are available. The goal of this chapter is to construct HIC one-dimensional PBG, which consists of several numbers of pairs with excellent uniformity and reflectivity across the surface.

5.3 VisPBG designing

To expand the stop-band over the visible light wavelength (400-700nm), it is desirable to construct PBG with high index contrast. Below are three PBG examples with Δn=0.1, 0.5 and 2.0, where center wavelength is 530nm and absorption is not included. As shown in figure 5.2, stop band becomes wider and reflection gets higher with higher index contrast.

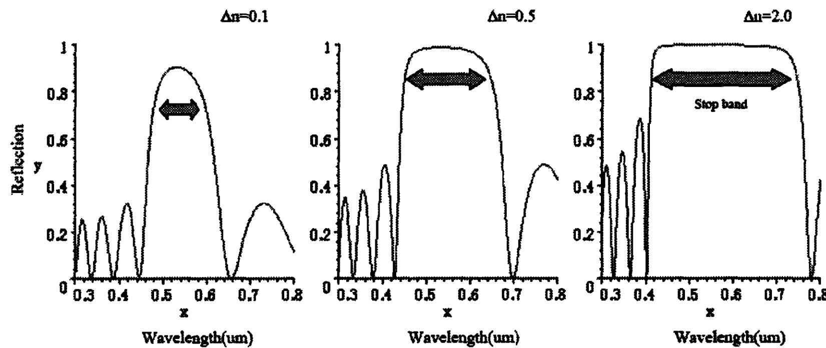

Figure 5.2: Reflection plots for Dn=0.5, 1.0 and 2.0. Stop band becomes wider and reflection also gets higher with Δn.

Therefore, it seems to be the natural choice to use silicon(n=3.5) and SiO_2(n=1.46), where index difference is as much as 2.0. However, Silicon has large absorption coefficient at visible light wavelength as shown in figure 5.3 [67] since silicon's badgap is 1.1eV which corresponds to 1.1μm, so it is necessary to suppress this absorption to achieve high reflectance.

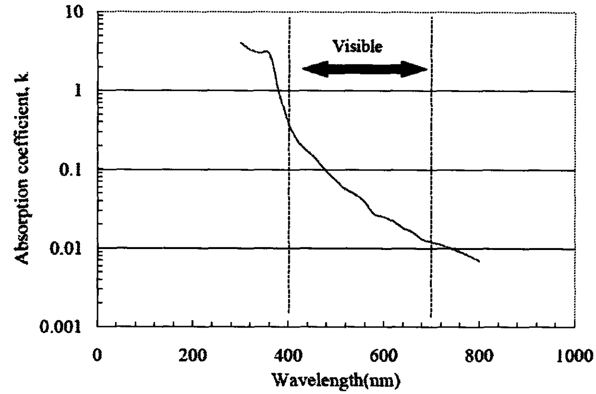

Figure 5.3: Optical absorption of crystalline silicon [67]

Figure 5.4 is an example of the theoretical reflectance where crystalline silicon's absorption coefficient is used [67]. To get theoretical reflectance, matrix propagation approach is employed, which is described in appendix B.

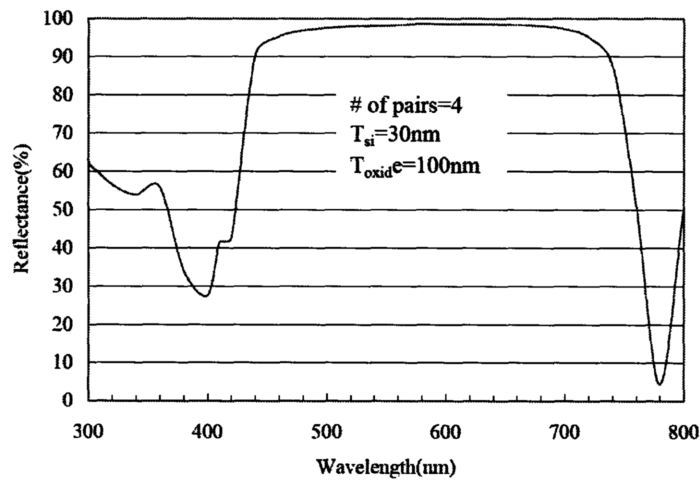

Figure 5.4: Reflectance of 4 pair-PBG based on crystalline silicon's absorption. The maximum reflectance is 98.5%

The origin of photonic badgap can be explained by the analogy with bandgap in semiconductor. In semiconductor, when the probability density has the same period as atomic distance "a", then the standing wave can have only conditions.

$$|\Psi_a^2| = 4\sin^2\frac{\pi}{a}x \quad \text{(corresponds to valence band)}$$

$$|\Psi_s^2| = 4\cos^2\frac{\pi}{a}x \quad \text{(corresponds to conduction band)}$$

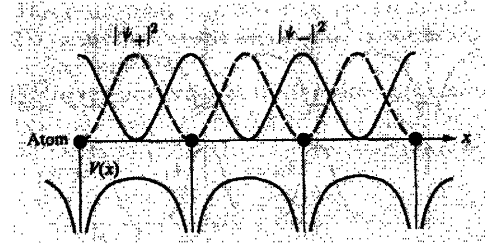

Figure.5.5: Spatial distributions of electrons described by the functions Ψ+ and Ψ− [68]

At this wavelength, there is no other solutions possible. This is the origin of bandgap in semiconductor. Similarly, we can understand the photonic badgap's physical origin by considering the electric field mode profiles for the states immediately above and below the gap. The gap between bands n_L and n_H occurs at the edge of the Brillouin zone, at $k = \pi/a$. With this wave vector, the modes are standing waves with $\lambda = 2a$, twice the photonic crystal's lattice constant where low-frequency modes concentrate their energy in the high n (high-ε) region and high-frequency modes concentrate their energy in the low n (low-ε) region as shown in figure 5.6. Therefore, when the lattice constant "a" matches half of the wavelength of incident light, where each layer has $\lambda/4n_{(L\ or\ H)}$ thickness, the reflection gets maximized. As a conclusion, we can simply stack $\lambda/4n_{(L\ or\ H)}$ thick layers alternatively if the constant ε is assumed over the range of interest.

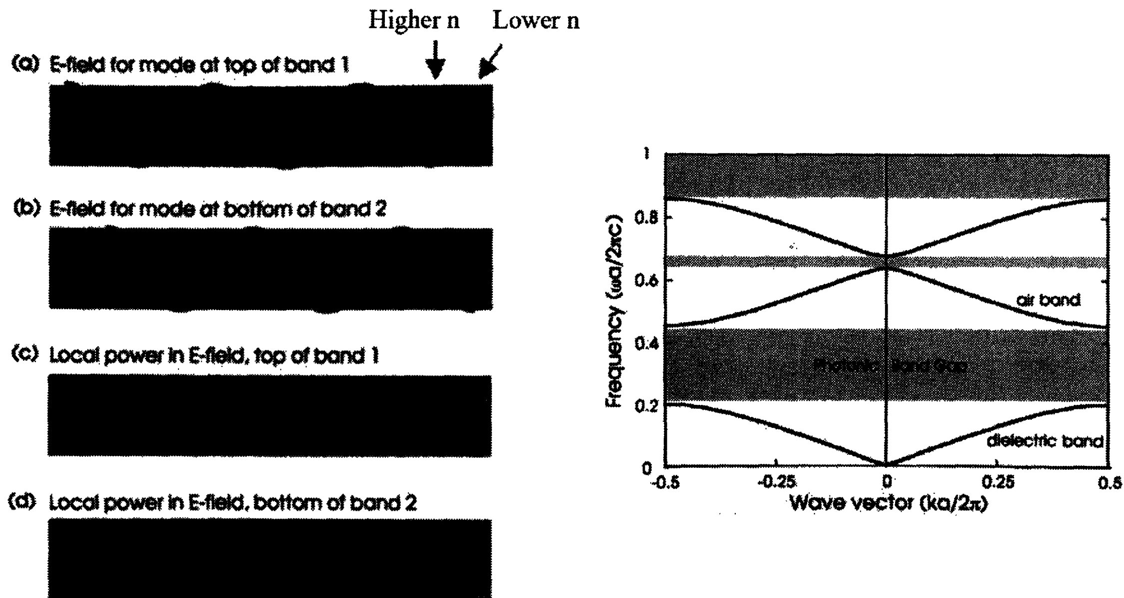

Figure 5.6: (Left) E-field distribution and power distribution inside PBG stack. (a) and (c) corresponds to dielectric band in the band structure. (b) and (d) corresponds to air band [69].

5.4 Fabrication

The first goal was set to achieve the close reflectance to theory. To achieve high reflectance, various approaches were tried and evaluated as described below.

A: Prototype1 (LPCVD poly-Si + thermal oxide)

Poly-Si and thermal oxide were chosen as HIC materials. The process scheme is outlined in figure 5.7. Thermal oxide is known as the best material as a low index material among various oxides such as CVD oxide, in terms of its stoichiometry or low absorption [66]. After growing thermal oxide by 1100°C wet oxidation using a BTU BDF-4 tube, then poly-silicon is deposited by a BTU BDF-4 LPCVD system at 620°C under 200mTorr pressure. Then poly-Si is partially oxidized by 1100°C wet oxidation to form SiO_2. By repeating poly-Si deposition and thermal oxidation, 3pair-PBG was fabricated. Target thickness of poly-Si and oxide are 35nm and 103nm, respectively.

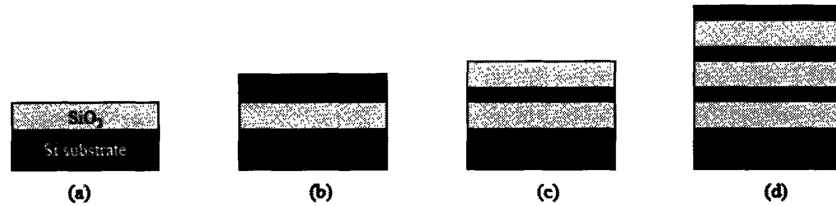

Figure 5.7: Fabrication scheme of prototype1. LPCVD poly-Si deposition and thermal oxidation are employed. (a) Grow thermal oxide, (b) Deposit poly-Si, (c) Partially oxidize poly-Si layer. (d) Repeat step (b) and (c)

Figure 5.8 is the theoretical and experimental reflectance. A Cary 5E spectrophotometer was used for the reflectance measurement where an error is less than $\pm 0.2\%$. Matrix propagation method was employed to obtain theoretical reflectance (Appendix B). The peak reflectance (96.8%) is almost the same as theoretical one (97.8%), however, the large degradation can be observed at the edges of stop-band. This can be attributed to the interface roughness of interfaces between oxide and poly-Si layers. Figure 5.9 is a cross sectional TEM (xTEM) image of this PBG. The rough interfaces are observed and the roughness of top poly-Si layer was found to be RMS=17.173nm for $1 \times 1 \mu m^2$ scanning range. The source of the interface roughness is grains of silicon layers. During thermal oxidation, grains grow to minimize the surface energy and oxidation rate is not identical between grains and grain boundaries [66], which make the surface/interface degraded as shown in figure 5.9.

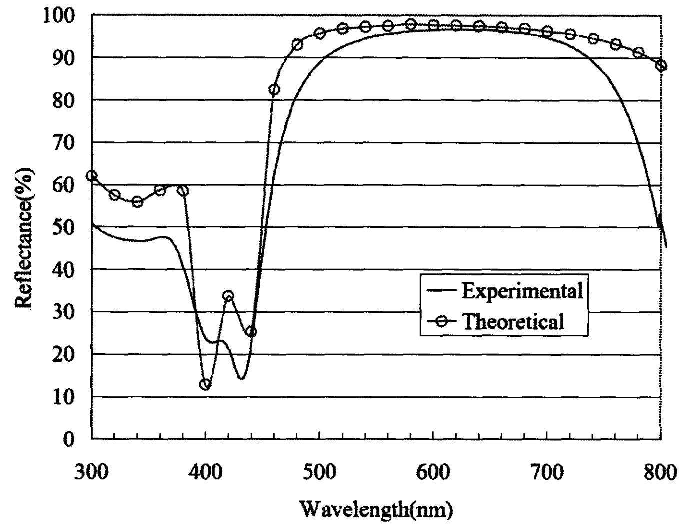

Figure 5.8: Theoretical and experimental reflectance of 3pair-PBG. Degradations of reflectance at the stop-band edges are observed.

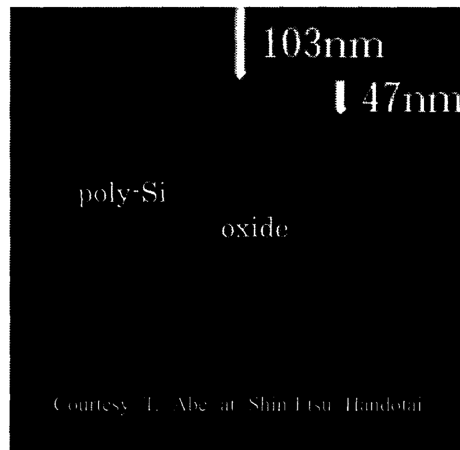

Figure 5.9: Cross sectional TEM image of PBG made by p-Si deposition and thermal oxidation. Courtesy of Dr. T. Abe at Shin-Etsu Handotai Co.,Ltd.

Therefore, it can be tentatively concluded that interface roughness has to be minimized to suppress scattering and the film quality of silicon and oxide in terms of optical properties,

such as refractive index and absorption, are close to those of crystalline silicon and quartz judging from the maximum reflectance.

B: Prototype2 (LPCVD poly-Si + LTO)

To suppress the interface roughness, LPCVD poly-Si and CVD oxide were chosen as HIC materials. The process scheme is shown in figure 5.10. This CVD oxide is often referred to as Low Temperature Oxide (LTO). LTO is grown at low pressure such as 200mTorr and the deposition temperature is 400-425°C. Therefore, LTO is not as dense as stoichiometric SiO_2. The reason why the deposition is done at such low temperature is that the reaction gases are SiH_4 and O_2 and they are explosive at higher temperature such as 500C or more [66]. It is necessary to apply high temperature annealing to densify LTO film after deposition to get the same property as thermal oxide. It is known that LTO is oxygen rich oxide and excess oxygen has to be removed out of the film to get stoichiometric SiO_2. The process procedure is as follows. SVG/Thermco 7000 furnaces were used for deposition and densification. Poly-silicon is deposited at 620°C under 200mTorr pressure. Then LTO is deposited at 400°C under 200mTorr, then the LTO is densified at 950°C for 30min in N_2 ambient. By repeating poly-Si deposition, LTO deposition and densification 5 times, 5pair-PBG was fabricated. Target thickness of poly-Si and oxide are 31nm and 89nm, respectively. Figure 5.11 shows the theoretical and experimental reflectance. The peak reflectance (97.3%) is closer to theoretical one (98.1%), however, the degradation at the edges of stop-band are still observed. Figure 5.12 is a XTEM picture of this PBG. As shown in figure 5.11, the interface roughness is suppressed and the roughness of the top poly-Si layer was RMS=3.385nm for $1x1\mu m^2$ by AFM analysis. Since poly-Si is partially oxidized by excess oxygen in LTO during densification, the interface roughness was not

totally suppressed.

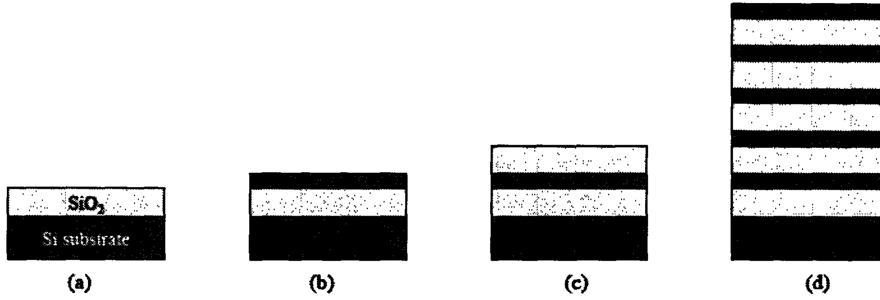

Figure 5.10: Fabrication scheme of prototype2. LPCVD poly-Si deposition and LTO are employed. (a) Grow thermal oxide, (b) Deposit poly-Si, (c) Deposit LTO and densify it (d) Repeat step (b) and (c)

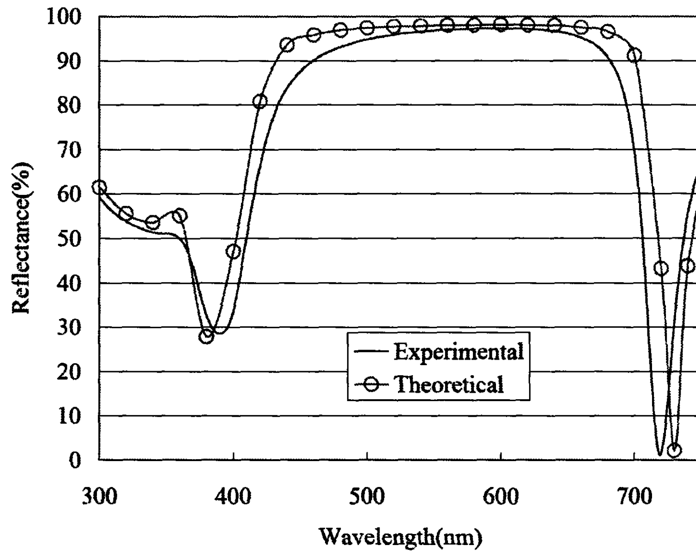

Figure 5.11: Theoretical and experimental reflectance of prototype2 (poly-Si and LTO 5pair-PBG). The performance as compared o theory was improved.

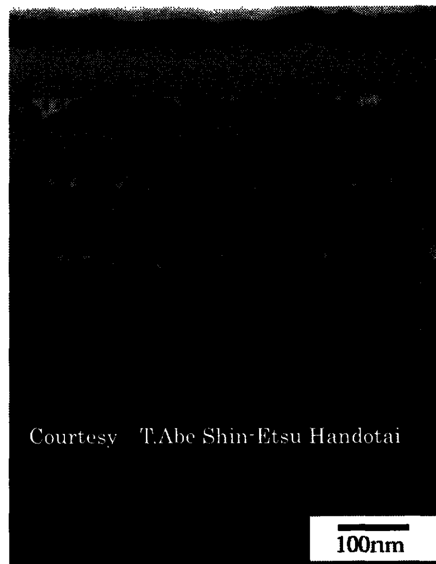

Figure 5.12: xTEM picture of prototype2 (LPCVD poly-Si and LTO PBG). Interface roughness is suppressed as compared to prototype1, however, slight roughening can be observed due to partial oxidation by LTO's excess oxygen.

C: Prototype3 SmartCut™ SOI PBG

To minimize the scattering loss at the interface, SmartCut™ technique was employed to realize atomically flat interface [70]. The approach has been proposed by Abe et al. [71]. The whole process can be explained briefly in figure 5.13. After growing thermal oxide, hydrogen ion is implanted and the wafer is bonded with another bare wafer. Then the wafer is delaminated by applying heat treatment. Then CMP is employed to planarize the surface. These processes are repeated and 3pair-PBG was fabricated. Figure 5.14 is a xTEM picture where flat interfaces are observed and Si layers are crystalline. After getting the thickness of each layer, the comparison between theoretical and experimental reflectance was carried out. Figure 5.15 is the result. The experimental result showed even higher reflectance than theoretical one. This result indicates that high

performance can be achieved by realizing flat interface and crystalline material. This sample was made by Dr. Abe at Shin-Etsu Handotai Co., Ltd and lent to us. The process technique was also developed by Abe et al.

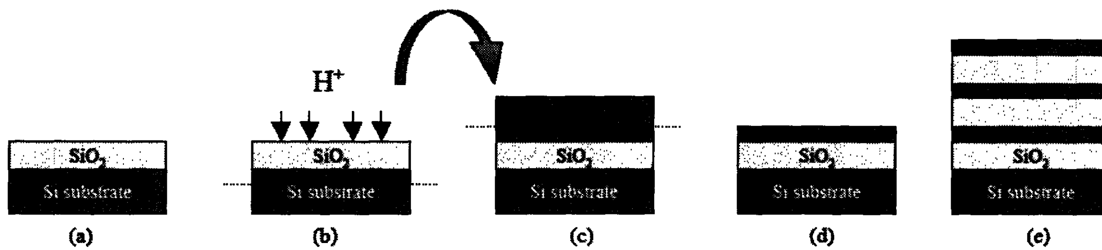

Figure 5.13: Fabrication scheme of prototype3. (a) Grow thermal oxide, (b) implant H+ ion, (c) Wafer bonding with a base wafer, (d) Delamination, annealing and CMP, (e) Repeat steps (b)-(d)

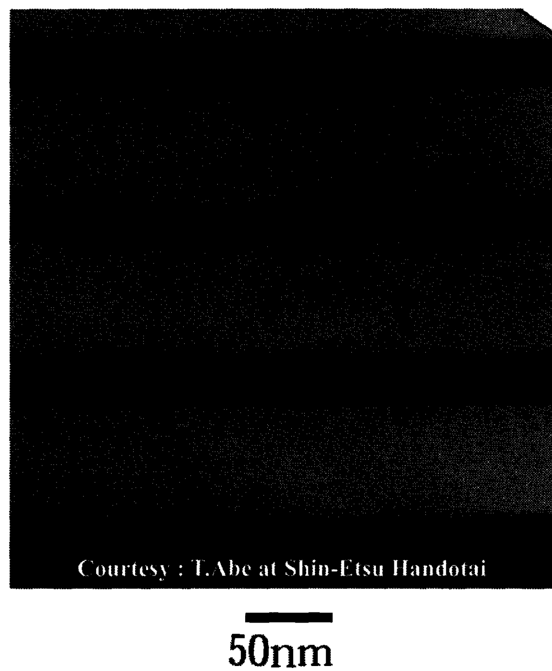

Figure 5.14: XTEM picture of prototype3 (SmartCut™ PBG) It is observed that Interface roughness is totally suppressed and Si layers are crystalline.

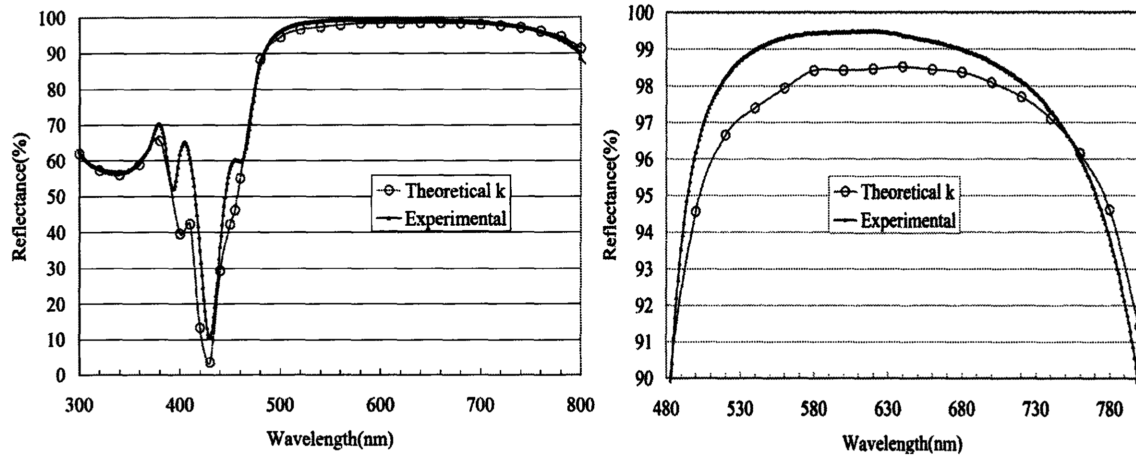

Figure 5.15: Theoretical and experimental reflectance of prototype3 (SmartCut® PBG). The experimental data shows higher reflectance over the stop-band.

Figure 5.15 indicates that experimental absorption coefficient (*k*) obtained here is smaller than theoretical *k*. It is considered that *k* was lowered by film stress caused by wafer bonding and successive heat treatment since the bonding interface relaxes at high temperature heat treatment around 1000-1100°C [70] then the bonded wafer is cooled down to room temperature. Due the difference of expansion coefficient between silicon and oxide (α_{si}= 2.6 e-6 K^{-1} , α_{ox}= 0.56 e-6 K^{-1})[55], it is expected that the tensile strain was introduced to silicon layer. The detailed analysis is done in the following section. To match the theoretical k to the experimental reflectance, theoretical *k* was manipulated and found that actual *k* is almost equal to 40% of theoretical *k* for visible light. Figure 5.16 is a fit curve where *k* is decreased by 60% (0.4*k*). It is shown that both curves fit well to each other for 400-700nm range.

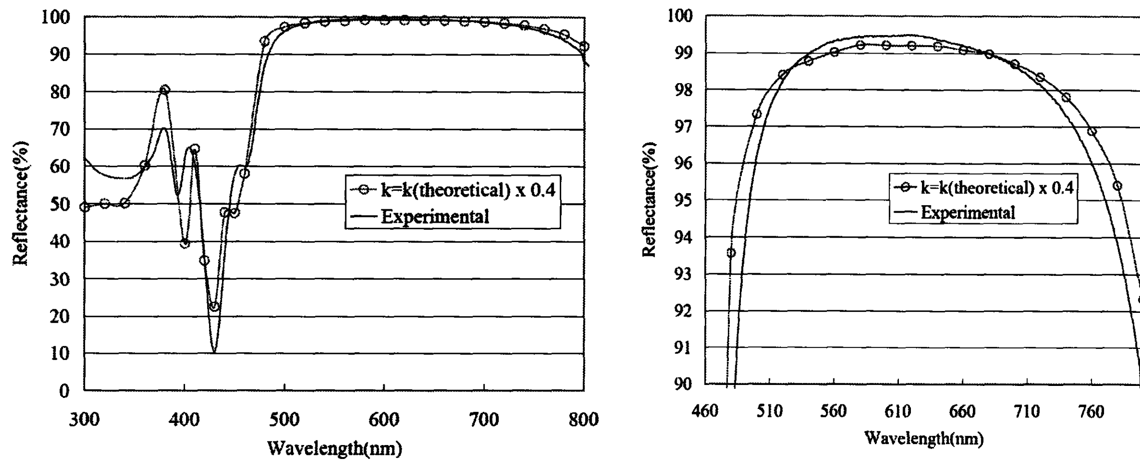

Figure 5.16: Actual and modified reflectance with 0.4 x $k_{theoretical.}$ Both curves fit well with each other. It is shown that k was changed by external factor.

D: Prototype4 (LPCVD poly-Si + thin nitride + LTO)

Even for prototype2, interface roughness was observed due to sacrificial oxidation of poly-Si layer by oxygen-rich LTO. To suppress interface roughness caused by this oxidation, thin nitride (-25A) was inserted into poly-Si/LTO interface. The process scheme is outlined in figure 5.17.

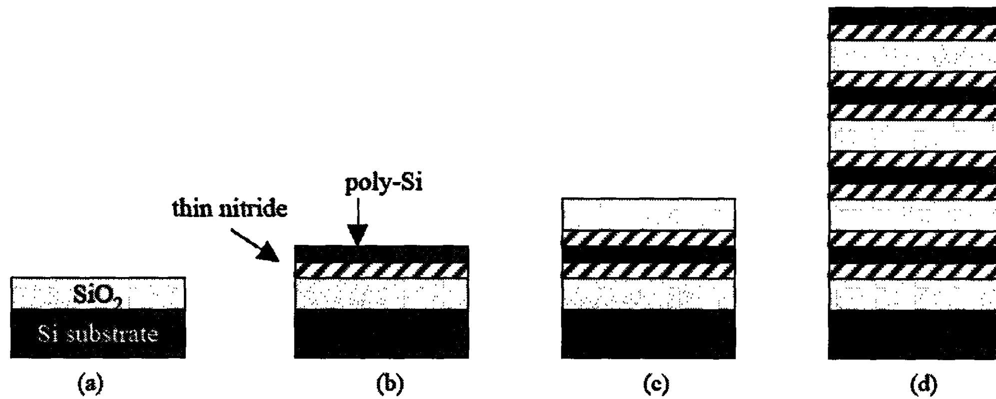

Figure 5.17: Fabrication scheme of prototype4. (a) Grow thermal oxide, (b) Thin nitride and poly-Si are deposited, (c) Thin nitride and poly-LTO are deposited. LTO is densified at 950C (d) Repeat steps (b)-(c)

Nitride is known as an efficient diffusion barrier against oxidation. It is expected to suppress the interface roughness by inserting thin nitride films. Basic fabrication scheme is the same as in prototype2 (poly-Si + LTO). Nitride (n=2.0) was deposited using a SVG/Thermco tube. The reaction gases are SiH_2Cl_2 250sccm and NH_3 25 sccm. The deposition was done at 775°C under 200mTorr pressure. The deposition rate is approximately 23Å/min. Figure 5.18 is a comparison of theoretical and experimental reflectance. Target thickness for poly-Si, nitride and densified LTO are 30nm, 2.5nm and 100nm, respectively.

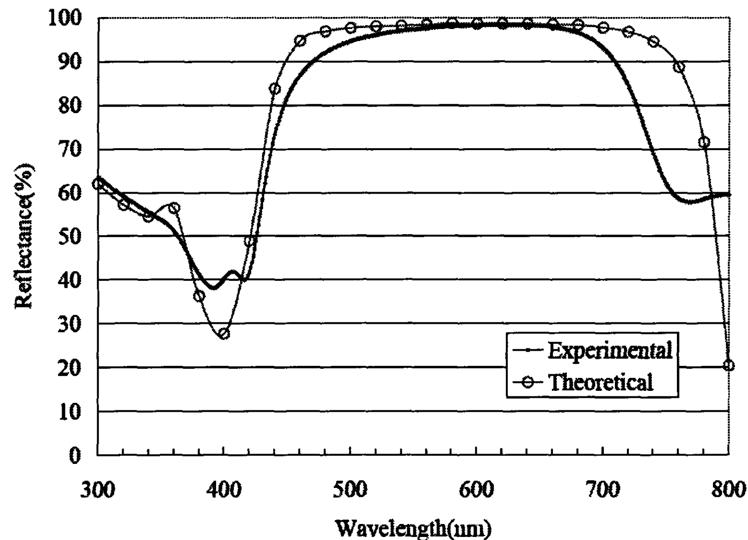

Figure 5.18: Theoretical and experimental reflectance of prototype4 (poly-Si + nitride + LTO 4pair-PBG). The performance as compared o theory was slightly improved.

As compared to protype2, the reflectance over the stop-band was slightly improved by 1.2% at peak. Since nitride is transparent in this wavelength and film quality except interface roughness should be the same, this is considered to be attributable to the effect of interface roughness.

5.5 Data analysis

Table 6.1 is a summary for the PBGs evaluated in the previous sections. Roughness was obtained by AFM analysis. The scanning size is 1μm^2. In table 6.1, "max. reflectance" denotes the peak reflectance observed by the experimental observation. "Mean deviation from the theory over stop-band" denotes the average deviation from the theory around center wavelength. For theoretical reflectance, absorption coefficient of crystalline silicon was used for that of poly-Si layers.

	Prototype1 (poly-Si + thermal oxide)	Prototype2 (poly-Si + LTO)	Prototype3 (SmartCut® SOI)	Prototype4 (poly-Si+nitride+ LTO)
Roughness (RMS: 1μm^2)	17.173nm	3.385nm	0.157nm	2.568nm
Max. reflectance(%)	**96.8**	**97.3**	**99.6**	**98.4**
Mean deviation from the theory over stop-band (theory-exptl.)	3.607% (480-780nm)	2.253% (440-680nm)	-1.424% (480-800nm)	1.604% (460-700nm)

Table 5.1: Summary of experimental results for VisPBGs. Roughness were obtained from AFM analysis and scanning range is 1μm^2. Theoretical maximum reflectance is about 98.6% for all the samples.

It is shown that the roughness and reflectance is strongly related to each other and figure 5.19 is a plot of reflectance for prototype1, 2 and 4, where prototype3 is excluded. It is shown that the roughness reduction is required to improve the PBG performance. And from the peak reflectance from protype4 (98.4%), which has the minimum roughness among 1, 2, and 4, it is concluded that poly-Si is acceptable to obtain as high reflectance as theoretical performance and it is more important to suppress surface/interface roughness.

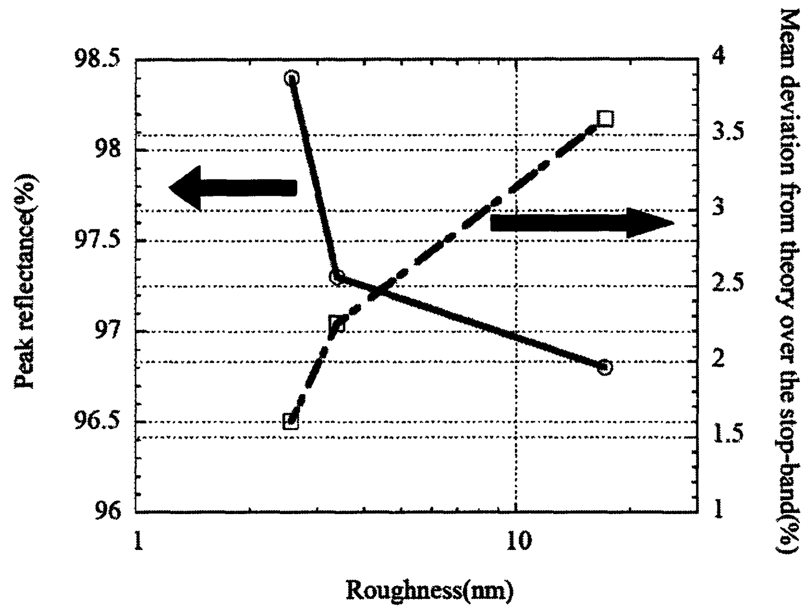

Figure 5.19: Relationship between surface roughness and PBG performances. It is shown that the roughness is quite important for higher reflectance.

5.6 The effect of film strain on reflectance improvement

As shown in figure 5.15, prototype3 (SmartCut® SOI PBG) showed higher reflectance than theory. It is assumed to be attributable to the film strain in silicon layer. After wafer bonding (step (c) in figure 5.13), high temperature (-1150°C) anneal was applied to strengthen the bonding strength [70]. Silicon is relaxed at this temperature and then cooled down to room temperature. Due to the difference of thermal expansion coefficients between Si and oxide (α_{si}= 2.6 e-6 K^{-1} , α_{ox}= 0.56 e-6 K^{-1})[55], a large amount of tensile strain is introduced into Si layer. If tensile strain is introduced in Si, then the band gap determined by light hole band, Eg(lh), will decrease, but heavy hole band, Eg(hh), will increase. Since Eg(hh) has much higher density of states than Eg(lh), the net effect is a decrease in absorption as compared with the unstrained case. The background physics is explained as follows. The bandgap dependence on film strain has been widely studied and I

employed the method developed by Van de Walle et.al's approach [72]. The detail is discussed below.

Stress σ:the force applied to the unit space (Pa = N/m^2)

Strain ε: the displacement of lattice constant defined as

$e = \left(a_{stress} - a_0\right)/a_0$ where a_0 denotes the lattice constant without strain.

In cases of diamond and zinc blend structures, strain is expressed as follows.

$$\begin{bmatrix} \sigma_{xx} \\ \sigma_{yy} \\ \sigma_{zz} \\ \sigma_{xy} \\ \sigma_{yz} \\ \sigma_{zx} \end{bmatrix} = \begin{bmatrix} c_{11} & c_{12} & c_{12} & 0 & 0 & 0 \\ c_{12} & c_{11} & c_{12} & 0 & 0 & 0 \\ c_{12} & c_{12} & c_{11} & 0 & 0 & 0 \\ 0 & 0 & 0 & c_{44} & 0 & 0 \\ 0 & 0 & 0 & 0 & c_{44} & 0 \\ 0 & 0 & 0 & 0 & 0 & c_{44} \end{bmatrix} \begin{bmatrix} e_{xx} \\ e_{yy} \\ e_{zz} \\ 2e_{xy} \\ 2e_{yz} \\ 2e_{zx} \end{bmatrix}$$

where c_{ij}: elastic constant and x : [100], y: [010], z : [001]

when biaxial stress is introduced into [001] surface,

$$\sigma_{xx} = \sigma_{yy} = \sigma_{//}$$
$$\sigma_{zz} = 0$$

Then

$$e_{xx} = e_{yy} = e_{//}$$
$$e_{zz} = e_{\perp} = -\left(2c_{12}/c_{11}\right)e_{//}$$

If $e_{//} > 0$, then tensile strain and if $e_{//} < 0$, then compressive strain.

In the case of silicon, elastic constants are [72]

$$c_{11} = 167.5 \text{ Gpa}$$

$$c_{12} = 65.0 \text{ Gpa}$$

When Bandgaps at Γ point are expressed as follows. The origin is set at the top of valence band without strain.

The top of valence band (hh: heavy hole, lh: light hole and so: split-off band)

$$E_{v-hh} = -P_\varepsilon - Q_e$$
$$E_{v-lh} = -P_\varepsilon + \frac{1}{2}\left(Q_e - \Delta + \sqrt{\Delta^2 + 2\Delta \cdot Q_e + 9Q_e^{\ 2}}\right)$$
$$E_{v-so} = -P_\varepsilon + \frac{1}{2}\left(Q_e - \Delta - \sqrt{\Delta^2 + 2\Delta \cdot Q_e + 9Q_e^{\ 2}}\right)$$

$$P_\varepsilon = a_v\left(e_{xx} + e_{yy} + e_{zz}\right)$$
$$Q_e = -\frac{b}{2}\left(e_{xx} + e_{yy} - 2e_{zz}\right)$$

where a_v denotes the deformation potential of valence band to hydrostatic pressure and b denotes the deformation potential to shear stress.

The bottom of conduction band

$$E_c^{direct} = E_g^{direct} + a_c^{direct}\left(e_{xx} + e_{yy} + e_{zz}\right)$$

a_c^{direct} denotes the deformation potential of conduction band to hydrostatic pressure

Then hydrostatic deformation pressure can be obtained by

$$a = a_c^{direct} - a_v$$

Parameters are obtained from [72]. Units are eV

$$a_v = 2.46$$
$$a_c^{direct} = 1.98$$
$$b = -2.35$$
$$\Delta = 0.04$$

The bottom of silicon's conduction band which is often referred to as X or Δ point is expressed as follows.

[001] direction

$$E_c^{indirect} = E_g^{indirect} + \left[a_c^{indirect}(2-\lambda) - 2\Xi_u^{\Delta}(1+\lambda)/3\right]\varepsilon_{//}$$

[100] or [010] direction

$$E_c^{indirect} = E_g^{indirect} + \left[a_c^{indirect}(2-\lambda) + \Xi_u^{\Delta}(1+\lambda)/3\right]\varepsilon_{//}$$

$$\lambda = 2c_{12}/c_{11}$$

parameters are obtained from [72]. Units are eV

$$a_c^{indirect} = 4.18$$
$$\Xi_u^{\Delta} = 9.16$$

As shown in figure 5.20, the bandgap of heavy hole (E_g^{hh}) increases and that of light hole (E_g^{lh}) decreases by introducing in-plane strain. Since the density of states of heavy hole is much higher than that of light hole as is shown figure 5.20 (left), the effective bandgap increases and it is expected that the optical absorption decreases.

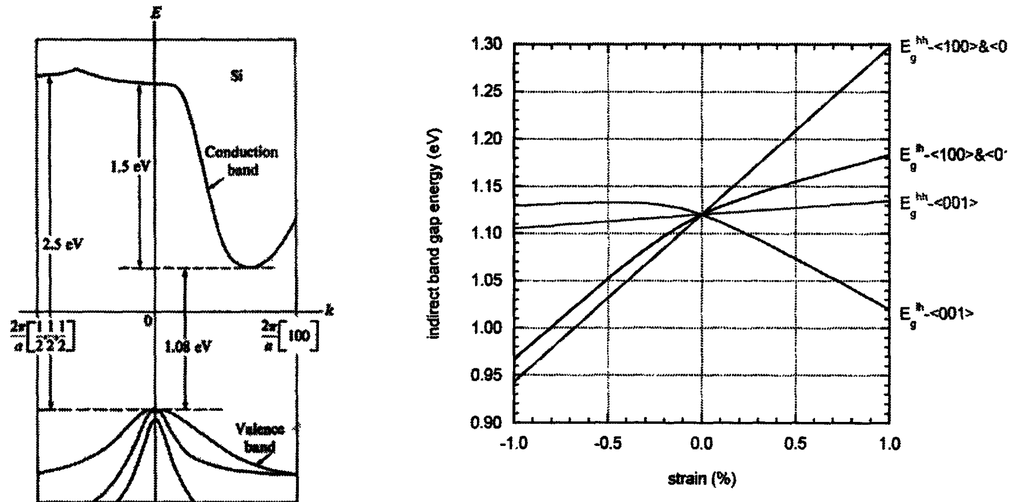

Figure 5.20: (Left) Band structure of Si plotted along the [100] and [111] directions [68]. (Right) Calculated bandgaps depending on the film strain.

It is challenging to obtain quantitative absorption-reduction from this theory, but the additional experiment was done to confirm this strain effect on reflectance. The sample used was prototype4 in section 6.4. To introduce film strain into silicon layer, Rapid thermal annealing was applied to this PBG. The RTP conditions are as follows.

Peak temperature: 1100-1125°C

Duration time: 1min.

Lamp-up rate: 50°C/sec.

Lamp-down rate: 50°C/sec.

Ambient: N_2

The system used here was an AG associates model 8108. It is expected that silicon layer is relaxed at peak temperature at 1100°C and no strain is assumed at this point and a film strain is introduced after rapid cooling sue to the large difference of thermal expansion coefficients of silicon and oxide. For this RTP process, the nitride cap layer (-150A) was deposited to avoid surface migration of top silicon layer. This nitride was removed after RTP using BOE solution. Figure 5.21 shows the reflectance before and after RTP. After RTP, it is shown that the reflectance is improved especially for shorter wavelength range. It is considered to be attributable to the absorption reduction by film strain since it can be assumed that the roughness for both samples (before and after RTP) should be almost the same. In this case, poly-Si was used instead of crystalline silicon layer, however, absorption-reduction was clearly observed. This expands the possibility of Si/SiO_2 HIC PBG mirror.

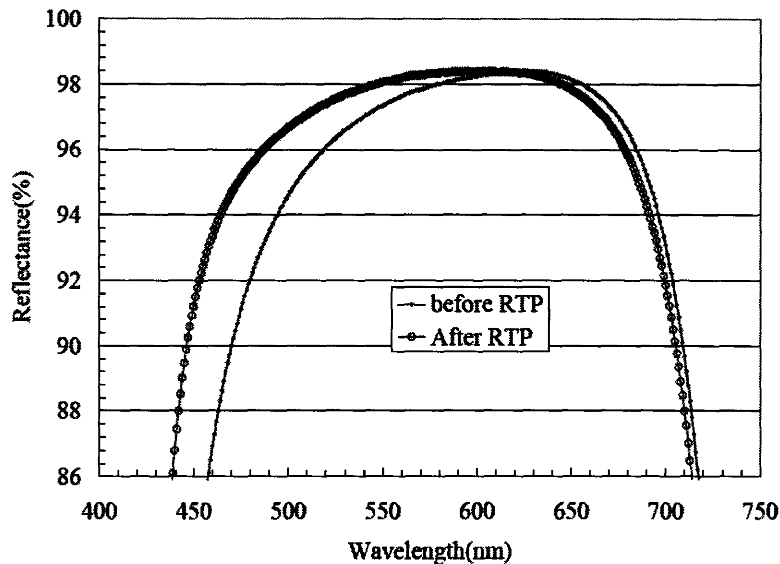

Figure 5.21: Reflectance change before and after RTP. The reflectance at shorter wavelength is improved without changing the stop-band width. It is considered to be attributable to the absorption reduction in silicon layer.

5.7 Summary

It has been shown that it is possible to improve the reflectance of Si/SiO_2 HIC PBG mirror for visible light by suppressing the surface/interface roughness and introducing the film strain by successive heat treatment. However, it is still challenging to achieve as high reflectance as 97% from 400-700nm. A new approach has to be developed for practical applications. This VisPBG is applicable not only to visible light reflector but also to other applications such as microcavity or other optics components for 850nm, which corresponds to GaAs's band gap, combining with plastic optical fiber (POF) for in-home applications.

Chapter 6: IR-PBG for semiconductor saturable absorber mirror (SESAM)

6.1 Background

Near infrared (NIR) is also an interesting wavelength range for photonic crystal since it is strongly related to 1.3μm or 1.55μm communication range. For example, commercially used laser mirrors are either based on a metal reflector or a dielectric Bragg reflector. Metal reflectors reflect light over a very broad range of wavelengths, but their reflectivity is not very high (e.g. <98%) due to the absorption of the metal. In addition, light of different wavelengths undergoes different phase shifts when reflected from the metal. Thus, because of loss and phase shift, these mirrors cannot be used in many laser systems. Dielectric mirrors, on the other hand, consist of a coating of dielectric layers of different refractive indices, which is deposited on a glass substrate. At each boundary between two adjacent layers a small fraction of the light is partially reflected, such that the coherent superposition of the many partial reflections results in a highly reflecting mirror. This partial reflection of light at the layer boundaries determines two of the most important properties of the mirror: reflectivity and bandwidth. These are properties of the material system and they can only slightly be modified upon selecting the layer thickness. The larger the contrast of refractive indices at each layer boundary, the larger the partial reflection in this place becomes, and as a result, the smaller the number of total layers becomes, that is needed to achieve a certain overall reflectivity. This is shown in Figure 6.1. The commonly used dielectric material system SiO_2/TiO_2 (indices n=1.45 and 2.3) has a partial reflectivity of 5% at each index discontinuity, and 11 layer pairs are needed for a 99.8% high reflector. In contrast, a mirror fabricated with Si/SiO_2 (indices n=3.5 and 1.45) has a three time larger partial reflection and achieves the same overall reflectivity with only six layer pairs. Even

more important, it achieves this reflectivity over almost twice the bandwidth. Figure 6.1 is a comparison of Si/SiO_2 6pair-PBG and TiO_2/SiO_2 11pair-PBG. The very large bandwidth in combination with a very high reflectivity and a flat phase response are the key features of Si/SiO_2 based laser mirrors. This combination of the benefits of both silver mirrors and dielectric mirrors determine the broad range of applications for Si/SiO_2 based laser mirrors. They can be used as extracavity mirrors, replacing silver mirrors, e.g. for combining laser beams of different wavelength, for broadband applications or for high-energy laser systems. In addition, they are excellent intracavity mirrors in broadband lasers, where their high reflectivity and bandwidth are useful. Furthermore, besides the simple high reflectors discussed so far, a variety of Si/SiO_2 based devices will be created which exploit the large fractional reflection at each layer boundary. Finally, the use of a semiconductor material such as Silicon allows for the design of active elements such as light modulators, and, in combination with Germanium, saturable absorbers for femtosecond lasers. The details about saturable absorber are discussed in later sections.

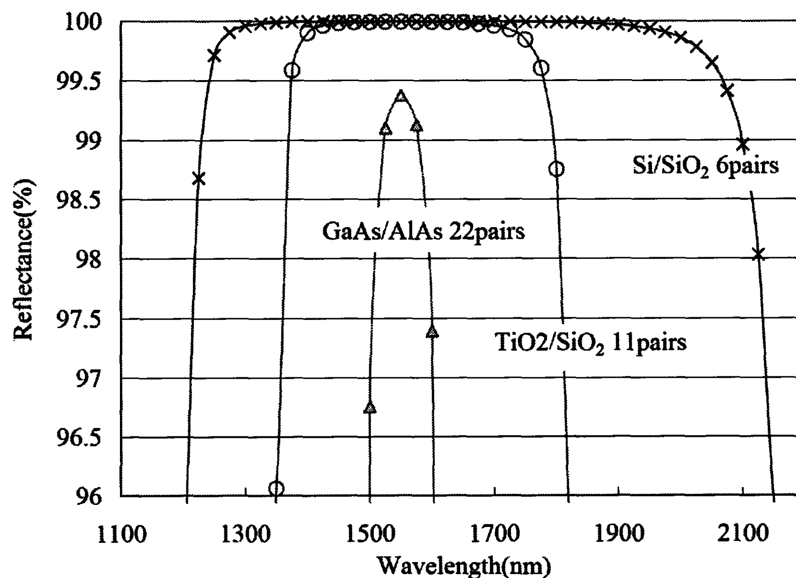

Figure 6.1: A comparison of Si/SiO_2 6pair-PBG, TiO_2/SiO_2 11pair-PBG and GaAs/AlAs 22pair-PBG. It is shown that Si/SiO_2 PBG has a stop-band twice as wide as TiO_2/SiO_2 PBG. Reflectance was obtained by theoretical simulation based on propagation matrices approach.

6.2 Fabrication of IR-PBG

One of the most important factors for IR-PBG is that the fabrication should be done using CMOS compatible process for lower production cost and to maintain high reflectance over the stop-band as high as 99.5% ideally. Different from VisPBG, which is discussed in chapter 5, the absorption of silicon layer is no more a serious problem [73]. To achieve precise thickness control and maintain easy processing, LPCVD poly-Si and thermal oxidation were employed to make high index contrast PBG. As is described in chapter 5, thermal oxidation causes interface roughness since oxidation rate is varied between grains and grain boundaries [74]. The fabrication is briefly explained in figure 6.2.

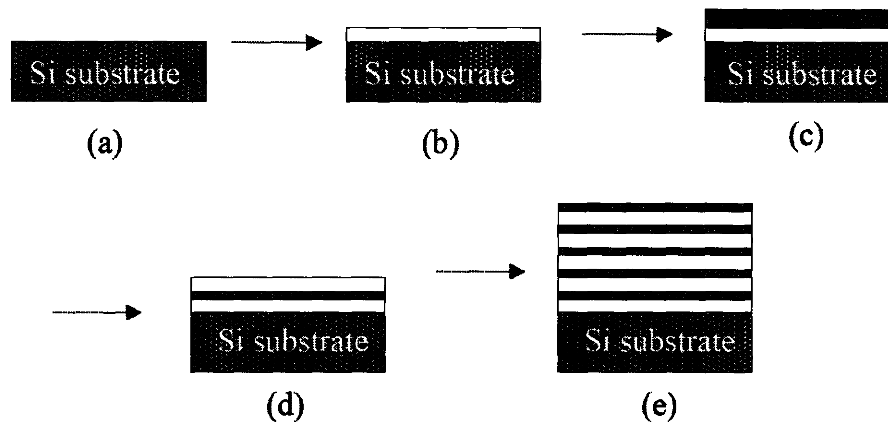

Figure 6.2: Schematic of IR-PBG fabrication. LPCVD poly-Si and thermal oxidation are employed for batch process. (a) Grow thermal oxide, (b) Deposit poly-Si, (c) Partially oxidize poly-Si layer. (d) Repeat step (b) and (c)

(a) Grow thermal oxide by 1100°C wet oxidation using a BTU BDF-4 diffusion tube.

(b) Poly-silicon is deposited by a BTU BDF-4 LPCVD system at 620°C under 200mTorr pressure.

(c) Poly-Si is partially oxidized by wet oxidation to form SiO_2.

(d) By repeating poly-Si deposition and thermal oxidation, 6pair-PBGs were fabricated. Target thickness of poly-Si and oxide are 103nm and 224nm, respectively.

In this process, wet oxidation temperature was varied from 900°C to 1100°C to evaluate the effect of oxidation temperature on the surface roughness. Figure 6.3 is the reflectance of these PBGs with 900°C, 1000°C and 1100°C oxidation temperatures.

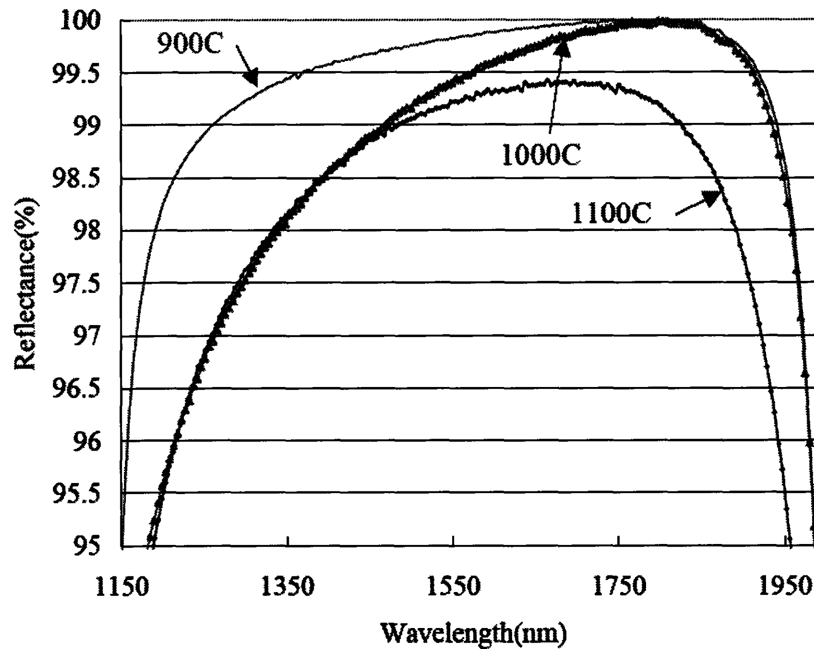

Figure 6.3: The effect of oxidation temperature on reflectance. It is shown that higher oxidation temperature degrades reflectance especially around short wavelength (1150-1550nm) within the stop-band.

AFM analysis was done for these PBGs. As shown in figure 6.4, the higher oxidation temperature causes rougher surface. At high temperature, it is expected that oxidation rate is varied between grains and grain boundaries and grain growth, which causes rough interface, is enhanced [74]. Hereafter, 900°C wet oxidation process is employed to form SiO_2 layers to minimize interface/surface roughness.

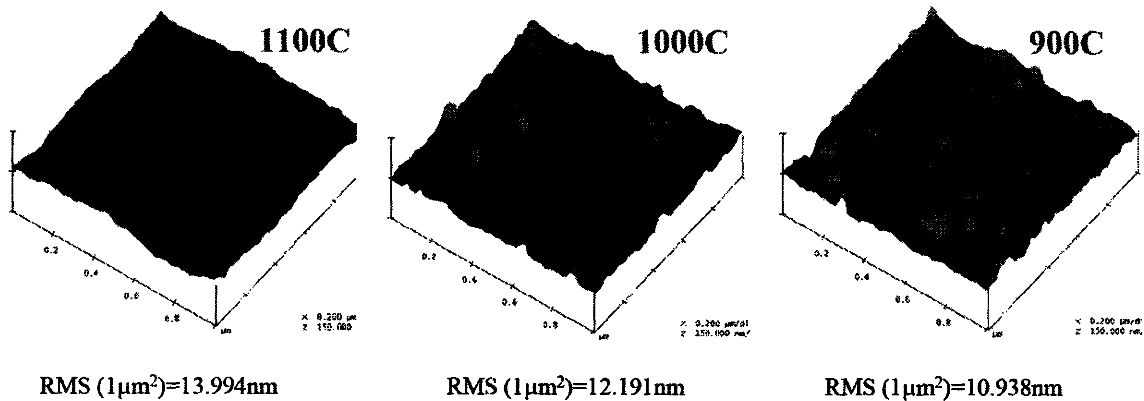

Figure 6.4: AFM images of PBGs made with various wet oxidation temperatures. It is shown that the surface is roughened as temperature goes up.

6.3 Bonded and Etched-back PBG (BE-PBG)

It is easily expected that the surface roughness increases gradually with each deposited layer pair. To solve this fundamental problem, the new process is proposed, which is described in figure 6.5. The PBG mirror is flipped upside down such that the layers with the lowest surface roughness are topmost, while those of lower quality are close to the bottom of the Bragg mirror where the field intensity is lowest (figure 6.6). Since the film quality for each poly-Si layer or each oxide layer should be identical, the effect of the top surface roughness can be evaluated. The lower interface of the first poly-Si layer (the bottom-most poly-Si as deposited.) is similarly formed by thermal oxidation of crystalline silicon during the formation of the first low-index layer of the Bragg mirror in our fabrication process (figure 6.5a). Thus, all interfaces exposed to high field intensities are of highest quality, leading to a minimum of scattering loss. Since the topmost layer is exposed to the highest intensity of the light over the stop-band, its roughness has to be minimized for better performance.

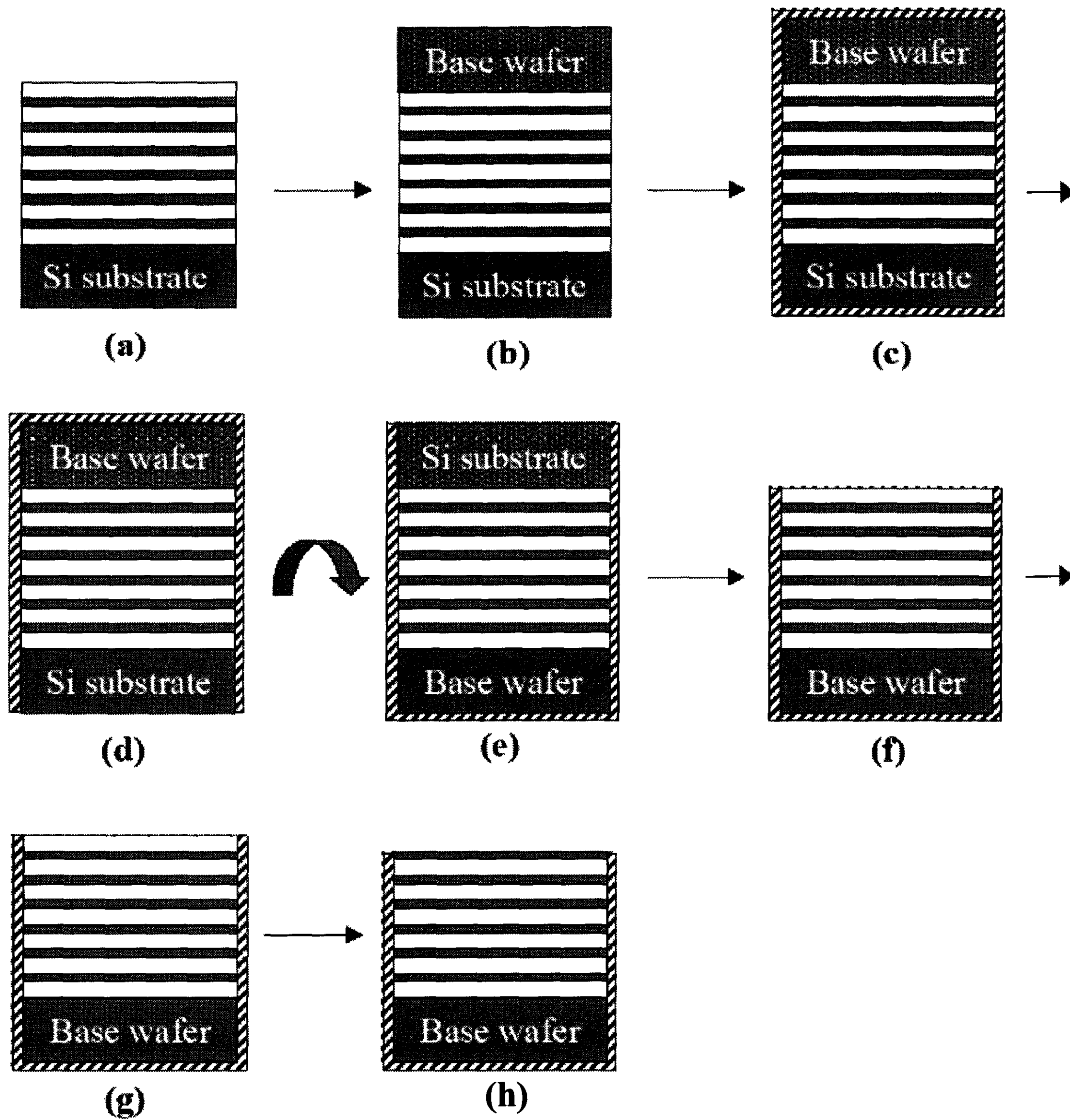

Figure 6.5: Schematic of the fabrication of a Bonded and Etched-back (BE) PBG.

(a): Fabricate normal 6pair-PBG using the same procedure as in section.6.2. Apply Chemo mechanical polishing (CMP) to planarize the bonding surface. CMP is done by Strasbaugh Harmony 6EG. Polishing conditions are as follows. Quill speed = 40rpm, Table speed = 25rpm, Down force = 3.0psi, Back pressure = 2.0psi and Slurry amount

= 150ml/min.

(b): A PBG wafer is bonded with a base wafer using Electronic Vision model 620. The bonded wafers are annealed at 1050°C for 2hours to strengthen the bonding energy [70]. Then the bonding quality is inspected by IR camera. Figure 6.7 is an example for three different bonded wafers.

(c): Si-rich low-stress nitride is deposited using LPCVD process by SVG/Thermco 7000 vertical thermal reactor (VTR). The reaction gases are SiH_2Cl_2 (DCS) 250sccm and NH_3 25sccm. The pressure and deposition temperature are 250mTorr and 775°C, respectively. This nitride is used as a KOH etching mask in step (f).

(d): Nitride on the backside (Si substrate side) is removed by CMP. The polishing conditions are the same as step (a) except the down force at 7.0psi.

(e): The bonded wafer is flipped.

(f): Si substrate is etched with 10% wt KOH solution at 70C. The etch rate is approximately 0.6-0.7μm/min.

(g): The wafer is cleaned by Piranha solution (50% H_2SO_4 : 30% H_2O_2 = 4 : 1).

(h): Buffered oxide (BOE) is applied to remove oxide on top layer. The fabricated PBG wafer is called "Bonded and Etched-back PBG (BE-PBG)"

Then reflectance was measured using Varian® Cary 5E photospectrometer. Figure 6.8 shows the comparison between as-deposited PBG and BE-PBG. It is shown that the reflectance of BE-PBG is improved significantly. Figure 6.9 is a set of AFM images of as-deposited and BE-PBG wafers. The roughness was suppressed from 10.938nm(/μm^2) to 0.782nm(/μm^2) by a factor of 14.

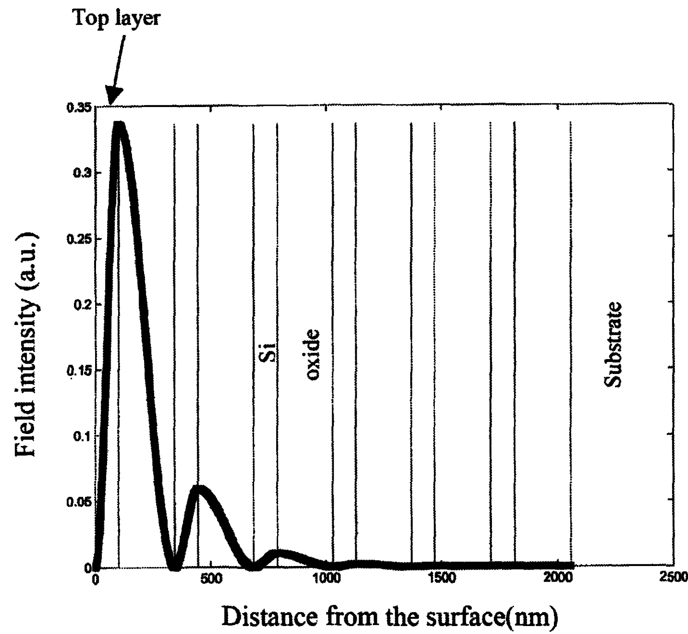

Figure 6.6: Field intensity of 6pair-PBG at center wavelength 1.4μm. The most of the filed is located in the first pair.

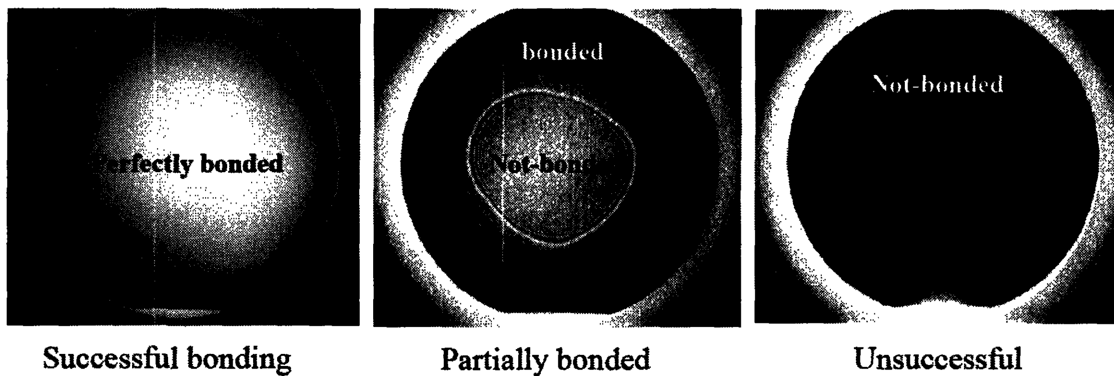

Figure 6.7: IR images of bonded wafers. (left): two wafers are nicely bonded. (middle): Central part is not bonded and edge part is bonded but bonding quality is not so good as left example. (right): Bonding is unsuccessful. This is due to rough surface. Wafers are delaminated and re-polished and bonded again.

From figure 6.8, it is confirmed that high reflectance (99.5%) was achieved over 700nm in the stop-band.

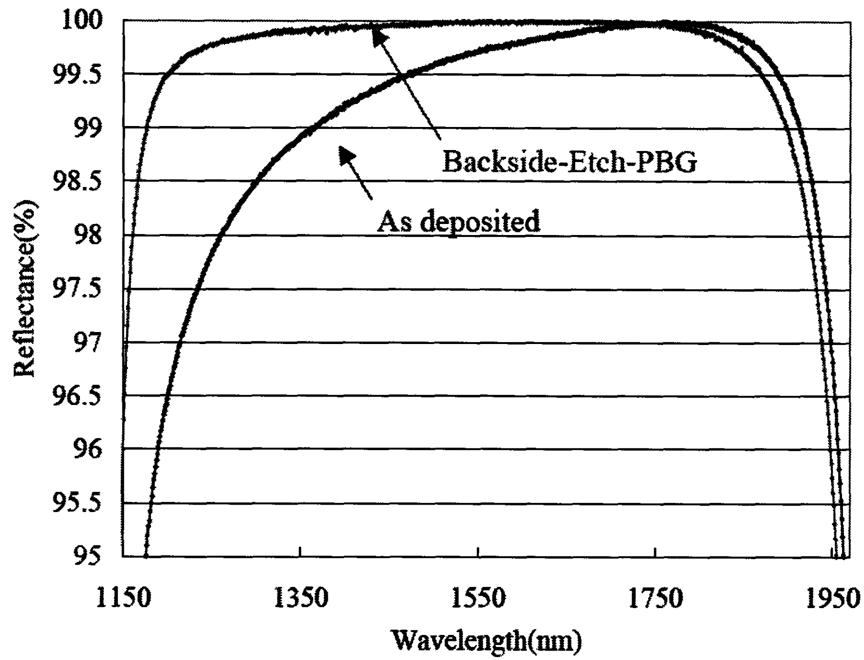

Figure 6.8: Reflectance of as-deposited and BE-PBGs. Reflectance is improved by bonded and etched-back process especially for the shorter wavelength in the stop-band.

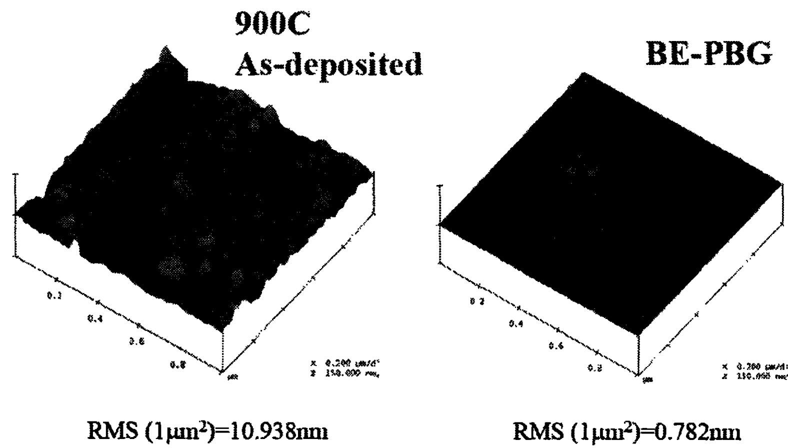

Figure 6.9: AFM images of as-deposited and BE-PBGs. The surface roughness is minimized by a factor of 14.

6.4 CMOS-compatible semiconductor saturable absorber (SESAM)

So far I have discussed IR-PBG mirror as a passive optical mirror. However, this PBG is also applicable to other active optical devices such as saturable absorber. Semiconductor saturable absorber mirrors (SESAMs) or saturable bragg reflectors (SBR) have been extensively used for passive modelocking of solid state lasers over the last decade [75-80]. However, deployment of such lasers in the optical telecommunications market has not happened so far even though mode-locked lasers with 3ps pulse-widths at the communications wavelength of 1.55 μm and with repetition rates of up to 10 GHz [81] have been demonstrated. This is due to a number of reasons: First of all, lasers modelocked with a SESAM tend to Q-switch if the saturable absorber relaxes faster than the gain medium in the absence of additional stabilizing mechanisms in the laser cavity. This problem is especially pronounced in lasers with high repetition rates that are of interest for the telecom industry. Second, the lifetime of the saturable absorber is drastically shortened due to a heavy thermal load if pulses of high fluence are incident on the SESAM, a technique frequently applied to prevent Q-switching. Finally, SESAMs have been grown out of III-V materials such as GaAs, AlAs, InP or compound semiconductors that are fairly expensive, and that are incompatible with future generations of integrated silicon optoelectronic devices. To overcome these obstacles, and to produce ultra-broadband SESAMs at the telecom wavelength, the application of the IR PBG, which has been studied in the previous sections, to SESAMs in the Silicon / SiO_2 / Germanium material system (Figure 6.10) was carried out. The high index contrast PBG has been achieved and with a record 98% bandwidth of over 700nm with a peak reflectivity of 99.8% with only six layer pairs (figure 6.8). In contrast, conventional SESAMs made of the common III-V materials GaAs and AlAs require 22 layer pairs to achieve the same peak reflectivity, but provide only 90nm of usable bandwidth (figure 6.1). On top of the Si/SiO_2 Bragg mirror a

Germanium layer is embedded in a Silicon layer of 3/4λ optical thickness as shown in figure 6.10. The germanium layer has a dual functionality: It provides the desired amount of saturable absorption to modelock the laser and in addition, the strong amount of two-photon absorption (TPA) in this layer can be employed to stabilize high repetition rate lasers against Q-switching [82-87]. As can be observed in figure 6.10, the germanium absorber layer is located in a peak of the standing wave pattern of the electric field to maximize absorption, while the field decays rapidly upon further penetration in the mirror and barely reaches the lower part of the mirror structure.

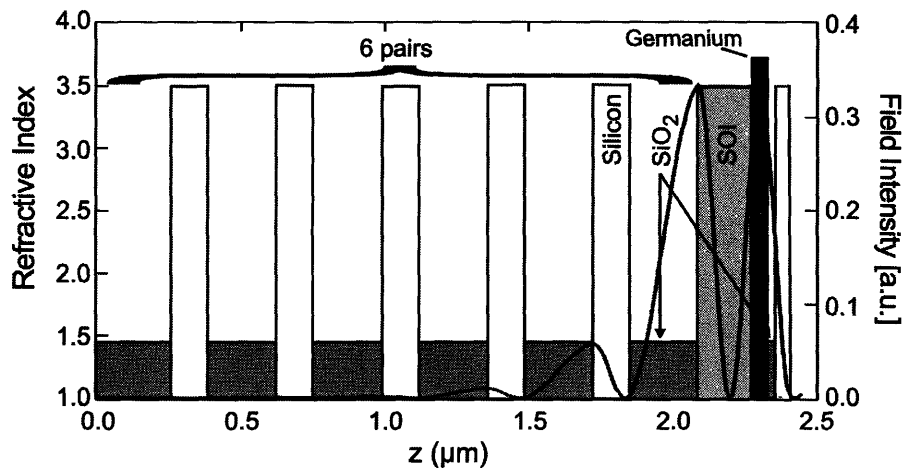

Figure 6.10: Refractive index profile and standing wave pattern of the SESAM. The fields decays rapidly in the 6-pair Si/SiO2 mirror due to the large index contrast. All interfaces of exposed to high field intensities are created by thermal oxidation, reducing scattering loss. The Bragg mirror is terminated with an SOI layer that allows for subsequent growth of crystalline Germanium. Figure courtesy: F. J. Grawert.

6.5 Fabrication of SESAM

The same process as BE-PBG was applied to fabricate SESAM. The only difference from BE-PBG is the fact that the starting material is Silicon-On-Insulator (SOI) wafer. Figure 6.11 is a schematic of the fabrication of a bonded and etched-back-SOIPBG (Hereafter, BE-SOI-PBG).

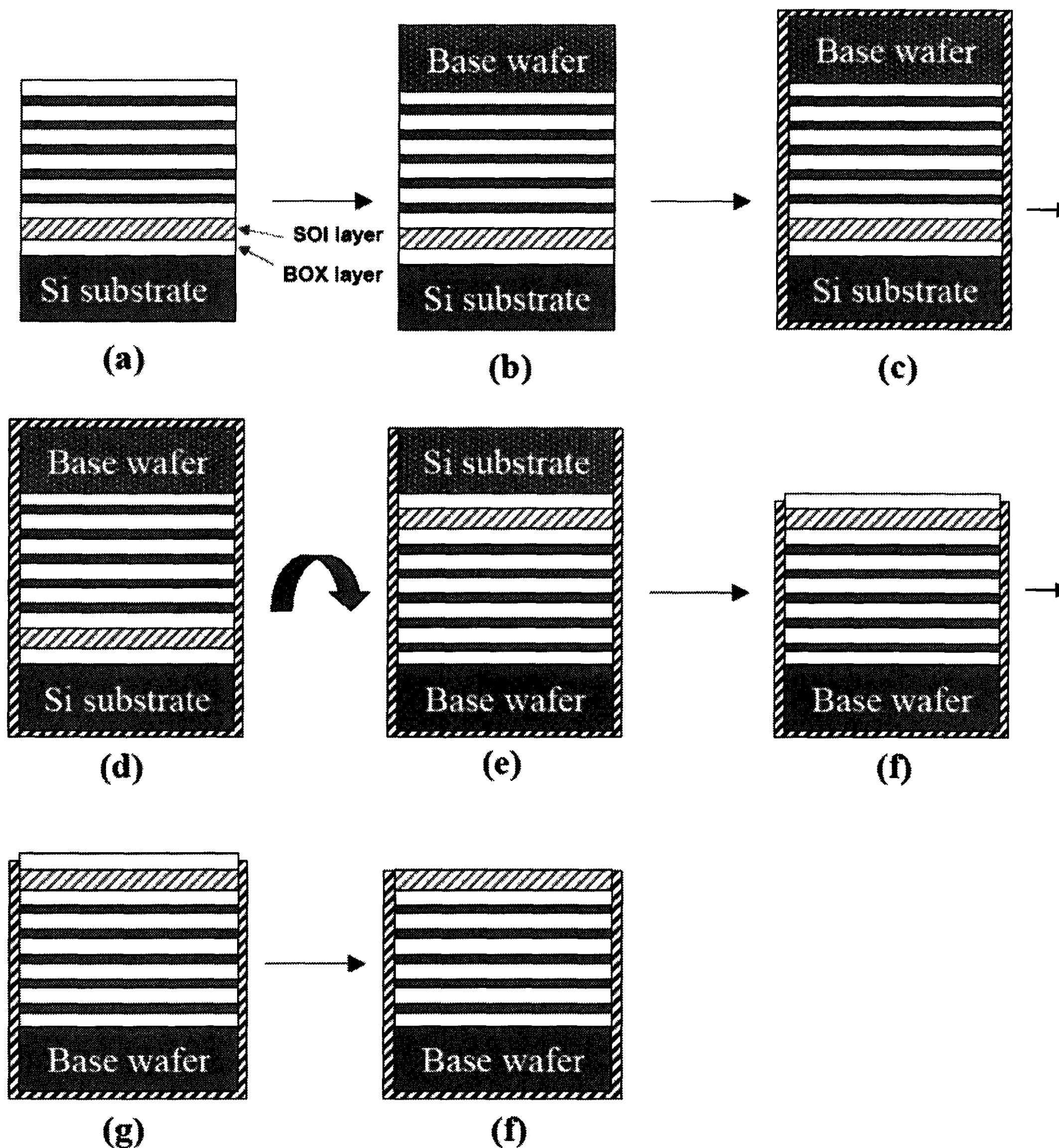

Figure 6.11: Schematic of fabrication of BE-SOI-PBG.

By employing this process, better surface roughness can be expected since crystalline silicon (SOI layer) can be placed on top. Even more important, germanium can be epitaxially grown on this crystalline silicon while achieving high reflectance over the stop-band as shown in the previous section. Figure 6.12 is the AFM image of this BE-SOI-PBG. As shown in Figure 6.12, the surface shows the lowest RMS among PBGs discussed so far. Table 6.1 shows surface roughness and mean reflectance over the stop-band. It is shown that reflectance is improved by suppressing surface roughness.

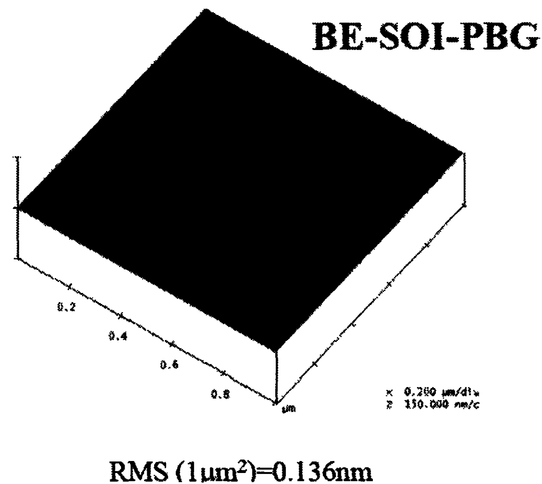

RMS (1μm²)=0.136nm

Figure 6.12: AFM image of BE-SOI-PBG. The surface roughness is as low as RMS 0.136nm(/1μm^2)

	1100C wet as-deposited	1000C wet as-deposited	900C as-deposited	BE-PBG	BE-SOI-PBG
Roughness RMS(/μm^2)	13.994	12.191	10.938	0.782	0.136
Mean reflectance (%) over the stop-band (1250-1900nm)	98.787	99.135	99.500	99.779	99.896

Table 6.1: Roughness and mean reflectance over the stop-band for PBGs discussed so far.

6.6 Germanium epitaxial growth

The next step is to grow germanium layer on crystalline silicon layer (SOI layer), which functions as an absorption layer. Germanium and silicon have 4% mismatch to each other and direct epitaxial growth of germanium on silicon has been considered to cause island structures and generate threading dislocations in epitaxial germanium film [88]. For our purpose, the new approach has been developed based on the technique proposed by Luan et al. [88]. The basic structure is explained in Figure 6.13. Germanium is placed on SOI top layer and thin oxide is deposited on germanium as a passivation layer on which poly-Si is deposited. Germanium, oxide and poly-Si are placed so that the peak of field intensity resides in germanium layer.

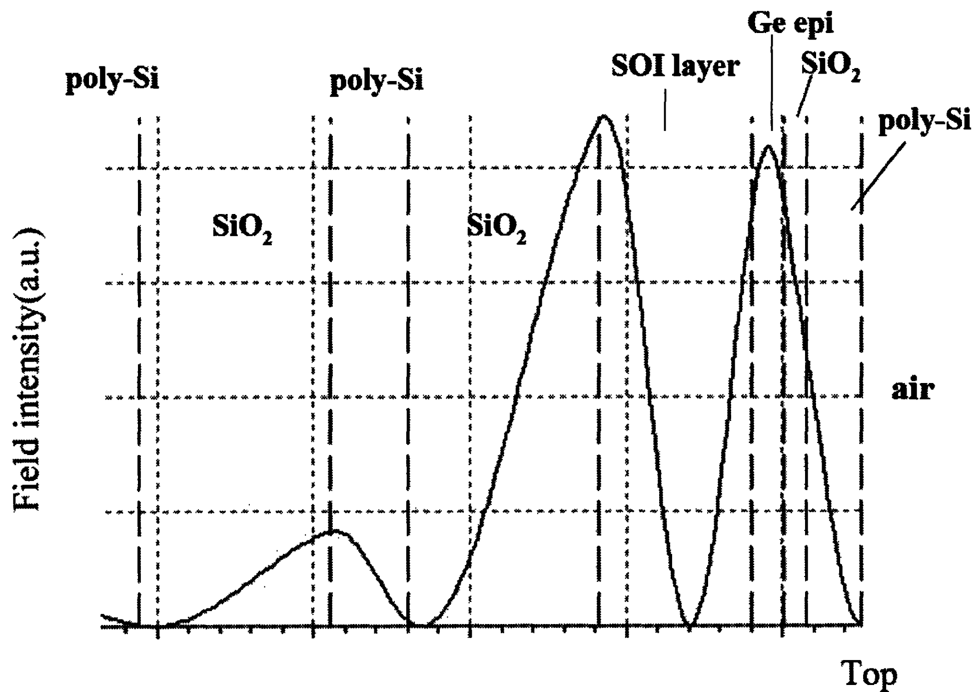

Figure 6.13: Standing wave pattern of saturable absorber. Design is optimized so that the peak field intensity resides in Ge absorption layer.

The passivation of germanium film by thin oxide has been proposed by Cannon et al [89]. The detailed design was optimized using Optilayer™. The optimized thickness for layers are 196nm, 30nm, 40nm and 70nm for SOI layer, oxide, germanium and poly-Si, respectively. The fabrication process is outlined in figure 6.14. All steps are CMOS-compatible and batch-process, which brings much lower fabrication cost as compared to conventional III-V based technology.

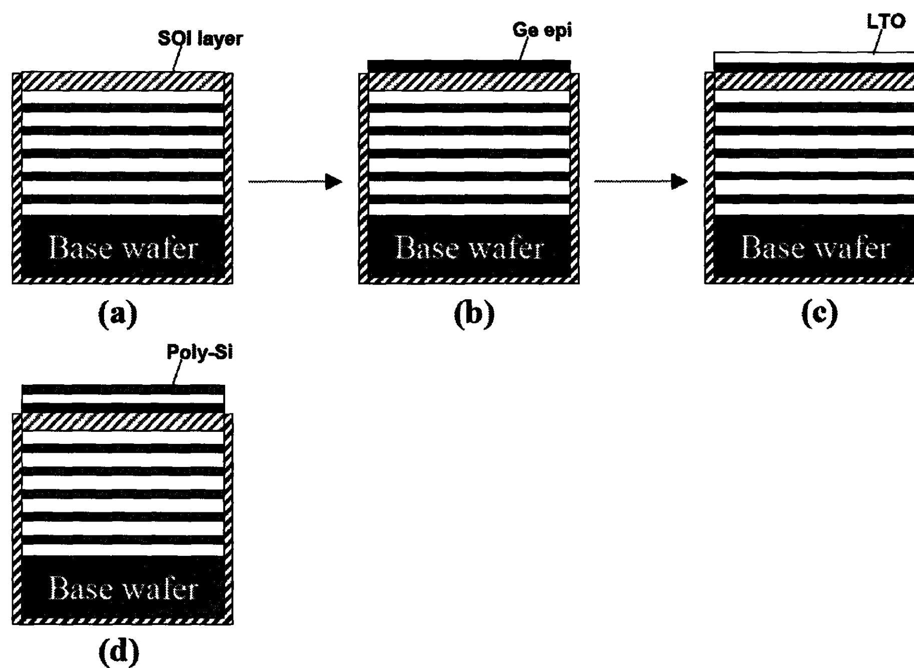

Figure 6.14: Schematic of fabrication of saturable absorber based on Si/SiO_2 PBG

(a): BE-SOI-PBG is cleaned using piranha solution (50% H_2SO_4 : 30% H_2O_2 = 4 : 1) then dipped in 2% HF solution to make the surface hydrogen-terminated.

(b): Germanium is epitaxially grown at ultra high vacuum condition (~10^{-9} Torr) at 350°C to avoid islanding of germanium film on Si surface [88]. GeH_4 gas is used as germanium source.

(c): After modified RCA cleaning [89], CVD low temperature oxide (LTO) is deposited at

400°C. The sequence of modified RCA is described below. Normal RCA process is known to etch Ge layer [90].

1. $NH_4OH : H_2O = 1 : 4$ (tank 1) for 5 min. to etch native oxide
2. rinse (rinser 1)
3. H_2O_2 30 sec. to grow about 20Å of GeO_2 (tank 1)
4. rinse (rinser 1)
5. HF 30 sec.
6. rinse (rinser 1)
7. H_2O_2 30 sec. (tank 2)
8. rinse (rinser 1)
9. $HCl : H_2O$ 1 : 4 30 sec. (tank 2)
10. rinse (rinser 2)
11. spin-dry

(d): Poly-Si is deposited at 625°C. Obtained thickness for each film are 323Å, ~420Å and 699Å for LTO, germanium and poly-Si, respectively. The thickness of poly-Si and LTO were obtained by KLA tencor UV1280 Prometrix thin film thickness measurement system.

X-ray diffraction was employed to analyze the crystallinity of the epitaxially grown germanium film. Rigaku 250mm high resolution Gragg Brettano diffractometer was used with Cu target. Figure 6.15 shows the X-ray diffraction peak from as-grown germanium. A single peak fitting approach was employed, where

Raw intensity = baseline + $K\alpha_1$ Gaussian (peak ht. and width) + $K\alpha_2$ Gaussian (peak ht. and width).

It is shown that this germanium film is crystalline and compressively strained as much as –0.24%. Thickness was determined to be 420±20Å from FWHM of the peak.

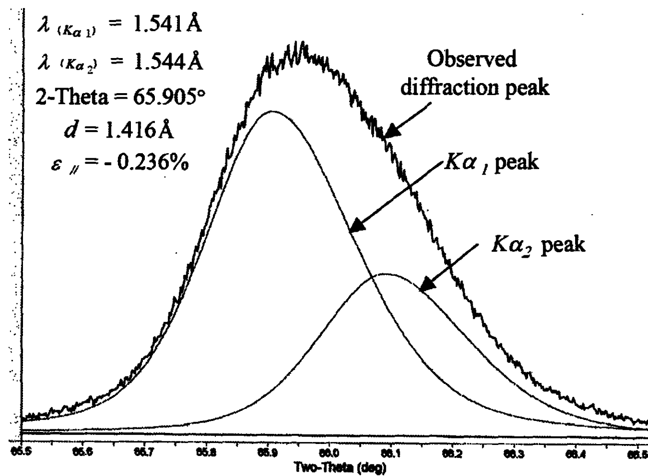

Figure 6.15: X-ray diffraction peak from (100) germanium epitaxially grown at 350°C directly on silicon. It is shown germanium is crystalline even at low growth temperature. The film is compressively strained as much as –0.236%. Measurement courtesy: J. Liu.

A double side polished (DSP) wafer was also put in the process in addition to SOI-PBG to evaluate germanium's optical properties with this layer configuration (poly-Si on LTO on Ge). The evaluation was done using Varian® Cary 5E by checking the reflectance and transmittance for a pure DSP wafer and a poly-Si/LTO/Ge on DSP wafer. Germanium's absorption was obtained by the following procedures.

R_1: = Reflectance of DSP wafer

T_1: = Transmittance of DSP wafer

Then absorption of DSP substrate was obtained from:

$$Abs_{DSP}: = 100\text{-}R_1\text{-}T_1$$

R_2: = Reflectance of poly-Si/LTO/Ge on DSP wafer

T_2: = Transmittance of poly-Si/LTO/Ge on DSP wafer

Then absorption from poly-Si/LTO/Ge layers was obtained from

$$Abs_{Ge}: = 100\text{-}R_2\text{-}T_2\text{-}Abs_{DSP}.$$

Figure 6.15 is an absorption profile from poly-Si/LTO/Ge layers. Absorption is observed below 1700nm, which corresponds to germanium's bandgap ($E_g^{\Gamma} = 0.8eV$)

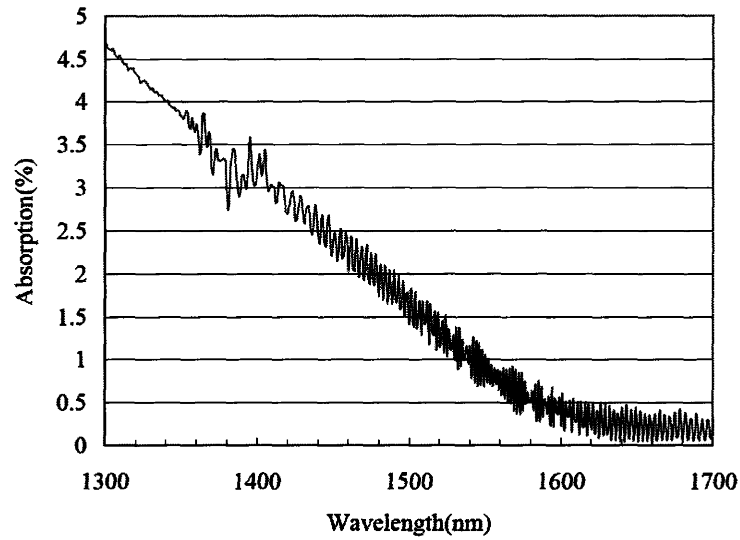

Figure 6.16: Absorption in poly-Si/LTO/Ge layers. Absorption is observed below 1600nm, which corresponds to gemanium's bandgap.

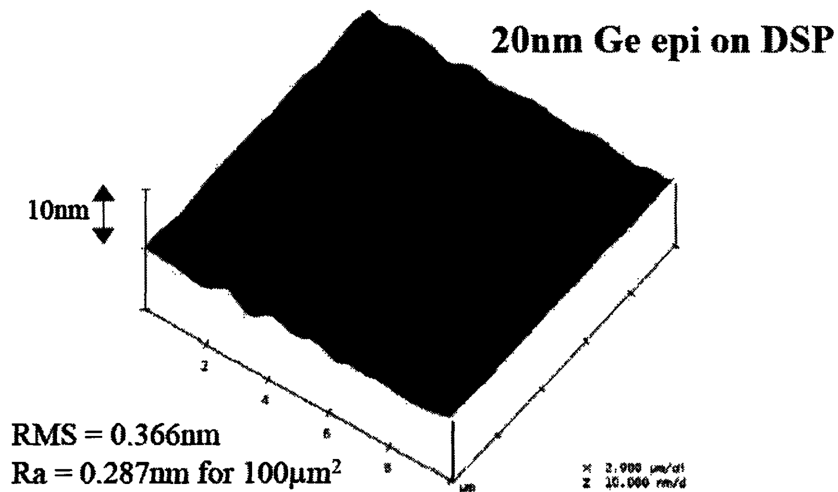

Figure 6.17: AFM image of 20nm Ge on DSP wafer. It is shown that no islanding occurred due to lattice mismatch. It is expected that Ge is amorphous as deposited. No islanding is observed.

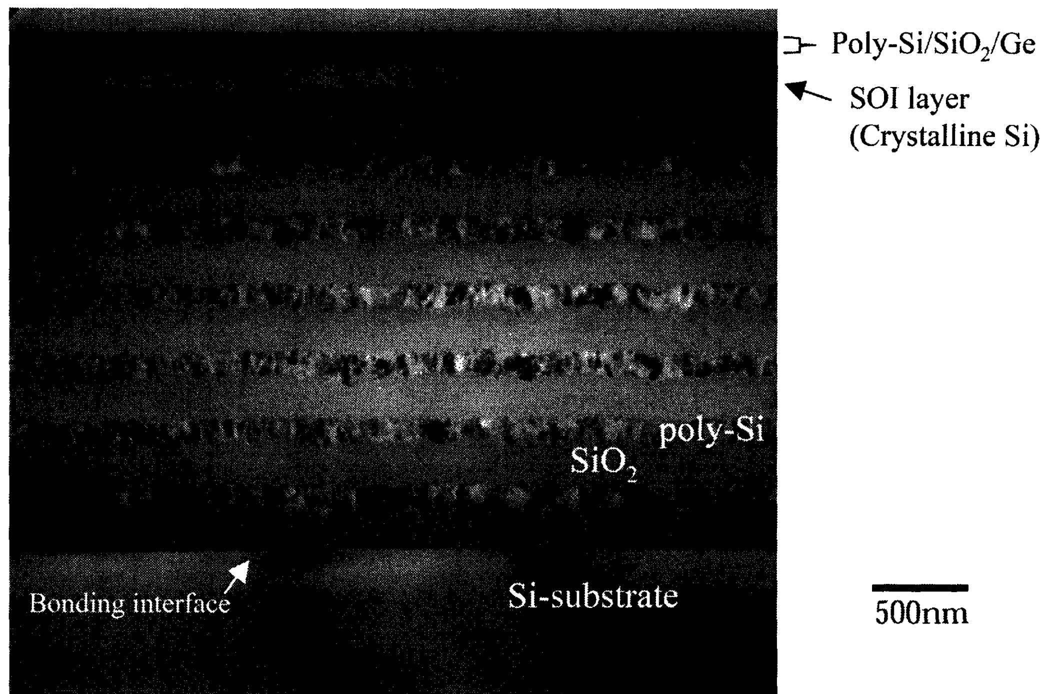

Figure 6.18: Cross sectional TEM image of SESAM. It is shown that roughness is suppressed at the interface between top poly-Si and SiO_2 layers. Courtesy of Dr. T. Abe at Shin-Etsu Handotai. Co., Ltd.

Figure 6.16 is an AFM image for Ge as-grown wafer. Island structures are not observed. Figure 6.17 is a cross sectional TEM image for a fabricated saturable absorber. It is shown that interface roughness is suppressed at the top interface between poly-Si and SiO_2 layers and crystalline silicon is on top of PBG structure.

6.7 Evaluation of Si/Ge SESAM (or Si/Ge SBR)

Since desirable germanium absorption is observed in figure 6.15, the evaluation of PBG-based germanium saturable absorber is discussed hereafter. The germanium absorber layer has a dual functionality: On the one hand, it provides the desired amount of saturable absorption for modelocking the laser: A pulse can saturate and thus reduce the absorption in

this layer, while cw-light undergoes a higher loss. This shifts the equilibrium in the laser toward pulsed operation. On the other hand, the large amount of two-photon absorption (TPA) in this layer can be employed to stabilize high repetition rate lasers against Q-switching [82-87]. Lasers modelocked with a saturable Bragg reflector (SBR) become unstable if the saturable absorber relaxes faster than the gain medium. Since all gain media available for 1550nm lasers have long upper state lifetimes, Q-switching has prevented successful modelocking of very high repetition rate lasers until recently and constitutes a major obstacle to higher monolithic integration of modelocked lasers. However, stable modelocking can be obtained in a high repetition rate laser if TPA is added for stabilization: For very high fluence values, during a Q-switch cycle, TPA in this layer leads to additional loss (inverse saturable absorption) that eventually restores equilibrium. To date, thick TPA layers out of III-V semiconductor material are employed, causing a significant reduction of the optical bandwidth. Alternatively, the SBR is driven with a high fluence leading to heavy thermal loading and a limited device lifetime. Our design addresses both problems since TPA is significantly larger in germanium than in conventional III-V based SBRs ($\beta_{Ge, 1550nm}$=300cm/GW, $\beta_{GaAs, 1550nm}$=60cm/GW) [92-93]. Consequently, stabilization of the laser against Q-switching can be achieved at much lower fluences. While we employ the saturable and inverse saturable absorption of the germanium absorber for laser modelocking and stabilization, in future waveguide devices it paves the way to a variety of nonlinear devices, from optical limiters to nonlinear optical gates.

The Si/Ge-SBR allowed us to obtain the shortest pulse and the broadest spectrum from a bulk modelocked erbium-ytterbium glass laser to date [94]. The phosphate glass Kigre QX/Er co-doped with 7.3e19 Er-ions/cm^3 and 1.8e21 Yb-ions/cm^3 serves as gain medium. It is flat-Brewster polished, coated with a 99.8% high reflector and placed at one

end of the cavity (figure 6.18). The laser, built as an L-cavity, is pumped with a Bookham G07 fiber-coupled 450 mW pump diode, temperature-tuned to 976nm. An anamorphic prism pair provides for the ellipticity of the pump mode in the gain medium (26x40um). Its shape matches the laser mode, which is slightly larger (30x45μm) to obtain small reabsorption losses in the wings and to avoid lasing in higher-order modes. The flat-Brewster cut of the erbium-ytterbium glass permits to vary the insertion of the gain medium. The optimum length of 2mm was used throughout the experiment, yielding an output power of 90 mW and a slope efficiency of 25% when the Si/Ge-SBR and its focussing mirror were replaced with a 2% output coupler. When the SBR forms a cavity end-mirror during modelocking, the 99.8% high reflector deposited on the gain medium acts as an output coupler. Thus, with 99.95% reflecting curved mirrors and the 99.8% reflecting Si/Ge-SBR, the intracavity losses are minimized, and a high intracavity power of 8.7 W is obtained from only 360 mW absorbed pump power. In modelocked state, the laser is pumped 15 times over the threshold of about 25mW. The small amount of intracavity loss results in a highly saturated gain and in a low inversion of the gain medium, which leads to a flat net gain profile. Obtaining a flat gain profile via low inversion is essential for obtaining broad optical spectra in the erbium-ytterbium glass three-level system. Here, unlike four-level systems, the net gain profile depends on the balance of emission and absorption at the laser wavelength and thus varies significantly with the inversion. The low inversion plays the key role for a broad optical spectrum and a short pulse.

We obtaind an optical spectrum of 11.2nm FWHM bandwidth, covering the entire C-band of optical communications at ±10dB level (figure 6.20). After dechirping the pulses extracavity with 1.0m SMF an intensity autocorrelation with 300fs FWHM is measured. Phase retrieval with the Picaso algorithm reveals a pulse width of 216fs, which is to within 10% of the transform limit of the optical spectrum. To our knowledge, this is the shortest

pulse generated in a bulk erbium-ytterbium glass laser in general [94-95], and by far the shortest pulse from this class of laser obtained solely from modelocking it with an SBR [95]. The laser is operated at 169MHz repetition rate with a clean RF spectrum and a noise floor more than 70dB below the signal level. At no level of pump power, Q-switching was observed despite the long upper-state lifetime and the small emission cross section of the gain medium. We attribute the high stability against Q-switching to the large amount TPA in the Si/Ge-SBR. This stability manifests itself also in a small number of relaxation oscillations when the laser is chopped intracavity. By simultaneously measuring output power and the second harmonic intensity of the output beam focused tightly on a silicon photodiode, the modelocking buildup time could be measured to be as short as 65us, corresponding to only 11,000 cavity round trips. To summarize, we have obtained the shortest pulse to date from an erbium-ytterbium glass laser modelocked with a novel Si/Ge-SBR.

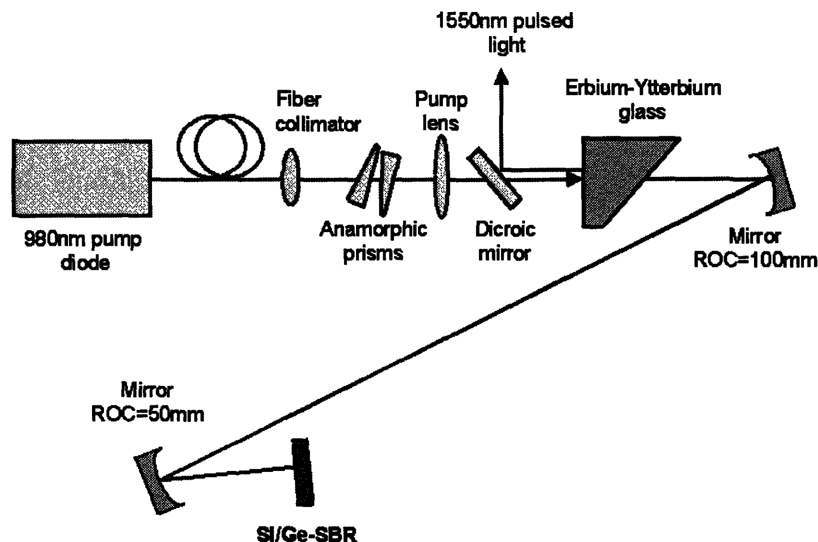

Figure 6.19: The experimental set-up for Erbium-Yitterbium glass laser. Figure courtesy: F. J. Grawert.

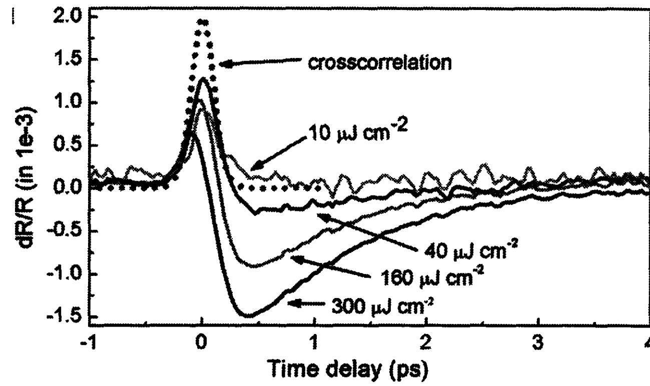

Figure 6.20: Pump-probe traces of the Si/Ge-SBR taken at various fluence values along with the cross correlation of the pump probe laser source. Courtesy of F. J. Grawert.

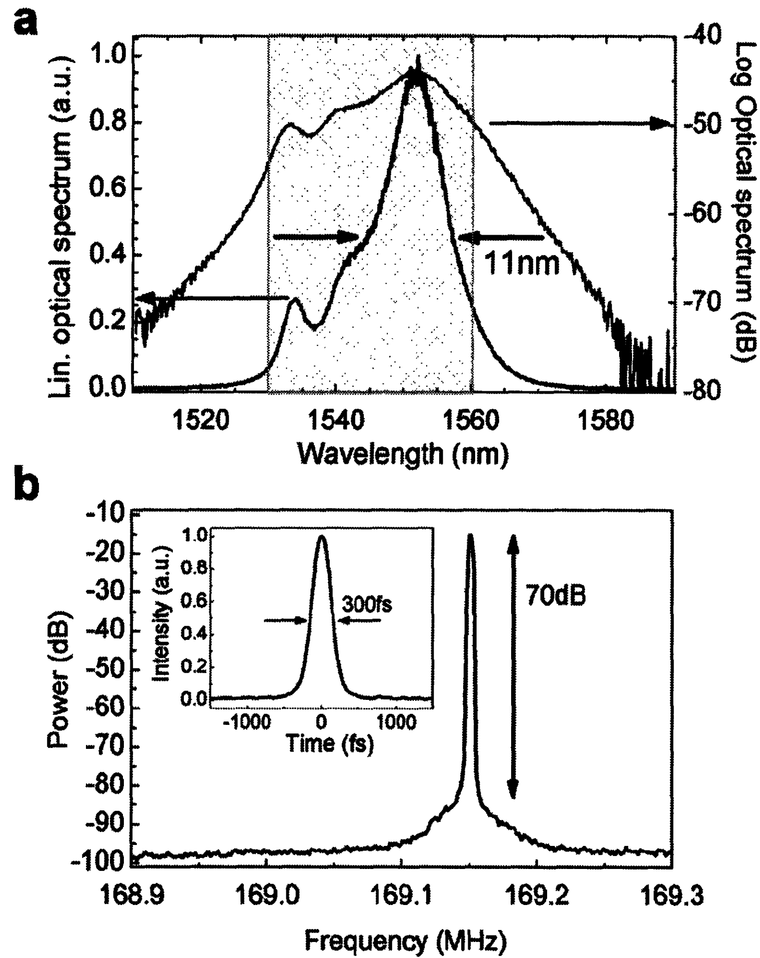

Figure 6.21: Optical spectrum of the Er-Yb:glass laser modelocked with the Si/Ge-SBR on linear and logarithmic scale. Width of the C-band of optical communications (shaded). **b**, RF-spectrum of the laser and autocorrelation (inset). Courtesy of F. J. Grawert.

6.8 Summary

In conclusion, we have developed a fully CMOS-compatible process for fabrication of a silicon/germanium SESAM or SBR, whose nonlinear response has been characterized by pump probe measurements. Our Si/Ge SESAM/SBR showed the shortest pulse generated in a bulk erbium-ytterbium glass. The device has been exploited to attain self-starting operation of a passively modelocked Erbium-Ytterbium:glass laser with an optical spectrum covering the entire C-band of optical communications. We believe that this Si/Ge SESAM/SBR will contribute to the optical communication world by realizing the better performance which has not been achieved by conventional III-V SESAM/SBRs.

Chapter 7: PBG filter for TPV application

7.1 Introduction

This chapter features another PBG application for thermo photovoltaic (TPV) device. PBG is used as a wavelength filter, which is designed to reflect long wavelength (λ > λ_g), which cannot be incorporated to PV cell due to semiconductor's bandgap limitation. TPV is used for a portable electric power such as automobiles, which will experience the new 42V standard instead of conventional 12V standard in the near future [96], or other portable electric generators. It is also useful for cogeneration of electricity/heat or industrial waste heat recapture such as in glass or metals industries [97]. TPV is a static energy converter, which convert thermal radiation from a high temperature heat source to electricity by means of photovoltaic (PV) cell. The differences from a solar cell are that a TPV cell is placed closer to a heat source and the source temperature is much lower, which ranges from 1000 to 1800K whereas that of the sun is approximately 4700K. To work with low temperature heat source, it is necessary to use low bandgap semiconductors such as GaSb (0.73eV:direct), InGaAs (0.36-1.44eV:direct), InGaAsSb (0.36-0.73eV:direct) or Ge (0.66eV:indirect) to achieve acceptable system efficiency and power density. However, the advantage over solar cell is that the close proximity to a heat source and PV cell leads to larger incident radiation flux density. Close proximity of emitter and PV cell allows energy recycling which leads to the improvement of system efficiency. If a photon has smaller energy (λ > λ_g) than the PV semiconductor's bandgap, then it can be reflected back to the heat source (emitter) while incorporating a photon with higher energy (λ < λ_g) than the bandgap, the system efficiency and power density can be significantly improved [97]. In this section, one-dimensional PBG as wavelength filter,

which is placed directly on PV cell to improve the system efficiency and power density, is proposed and. For this application, high index contrast (HIC) PBG is also suitable since the stop-band width depends on index contrast. One dimensional PBG has been widely studied in recent years for the purpose of TPV application. However, materials used in these studies are lower index contrast materials such as ZnS (n=2.4) and MgF_2 (n=1.4), which require 70 layers or more to achieve high reflectance while opposing narrow stop-band [97]. In this chapter, optical characteristics of one dimensional PBG in infrared range is mainly studied by exploring both pass-band and stop-band characteristics. To achieve wider stop-band, Si/SiO_2 are employed as HIC materials. The final goal is to construct HIC PBG, which has the following characteristics.

1. Low process temperature (-700ºC) so that PBG filter can be placed directly on PV cell since melting points of Ge and GaSb are 936°C and 712°C, respectively.
2. CMOS-compatible for mass production and cheaper production cost.
3. High reflectance over stop-band and high transmittance over pass-band to maximize the system efficiency.

7.2 Prior arts

In general, thermo photovoltaic system consists of two major components. Emitter and the PV cell (diode). This section focuses on the one-dimensional photonic crystal wavelength filter, which is placed between emitter and PV cell to improve the efficiency. Figure 7.1 depicts the brief structure of TPV system.

Blackbody radiation from the heat source (emitter) can be expresses as:

$$E = \frac{2\pi hc^2}{\lambda^5\left(exp\left(\frac{hc}{\lambda kT}\right)-1\right)}$$

where E is energy density ($W/m^2/m$), h, c, k and T are Planck constant, speed of light,

Boltzmann constant and temperature (K), respectively.

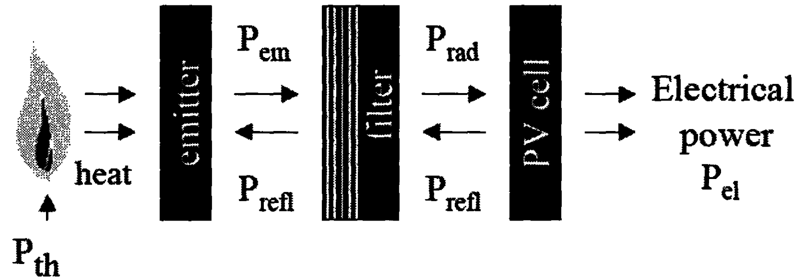

Figure 7.1: Basic scheme of TPV system. This research focuses on the filter performance to improve the total efficiency.

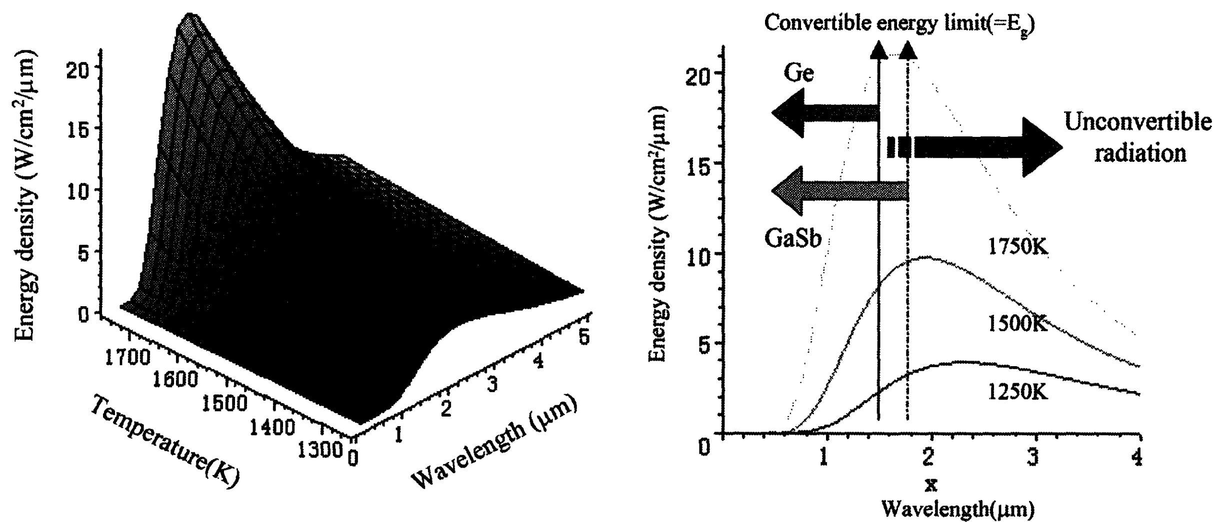

Figure 7.2: (Left): Three dimensional plot of blackbody radiation. As temperature goes up, the peak intensity rises and the peak wavelength shifts to shorter wavelength. (Right): Blackbody radiations from 1250, 1500 and 1750K heat sources. The most of the radiated light is not converted especially at lower temperature.

It is shown in figure 7.2 (right) that the most of the radiated light is not converted due to semiconductor's bandgap limitation. In the case of GaSb cell, 20.6% of the radiated light is incorporated and in the case of Ge cell, only 11.3% is incorporated even at 1500K. These values drop as heat source temperature goes down. Therefore, it is necessary to utilize this unconverted radiation to improve the system efficiency. As a concrete example, it is required to place an optical filter between the emitter and the cell to reflect back radiation

with long wavelength ($\lambda > \lambda_g$) to the emitter to "recycle photons" to improve system efficiency. For filter applications, various filters have been proposed so far such as plasma filter, back surface reflector, and dielectric stacks. The properties of those filters are discussed below.

A. Plasma filter

Plasma filter has been proposed by Coutts et al.[98] as a TPV filter which reflects back long wavelength which does not contribute to the electricity generation. A Plasma filter utilizes plasma resonance with light, which is expresses by the following equation.

$$\omega_p = \sqrt{\frac{ne^2}{m^*}}$$

where ω_p , m^* , n and e are the plasma frequency of semiconductor, an effective mass, electron concentration and electron charge, respectively. The response of the light is as below.

When $\omega < \omega_p$, charge moves faster than light, then light is reflected.

When ω matches plasma frequency ω_p, light is absorbed by resonance.

When $\omega > \omega_p$, charge can not respond to light, then light is transmitted.

Figure 7.3 shows light response depending on the wavelength [98]. From figure 7.3, it is shown that high dopant concentration and high mobility are required to achieve high reflectance and low absorbance. Therefore, CMOS-compatible semiconductors, such as silicon or Ge is not suitable for this filter due to their acceptable dopant concentration and electron mobility (μ_n(Si)<150, μ_n(Ge)<900cm^2/V-sec. when N_D=10^{19}/cm^3 [97]). As a conclusion, it is challenging to integrate this type of filter with TPV cell.

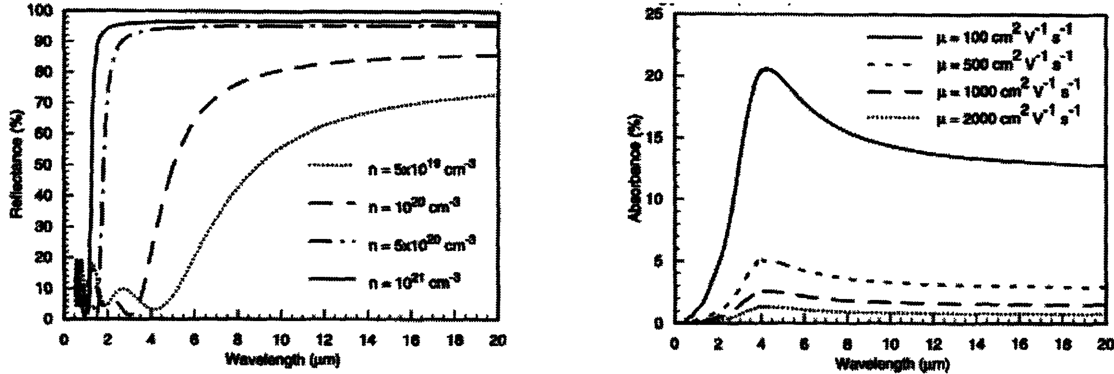

Figure 7.3: Theoretical calculations for plasma filter. Reflectance (left) and absorbance (right) of light depending on wavelength [98]. it is shown that high μ and high doping level are required. 10^{21} cm^{-3} for electron concentration and $1000cm^2/Vs$ for mobility are required for sharp edge and low loss, respectively.

B. Back surface reflector

A highly reflective backside reflector is placed on the backside of PV cell to reflect the incident light where noble metals such as Au or Ag is used since they have very short plasma frequency which leads to the high reflectance for all of infrared light. Figure 7.4 shows the reflectance of the back surface reflector which is made of InP/MgF_2/Ti/Au [100].

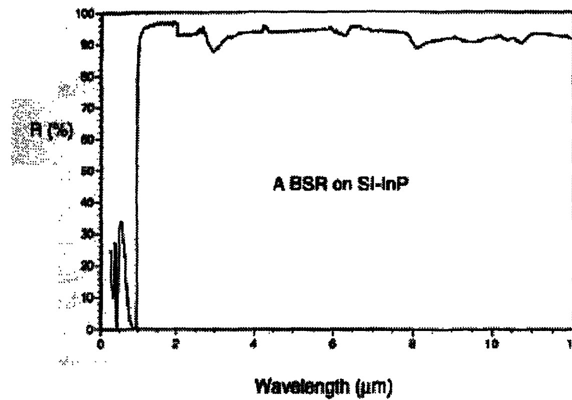

Figure 7.4: Reflectance from InP/MgF_2/Ti/Au backside reflector [100]. This type of reflector shows high reflectance for all of infrared.

However, the semiconductor substrate has to be un-doped to avoid free carrier absorption and the integration with semiconductor PV cell poses significant challenge to minimize

metal contamination from the metal reflector. In addition, series resistance is usually too high unless it has top contacts only [100]. Therefore, the integration of this type of reflector requires un-doped substrate while incorporating metal film beneath the semiconductor cell and also needs advanced top contact designs to suppress top contact series resistance. It can be concluded this type of reflector is not suitable for our purpose.

C. Dielectric stack

A dielectric stack has been proposed for wavelength filter [97]. The dielectric stack is designed so that it can be directly deposited on PV cell. Since high temperature process cannot be employed due to low thermal budget of PV cell, physical vapor deposition (PVD) technique such as sputtering is often used to deposit dielectric stack directly on PV cell. Coutts et al. proposed ZnS (n=2.4)/MgF_2 (n=1.4) dielectric stack which is directly sputtered on PV cell. Transmittance is shown in figure 7.5. However, it is required to deposit more than 70 layers to achieve high reflectance over the stop-band and wide stop-band. Therefore, it is concluded that this is not practical approach as wavelength filter for TPV application.

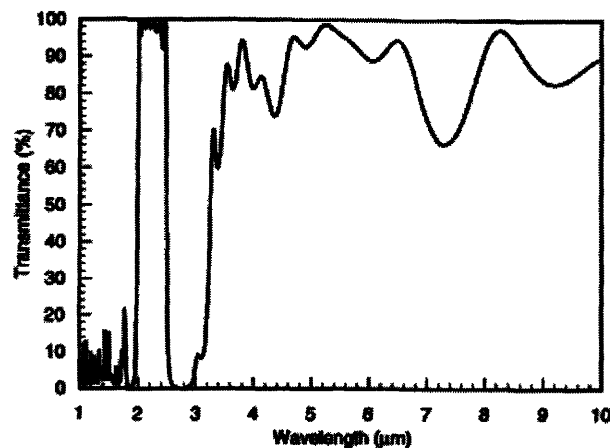

Figure 7.5: Transmittance spectrum for ZnS/MgF_2 dielectric spectrum [97]. The stop-band ranges from 2.6 to 3.2μm.

As a conclusion of prior arts, it seems that there is no ideal wavelength filter, which can be integrated with PV cell using conventional approaches. In this chapter, the combination of high index contrast (HIC) PBG stack as a wavelength filter and Ge PV cell is proposed. Since Ge has higher melting point (938 ° C) as compared to other small-bandgap semiconductors, direct deposition on PV cell using conventional CMOS techniques can be employed.

7.3 TPV system modeling

As is shown in figure 7.1, TPV consists of three components, the emitter, the filter and PV cell (diode). The emitter is a blackbody source with refractive index n_{BB} and it is assumed that the diode is made of Ge whose refractive index and electronic bandgap are 4.0 and 0.8eV, respectively. The role of PBG stack directly deposited on PV cell is to incorporate all the photons with energies above E_g to the diode and reflect back all the photons with energies below E_g while minimizing absorption by PBG filter itself.

When the emitter is a blackbody with temperature T_{BB}, the amount of the power radiated to the diode can be obtained using the thermodynamic model as [101-103],

$$P_{rad} = \int_0^{\infty}\int_0^{\theta_1} \frac{n_{BB}^2\omega^2}{(2\pi)^2c^2}\frac{\hbar\omega}{exp\left(\frac{\hbar\omega}{kT_{BB}}\right)-1}T_{13}(\omega,\theta)\cos\theta\sin\theta\,d\theta\,d\omega$$
$$-\int_0^{\infty}\int_0^{\theta_3} \frac{n_{PV}^2\omega^2}{(2\pi)^2c^2}\frac{\hbar\omega}{exp\left(\frac{\hbar\omega-eV}{kT_{PV}}\right)-1}T_{31}(\omega,\theta)\cos\theta\sin\theta\,d\theta\,d\omega \quad -(1)$$

where c is the speed of light, h is Planck constant, k is Boltzmann constant, T_{PV} is the diode temperature, n_{BB} and n_{PV} are the blackbody temperature and diode refractive indices, respectively. $T_{13}(\omega,\theta)$ is the sum of TE and TM mode transmittance from blackbody to

diode, $T_{31}(\omega,\theta)$ is the sum of TE and TM mode transmittances from diode to blackbody, θ is the incident angle of radiation from blackbody source, θ_1 =arcsin(n_{PV}/n_{BB}) for $n_{PV} < n_{BB}$ and $\theta_1 = \pi/2$ otherwise, θ_3 = arcsin(n_{BB}/n_{PV}) for $n_{PV}>n_{BB}$ and $\theta_3 = \pi/2$ otherwise. The first term in the above equation represents the total power transferred from the blackbody to the diode and second term represents the power reflected back from the diode to the emitter. The equation can be also expressed as:

$$P_{rad} = \int_0^{\infty} \frac{n_{BB}^2\omega^2}{(2\pi)^2c^2} \frac{\hbar\omega}{exp\left(\frac{\hbar\omega}{kT_{BB}}\right)-1} \overline{T_{13}}(\omega)d\omega - \int_0^{\infty} \frac{n_{PV}^2\omega^2}{(2\pi)^2c^2} \frac{\hbar\omega}{exp\left(\frac{\hbar\omega - eV}{kT_{PV}}\right)-1} \overline{T_{31}}(\omega)d\omega \quad \text{-(2)}$$

where

$$\overline{T_{13}}(\omega) = \int_0^{\theta_1} \{T_{13TE}(\omega,\theta) + T_{13TM}(\omega,\theta)\} cos\theta\, sin\theta\, d\theta \quad \text{-(3)}$$

T_{13TE} and T_{13TM} are TE and TM mode transmittances, respectively. These are the functions of the frequency ω, incident angle θ, and the gap length L_0. The above equation is interpreted as the mean transmittance from the diode to the emitter. Accordingly, the total electrical power generated in the photodiode is calculated as follows:

$$P_{PV} = eV\left\{ \int_{\omega_g}^{\infty} \frac{n_{BB}\omega^2}{(2\pi)^2c^2} \frac{1}{exp\left(\frac{\hbar\omega}{kT_{BB}}\right)-1} - \int_{\omega_g}^{\infty} \frac{n_{PV}^2\omega^2}{(2\pi)^2c^2} \frac{1}{exp\left(\frac{\hbar\omega - eV}{kT_{BB}}\right)-1} \overline{T_{31}}(\omega)d\omega \right\} \quad \text{-(4)}$$

Efficiency is obtained using these equations as:

$$\eta_{TPV}(T_{BB}, \omega_g, T_{PV}, V) = \frac{P_{PV}(T_{BB}, \omega_g, T_{PV}, V)}{P_{rad}(T_{BB}, \omega_g, T_{PV}, V)} \qquad -(5)$$

From the above equation, it is obvious that the system's power density and efficiency depends on $\bar{T}_{13}$ and that the system performance can be improved by optimizing $\bar{T}_{13}$. In this chapter I characterize the PBG performance not only with reflectance but also with diode power density and diode efficiency which is expressed in equation (5). Additionally, the spectral efficiency, which is used to evaluate a figure of merit for PBG filter performance, is expressed as [101-103]:

$$\eta_{spectral}(T_{BB}, \omega_g, T_{PV}) = \frac{\int_0^{\omega_g} \frac{n_{BB}^2\omega^2}{(2\pi)^2c^2} \frac{\hbar\omega}{exp\left(\frac{\hbar\omega}{kT_{BB}}\right)-1} \overline{T_{13}}(\omega)\, d\omega}{\int_0^{\infty} \frac{n_{BB}^2\omega^2}{(2\pi)^2c^2} \frac{\hbar\omega}{exp\left(\frac{\hbar\omega}{kT_{BB}}\right)-1} \left(1-\overline{R_{13}}(\omega)\right) d\omega} \qquad -(6)$$

where $\bar{R}_{13}(\omega)$ is the mean reflectance of the PBG filter defined similarly as is Eq.(3). The spectral efficiency, as is defined in Eq.(6), gives the ratio of the above bandgap transmitted power to the total emitted power that reaches the diode-filter system. Ideal properties of PBG filter are:

$$\begin{aligned} \overline{T_{13}} &= 1 \; for \; \omega > \omega_{gap} \\ \overline{T_{13}} &= 0 \; for \; \omega < \omega_{gap} \end{aligned} \qquad -(7)$$

In this case, the spectral efficiency of PBG filter would be 1. The PBG filter is placed to maximize the TPV system efficiency.

7.4 PBG filter designing and fabrication

The basic principle of photonic crystal is explained in the precious chapters. Basic strategy is just to stack $\lambda/(4n_{L\ or\ H})$ thick layers alternatively. Silicon and SiO_2 are chosen as high index contrast material. Due to the huge index difference (Δn=2.0), wide stop-band and high reflectance can be expected. Central wavelength (λ_c) is set at 2.0μm and the target thickness of silicon and SiO_2 are 170nm and 340nm, respectively. One of the most important process parameters is process temperature. This PBG filter is designed to be deposited directly on PV cell, therefore, the process temperature is minimized while maintaining high film quality and CMOS compatibility. For GaSb or Ge PV cell, the maximum process temperature has to be suppressed below 650°C and 750°C, respectively not to disturb the dopant distribution and to avoid device degradation [97]. The process described in figure 7.6 is proposed to achieve high PBG performance and maintain CMOS batch process.

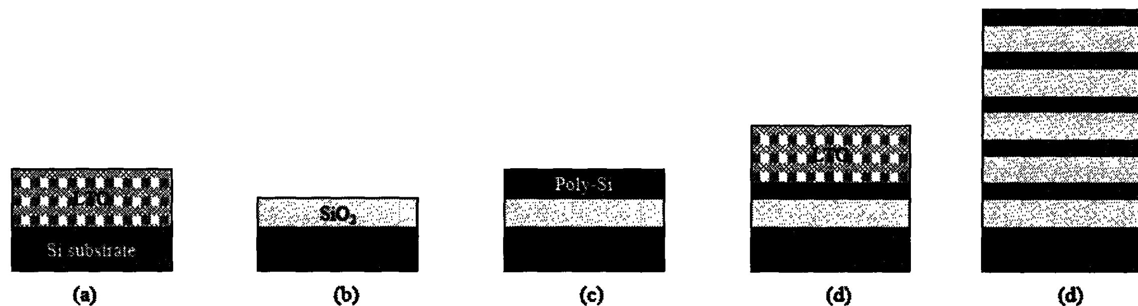

Figure 7.6: Process scheme for TPV PBG filter (not to scale). All steps are done using conventional CMOS processes. Films are deposited on both sides of the wafer actually.

(a): Deposit LPCVD low-temperature-oxide (LTO) at 400C under 200mTorr using SiH_4 xx sccm and O_2 xx sccm as reaction gases. LTO is not SiO_2 in terms of stoichiometry and is oxygen-rich oxide as deposited.

(b): LTO is consolidated by 650C N_2 annealing for 3hours. This time, the LTO layer shrinks due to oxygen out-diffusion. Silicon layer beneath LTO is slightly oxidized by excess oxygen in LTO.

(c): Poly-Si is deposited at 625C under 200m Torr using SiH_4 xx sccm as a reaction gas.

(d): Repeat steps (a)-(c).

The deposition rates for poly-Si and LTO are approximately 98A/min. and 58A/min., respectively.

Figure 7.7 is a cross sectional TEM picture for 5pair-PBG. It can be seen that fabrication was done as expected and flat and uniform layers are achieved. Figure 7.8 is the experimental reflectance results for 3, 4 and 5pair-PBGs. For absolute reflectance measurement, Varian Cary-5E was used. From figure 7.8, it is shown that even with 3pairs, high reflectance as much as 98.5% is realized due to high index difference between Si and SiO_2.

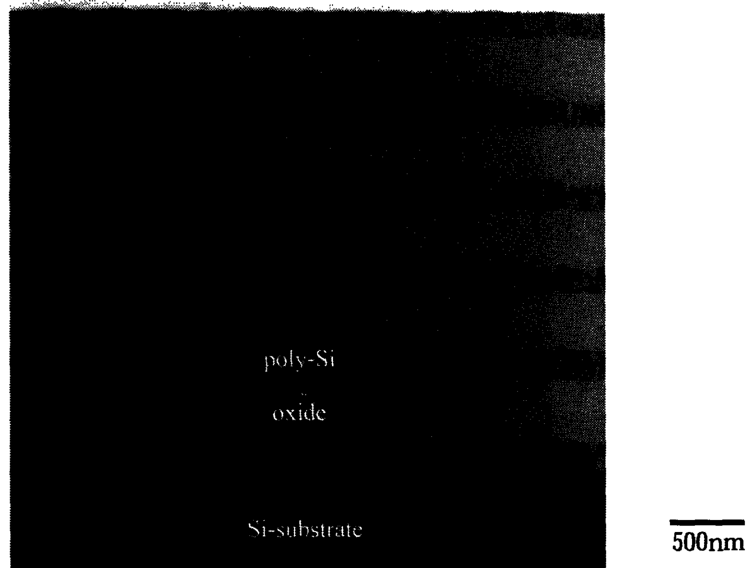

Figure 7.7: Cross sectional TEM picture for 5pair-PBG.(Courtesy of Dr. T.Abe at Shin-Etsu Handotao Co.,Ltd.)

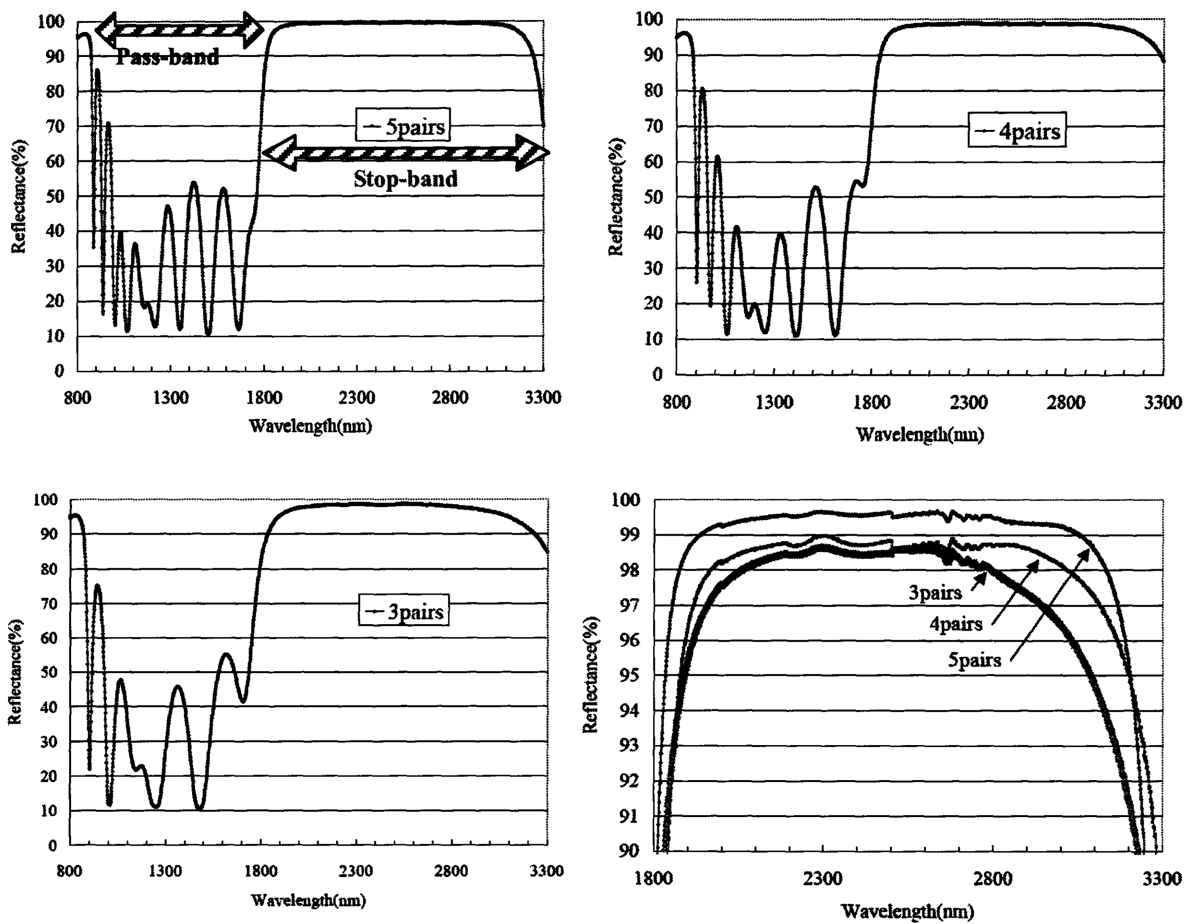

Figure 7.8: Reflectance of 5pair-PBG (Top-left), 4pair-PBG (Top-right), 3pair-PBG (Bottom-left) and Comparison of 3 PBGs over the stop-band.

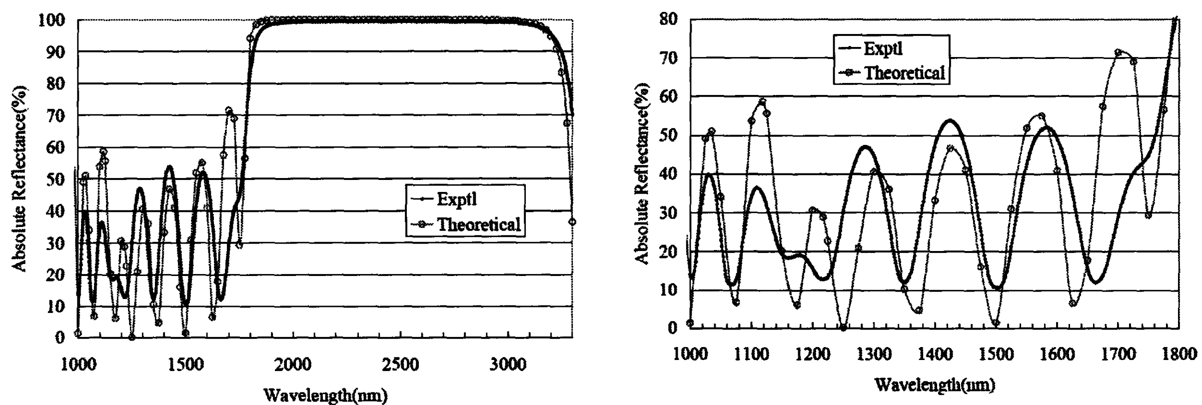

Figure 7.9: A Comparison between theoretical and experimental reflectance. (Left): Pass-band and stop-band and (right): Pass-band. It is shown that both theoretical and experimental reflectance fairly matches each other.

Figure 7.9 is a comparison between theoretical and experimental reflectance. It is shown the experimental reflectance qualitatively matches theoretical one. For theoretical reflectance simulation, the propagation matrix approach was employed, which is described in chapter 4.

7.5 Anti-reflection coating (ARC) for pass-band

As is shown in figure 7.9 (right), there are several photonic states over the pass-band, which ranges from 1000nm to 1700nm. These photonic states degrades the system efficiency as shown in equations (6) and (7) since the system efficiency depends on $\bar{T}_{13}$ in equation (7) which has to be 1 ideally. In the above case, light transmission over the pass-band (1000-1750nm) is 70.51%. To understand what is happening inside PBG stack at these wavelengths, theoretical analysis was carried out. Figure 7.10 is a theoretical reflectivity of 5pair-Si/SiO_2 PBG whose center wavelength is 2.1μm.

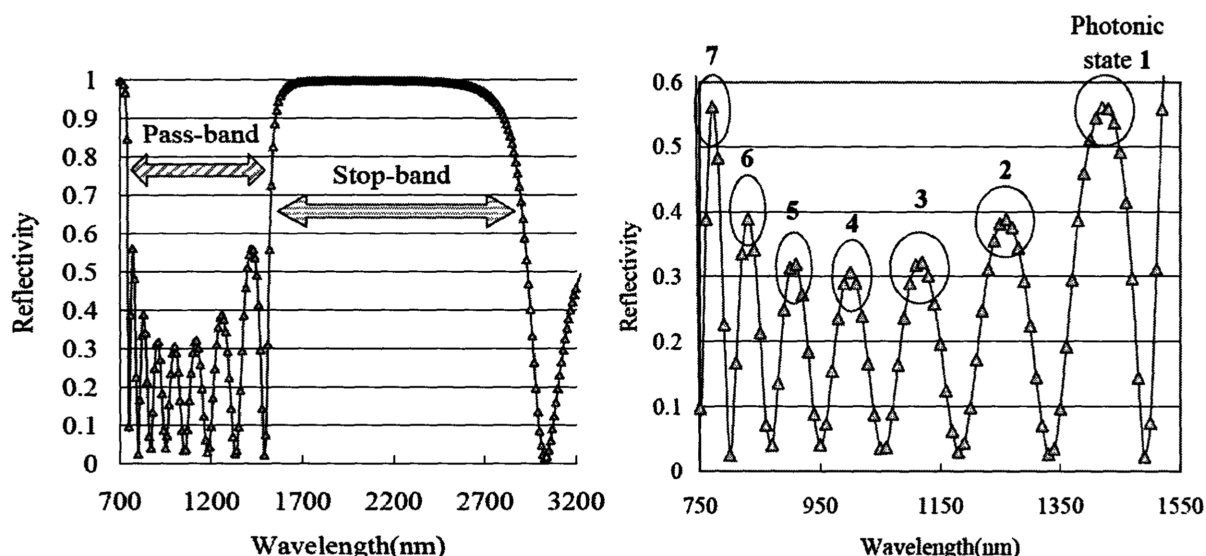

Figure 7.10: Theoretical reflectivity of 5pair-Si/SiO_2 PBG. (Left): Pass-band and stop-band and (right): pass-band where seven photonic states exist.

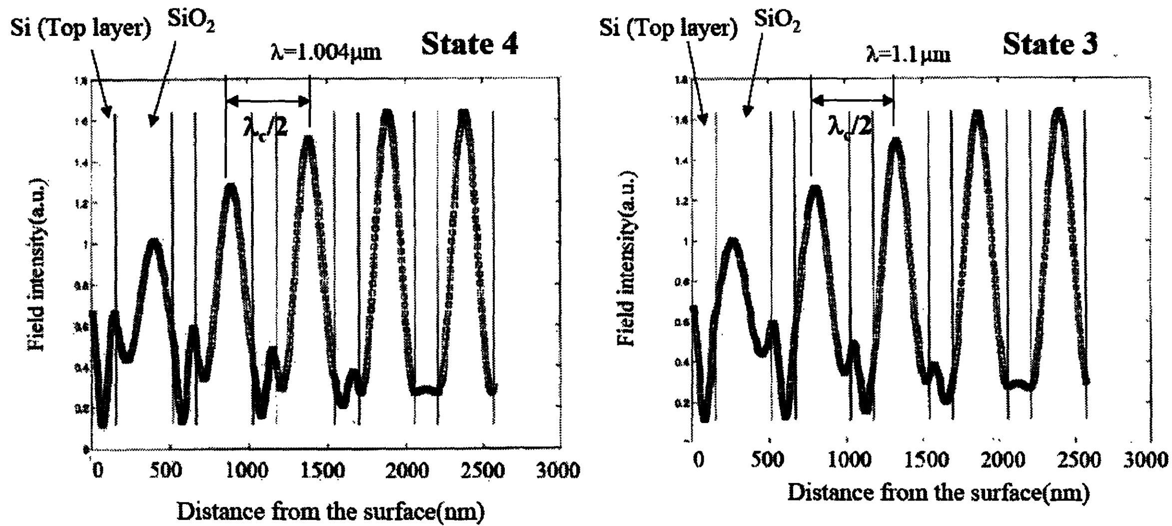

Figure 7.11: Filed intensity distribution inside PBG layers with state 4(left: λ=1.004mm) and state 3(right: λ=1.1mm). It is shown that standing waves are formed with λc/2 period in both cases.

Figure 7.11 shows that how the standing waves are formed inside PBG layers at photonic states 3 and 4 as examples. For both states, standing waves have the period of $\lambda_c/2$. For other states, similar standing waves are observed. Therefore, it is expected to be effective to put anti-reflection coating (ARC) centered on pass-band according to the following equations.

$(\lambda_c/2)/4 = \lambda_c/8$ *thick ARC layer on top with*

$n_{ARC} = \sqrt{n_{top\,(Si)} \times n_{air}}$ *to satisfy impedance matching condition*

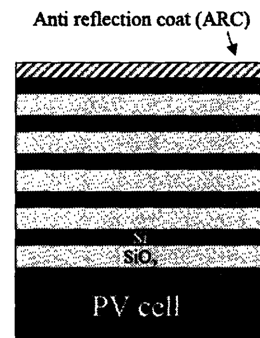

In this case, n_{ARC} = 1.87. Figure 7.12 is the theoretical calculation results for reflectance with ARC. As shown in figure 7.12, the light transmittance over the pass-band is improved

from 76% to 89%.

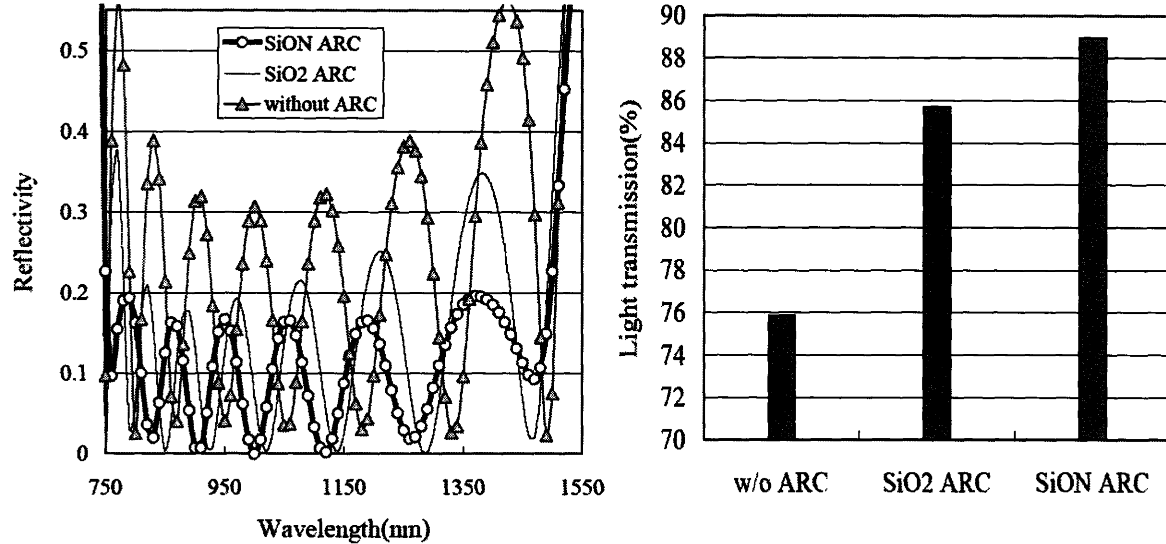

Figure 7.12: Theoretical simulation results for PBG with and without ARCs. It is shown that transmission over the pass-band is improved by adding ARC on top.

7.6 ARC fabrication and evaluation

For SiO_2 ARC, densified LTO was used as in PBG fabrication process. For SiON ARC, PECVD technique was employed. Applied Materials high density (HD) PECVD system Centura was used. To obtain n_{ARC}=1.87, SiH_4 221sccm, N_2O 44sccm and N_2 4200sccm were used as precursors. The RF source power was 575. The deposition rate is 5340Å/sec. The obtained thickness and refractive index at 633nm are 0.188μm and 1.867, respectively. The refractive index is expected to be 1.864 at 2.1μm. TEM pictures for PBG with SiO_2 ARC and SiON ARC are shown in figure 7.14. It is shown in figure 7.14 that both ARCs are on top of PBG. For PBG pass-band, which ranges 1.0 to 1.7μm, the experimental transmission for w/o ARC, w/ SiO_2 ARC and w/ SiON ARC are 70.51%, 87.77% and 95.81%, respectively as shown in figure 7.13.

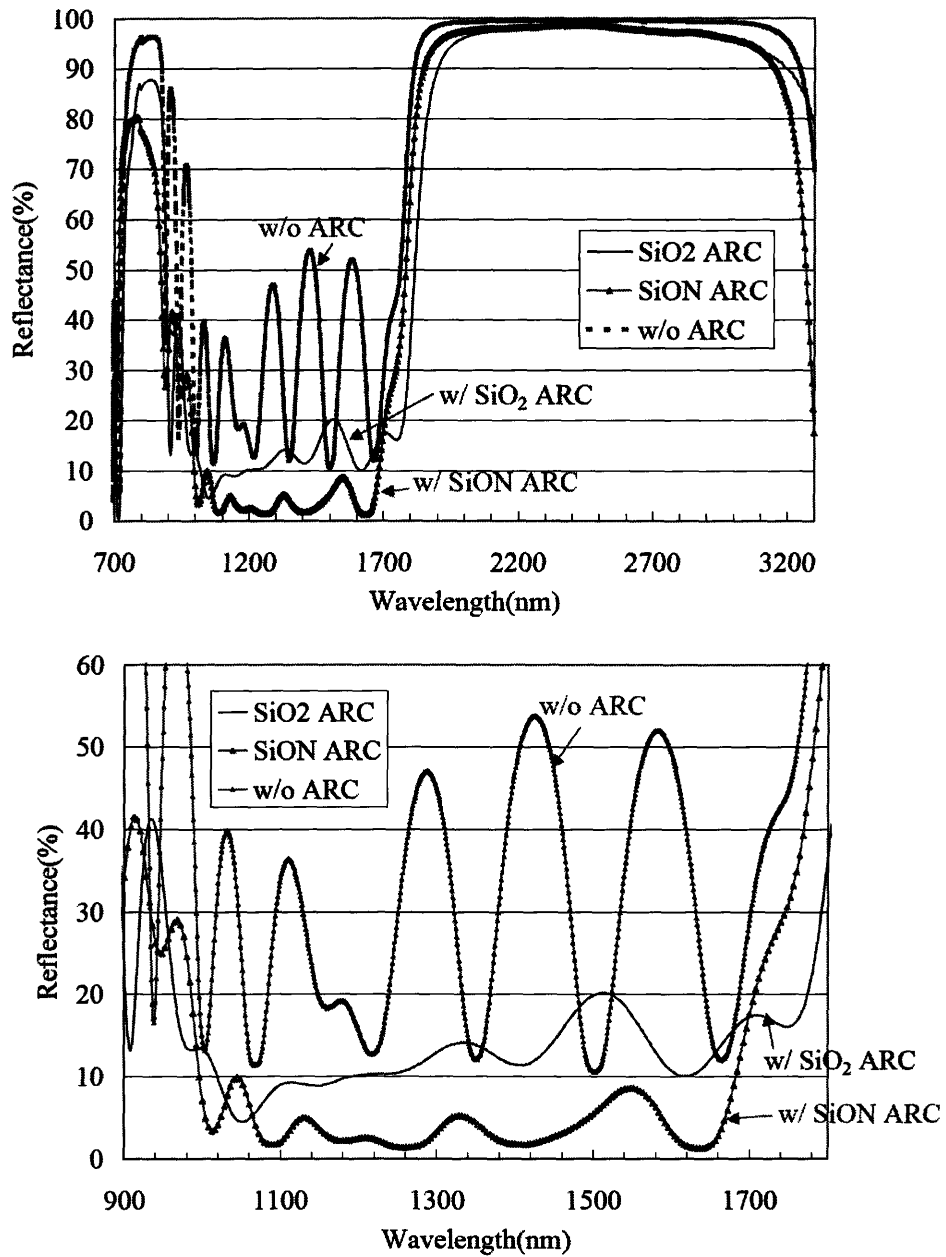

Figure 7.13: Reflectance spectrum for PBGs with and without ARC. It is shown that photonic states are suppressed by adding ARC layers.

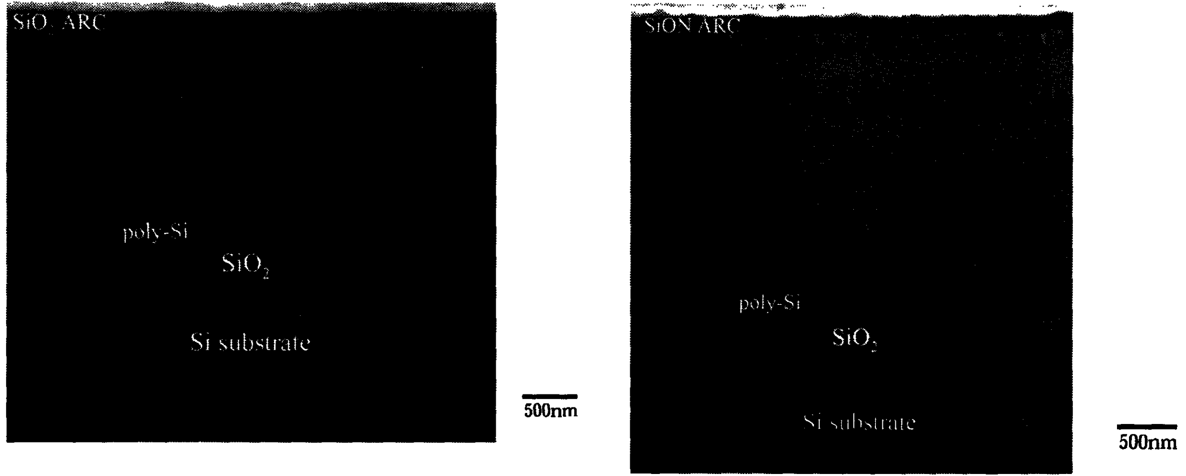

Figure 7.14: Cross sectional TEM images of PBGs with ARC. (Top) 4pair-PBG with SiO_2 ARC and (Bottom) 5pair-PBG with SiON ARC. Courtesy of Dr. T. Abe Shin-Etsu Handotai Co.,Ltd

7.7 System efficiency improvement by PBG filter

Total system schematic is shown in figure 7.15. To determine total system efficiency, many factors have to be taken into account such as emitter and cell temperatures, photon recycling loss, responsivity of the cell, pass-band transmission in PBG filter and so on. System efficiency can be obtained using Eqns (5-6). By adding responsivity (*R*) of the cell and photon recycling loss (L), the total system efficiency can be approximated using a geometrical series as:

$$\eta\ (efficiency) = R \times \left(\frac{\int_0^{\lambda_g} Tr(\lambda) I(\lambda,T)\, d\lambda}{\int_0^{\infty} I(\lambda,T)\, d\lambda} \right) \times \frac{r}{1-r} \qquad \text{-(8)}$$

$$where\ r := (1-L) \times \left(1 - \frac{\int_0^{\lambda_g} Tr(\lambda) I(\lambda,T)\, d\lambda}{\int_0^{\infty} I(\lambda,T)\, d\lambda} \right) \qquad \text{-(9)}$$

where $Tr(\lambda)$, $I(\lambda,T)$, R and L denote the transmission of PBG filter below λ_g, blackbody

radiation(energy density from emitter) and photon recycling loss, respectively. It is assumed that the radiation with $\lambda > \lambda_g$ is reflected by cascading PBG stacks with different center wavelengths. Ideally, photons are recycled permanently until they are incorporated into the PV cell, however, there should be some inevitable loss during photon recycling. In figure 7.17, the photon recycling Loss (*L(%)*) is varied from 10-100%.

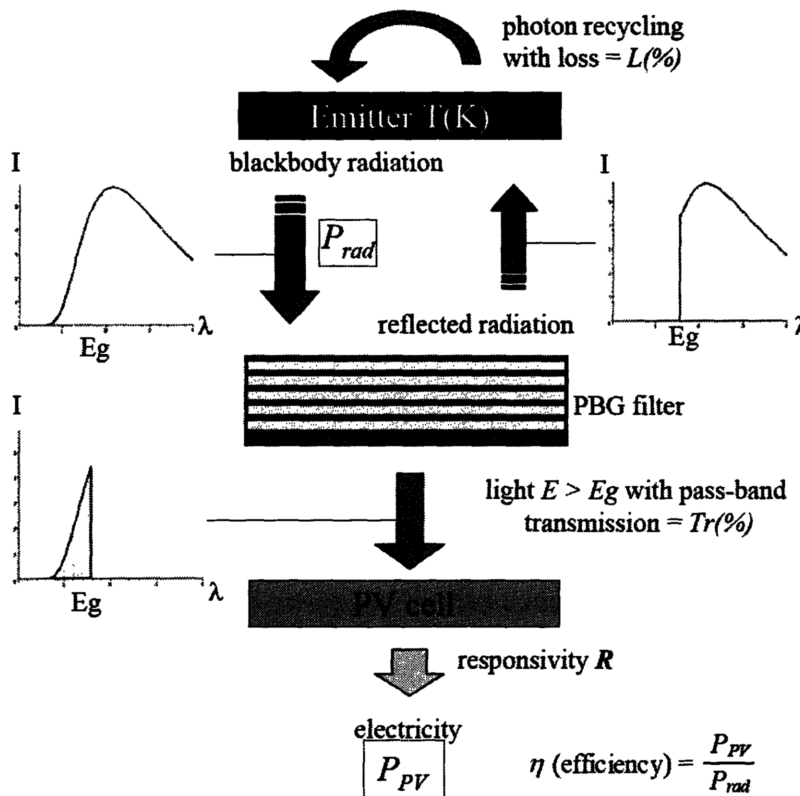

Figure 7.15: TPV system schematic. The factors which determine the system efficiency are mainly emitter temperature *T(K)*, *L*, *Tr*, and *R*.

For responsivity *R*, it was reported that epitaxially grown Ge directly on Si substrate using the technique developed at Professor Kimerling's group at M.I.T. shows higher responsivity than theory even when applied bias is zero [104] due to film strain. *R* was set at 0.90 tentatively hereafter.

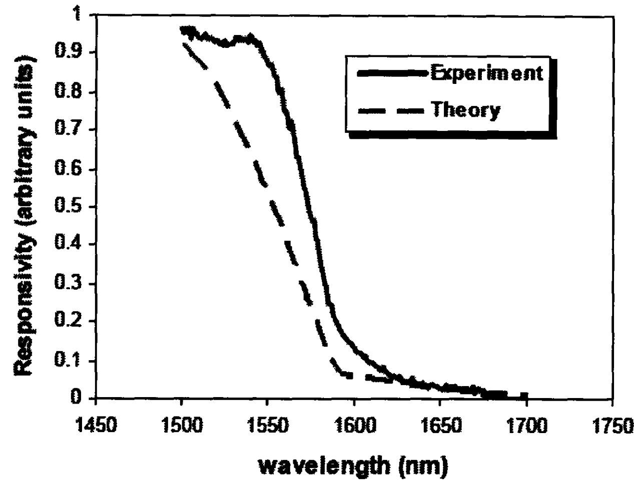

Figure 7.16: Experimental responsivity of Ge epitaxially grown directly on Si substrate reported by Cannon et. al. [89].

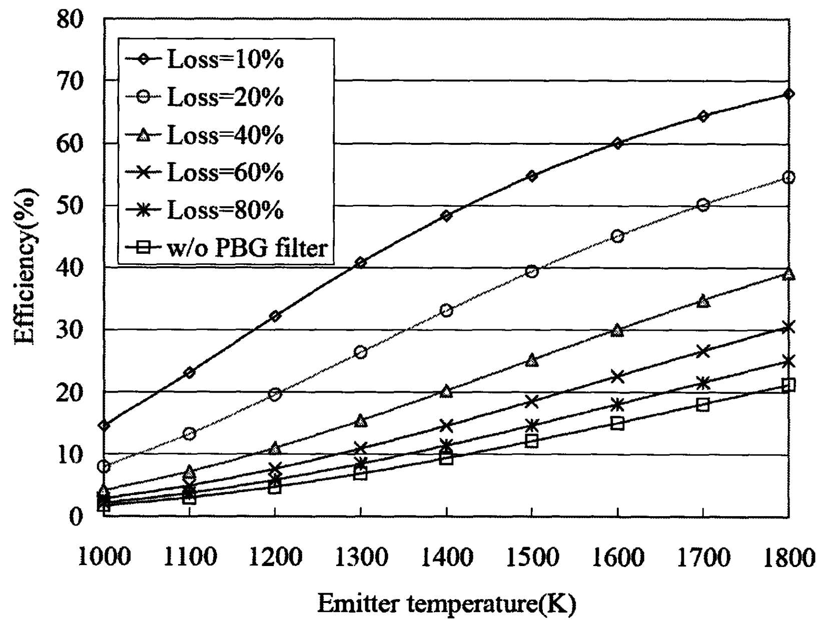

Figure 7.17: System efficiency depending on emitter temperature and photon recycling loss. It is shown that higher efficiency can be expected by adding PBG filter and realizing low-loss photon recycling.

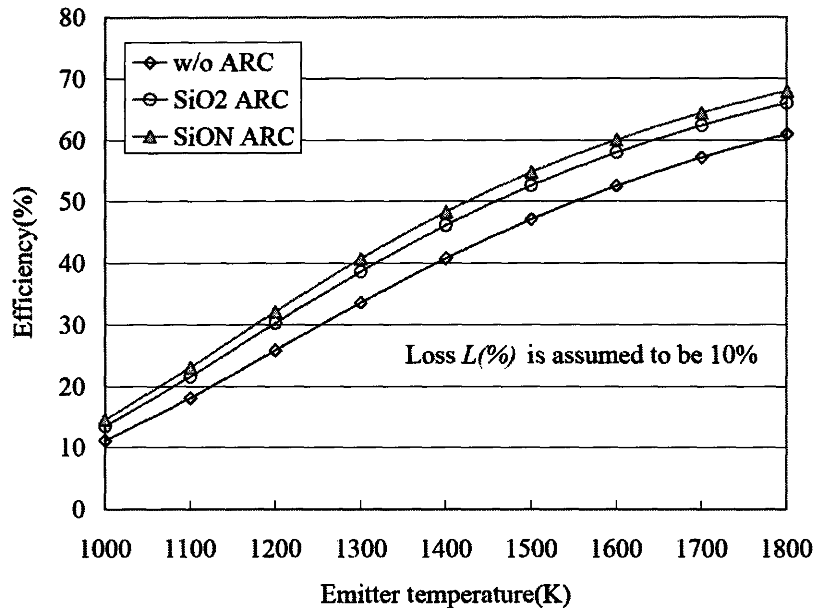

Figure 7.18: System efficiency with and without Anti reflection coatings(SRCs). It is shown that efficiency is improved by adding ARCs.

7.8 Discussion and summary

From figures 7.17 and 7.18, it is shown that the most effective way to improve the efficiency is to raise the emitter temperature. However, this is limited by the system configuration or working environment depending on applications. Other ways to achieve higher efficiency are to reduce the photon recycling loss and add ARC on the top of PBG filter. As an example, in the case of L=10% and $T(K)$=1200K, the efficiency is drastically improved from 5% to 32% although this is almost an ideal case. In addition to employing PBG filter, it is also important to select the materials for emitter and contact on the cell, to develop germanium PV cell with high responsivity, and to design the whole system. It is desirable for emitter and PV cell to have large area and to be placed in parallel to each other to interchange photons between them effectively. By cascading rectangular parallelepiped

TPV units as shown in figure 7.20, the system can have large area for both emitter and PV cell and can share cooling system (liquid or air) with neighboring unit. The detail has to be changed according to the required performance or applications.

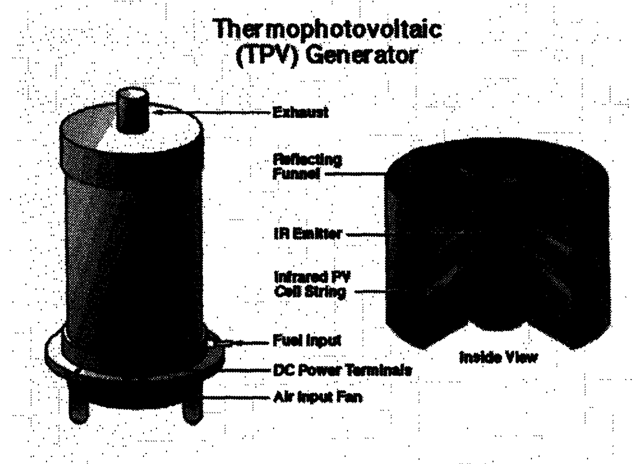

Figure 7.19: A conventional TPV generator [97]. It usually has a cylindrical shape.

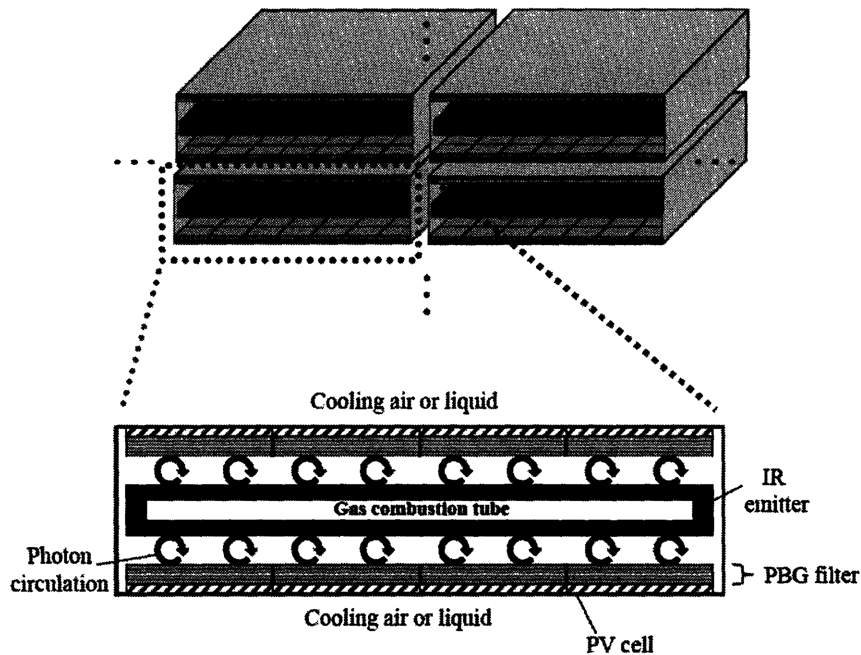

Figure 7.20: A proposed configuration of TPV cell. Unit cells are cascaded to share cooling system and both emitter and PV cell have large area and are placed parallel to each other for effective photon interchange.

With conventional III-V semiconductors, such as GaAs, the configuration shown in figure 7.20 is almost impossible since the system requires PV cells with large area. Only by employing Ge PV cell, which is directly grown on Si wafer, which is as large as 300mm in diameter, and PBG wavelength filter, this configuration can be realized. The combination of Ge cell on Silicon and PBG filter with the system configuration shown in figure 7.20 may open the new realm to TPV application in addition to automobile industry [105].

Chapter 8: Summary and Future Work

I have presented six applications based on high index contrast optical platform. All of these examples can be applied to commercial applications since all of these are based on mature CMOS-compatible technologies. I would like to challenge to commercialize these applications by sophisticating fabrications techniques and improving design parameters. In this thesis, I have mainly focused on integrated photonics and telecommunication and energy applications. It is expected that all of these will be promising field and I hope I can contribute to this future opto-electronics world by using the approaches described in this thesis.

For chapter 2 (HIC waveguide), it is required as a future work to reduce sidewall roughness to suppress total propagation loss. And it is also important not only to suppress the loss but also to maintain high aspect ratio during dry etching process to achieve coherent coupling with ring resonators for WDM applications.

For chapter 3 (AT waveguide), it is necessary to realize a WDM component such as arrayed waveguides (AWGs) to compete with HIC waveguide. For HIC waveguides, ring resonators can be used for WDM application. In addition, other applications can be realized using air trench structures, such as air trench waveguide amplifier by integrating long AT waveguide on a small chip, or polarization filter using high AT waveguide with high aspect ratio.

For chapter 4 (PBG waveguide), it is required to improve the fabrication process to improve the performance. By using PBG waveguide, various applications can be realized due to its unique properties. Especially, its large core size realizes easy fiber/waveguide alignment and this may open new applications of PBG waveguide, such as the combination with (plastic optical fiber) POF and other various fibers.

For chapter 5 (Vis-PBG), it was shown that it is possible to achieve good performance even with Si/SiO_2 platform for this wavelength. In this chapter, we focused on visible wavelength, however, it is also possible to apply this PBG to 650/850nm optics and other applications. Since this PBG is strongly related to man-to-machine interface, various applications can be expected.

For chapter 6 (NIR-PBG: Si/Ge saturable absorber), we first demonstrated CMOS-compatible Si/Ge saturable absorber and it showed the world-record performance from Yb/Eb glass laser. As a future work, it is necessary to fully optimize the designing parameters, especially Ge growth conditions since it is the most important parameter to improve the performance. The stress control is also considered to be important to achieve the satisfactory absorption in Ge layer.

For chapter 7 (MIR-PBG: TPV wavelength filter), we showed that PBG filer works well for this application. Next goal is to integrate with Ge PV and to prove the actual system efficiency improvement. The combination of PBG filter and Ge PV cell can contribute to new applications of TPV devices.

Appendix A: Basic Waveguide Theory

A.1 Waveguide structure

In this chapter, the basic waveguide designing theory, which is used for the following chapters, is discussed. The discussion is mainly based on well-written references [103-104]. Dielectric optical waveguides consist of core and cladding, where the core index (n_{core}) is higher than the cladding index (n_{clad}). The light is guided by total internal reflection where the light is confined in higher index region. The critical condition for the total internal reflection is given by:

$$\theta \leq \sin^{-1}\sqrt{n_1^2 - n_0^2} \equiv \theta_{max} \quad \text{-(1)}$$

If low index contrast platform, where Δn ranges up to 0.01, is assumed, eqn.(1) is approximated as:

$$\theta \cong \sqrt{n_1^2 - n_0^2} \quad \text{-(2)}$$

where θ_{max} denotes the numerical aperture (NA), the maximum light acceptance angle. The normalized refractive index difference (Δ) is defined by:

$$\Delta = \frac{n_1^2 - n_0^2}{2n_1^2} \cong \frac{n_1 - n_0}{n_1} \quad \text{-(3)}$$

And NA is also expressed as:

$$NA = \theta_{max} \cong n_1\sqrt{2\Delta} \quad \text{-(4)}$$

A.2 Concept of guided modes

Even if the angle is smaller than ϕ, light rays cannot propagate with arbitrary angle. Figure A.1 shows light rays and their phase fronts in the slab waveguide. The propagation

constants along z and x (lateral direction) are given by:

$$\beta = kn_1 cos\ \phi$$
$$\kappa = kn_1 sin\ \phi \quad -(5)$$

The reflection coefficient of the light, which is assumed to be polarized perpendicular to the incident plane, is given by [103],

$$r = \frac{A_r}{A_i} = \frac{n_1 sin\ \phi + j\sqrt{n_1^2 cos^2\phi - n_0^2}}{n_1 sin\ \phi - j\sqrt{n_1^2 cos^2\phi - n_0^2}} \quad -(6)$$

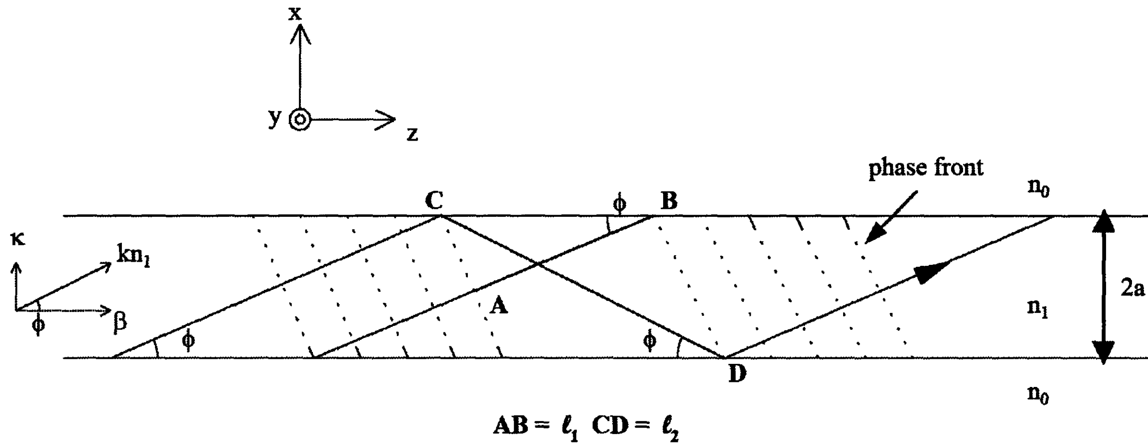

Figure A.1: Light rays and phase fronts in the slab waveguide

ϕ is the phase shift and it is described using eqn. (3) as:

$$\phi = -2tan^{-1}\frac{\sqrt{n_1^2 cos^2\phi - n_0^2}}{n_1 sin\ \phi} = -2tan^{-1}\sqrt{\frac{\Delta}{sin^2\phi} - 1} \quad -(7)$$

the complex reflection coefficient can be expressed as $r = exp(-j\phi)$. The foregoing phase shift is often referred to as Goos-Hänchen shift [103]. The distance between 2 phase fronts (referred to as ℓ_1 in figure A.1) is expressed as:

$$\ell_1 = \left(\frac{2a}{tan\ \phi} - 2a\ tan\ \phi\right)cos\ \phi = 2a\left(\frac{1}{sin\ \phi} - 2sin\ \phi\right) \quad -(8)$$

and the distance between 2 reflection points (referred to as ℓ_2) as:

$$\ell_2 = \frac{2a}{\sin\phi} \quad \text{-(9)}$$

then the phase matching condition for ℓ_1 and ℓ_2 is:

$$(kn_1\ell_2 + 2\phi) - kn_1\ell_1 = 2m\pi \quad \text{-(10)}$$

where m is an integer. By plugging eqns. (7-9) into eqn. (10), the following equation is obtained.

$$\tan\left(kn_1 a \sin\phi - \frac{m\pi}{2}\right) = \sqrt{\frac{2\Delta}{\sin^2\phi} - 1} \quad \text{-(11)}$$

Eqn. (11) indicates that propagation angle, ϕ, is discrete and a function of a, n_1 and Δ. m is called "mode number". The mode with minimum angle ϕ is called the fundamental mode ($m = 0$) and the other modes are called higher order modes ($m > 0$). Figure A.2 is an example of fundamental mode and higher order mode when $m = 1$.

By introducing the new parameter ξ, which is given by:

$$\xi = \frac{\sin\phi}{\sqrt{2\Delta}} \quad \text{-(12)}$$

Then eqn. (11) is rewritten as:

$$kn_1 a\sqrt{2\Delta} = \frac{\cos^{-1}\xi + \frac{m\pi}{2}}{\xi} \quad \text{-(13)}$$

The left-hand side is often referred to as the normalized frequency, which is a useful parameter for the later discussions, and expressed by:

$$\upsilon = kn_1 a\sqrt{2\Delta} \quad \text{-(14)}$$

The eqn. (13) is called the dispersion equation. Figure A.2 shows the dispersion curves for m = 0 - 6. The only fundamental mode with $m = 0$ exists can exist when υ is less than

$\upsilon_c = \pi/2$. This is called single-mode consition of the slab waveguide. With this condition, other higher modes are cut off. υ is also called cutoff υ-value. In terms of the wavelength, cutoff condition is expressed as:

$$\lambda_c = \frac{2\pi}{\upsilon_c} a n_1 \sqrt{2\Delta} \qquad \text{-(15)}$$

λc is called cutoff wavelength.

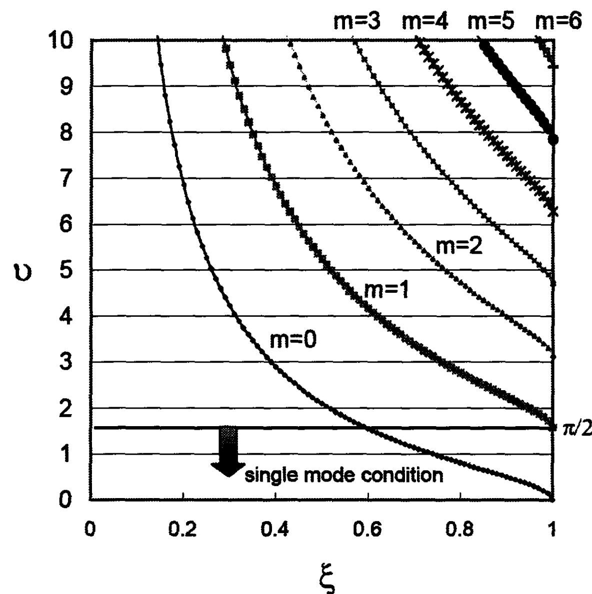

Figure A.2: Dispersion curves of a slab waveguide. When v is less than $\pi/2$, only the fundamental mode with m=0 exists.

A.3 Maxwell's equations

In a homogeneous dielectric medium, Maxwell equations re given by:

$$\nabla x \boldsymbol{e} = -\mu \frac{\partial \boldsymbol{h}}{\partial t} \qquad \text{where } \mu = \mu_0$$

$$\nabla x \boldsymbol{h} = \varepsilon \frac{\partial \boldsymbol{e}}{\partial t} \qquad \text{where } \varepsilon = \varepsilon_0 n^2 \qquad \text{-(16)}$$

The wavenumber is expressed using pemittivity and peamiability as:

$$\Gamma = \omega\sqrt{\varepsilon\mu} = \omega n \sqrt{\varepsilon_0 \mu_0} = kn \qquad \text{-(17)}$$

where k is the wavenumber in a vacuum.

And wavelength λ can be also expressed in terms of k.

$$\lambda = \frac{c}{f} = \frac{(\omega / k)}{f} = \frac{2\pi}{k} \quad where\ \omega = 2\pi f \qquad \text{-(18)}$$

When **e** and **h** are assumed to be sinusoidal functions of time, the electric field is expressed as:

$$e(t) = |\boldsymbol{E}| cos(\omega t + \phi) \qquad \text{-(19)}$$

where *f* represents the phase. Eqn. (19) cab rewritten by defining the complex amplitude.

$$\boldsymbol{E} = |\boldsymbol{E}| e^{j\phi} \quad \text{then} \quad e(t) = Re\{\boldsymbol{E} e^{j\omega t}\} \qquad \text{-(20)}$$

Eqn. (20) is also expressed as:

$$e(t) = \boldsymbol{E} e^{j\omega t} \qquad \text{-(21)}$$

When an electromagnetic wave is considered to propagate along z-direction as shown in figure A.1, electric and magnetic fields are given by:

$$\begin{aligned} \boldsymbol{e} &= \boldsymbol{E}(\boldsymbol{r}) e^{j(\omega t - \beta z)} \\ \boldsymbol{h} &= \boldsymbol{H}(\boldsymbol{r}) e^{j(\omega t - \beta z)} \end{aligned} \qquad \text{-(22)}$$

By applying Maxwell's equation eqn. (16), the following set of equations are obtained.

$$\begin{aligned} &\frac{\partial E_z}{\partial y} + j\beta E_y = -j\omega \mu_0 H_x \\ &-j\beta E_x - \frac{\partial E_z}{\partial x} = -j\omega \mu_0 H_y \\ &\frac{\partial E_y}{\partial x} - \frac{\partial E_x}{\partial y} = -j\omega \mu_0 H_z \\ &\frac{\partial H_z}{\partial y} + j\beta H_y = j\omega \varepsilon_0 n^2 E_x \\ &-j\beta H_x - \frac{\partial H_z}{\partial x} = j\omega \varepsilon_0 n^2 E_y \\ &\frac{\partial H_y}{\partial x} - \frac{\partial H_x}{\partial y} = j\omega \varepsilon_0 n^2 E_z \end{aligned} \qquad \text{-(23)}$$

These equations are used to analyze slab or rectangular waveguides.

And the boundary conditions also have to be met.

$$E_t^{(1)} = E_t^{(2)}$$
$$H_t^{(1)} = H_t^{(2)} \qquad \text{-(24)}$$

where t denotes tangential components to the boundary and superscripts denote the medium.

A.4 Slab waveguides

Maxwell's equations are given by:

$$\nabla \times \tilde{\boldsymbol{E}} = -\mu_0 \frac{\partial \tilde{\boldsymbol{H}}}{\partial t}$$
$$\nabla \times \tilde{\boldsymbol{H}} = \varepsilon_0 n^2 \frac{\partial \tilde{\boldsymbol{E}}}{\partial t} \qquad \text{-(25)}$$

When the plane wave propagation is assumed, then electric and magnetic fields are expressed as:

$$\tilde{\boldsymbol{E}} = \boldsymbol{E}(x, y) e^{j(\omega t - \beta z)}$$
$$\tilde{\boldsymbol{H}} = \boldsymbol{H}(x, y) e^{j(\omega t - \beta z)} \qquad \text{-(26)}$$

By plugging eqn. (26) into eqn. (25), the following set of equations are obtained.

$$\frac{\partial E_z}{\partial y} + j\beta E_y = -j\beta \mu_0 H_x$$
$$-j\beta E_x - \frac{\partial E_z}{\partial x} = -j\omega \mu_0 H_y$$
$$\frac{\partial E_y}{\partial x} - \frac{\partial E_x}{\partial y} = -j\omega \mu_0 H_z \qquad \text{-(27)}$$

and

$$\frac{\partial H_z}{\partial y} + j\beta H_y = j\omega \varepsilon_0 n^2 E_x$$

$$-j\beta H_x - \frac{\partial H_z}{\partial x} = j\omega \varepsilon_0 n^2 E_x$$

$$\frac{\partial H_y}{\partial x} - \frac{\partial H_x}{\partial y} = j\omega \varepsilon_0 n^2 E_z \quad -(28)$$

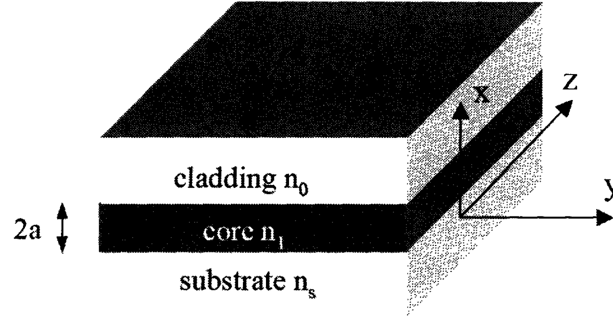

Figure A.3: Schematic of dielectric slab waveguide.

In the slab waveguide shown in figure A.3, electro and magnetic fields E and H do not depend on y-direction. Therefore, it is assumed that

$$\frac{\partial \mathbf{E}}{\partial y} = 0 \text{ and } \frac{\partial \mathbf{H}}{\partial y} = 0 \quad -(29)$$

For Transverse electric (TE) mode, the following wave equation is obtained.

$$\frac{d^2 E_y}{dx^2} + \left(k^2 n^2 - \beta^2\right) E_y = 0 \quad -(30)$$

where

$$H_x = -\frac{\beta}{\omega \mu_0} E_y$$

$$H_z = \frac{j}{\omega \mu_0} \frac{dE_y}{dx}$$

$$E_x = E_z = H_y = 0 \quad -(31)$$

For transverse magnetic (TM) mode, the wave equation is expressed as:

$$\frac{d}{dx}\left(\frac{1}{n^2}\frac{dH_y}{dx}\right)+\left(k^2-\frac{\beta^2}{n^2}\right)H_y=0 \qquad \text{-(32)}$$

where

$$E_x=\frac{\beta}{\omega\varepsilon_0 n^2}H_y$$

$$E_z=-\frac{j}{\omega\varepsilon_0 n^2}\frac{dH_y}{dx}$$

$$E_y=H_x=H_z=0 \qquad \text{-(33)}$$

A.5 Dispersion equations

For the slab waveguide shown in figure A.3, the guided light is confined in the core and exponentially decay in the cladding, the electric field distribution is expressed as:

$$E_y=\begin{cases} A\cos(\kappa a-\phi)e^{-\sigma(x-a)} & if\ x>a \\ A\cos(\kappa x-\phi) & if\ -a\le x\le a \\ A\cos(\kappa a+\phi)e^{\xi(x+a)} & if\ x<a \end{cases} \qquad \text{-(34)}$$

where κ, σ, and ξ are wavenumbers along the x-axis in the core and cladding and are given by:

$$\kappa=\sqrt{k^2n_1^2-\beta^2}$$

$$\sigma=\sqrt{\beta^2-k^2n_0^2}$$

$$\xi=\sqrt{\beta^2-k^2n_s^2} \qquad \text{-(35)}$$

To satisfy the boundary conditions at the interface of core and cladding, dE_y/dx also has to be continuous at the interfaces.

$$\frac{dE_y}{dx} = \begin{matrix} -\sigma A\cos(\kappa a - \phi)e^{-\sigma(x-a)} \\ -\kappa A\sin(\kappa x - \phi) \\ \xi A\cos(\kappa a + \phi)e^{\xi(x+a)} \end{matrix} \qquad \text{-(36)}$$

From eqns. (35) and (36), the following equations are obtained.

$$\begin{aligned} \kappa A\sin(\kappa a + \phi) &= \xi A\cos(\kappa a + \phi) \\ \sigma A\cos(\kappa a - \phi) &= \kappa A\sin(\kappa a - \phi) \end{aligned} \qquad \text{-(37)}$$

By removing A in eqn. (37), the following equation is obtained.

$$\begin{aligned} \tan(u + \phi) &= \frac{w}{u} \\ \tan(u - \phi) &= \frac{w'}{u} \end{aligned} \qquad \text{-(38)}$$

where

$$\begin{aligned} u &= \kappa a \\ w &= \xi a \\ w' &= \sigma a \end{aligned} \qquad \text{-(39)}$$

From eqn. (38), the eigenvalue equations are obtained.

$$\begin{aligned} u &= \frac{m\pi}{2} + \frac{1}{2}\tan^{-1}\left(\frac{w}{u}\right) + \frac{1}{2}\tan^{-1}\left(\frac{w'}{u}\right) \quad (m = 0, 1, 2, 3...) \\ \phi &= \frac{m\pi}{2} + \frac{1}{2}\tan^{-1}\left(\frac{w}{u}\right) + \frac{1}{2}\tan^{-1}\left(\frac{w'}{u}\right) \end{aligned} \qquad \text{-(40)}$$

Using eqns. (35) and (39), the following relationships are obtained.

$$\begin{aligned} u^2 + w^2 &= k^2a^2\left(n_1^2 - n_s^2\right) \equiv \upsilon \\ w' &= \sqrt{\gamma\,\upsilon^2 + w^2} \\ \gamma &= \frac{n_s^2 - n_0^2}{n_1^2 - n_s^2} \end{aligned} \qquad \text{-(41)}$$

υ is called normalized frequency. And γ is a measure of the asymmetry of the cladding

refractive indices. Eqn. (41) indicated that once the dimensions of the waveguide and the wavelength of the light are determined, the normalized frequency υ and γ are also determined. u, w, w' and ϕ are determined by solving eqn. (40) and (41). In the case of asymmetrical waveguide ($n_s > n_0$), higher refractive index ns is used as the cladding refractive index since the cutoff conditions are determined when the normalized propagation constant β/k is equal to the higher cladding refractive index. Eqns. (40) and (41) are the dispersion equations or eigenvalue equations for TE_m modes. When the wavelength of the light and the dimensions of the waveguide are given or normalized frequency υ and asymmetrical parameter γ are obtained, the propagation constant β can be determined. From eqn. (35), it is obvious that k has to be real number for the main part of optical field to be confined in the core region. And s and x also have to be real to have exponential decay in the cladding. Then the following condition should be met.

$$n_s \leq \frac{\beta}{k} \leq n_1 \quad \text{-(42)}$$

β/k is often referred to as the effective index.

$$n_e = \frac{\beta}{k} \quad \text{-(42)}$$

If n_s is larger than n_e, the electromagnetic field in the cladding becomes oscillatory as is indicated in eqn. (34). Then the field is dissipated as the radiation mode. As is in eqn. (42), $\beta = kn_s$ represents the critical condition under which the field is cut off and becomes the radiation mode (non-guided mode), this is called cutoff condition. By introducing a new parameter, b, shown below,

$$b = \frac{n_e^2 - n_s^2}{n_1^2 - n_s^2} \quad \text{-(43)}$$

then, the condition for the guided mode is expressed as below by using eqn. (42),

$$0 \leq b \leq 1 \quad \text{-(44)}$$

The cutoff condition is rewritten as:

$$b = 0 \quad \text{-(45)}$$

b is often called the normalized propagation condition and is very useful expression to judge cutoff condition. The dispersion equation, eqn. (40), can be rewritten using *u* and *b* shown below.

$$2\upsilon\sqrt{1-b} = m\pi + \tan^{-1}\sqrt{\frac{b}{1-b}} + \tan^{-1}\sqrt{\frac{b+\gamma}{1-b}} \quad \text{-(46)}$$

and eqn. (35) can be rewritten as:

$$\begin{aligned} u &= \upsilon\sqrt{1-b} \\ w &= \upsilon\sqrt{b} \\ w' &= \upsilon\sqrt{b+\gamma} \end{aligned} \quad \text{-(47)}$$

As a simple example where $n_0 = n_s$ and $\gamma = 0$, dispersion equations can be written as:

$$\begin{aligned} & u = \frac{m\pi}{2} + \tan^{-1}\left(\frac{w}{u}\right) \quad or \quad w = u\tan\left(u - \frac{m\pi}{2}\right) \\ & \phi = \frac{m\pi}{2} \\ & or \quad \upsilon\sqrt{1-b} = \frac{m\pi}{2} + \tan^{-1}\sqrt{\frac{b}{1-b}} \end{aligned} \quad \text{-(48)}$$

A.6 Obtaining propagation constant

The propagation constant is obtained graphically. Figure A.4 is an *u-w* relationship of the symmetrical slab waveguide. *u* and *w* are plotted so that eqn. (48) is satisfied. This relation is also plotted for the case of υ = 1, 2, 3 and 4. The solutions of this dispersion equation are given as intersections in this figure. In figure A.4, there is only one intersection for *u* =1. This indicates that there is only one guided mode when the waveguide dimension

and the wavelength of the light satisfy $\upsilon > \pi/2$. $\upsilon_c = \pi/2$ is called the cutoff normalized frequency below which only one guided mode can exist. υ_c is obtained from the cutoff condition for

$m = 1$. If $\upsilon > \upsilon_c$, then two or more than two guided modes exist.

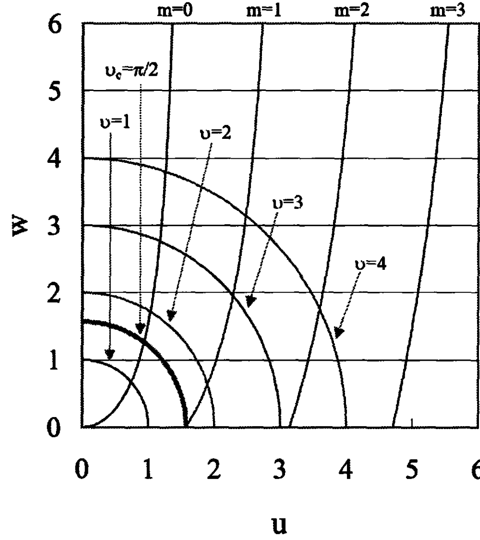

Figure A.4: An u-w relationship for the symmetric slab waveguide.

More generally, the cutoff υ value for TE and TM modes are written as:

$$\upsilon_{c,TE} = \frac{m\pi}{2} + \frac{1}{2}\tan^{-1}\sqrt{\gamma} \qquad \text{for TE mode}$$

$$\upsilon_{c,TM} = \frac{m\pi}{2} + \frac{1}{2}\tan^{-1}\left(\frac{n_1^2}{n_0^2}\sqrt{\gamma}\right) \qquad \text{for TM mode} \qquad \text{-(49)}$$

By modifying eqn. (48), the new dispersion equation is obtained.

$$f(\upsilon, m, b) = \upsilon\sqrt{1-b} - \frac{m\pi}{2} - \tan^{-1}\sqrt{\frac{b}{1-b}} = 0 \qquad \text{-(50)}$$

Figure A.5 is the plot of $f(\upsilon, m, b)$ for $\upsilon = 5$ and $\gamma = 0$ (symmetric waveguide). The value of b when $f(\upsilon, m, b) = 0$ gives the normalized propagation constant b for the given υ-value

which is determined by the wavelength, refractive indices for core, cladding and substrate, and the waveguide dimensions. the normalized propagation constant b is obtained for each normalized frequency υ. This υ–b relationship is called the dispersion curve. Figure A.6 is dispersion curves for TE modes in the slab waveguide [103]. This curve depends only on mode number m and the measure of asymmetry γ. Therefore this dispersion curve is constant once m and γ are determined and is useful for single-mode waveguide designing.

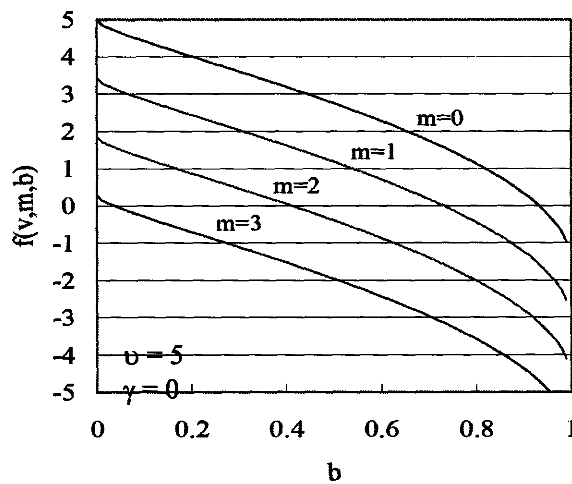

Figure A.5: Dispersion plot for the calculation of the eigenvalue.

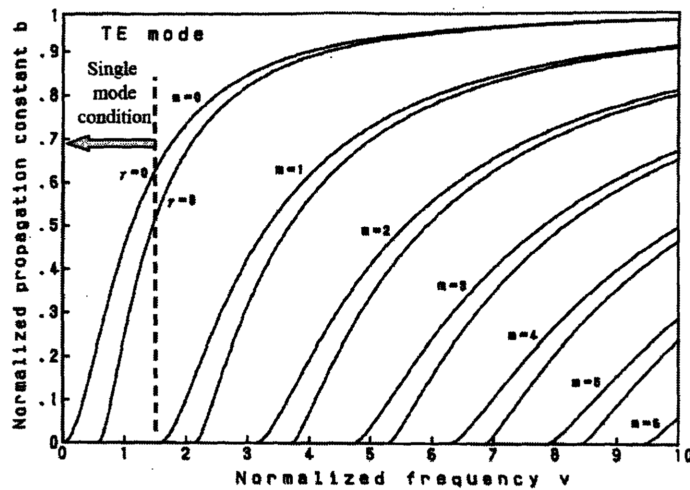

Figure A.6: Dispersion curves for TE modes in the slab waveguide [103].

A.7 Electric field distribution

If the eigenvalue of the waveguide is obtained using the previous approach, the electric distribution is also obtained using eqn. (34). Power is written as:

$$P = \int_0^1 dy \int_{-\infty}^{\infty} \frac{1}{2} (\boldsymbol{E} \times \boldsymbol{H}^*) \cdot \boldsymbol{u}_z \, dx = \int_{-\infty}^{\infty} \frac{1}{2} \left(E_x H_y^* - E_y H_x^* \right) dx \qquad \text{-(51)}$$

For TE mode, eqn. (50) is rewritten using eqns. (30) and (31) as:

$$P = \frac{\beta}{2\omega\mu_0} \int_{-\infty}^{\infty} |E_y|^2 dx \qquad \text{-(52)}$$

Using eqn. (34), the following equations are obtained.

$$P_{core} = \frac{\beta a A^2}{2\omega\mu_0} \left\{ 1 + \frac{\sin^2(u+\phi)}{2w} + \frac{\sin^2(u-\phi)}{2w'} \right\} \quad \text{if } -a \le x \le a$$

$$P_{sub} = \frac{\beta a A^2}{2\omega\mu_0} \frac{\cos^2(u+\phi)}{2w} \quad \text{if } x \le -a$$

$$P_{clad} = \frac{\beta a A^2}{2\omega\mu_0} \frac{\cos^2(u-\phi)}{2w} \quad \text{if } x \ge a \qquad \text{-(53)}$$

Then total power is given by:

$$P = P_{core} + P_{sub} + P_{clad} = \frac{\beta a A}{2\omega\mu_0} \left\{ 1 + \frac{1}{2w} + \frac{1}{2w'} \right\} \qquad \text{-(53)}$$

The constant A in eqn. (34) is then expressed using P as:

$$A = \sqrt{\frac{2\omega\mu_0 P}{\beta a(1 + 1/2w + 1/2w')}} \qquad \text{-(54)}$$

The confinement factor is defined as P_{core}/P and written as:

$$\Gamma = \frac{P_{core}}{P} = \frac{1 + \frac{\sin^2(u+\phi)}{2w} + \frac{\sin^2(u-\phi)}{2w'}}{1 + \frac{1}{2w} + \frac{1}{2w'}} \qquad \text{-(55)}$$

Figure A.7 is an example where $\upsilon = 4$, $n_1 = 3.38$, $n_s = 3.17$, $n_0 = 0$ and $\gamma = 6.6$. In this configuration, three modes exist for TE mode [103].

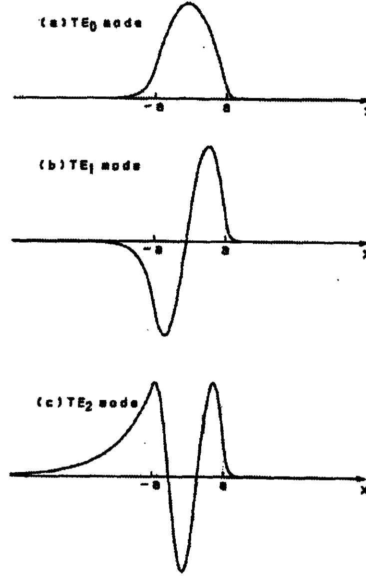

Figure A.7: Examples of electric field distributions in the slab waveguide [103].

A.8 TM mode dispersion equation

Using eqns. (32) and (33), the dispersion equation for TM mode is obtained in a similar approach to that for TE mode. The magnetic field H_y is expressed similarly.

$$H_y = \begin{cases} A\cos(\kappa a - \phi)e^{-\sigma(x-a)} & \text{if } x > a \\ A\cos(\kappa x - \phi) & \text{if } -a \le x \le a \\ A\cos(\kappa a + \phi)e^{\xi(x+a)} & \text{if } x < -a \end{cases} \quad \text{-(56)}$$

After applying the boundary conditions, where H_y and E_z are continuous at the interfaces, the dispersion equation is obtained.

$$u = \frac{m\pi}{2} + \frac{1}{2}\tan^{-1}\left(\frac{n_1^2 w}{n_s^2 u}\right) + \frac{1}{2}\tan^{-1}\left(\frac{n_1^2 w'}{n_0^2 u}\right) \quad \text{-(57)}$$

This equation can be rewritten using normalized frequency υ and normalized propagation

constant b.

$$2\upsilon\sqrt{1-b} = m\pi + tan^{-1}\left(\frac{n_1^2}{n_s^2}\sqrt{\frac{b}{1-b}}\right) + \frac{1}{2}tan^{-1}\left(\frac{n_1^2}{n_0^2}\sqrt{\frac{b+\gamma}{1-b}}\right) \quad \text{-(58)}$$

Figure A.8 is an example of dispersion curves for TM and TE modes, where $n_1 = 3.38$, $n_s = n_0 = 3.17$ and $\gamma = 0$ [103]. As shown in figure A.8, b for TE mode is larger than that for TM mode. This indicated that the TE mode is better confined in the core than the TM mode. The power for TM mode is similarly obtained.

$$P = \frac{\beta}{2\omega\varepsilon_0}\int_{-\infty}^{\infty}\frac{1}{n^2}|H_y|^2 dx \quad \text{-(59)}$$

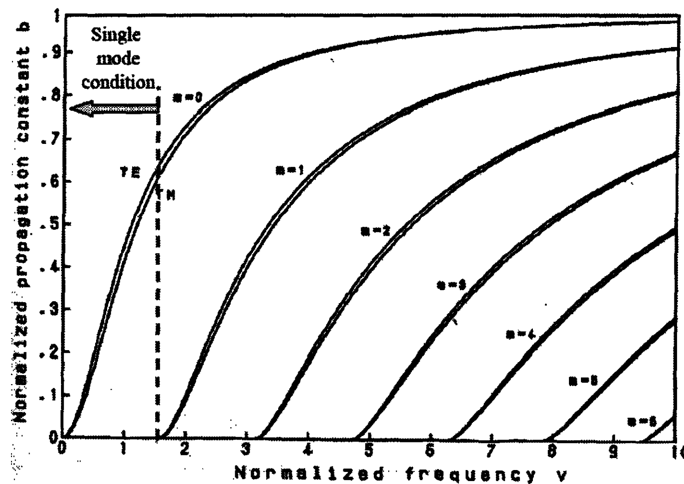

Figure A.8: Dispersion curves for the TE and TM modes is the slab waveguide [103].

A.9 Channel waveguide

In this section, the approach developed by Marcatitli [4] is employed to carry out the analysis to handle channel waveguide shown in Figure A.9.

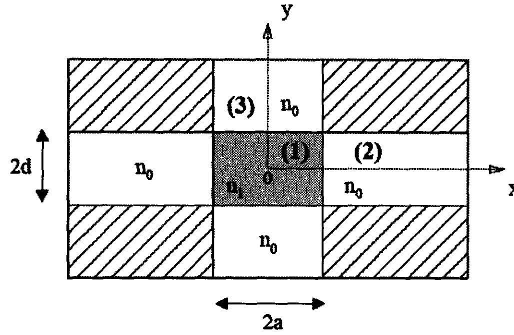

Figure A.9: Three dimensional channel waveguide.

In this approach, shaded area in Figure A.9 is ignored since the electromagnetic field in the shaded area experiences rapid decay if the light is well guided. And the boundary conditions are not imposed to shaded area. It is first assumed that E_x and H_y are predominant. Then wave equations are obtained as:

$$\frac{\partial H_y}{\partial x^2} + \frac{\partial H_y}{\partial y^2} + (k^2 n^2 - \beta^2) H_y = 0$$

$$H_x = 0$$

$$E_x = \frac{\omega \mu_0}{\beta} H_y + \frac{1}{\omega \varepsilon_0 n^2 \beta} \frac{\partial^2 H_y}{\partial x^2}$$

$$E_y = \frac{1}{\omega \varepsilon_0 n^2 \beta} \frac{\partial^2 H_y}{\partial x \partial y}$$

$$E_z = \frac{-j}{\omega \varepsilon_0 n^2} \frac{\partial H_y}{\partial x}$$

$$H_z = \frac{-j}{\beta} \frac{\partial H_y}{\partial y} \qquad -(60)$$

On the other hand, if E_y and H_x are predominant, then the following wave equations are obtained as:

$$\frac{\partial^2 H_x}{\partial x^2} + \frac{\partial^2 H_x}{\partial y^2} + (k^2 n^2 - \beta^2) H_x = 0$$

$$H_y = 0$$

$$E_x = -\frac{1}{\omega \varepsilon_0 n^2 \beta} \frac{\partial^2 H_x}{\partial x \partial y}$$

$$E_y = -\frac{\omega \mu_0}{\beta} H_x - \frac{1}{\omega \varepsilon_0 n^2 \beta} \frac{\partial^2 H_x}{\partial y^2}$$

$$E_z = \frac{j}{\omega \varepsilon_0 n^2} \frac{\partial H_x}{\partial y}$$

$$H_z = \frac{-j}{\beta} \frac{\partial H_x}{\partial x} \qquad \text{-(61)}$$

When E_x and H_y are predominant, the modes are expressed as E_{pq}^{x}, where p and q are integers. And when E_y and H_x are predominant, the modes are expressed as E_{pq}^{y}.

A.10 Dispersion equation for E_{pq}^{x} and E_{pq}^{y}

When E_x and H_y are predominant, the solution is expressed as:

$$H_y = \begin{cases} A\cos(k_x x - \phi)\cos(k_y y - \psi) & \text{for region(1)} \\ A\cos(k_x a - \phi)e^{-\gamma_x(x-a)}\cos(k_y y - \psi) & \text{for region(2)} \\ A\cos(k_x x - \phi)e^{-\gamma_y(x-d)}\cos(k_y d - \psi) & \text{for region(3)} \end{cases} \qquad \text{-(62)}$$

where transverse numbers k_x, k_y, γ_y and optical phases ϕ and ψ are given by:

$$-k_x^2 - k_y^2 + k^2 n_1^2 - \beta^2 = 0 \qquad \text{for region(1)}$$

$$\gamma_x^2 - k_y^2 + k^2 n_0^2 - \beta^2 = 0 \qquad \text{for region(2)}$$

$$-k_x^2 + \gamma_y^2 + k^2 n_0^2 - \beta^2 = 0 \qquad \text{for region(3)} \qquad \text{-(63)}$$

and

$$\phi = (p - 1)\frac{\pi}{2} \qquad where\ p = 1, 2, 3, \ldots$$

$$\psi = (q - 1)\frac{\pi}{2} \qquad where\ q = 1, 2, 3, \ldots \qquad \text{-(64)}$$

By applying the boundary conditions shown below,

$$E_z \propto \frac{1}{n^2}\frac{\partial H_y}{\partial x} \Rightarrow continuous\ at\ x = a$$

$$H_z \propto \frac{\partial H_y}{\partial y} \Rightarrow continuous\ at\ y = d \qquad \text{-(65)}$$

the following dispersion equations are obtained.

$$k_x a = (p - 1)\frac{\pi}{2} + tan^{-1}\left(\frac{n_1^2 \gamma_x}{n_0^2 k_x}\right)$$

$$k_y d = (q - 1)\frac{\pi}{2} + tan^{-1}\left(\frac{\gamma_y}{k_x}\right) \qquad \text{-(66)}$$

Transverse numbers k_x, k_y, γ_y and optical phases ϕ and ψ are given by eqn. (63)

$$\gamma_x^2 = k^2(n_1^2 - n_0^2) - k_x^2$$

$$\gamma_y^2 = k^2(n_1^2 - n_0^2) - k_y^2 \qquad \text{-(67)}$$

Then the propagation constant is obtained as:

$$\beta^2 = k^2 n_1^2 - (k_x^2 - k_y^2) \qquad \text{-(68)}$$

The same approach can be applied to calculate the dispersion equation for E_{pq}^{y} mode. H_x is expressed as:

$$H_x = \begin{cases} A cos(k_x x - \phi) cos(k_y y - \psi) & for\ region(1) \\ A cos(k_x a - \phi) e^{-\gamma_x (x - a)} cos(k_y y - \psi) & for\ region(2) \\ A cos(k_x x - \phi) e^{-\gamma_y (y - d)} cos(k_y d - \psi) & for\ region(3) \end{cases} \qquad \text{-(70)}$$

By applying the boundary conditions shown below,

$$H_z \propto \frac{\partial H_x}{\partial x} \Rightarrow \textit{continuous at } x = a$$

$$E_z \propto \frac{1}{n^2}\frac{\partial H_x}{\partial y} \Rightarrow \textit{continuous at } y = d \qquad \text{-(71)}$$

the following dispersion equations are obtained. Figure A.10 is a set of examples of mode definitions.

$$k_x a = (p-1)\frac{\pi}{2} + tan^{-1}\left(\frac{\gamma_x}{k_x}\right)$$

$$k_y d = (q-1)\frac{\pi}{2} + tan^{-1}\left(\frac{n_1^2 \gamma_y}{n_0^2 k_y}\right) \qquad \text{-(72)}$$

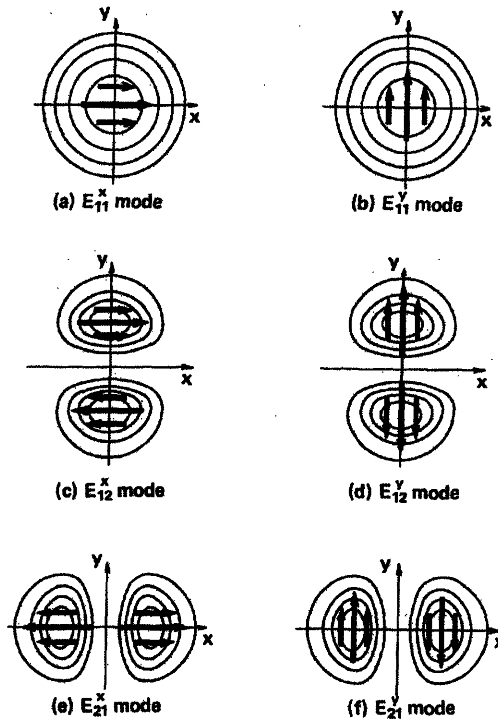

Fig. A.X: Mode definitions of electric field distributions in Marcatili's method [103].

For other approaches, it is possible to employ Kumar's method [105] or effective index

method [4]. Kumar's method offers better accuracy rather than Marcatili's method by taking into account the contribution of the fields in the shaded area in figure A.9. The effective index method is often used for ridge waveguide, where it is too complicated to apply Marcatili's or Kumar's method.

Appendix B: Basic physics of photonic crystal

B.1 Maxwell's equaltions

The propagation of light in dielectric media can be expressed by the macroscopic Maxwell equations.

$$\nabla \cdot D = \rho$$
$$\nabla \cdot B = 0$$
$$\nabla \times E = -\frac{\partial B}{\partial t}$$
$$\nabla \times H = \frac{\partial D}{\partial t} + j \qquad (1)$$

where ***E*** and ***H*** represent the electric and the magnetic field, respectively and ***D*** and B the displacement and magnetic induction, respectively. ρ and j represents the free charges and currents, respectively. ***D*** and ***B*** can be expressed as follows by assuming linear and homogenous optical materials.

$$\boldsymbol{D} = \varepsilon_0 \varepsilon E$$
$$\boldsymbol{B} = \mu_0 \mu H \qquad (2)$$

where μ and ε are the magnetic permeability and the dielectric constant, respectively. μ_0 and ε_0 are those for free space. In most cases of interest, the permeability is unity or close to unity. Moreover, in the media with no charge and current, which is often the case with our cases, we can assume that $\rho = j = 0$. Using these assumptions, simple harmonic wave equations are obtained as below.

$$H(r,t) = H(r)e^{-i\omega t}$$
$$E(r,t) = E(r)e^{-i\omega t} \qquad (3)$$

By combining (1)-(3), the time dependence can be removed and the master equation can be obtained as below.

$$\nabla \times \left(\frac{1}{\varepsilon(r)} \nabla \times H(r) \right) = \left(\frac{\omega}{c} \right)^2 H(r) \qquad (4)$$

Equation (4) determines the distribution of the magnetic field H and corresponding frequency ω inside the photonic crystal which is defined by dielectric constant ε. Equation (4) is called "Master equation". A several computational techniques have been developed to solve this equation for 2-D and 3-D systems. Photonic bandgaps for 1-D structures can also be solved using this equation. Due to the relative simplicity of 1-D structures, a different approach based on matrix multiplication provides an easier alternative to a solution of eqn. (4) [109].

B.2 Plane wave reflection from a layered medium

A. TE polarization

The electric field of plane wave incident on a planar boundary can be expressed as below.

$$E_i = \hat{y}E_y = \hat{y}E_0 e^{-ik_{1x}x + ik_{1y}z} \qquad -(5)$$

and the magnetic field by

$$H_i = \frac{1}{i\omega\mu_1} \nabla \times E_i = \frac{-1}{\omega\mu_1} \left(k_{1x}\hat{x} + k_{1z}\hat{z}\right) E_0 e^{-ik_{1x}x + ik_{1z}z} \qquad -(6)$$

where the components of the wave vector satisfy the dispersion relation as follows.

$$k_{1x}^2 + k_{1z}^2 = \omega^2 \mu_1 \varepsilon_1 = k_0 n^2 \quad \text{where} \quad k_0 = \omega\sqrt{\mu_0\, \varepsilon_0} = \frac{\omega}{c} \quad \text{and}$$

$$n_1 = \sqrt{\mu_1 \varepsilon_1 / (\mu_0 \varepsilon_0)} \quad \text{-(7)}$$

In most cases, especially for dielectric materials, it can be assumed

$$\mu_1 = \mu_0$$

The reflected electric and magnetic fields are given by

$$E_r = \hat{y}\, r\, E_0 e^{i K_{1x} x + i K_{1z} z} \text{ and } H_r = \frac{1}{\omega \mu}(-k_{1x} x + k_{1z} z)\, r\, E_0 e^{i K_{1x} x + i K_{1z} z}$$

$$\text{where } k_{2x}^2 + k_{2z}^2 = \omega^2 \mu_2 \varepsilon_2 = k_0^2 n_2^2 \quad \text{-(8)}$$

If we assume that the medium is inhomogeneous along x direction $\varepsilon=\varepsilon(x)$ and $\mu=\mu(x)$, it is possible to employ propagation matrix method. By defining the permittivity and permeability as

$$\mu_l=\mu(x_l) \quad \text{and} \quad \varepsilon_l=\varepsilon(x_l) \quad \text{for} \quad -d_{l-1} \geq x \geq -d_l \; (1^{\text{th}} \text{ layer}) \qquad \text{-(9)}$$

as shown Fig.x. For TE polarized incident wave

$$E_i=\hat{y} E_0 e^{-ik_{0x}x + ik_{0z}z} \quad \text{and for the reflected wave,} \quad E_r=\hat{y} r E_0 e^{ik_{0x}x + ik_{0z}z} \quad \text{.-(10)}$$

In the 1th layer, the electric field id given by

$$\text{where } E_y^l = \left(A_l\, e^{-ik_{lx}(x+d_l)} + B_l\, e^{+ik_{lx}(x+d_l)}\right) e^{ik_{lz}z} \quad \text{and}$$

$$H_z^l = \frac{1}{i\omega\mu_l}\frac{\partial}{\partial x}E_y^l = \frac{-k_{lx}}{\omega\mu_l}\left(A_l\, e^{-ik_{lx}(x+d_l)} + B_l\, e^{+ik_{lx}(x+d_l)}\right) e^{ik_{lz}z} \quad \text{-(11)}$$

and $k_{lx} = \sqrt{\omega^2 \mu_l\, \varepsilon - k_{0z}^2}$, $k_{lz} = k_{0z}$ for all l. From the boundary conditions, where E_y and

H_z are continuous at $x = -d_l$ lead to

$$A_l + B_l = A_{l+1}\, e^{-ik_{(l+1)x}(-d_l + d_{l+1})} + B_{l+1}\, e^{ik_{(l+1)x}(-d_l + d_{l+1})}$$ and

$$A_l - B_l = \frac{\mu_l\, k_{(l+1)x}}{\mu_{l+1}\, k_{lx}} \left(A_{l+1}\, e^{-ik_{(l+1)x}(-d_l + d_{l+1})} - B_{l+1}\, e^{ik_{(l+1)x}(-d_l + d_{l+1})}\right) \quad \text{-(12)}$$

I define $P_{l(l+1)} = \dfrac{\mu_l\, k_{(l+1)x}}{\mu_{l+1}\, k_{lx}}$ and the thickness of the lth layer $h_{(l+1)} = d_{l+1} - d_l$, then get

$$\begin{bmatrix} A_l \\ B_l \end{bmatrix} = \overline{\mathrm{B}}_{l(l+1)} \begin{bmatrix} A_{l+1} \\ B_{l+1} \end{bmatrix}$$ where the backward-propagation matrix is defined as

$$\overline{\mathrm{B}}_{l(l+1)} = \frac{1}{2} \begin{bmatrix} (1+P_{l(l+1)})e^{-ik_{(l+1)x} h_{l+1}} & (1-P_{l(l+1)})e^{ik_{(l+1)x} h_{l+1}} \\ (1-P_{l(l+1)})e^{-ik_{(l+1)x} h_{l+1}} & (1+P_{l(l+1)})e^{ik_{(l+1)x} h_{l+1}} \end{bmatrix} \quad \text{-(13)}$$

I can also define a forward-propagation matrix as follows

$$\begin{bmatrix} A_{l+1} \\ B_{l+1} \end{bmatrix} = \overline{\mathrm{F}}_{(l+1)l} \begin{bmatrix} A_l \\ B_l \end{bmatrix}$$ where

$$\overline{\mathrm{F}}_{l(l+1)} = \frac{1}{2} \begin{bmatrix} (1+P_{(l+1)l})e^{ik_{(l+1)x} h_{l+1}} & (1-P_{(l+1)l})e^{ik_{(l+1)x} h_{l+1}} \\ (1-P_{(l+1)l})e^{-ik_{(l+1)x} h_{l+1}} & (1+P_{l(l+1)})e^{-ik_{(l+1)x} h_{l+1}} \end{bmatrix} \quad \text{-(14)}$$

The intensities of the incident and reflected waves are related to those intensities in the transmitted region N+1 by

$$\begin{bmatrix} E_0 \\ rE_0 \end{bmatrix} = \overline{\mathrm{B}}_{01}\, \overline{\mathrm{B}}_{12}\, \overline{\mathrm{B}}_{23} \cdots \overline{\mathrm{B}}_{N(N+1)} \begin{bmatrix} A_{N+1} \\ B_{N+1} \end{bmatrix} = \begin{bmatrix} b_{11} & b_{12} \\ b_{21} & b_{22} \end{bmatrix} \begin{bmatrix} tE_0 \\ 0 \end{bmatrix} \quad \text{-(15)}$$

where BN+1=0, since I assume that there is no incident wave from the bottom. Then I can obtain the transmission and reflection coefficients of the multi layered medium as follows.

$$t = \frac{1}{b_{11}} \quad \text{and} \quad r = \frac{b_{21}}{b_{11}} \quad \text{-(16)}$$

B. TM polarization

For TM polarization, I can use the duality principle, that is,

$$\mathrm{E} \Rightarrow \mathrm{H} \quad \mathrm{H} \Rightarrow -\mathrm{E} \quad \mathrm{J} \Rightarrow \mathrm{M} \quad \mathrm{M} \Rightarrow -\mathrm{J}$$

$$\mu_l \Rightarrow \varepsilon_l \quad \varepsilon_l \Rightarrow \mu_l \quad \rho_{\mathrm{e}} \Rightarrow \rho_{\mathrm{M}} \quad \rho_{\mathrm{M}} \Rightarrow -\rho_{\mathrm{e}} \qquad \text{-(17)}$$

Then, from TE to TM polarization can be done.

Bibliography

Chapter 2:

[1] L. C. Kimerling, "Silicon Microphotonics", *Applied Surface Science*, **159**, 8 (2000).

[2] K. K. Lee, Ph.D. Thesis, Massachusetts Institute of Technology, 2000.

[3] D. Edelstein, J. Heidenreich, R. Goldblatt, W. Cote, C. Uzoh, N. Lustig, P. Roper, T. McDevitt, W. Mostiff, A. Simon, J. Dukovic, R. Wachnik, H. Rathore, R. Shulz and L. Digests, *IEEE, New York*, pp.773-776 (1997).

[4] E.A. J. Marcatili, *Bell Sys. Tech. J.* **48**, 2103, (1969).

[5] A. Kaneko, T. Goh, H. Yamada, T. Tanaka and I. Ogawa "Design and Application of Silica-Based Lightwave Circuits" *IEEE journal of selected topics in quantum electronics*, **5**, pp.1227-1235 (1999).

[6] M. Kawachi, "Silica waveguide on silicon and their application to integrated-optic components" *Opt. Quantum. Electron*, **22**, pp.391-410 (1999).

[7] K.Okamoto, "Planar Lightwave Circuits (PLCs)" Photonic Networks edited by Giancarlo Prati, *New York: Springer-Verlag*, pp.118-132 (1999)

[8] D. R. C. Lim, Ph.D. Thesis, Massachusetts Institute of Technology, 2000.

[9] C. Manolatou, S. G. Johnson, S. Fan, P.R. Villeneuve, H.A. Haus and J. D. Joannopoulos, *J. Lightwave Technol.*, **17**, pp.1682 (1999).

[10] K. Wörhoff, A. Driessen, P. V. Lambeck, L. T. H. Hilderink, P. W. C. Linders and Th. J. A. Popma, "Plasma enhanced chemical vapor deposition silicon oxynitride optimised for application in integrated optics" *Sensors and Actuato*rs, **74,** pp.9-12 (1999).

[11] R. Germann, H.W. M. Salemink, R. Beyeler, G.L.Bona, F. Horst, I. Massarek and B.J. Offrein "Silicon oxynitride layers for optical waveguide application" *J.electrochem.Soc.* **147**, (6) pp.2237-2241 (2000).

[12] A. del Prado, I. Martil, M. Fernandez and G. Gonzalez-Diaz, *Thin Solid Films*, **343-344**, pp.437-440 (1999).

[13] C. M. M. Denisse, K. Z. Troost, F. H. P. M. Habrachen and W. F. van der Weg "Annealing of plasma silicon oxynitride films" *J. Appl. Phys.* **60**(7), (1986).

[14] A. Sakai, G. Hara, and T. Baba, "Propagation Characteristics of Ultrahigh-Δ Optical Waveguide on Silicon-on-Insulator substrate," *Jpn. J. Appl. Phys.* **40,** pp. L383-L385, (2001).

[15] R. M. de Ridder, K. Worhoff, A. Driessen, P. V. Lambeck and H. Albers, "Silicon Oxynitride Planar Waveguiding Structures for Application in Optical Communication," *Selected Topics in Quantum Electronics, IEEE Journal.*, vol. 4, pp. 930-937 (1998).

[16] N. Somasiri, and B. M. Azizur Rahman, "Polarization Control in High Index Contrast Planar Silica Waveguides With Slanted Sidewalls," J. Lightwave Technol., vol.21, pp. 54-60 (2003).

[17] M. Maeda and M. Itsumi, "Thermal dissociation process of hydrogen atoms in plasma-enhanced chemical vapor deposited silicon nitride films," *J. Appl. Phys.* Vol. 84, pp. 5243-5247, 1998.

[18] S. S. He, and V. L. Shannon, "Hydrogen diffusion and redistribution in PECVD Si-rich Silicon Nitride during Rapid Thermal Annealing," *Solid-State and Integrated Circuit Technology,* 1995 4th International on 24-28 Oct. 1995, pp.269-271.

Chapter3:

[19] T. Miya, "Silica-based planar lightwave circuits: passive and thermally active devices," *IEEE J. of Sel. Topics in Quan. Electron.*, **6**, pp. 38-45, Jan. (2000).

[20] E. A. J. Marcatili, "Bends in optical dielectric waveguides," *Bell Sys. Tech. J.*, vol. 48, pp. 2103-2132, Sep. 1969.

[21] M. Heiblum and J. H. Harris, "Analysis of curved optical waveguides by conformal transformation," *IEEE J. of Quan. Electron.*, QE-11, pp. 75-83, Feb. 1975.

[22] D. Rowland, "Nonperturbative calculation of bend loss for a pulse in a bent planar waveguide," *IEE Proc.-Optoelectron.*, **144**, pp. 91-96, Apr. 1997.

[23] I.C. Goyal, R.L. Gallawa and A.K. Ghatak, "Bent planar waveguides and whispering gallery modes: a new method of analysis," *J. Lightwave Technol.*, vol. 8, pp. 768-774, May 1990.

[24] M.K. Smit, E.C.M. Pennings, and H. Blok, "A normalized approach to the design of low-loss optical waveguide bends," *J. Lightwave Technol.*, vol. 11, pp. 1737-1742, Nov. 1993.

[25] K. K. Lee, D. R. Lim, L. C. Kimerling, J, Shin, and F. Cerrina, "Fabrication of ultralow-loss Si/SiO_2 waveguides by roughness reduction," *Opt. Lett.*, vol. 26, pp.1888-1890, 2001.

[26] K. K. Lee, D. R. Lim, H-C. Luan, A. Anu, J. Foresi, and L. C. Kimerling, "Effect of size and roughness on light transmission in a Si/SiO_2 waveguide: Experiments and model, " *Appl. Phys. Lett.*, vol. 77, pp.1617-1619, 2000.

[27] M. Loncar, T. Doll, J. Vuckovic, A. Scherer, "Design and fabrication of silicon photonic crystal optical waveguides," *J. Lightwave Technol.*, vol. 18, pp. 1402-1411, 2000.

[28] A. Chuntinan and S. Noda, "Waveguides and waveguide bends in two-dimensional photonic crystal slabs," *Phys. Rev. B*, vol. 62, pp. 4488-4492, 2000.

[29] A. Talneau, L. L. Gouezigou, N. Bouadma, M. Kafesaki, C. M. Soukoulis, and M. Agio, "Photonic-crystal ultrashort bends with improved transmission and low reflection at 1.55μm," *Appl. Phys. Lett.*, vol. 80, 2002.

[30] R. Germann, H. W. Salemink, R. Beyeler, G. L. Bona, F. Horst, I. Massarek, and B. J. Offrein, "Silicon Oxynitride Layers for Optical waveguide Applications," *J. Electrochem. Soc.*, vol. 147. pp. 2237-2241, 2000.

[31] R. M. de Ridder, K. Worhoff, A. Driessen, P. V. Lambeck and H. Albers, "Silicon Oxynitride Planar Waveguiding Structures for Application in Optical Communication," *Selected Topics in Quantum Electronics, IEEE Journal.*, vol. 4, pp. 930-937, 1998.

[32] A. del Prado, I. Martil, M. Fernandez, G. Gonzalez-Diaz, "Full composition range silicon oxynitride films deposited by ECR-PECVD at room temperature," *Thin Solid Films*, vol. 343-344, pp. 437-440, 1999.

[33] C. M. M. Denisse, K. Z. Troost, F. H. P. M. Habraken, W. F. van der Weg, and M. Hendriks, "Annealing of plasma silicon oxynitride films," *J. Appl. Phys.*, vol. 69, pp. 2543-2547, 1986.

[34] D. Peters, K. Fischer, and J. Muller, "Integrated optics Based on Silicon Oxynitride Thin Films Deposited on Silicon Substaret for sensor Applications," *Sensors and Actuators A: Physical,* vol. 26, pp. 425-431, 1991.

[35] K. Worhoff, A. Driessen, P. V. Lambeck, L. T. H. Hilderink, P. W. C. Linders, and Th. J. A. Popma, "Plasma enhanced chemical vapor deposition silicon oxinitride optimized for application in integrated optics," *Sensors and Actuators A: Physical,* vol. 74, pp. 9-12, 1999.

[36] M. Popović, K. Wada, S. Akiyama, H. A. Haus, and J. Michel, *J. Lightwave Technol.*, "Air Trenches for Sharp Silica Waveguide Bends," vol. 20, pp. 1762-1772, 2002.

[37] J. Yamauchi, M. Ikegaya, and H. Nakano, "Bend loss of step-index slab waveguides with a trench section," *Microw. Optical Technol. Lett.,* **5**, pp. 251-254, June 1992.

[38] L. H. Spieksman, Y. S. Oei, E. G. Metaal, F. H. Groen, P. Demeester, and M. K. Smit, "Ultrasmall waveguide bends: The corner mirrors of the future?," in *Proc. Inst. Elect. Eng. –Optoelectronics,* **142**, Feb. 1995, pp. 61-65.

[39] E. C. M. Pennings, "Bends in optical ridge waveguides: Modeling and experiments, " Ph. D. dissertation, Dept. of Electrical Engineering, Delft University of Technology, Delft, the Netherlands, 1990.

[40] J. A. Kong, *Electromagnetic Wave Theory.* Canbridge, MA: EMW Publishing , 1999.

[41] K. Radhakrishnan and W. C. Chew, "An efficient Krylov-sub-space-based algorithm to solve the dielectric waveguide problem," *IEEE trans. Microwave Theory Tech.,* **49**, pp. 1345-1348, July 2001.

[42] W. P. Huang, C. L. Xu, W. Lui, and K. Yokohama, "The perfectly matched layer boundary condition for modal analysis of optical waveguides: Leaky mode calculations," *IEEE Photon. Technol. Lett.,* **8**, pp. 652-654, May 1996.

[43] S.Akiyama, M. Popović, P. T. Rakich, K. Wada, J. Michel, H. A. Haus, E. P. Ippen, L. C. Kimerling, "Air Trench Bends and Splitters for Dense Integration in Low Index Contrast," *J. Lightwave Technol.,* in press.

[44] R. Germann, H. W. Salemink, R. Beyeler, G. L. Bona, F. Horst, I. Massarek, and B. J. Offrein, "Silicon Oxynitride Layers for Optical Waveguide Applications," *J. Electrochem. Soc.*, 47, pp. 2237-2241, 2000.

[45] A. Sakai, G. Hara, and T. Baba, "Propagation Characteristics of Ultrahigh-Δ Optical Waveguide on Silicon-on-Insulator substrate," *Jpn. J. Appl. Phys.* **40,** pp. L383-L385, (2001).

Chapter 4:

[46] S. John, *Phys. Rev. Lett.* **58**, 2486 (1987).

[47] E. Yablonovitch, *Phys. Rev. Lett.* 58, 2059 (1987).

[48] A. Mekis, J. C. Chen, I. Kurland, S. Fan, P. R. Villeneuve, and J. D. Joannopoulos. Phys. Rev. Lett., **77**, 3787 (1996).

[49] M. Lončar, T. Doll, J. Vučković, A. Scherer, "Design and Fabrication Silicon Photonic Crystal Optical Waveguides," *J. Lightwave Technol.*, vol. 18, pp. 1402-1411, 2000.

[50] T. Zijlstra, E. W. J. M. van der Drift, M. J. A. de Dood, E. Snoeks, and A. Polman, *J. Vac. Sci. Technol.,* **B17**, pp.2734, (1999).

[51] B. H. Cumpston, S. P. Ananthavel, S. Barlow, D. L. Dyer, J. E. Ehrlich, L. L. Erskine, A. A. Heikal, S. M. Kuebler, I. Y. S. Lee, D. McCordmaughon, J. Q. Qin, H. Rockel, M. Rumi, X. L. Wu, S. R. Marder, and J. W. Perry, *Nature*, **398,** p.51, (1999).

[52] J. D. Plummer, M. D. Deal, and P. B. Griffin, *Silicon VLSI Technology*, Prentice hall, (2000).

[53] Metricon Corporation's home page, http://www.metricon.com/

[54] Y. Yi, Ph.D. Thesis, Massachusetts Institute of Technology, 2004.

[55] S. M. Sze, Physics of Semiconductor Devices, 2nd edition, New York, John Wiley & Sons, (1981).

[56] Y. Xu, G. X. Ouyoung, and R. K. Lee, "Asymptotic Matrix Theory of Bragg Fibers," *J. Lightwave. Technol.*, vol. 20, pp. 428-4440, 2002.

[57] A. Sharma and S. G. Schulman, "Introduction to Fluorescence Spectroscopy," John Wiley & Sons, (1999).

[58] M. Miyagi and S. Kawakami, "Design Theory of Dielectric-Coated Circular Metallic Waveguides for Infrared Transmission", *J. Lightwave Techol.*, **LT-2**, 116 (1984).

[59] N. Croitoru, J. Dror and I. Gannot, "Characterization of hollow fibers for the transmission of infrared radiation", *Appl. Optics*, **29**, 1805 (1990).

[60] Y. Kato and M. Miyagi, "Modes and Attenuation Constants in Circular Hollow Waveguides with Small Core Diameters for the Infrared", *IEEE Trans. Microwave Theory and Tech.,* **40**, 679 (1992).

[61] F. E. Vermeulen, T. Wang C.R.James and A.M. Robinson, "Propagation of Infrared Radiation in Hollow Microstructural Cylindrical Waveguides", *J. Lightwave Techol.*, *11*, 1956 (1993).

[62] R. L. Kozodoy, A.T. Pagkalinawan and J. A. Harrington, "Small-bore hollow waveguides for delivery of 3-υm laser radiation", *Appl. Optics,* **35**, 1077 (1996).

[63] T. Baba, A. Motegi, T. Iwai, N. Fukaya, Y. Watanabe and A. Sakai, "Light Propagation of Straight Single-Line-Defect Waveguide in Photonic Crystal Slabs Fabricated Into a Silicon-on-Insulator Substrate," *J. of Quan. Electron.*, vol. 38, No. 2, pp. 743-752, 2002.

[64] Borel et al., "Very low-losses for TM polarized light in photonic crystal waguide," *Lasers and Electro-optics*, CLEO/Pacific Rim 2003, The 5th Pacific rim conference on, vol. 1, pp. 15-19, Dec. 2003.

[65] J. Arentoft, T. Sondergaard, M. Kristensen, A. Boltasseva, M. Thorhauge and L. Frandsen, "Low-loss silicon-on-insulator photonic crystal waveguide," *Electron. Lett.*, vol. 38, issue 6, pp. 274-275, 14 March 2002.

Chapter 5:

[66] J. D. Plummer, M. D. Deal, and P. B. Griffin, *Silicon VLSI Technology*, Prentice hall, (2000).

[67] D. E. Aspens, *Properties of Silicon*, INSPEC, IEE, London, UK, ch.2, pp. 59-80.1988.

[68] M. A. Omar, *Elementary Solid State Physics*, ch.5, Addison Wesley Publishing, 1993.

[69] J. D. Joannopoulos, R. D. Meade, and J. N. Winn, *Photonic Crystals*, Princeton, 1995.

[70] M. Bruel, "Silicon on insulator material technology," *Electron Lett.*, **31**, pp.1201, 1995.

[71] U.S. Patent 6,380,556. "Optical function device with photonic band gap and/or filtering characteristics," April (2002).

[72] C. G. van der Walle, "Band lineups and deformation potentials in the model-solid theory," *Physical Review B.*, 39(3), pp. 1871-1883, (1989).

Chapter 6:

[73] D. E. Aspens, *Properties of Silicon*, INSPEC, IEE, London, UK, ch.2, pp. 59-80.1988.

[74] J. D. Plummer, M. D. Deal, and P. B. Griffin, *Silicon VLSI Technology*, Prentice hall, (2000).

[75] Steinmeyer, G., et al., *Frontiers in Ultrashort Pulse Generation: Pushing the Limits in Linear and Nonlinear Optics.* Science, 1999. 286: p. 1507-1511.

[76] S. Tsuda et al., Mode-locking ultrafast solid-state lasers with saturable Bragg reflectors. *IEEE J. sel. Topics in Quantum Electronics*, **2**: p. 454-464, 1996.

[77] D. E. Spence, , P.N. Kean, and W. Sibbett, 60-fsec pulse generation from a self-mode-locked Ti:Sapphire laser. *Optics Lett.,* 1991. **16**: p. 42-44, 1991.

[78] N. J. Doran, and D. Wood, Nonlinear-optical loop mirror. *Opt. Lett.,* **13(1)**: p. 56-58, 1988.

[79] L. Krainer et al., Compact Nd:YVO4 lasers with pulse repetition rates up to 160 GHz. *IEEE J. of Quantum Electronics*, **38(10)**: p. 1331-1338, 2002.

[80] S. C. Zeller et al., Passively mode-locked 40-GHz Er:Yb:glass laser. *Appl. Phys. B*, **76**: p. 787-788, 2003

[81] D. J. Jones, S. A. Diddams, J. K. Ranka, A. Stentz, R. S. Windeler, J. L. Hall, S. T. Cundiff, "Carrier-Envelope Phase Control of Femtosecond Modelocked Lasers and Direct Optical Frequency Synthesis," *Science,* **288(5466)**, 635-9 (2000).

[82] Thoen, E.R., et al., *Two-photon absorption in semiconductor saturable absorber mirrors.* Applied Physics Lett., 1999. **74**: p. 3927 -- 3929.

[83] R. Schibli et al., "Suppression of modelocked Q-switching and break-up into multiple pulses by inverse saturable absorption," *Applied Physics B*, **70**, pp. 41 – 49, 2000.

[84] U. Keller, "Recent developments in compact ultrafast lasers," *Nature*, **424**, pp.831-838, 2003.

[85] H. A. Haus, "Parameter ranges for cw passive modelocking," *IEEE J. Quantum Electronics*, **12**, pp. 169-176, 1976.

[86] F. X. Kärtner, I. D. Jung, and U. Keller, "Soliton Modelocking with Saturable Absorber," *Special Issue on Ultrafast Electronics, Photonics and Optoelectronics, IEEE J. Selected Topics in Quantum Electronics (JSTQE)*, **2(3)**: pp. 540-556, 1996.

[87] S. C. Zeller et al. "Passively mode-locked 50-GHz Er:Yb:glass laser," *in Conference on Lasers and Electro-Optics.* 2004. San Francisco: OSA.

[88] H.-C. Luan, D. R. Lim, K. K. Lee, K. Chen, M., J. G Sandland, K. Wada, and L. C. Kimerling, "High-quality Ge epilayers on Si with low threading-dislocation densities," *Applied Physics Letters*, 75, pp.2909 – 2911, 1997.

[89] Douglas D. Cannon, Ph.D. Thesis, Massachusetts Institute of Technology, 2004.

[90] Hsin-Ciao Luan, Ph.D. Thesis, Massachusetts Institute of Technology, 2001.

[91] G. W. Bryant, "Two-photon absorption in Ge: band effects," *Phys. Rev. B*, 22(4), pp.1992-1999, 1980.

[92] H. K. Tsang et al., "Optical dispersion, two-photon absorption and self-phase modulation in silicon waveguides at 1.5um wavelength," *Appl. Phys. Lett.*, 80(3), pp. 416-418, 2002.

[93] T. F. Boggess et al., "Optical limiting in GaAs," *IEEE J. of Quantum Electronics,* **QE-21(5),** pp.488-494, 1985.

[94] Wasik, G., et al. *Bulk Er:Yb:glass soliton femtosecond laser.* in *CLEO proceedimgs, CMA4.* 2001.

[95] Spuehler, G.J., et al., *Passively modelocked diode-pumped semiconductor saturable absorber mirror.* Electronics Letters, 1999. 35(7): p. 567-569.

Chapter 7:

[96] J. G. Kassakian, J. M. Miller, and N. Traub, "Automotive electronics power up," *Spectrum, IEEE,* **37**, Issue: 5, pp. 34-39, May 2000.

[97] T. J. Coutts, "A review of progress in thermophotovoltaic generation of electricity, " *Renewable and sustainable energy reviews,* **3**, pp.77-184, 1999.

[98] T. J. Coutts and X. Wu, Mulligan WP, "High performance transparent conducting oxides based on cadmium stannate," *Journal of electronic materials*, **25(6)**, pp.935-943, 1996.

[99] S. M. Sze, Physics of Semiconductor Devices, 2nd edition, New York, John Wiley & Sons, (1981).

[100] X. Wu, 4th TPV Gen. of Elec. Conf. (1998).

[101] M. Zenker, A. Heinzel, G. Stollwerck, J. Ferber, and J. Luther, "Efficiency and Power Density Potential of Combustion-Driven Thermophotovoltaic Systems Using GaSb Photovoltaics Cells," *IEEE trans, on Electron Devices,* 48, pp. 367-376, (2001).

[102] J. L. Pan, H. K. H. Choy, and C. G. Fonstad, "Very Large Radiative Transfer over Small Distances from a Black Body for Thermophotovoltaic Applications," *IEEE transactions on electron Devices,* **47**, pp. 241, (2000).

[103] I. Celanovic, F. O'Sullivan, M. Ilak, J. G. Kassakian, and D. Perreault, "Design and Optimization of One-Dimensional Photonic Crystals for Thermophotovoltaic Applications, in press.

[104] H.-C. Luan, D. R. Lim, K. K. Lee, K. Chen, M., J. G. Sandland, K. Wada, and L. C. Kimerling, "High-quality Ge epilayers on Si with low threading-dislocation densities," *Applied Physics Letters*, **75**, pp.2909 – 2911, 1997.

[105] Vehicle research institute at Western Washington University. http://vri.etec.wwu.edu/tpv.htm

Appendix A:

[106] K. Okamoto, "Fundamentals of Optical Waveguides," Academic press (2000).

[107] R. G. Hunsperger, "Integrated Optics 4th edition," Springer (1995).

[108] A. Kumar, K. Thyagarajan, and A. K. Ghatak, "Analysis of rectangular-core dielectric waveguides – An accurate perturbation approach," *Opt. Lett.*, **8**, pp. 63-65, 1983.

Appendix B:

[109] S.-L. Chuang, *Physics of optoelectronic devices*, John Wiley & Sons, Inc. (1995).